EXPERIMENTAL AND MODELING STUDIES OF LEAN AND RICH EXHAUST CONDITIONS FOR SELECTIVE CATALYTIC REDUCTION OF NO_X WITH NH_3

by

Michael Andrew Smith

A dissertation submitted in partial fulfillment
of the requirements for the degree of
Doctor of Philosophy
(Mechanical Engineering)
in The University of Michigan
2010

Doctoral Committee:

Professor Dionissios N. Assanis, Co-Chair
Research Scientist Stani V. Bohac, Co-Chair
Professor Levi T. Thompson Jr.
Professor Zoran S. Filipi
Research Scientist John W. Hoard

To my Family

ACKNOWLEDGMENTS

I would like to thank my wife, son, and family for their love and support making this possible for me.

I would like to thank Professor Assanis for giving me the chance to work with him these last 5 years. I would like to thank Christopher Depcik for all his guidance and initially getting me started. I would also like to thank Stani Bohac, John Hoard, George Lavoie, and Jason Martz for additional advising/insights they have provided throughout my research

I would like to thank Stephan Klinkert, John Hoard, Markus Shmitzberger, and Doohyun Kim for their work on the reactor bench.

I would like to thank Luke Hagen and Ann Marie Lewis for their valiant effort in obtaining engine results for me.

I would like to thank the Eaton Corporation for their support. Additionally I would like to acknowledge that this work was performed under a Contract 06-0624 "Collaborative Development of Clean Diesel Aftertreatment System through Modeling and Testing" from the Michigan Economic Development Corporation (MEDC) in collaboration with the Eaton Corporation.

Lastly, I would like to thank all my labmates for their support and various coffee time discussions

TABLE OF CONTENTS

LIST OF FIGURES

LIST OF TABLES

NOMENCLATURE

ρ_g = density of the gas phase (kg/m^3)

v_g = velocity of the gas phase (m/s)

t = time (s)

z = spatial coordinate in axial direction (m)

P_g = pressure of the system (Pa)

φ = Fanning friction factor (based on shape of monoliths)

d_{hyd} = hydraulic diameter (m)

ζ = friction factor (based on Reynolds number)

$w_{k,g}$ = mass fraction of species k

ε_g = open frontal area (m^3/m^3)

D_{eff} = effective diffusion coefficient

$\nu_{i,k}$ = stoichiometric coefficients

$\dot{r}\left(c_k^L, T_s\right)$ = molar reaction rate of the catalytic surface reactions with (mol/m^3*s)

c_k^L = concentration of species k at catalyst surface

T_g = gas temperature (K)

T_s = surface temperature (K)

h_k = enthalpy of component k (kJ/kg)

λ_g = thermal conductivity (W/m*K)

a_{trans} = total channel surface area per unit substrate volume (1/m)

k_h = convective coefficient (W/m^2*K)

Δh_i = heat of reaction of catalytic surface reactions (kJ/m^2)

$\dot{q}_{rad}$ = heat loss to surroundings (W/m^3)

λ_s = catalyst thermal conductivity (W/m*K)

$k_{k,m}$ = mass transfer coefficient for species k

$c_{k,g}$ = molar concentration of species k in bulk gas (kmol/m^3)

θ_k = surface coverage fraction of species k

Θ = site density

Re = Reynolds Number

Pr = Prandtl Number

Sc =Schmidt Number

v'_{ki} = reactants species stoichiometric coefficient

v''_{ki} = products species stoichiometric coefficient

κ_k = chemical symbol

v_{ki} = reaction stoichiometric coefficient

$\dot{r}_i$ = rate of production of species k

$\dot{q}_i$ = reaction rate

K_{fi} = forward reaction rate coefficient

K_{ri} = reverse reaction rate coefficient

$c_{k,g}$ = concentration of species k

k = Arrhenius pre-exponential (units vary, kmol/m^3*s)

T = temperature (K)

b = temperature exponential

E = activation energy (J/kmol)

$\bar{R}$ = universal gas constant (J/mol*K)

$\dot{m}$ = mass flow rate (g/s)

DP = different pressure (in H_2O)

B = calibration constant

C = calibration constant

μ_{std} = 191.87 (mp) = standard viscosity

μ_f = air viscosity at actual air temperature and humidity (mp) [from look up table]

ρ_{std} = 0.07488 (lb/ft^3) = standard density

$\frac{\rho_{wet}}{\rho_{dry}}$ = density ratio determined from air temperature and humidity [from look up table]

T_f = actual air temperature (K)

T_{std} = 294.25 (K) = standard temperature

P_f = ambient air pressure (kPa)

P_{std} = 101.3 (kPa) = standard pressure

e_A = error in measurement A

$e_{\text{Resolution}}$ = error in resolution

σ = standard deviation

ABSTRACT

To assist with SCR catalyst sizing and optimization of LNT-SCR aftertreatment systems, a predictive kinetic model is needed. In this dissertation, an iron based zeolite SCR catalyst has been used in a reactor bench to simulate cycling between lean rich exhaust conditions across the catalyst. Steady-state lean SCR kinetic mechanisms were studied with special attention given to quantifying the effects of oxygen on the lean SCR reactions. From these studies, a prominent reaction between NH_3 and N_2O under lean conditions has been discovered. Additionally it was found that kinetic rate forms from literature are inadequate due to their inability to capture the strong non-linear relationship between NO_x conversion and the amount of stored NH_3 on the catalyst. Due to the switch from lean to rich exhaust from the regeneration of the LNT, the effects of varying H_2O and CO_2 concentrations have been studied for the purposed lean SCR reactions. It was found that H_2O strongly affects the storage capacity of NH_3 on the SCR catalyst. From these results an additional reaction has been proposed to capture the effect of H_2O on NH_3 storage. The affects of H_2, CO, and C_3H_6 were studied to understand their roles in rich exhaust conditions. Experimental results have allowed the water gas shift reaction, the oxidations of H_2 and CO, and reactions between NO and H_2, CO, or C_3H_6 to be disregarded. It was observed that H_2, CO, and C_3H_6 have strong reactions with NO_2 yielding the need to include a reaction for each reductant with NO_2 in the kinetic mechanism. It was determined that these reactions with NO_2 can inhibit NO_x conversion on the SCR catalyst by affecting the NO to NO_x ratio at the catalyst, which can be accounted for using NO_2 reactions with CO, H_2, and C_3H_6. It was also observed that the oxidation of C_3H_6 will strongly increase the oxidation of NH_3 which have been accounted

for in a global reaction. CO and H_2 storage on the catalyst is negligible while C_3H_6 has been found to store on the catalyst by a non-traditional method to determine the storage of C_3H_6.

CHAPTER 1

INTRODUCTION

During our lifetimes we have seen the price of oil continue to rise. This has created a high demand for more fuel efficient cars. One popular opinion that exists today has been to move from spark ignition (SI) engines to diesel (CI) engines, especially in passenger cars [1].

Diesel engines operate using compression ignition and have shown great advancement in durability and operation during the last decade. In certain Europe countries, 80% of automobiles contain diesel engines. This is largely due to taxes imposed on engine displacement and fuel in Europe [2, 3]. Diesel engines offer an increase in torque when compared to an equal displacement spark ignition engine. This allows a smaller displacement diesel engine to take the place of a spark ignition engine. With a smaller displacement, engine fuel economy will be increased. When compared to spark-ignition engines, diesel engines also increase fuel economy by utilizing higher fuel conversion efficiencies, higher compression ratios, and by operating under lean conditions. Due to these enhancements, diesel engines will use approximately two thirds of the fuel of an equivalent SI will use under normal operating conditions [4].

While there can be significant gains by using diesel engines, emissions have proven problematic in these engines. Diesel engines utilizes high compression ratios and lean air-fuel mixtures to increase thermal efficiency; however the combination of these will lead to an increase in NO_x formation [4]. While operating at higher compressions

knock is limited by controlling combustion timing, which is done by directly injecting fuel into the cylinder during the compression stroke. Direct injection of fuel will lead to stratification of the air-fuel mixture in the cylinder, which typically increases particulate matter (PM) and hydrocarbon (HC) emissions. Traditional spark-ignition engine are less efficient, but are widely used due to the ease with which they control emissions. SI engines utilize combustion strategies to control PM emissions, and operate at a stoichiometric fuel air mixture which allows the use of a Three-Way Catalyst (TWC) to simultaneous reduce CO, HC, and NO_x emissions by using NO_x to oxidize CO and HC emissions [5, 6]. Due to the lean combustion characteristics of diesel engines, multiple catalytic devices are required to reduce all problematic species [4, 7, 8].

1.1 CO and HC Emissions Control

Until 2003, emissions standards were met by utilizing in cylinder strategies; which include adjusting injection timing and adding EGR. In 2004 aftertreatment devices became the most cost effective way to simultaneously meet CO, HC, NO_x, and PM emissions standards [2]. Initially TWC catalysts were tried, where it was found that TWC catalysts will only effect HC and CO emissions through oxidation with the excess oxygen in the exhaust stream. From the initial work using TWC catalysts on diesel engines, new formulations were proposed commonly referred to as Diesel Oxidation Catalysts (DOC). DOCs operate by using oxygen in warm diesel engine exhaust to induce reactions in non-oxidized exhaust species (CO and HC); however it should be noted that a DOC will not remove any NO_x from the exhaust stream but can reduce volatiles which can reduce PM emissions [9, 10].

1.2 PM Emissions Control

Once CO and HC emissions problems were solved with DOCs, efforts started to reduce NO_x and PM emissions. Simultaneous NO_x and PM reduction with in cylinder combustion strategies have proven difficult with limited operating ranges, and complex control schemes. A Diesel Particulate Filter (DPF) has proven effective and is currently being used to reduce PM emissions [11-13]. A DPF system works as a filter in the exhaust stream capturing and storing PM on the surface while letting the flow of gas phase species continue. As the DPF becomes full the back pressure in the exhaust system will increase, which will trigger a regeneration cycle where the catalyst temperature is increased until all the differential pressure of the DPF decreases to an acceptable level. The common method to increase the temperature of the DPF is to inject fuel into the exhaust stream. The major concerns when using a DPF are the increase in back pressure in the exhaust system, the fuel economy penalty or the regeneration cycle, and the longevity of the DPF due to temperature cycling. Recently DPFs have been combined with DOC catalysts commonly called a catalyzed DPF (cDPF). This catalyst stores oxygen on the surface to help with regenerations as well as oxidizes hydrocarbon and CO emissions in the tailpipe [14].

1.3 NO_x Emissions Control

1.3.1 Hydrocarbon Selective Catalytic Reduction

CO, HC, and PM emissions have proven less problematic by utilizing a DOC and a DPF (or cDPF), however as emissions regulations tighten NO_x emissions have proven to be especially problematic. Three competing technologies have been suggested to reduce NO_x emissions levels. Hydrocarbon Selective Catalytic Reduction (HC SCR) was the first to be studied due to its ability to simultaneously reduce CO, HC and NO_x emissions. The HC SCR systems works by storing and partially oxidizing the HC in the

exhaust and reacting the resulting products with NO_x produced by the engine to produce N_2. If more HC is needed in the exhaust additional fuel is injected, which results in a fuel economy penalty. Most manufacturers are not using HC SCR aftertreatment devices due to a very limited temperature range, and an increasing fuel economy penalty as emissions standards become lower [15].

1.3.2 Lean NO_x Trap

The Lean NO_x Trap (LNT) catalyst system has been investigated as an alternative to HC SCR technology. The LNT system works by storing NO_x molecules on a catalyst during normal lean engine operation, the stored NO_x is then reduced by periodically switching to rich exhaust reducing conditions. The rich exhaust reducing conditions have large H_2, CO, and small HC concentrations along with low oxygen concentrations which are generated by fuel reforming or rich engine operation. The reductants formed during rich exhaust conditions are oxidized by the stored NO_x on the catalyst to regenerate the catalyst by allowing for more storage potential of NO_x. This catalyst technology has been used in smaller diesel engines under 2.5L due to their ability to meet emissions regulations without carrying additional reductant on board. However, because the LNT catalysts are precious metal based they have proven cost prohibitive on heavy duty diesel engines. Additionally, LNTs are also very susceptible to sulfur poisoning and must use low sulfur fuels, and LNT catalysts also pose a fuel economy penalty to meet emissions standards.

1.3.3 Ammonia Selective Catalytic Reduction

Selective Catalytic reduction with ammonia (NH_3 SCR) is the final option for catalytic NO_x reduction. Due to the potential toxicity concerns of storing NH_3 directly on board a vehicle, an aqueous form of NH_3 called urea is commonly used as the onboard

reductant. As a standalone system, the reduction of NO_x with a NH_3 SCR system is a two step process. The first injects urea into the exhaust system upstream of the SCR catalyst [16]. While in the exhaust stream the urea will thermally decompose to NH_3 and CO_2 [17]. As the NH_3 molecules reach the SCR catalyst, reactions with the surface will allow NH_3 to reduce NO_x to N_2 and H_2O. One of the main benefits of using a NH_3 SCR system to lower NO_x production is that it allows the engine to be optimized for fuel economy by reducing the amount of in-cylinder NO_x control needed. The potential savings could allow a payback time for the system in a range of one to two years at current (oil, urea, etc.) prices [2, 18]. The drawbacks to using a NH_3 SCR include creating an infrastructure for refilling urea tanks, the high susceptibility to HC and sulfur poisoning, the high freezing temperature of urea (11ºC), the large overall size of the catalyst system needed due to the additional space required to store the reductant onboard the vehicle, the price of an injection system for urea, for safety concerns urea must be used as the onboard reductant which will increase of CO_2 emissions by 1 – 2% [2, 3]. While the actual catalyst is significantly cheaper then LNT or HC SCR catalysts, due to the high cost of the urea injection systems and the space requirements of the additional on board reductant for the NH_3 SCR system; it has been found that NH_3 SCR systems are ideal for heavy duty diesel engine applications (engines larger than 10L).

1.3.4 Combination Systems

When examining medium duty engines between 2.5 L and 10 L, LNT and NH_3 SCR aftertreatment options are debated since both are cost competitive. It has been proposed that a combination of an LNT and an NH_3 SCR (LNT-SCR) system might allow for the most cost and space effective solution for NO_x control. The LNT-SCR system operates by increasing the regeneration time on the LNT catalyst where H_2 can combine with stored NO_x to form NH_3 which can then be stored on the SCR catalyst to

be used to reduce any NO_x that slips by the LNT. An additional benefit is gained where the SCR will reduce the ammonia generated by the LNT which can be a concern for emissions regulations. The LNT-SCR removes the need for a second on board reductant since onboard fuel can be used to reduce NO_x on the LNT or be converted to NH_3 where it can be used to convert NO_x on the SCR. The LNT-SCR also provides the ability to reduce the size of the LNT which saves money due to the high cost of the catalyst.

The Eaton Aftertreatment System (EAS)

An example of a LNT-SCR catalyst system used for this dissertation is the Eaton Aftertreatment System (EAS), which has been designed to reduce all regulated emissions for a 2007 compliant engine to make it 2010 compliant for a medium duty diesel engine. The EAS (Figure 1.1) is a system of four catalysts that uses onboard reductant (fuel) to reduce NO_x and PM emissions. During normal operation the fuel reformer (REF) catalyst is used to oxidize CO and HC, the LNT is used to store NO_x, the DPF is used to store PM emissions, and the SCR uses stored NH_3 to reduce any NO_x that slips by the LNT. Once the LNT catalyst shows significant amount of slip, regeneration of the LNT is performed. For the LNT regeneration the engine is throttled to operate the engine under richer conditions to reduce the amount of oxygen in the exhaust stream. Fuel is then injected before the fuel reformer to increase the temperature to 350°C. Once the fuel reformer reaches 350°C, additional fuel is injected which is converted to approximately 4.5% H_2, 1.5% CO, and 1% HC (on a C1 basis). The H_2, CO, and HC are then oxidized by stored NO_x on the LNT reducing the amount of NO_x stored on the LNT. NH_3 is generated as a byproduct of the reduction of NO_x with H_2 on the LNT. The NH_3 will then flow to the SCR catalyst where it will store to reduce any NO_x that slips by the LNT [19, 20].

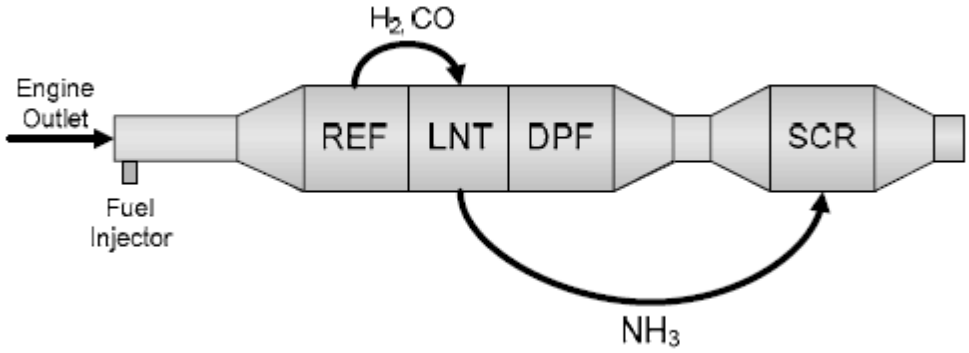

Figure 1.1 − Layout of the Eaton Aftertreatment System [19, 20].

Dykes [20] has studied the average integral NO_x conversion of the EAS system, the LNT, and the SCR, during several NO_x regeneration cycles where it can be seen that the SCR will contribute an additional 10% to the integral NO_x conversion as shown in Figure 1.2. Since catalyst become exponentially bigger as desired NO_x conversion increases, the 10% contribution to the integral NO_x conversion of the SCR has allowed a significant size reduction of the LNT.

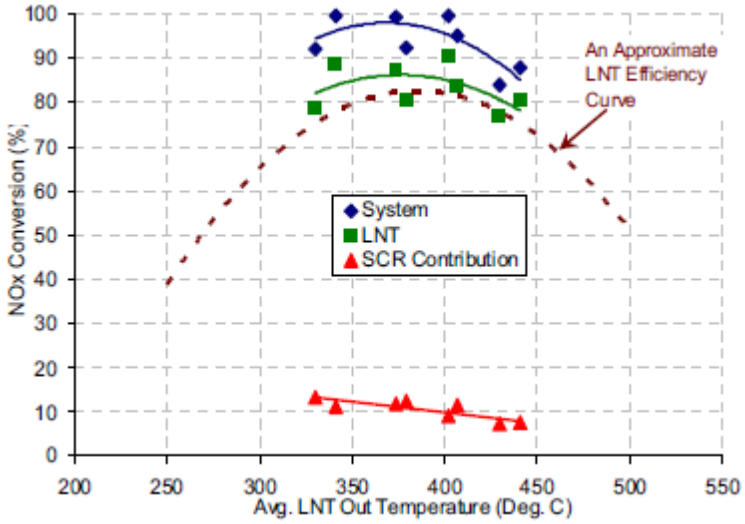

Figure 1.2 – Contribution of integral NO_x conversion of the LNT and SCR catalysts in the EAS [20]

1.4 Selective Catalytic Reduction of NO_x with NH_3

The Ammonia Selective Catalytic Reduction process was developed for powerplant applications as a method for the abatement of NO_x [21] with the first commercial demonstration occurring in the mid 1970s [22]. In this type of application, ammonia is injected into the exhaust stack reducing the NO_x in a homogeneous manner without catalytic material; which is commonly referred to as Selective Non-Catalytic Reduction (SNCR) [22-28]. Ammonia is the preferred reducing agent because it selectively reacts with NO_x in the presence of O_2, H_2O, CO_2 and SO_2 [29]. Without catalytic help, the reduction of NO_x requires temperatures normally in the range of 850 to 1100°C [24, 26, 27] which is significantly higher than seen in the exhaust of internal combustion engines (with a maximum of 600°C) [30], therefore SNCR is not feasible for automotive applications due to its temperature range.

The first research application into the NH_3 SCR process came about in 1957 when it was discovered that ammonia reacts with NO_x over a platinum catalyst even when oxygen is present [21, 29]. This discovery proved that it was possible to reduce NO_x levels at 150 – 250ºC, which are much lower temperatures than the operation criteria of a SNCR system in a lean environment [3, 29]. Since this discovery, there have been numerous development activities to adapt SCR technology for mobile diesel engines [31].

Once it was proven that ammonia could be used to reduce NO_x in a lean environment, research became geared towards finding a catalyst that would facilitate NO_x reduction for internal combustion engines [3, 32-40]. Research initially began with vanadium based catalysts [15, 17, 39], but has recently moved to zeolite base catalysts, while not perfect, have shown due to their increased activity for NO_x reduction with NH_3, and wider temperature windows [18, 41-43]. The two most common types of zeolite based catalysts are iron or copper based. Research has shown that iron based zeolites

have a larger temperature operating range [15, 29], while copper based zeolites are less sensitive to the NO to NO_x ratio in the feed gas into the SCR catalyst [15].

From vanadium and zeolite base catalysts the same reaction steps (shown in Table 1.1) for Selective Catalytic Reduction of NO_x with NH_3 in lean exhaust have been proposed [44-48], although the strength of each reaction steps will differ depending on the catalyst. It has been found that all of the proposed SCR catalysts show some ability to oxidize NO to NO_2 as seen in (R1). It has also been observed that NH_3 has the ability to store on the catalyst as shown in (R2). The stored NH_3 then has the ability to desorb from the catalyst or react with O_2, NO, or NO_2 as seen in (R3) – (R8). Since each of the catalysts have some ability to oxidize NO to NO_2 or reduce NO_2 to NO and O_2, the NO_x reduction reactions shown in (R4) – (R8) are considered to happen simultaneously.

Table 1.1 − Summary of literature global chemical reactions for the Selective Catalytic Reduction of NO_x with NH_3 in lean exhaust conditions.

	Chemical Reaction
(R1)	$NO + \frac{1}{2}O_2 \leftrightarrow NO_2$
(R2)	$Z + NH_3 \leftrightarrow Z(NH_3)$
(R3)	$4Z(NH_3) + 3O_2 \rightarrow 4Z + 2N_2 + 6H_2O$
(R4)	$4Z(NH_3) + 6NO \rightarrow 4Z + 5N_2 + 6H_2O$
(R5)	$4Z(NH_3) + 4NO + O_2 \rightarrow 4Z + 4N_2 + 6H_2O$
(R6)	$2Z(NH_3) + NO + NO_2 \rightarrow 2Z + 2N_2 + 3H_2O$
(R7)	$8Z(NH_3) + 6NO_2 \rightarrow 8Z + 7N_2 + 12H_2O$
(R8)	$2Z(NH_3) + 2NO_2 \rightarrow 2Z + N_2 + N_2O + 3H_2O$

1.5 Objectives

While Dykes [20] has shown that the SCR will increase the integral NO_x conversion of the EAS, it is still unclear how switching from rich and lean exhaust conditions will affect the ability of the SCR catalyst to reduce NO_x. The SCR catalyst in the EAS faces unique conditions where NH_3 is only available to the SCR catalyst during the regeneration of the LNT which is done when the engine is throttled to rich exhaust conditions, while NO_x breakthrough from the LNT to the SCR catalyst occurs during normal lean engine operation. The objective of this work is to propose a global kinetic model to assist with control strategy development as well as sizing of the SCR in a LNT-SCR system.

Initially a modeling study was performed by calibrating the reaction rates using global steady-state lean SCR reactions in literature [45, 49-56] to the experimental reactor bench data for the SCR catalyst in the EAS. Results from the kinetic model were then compared to ideal system operation conditions performed on the reactor bench, where it was discovered that changes to the kinetic mechanism were needed to accurately capture all effects of the LNT-SCR catalyst system. Therefore four independent experimental studies have been performed to study changes to the literature steady-state reaction mechanisms.

The first experimental study was done to test the expected global reactions from literature sources for steady-state lean operation of the SCR in the EAS. It was found that not all effects in lean engine exhaust have been completely quantified. The production of N_2O (R8) is not always included in reaction mechanisms but is commonly thought to occur due to a reaction between NH_3 and NO_2 [45, 57]. Although this has been debated by Kim et al. [47] where it is suggested that reactions with NH_3 and NO, O_2, or NO_2 can yield N_2O. Epling et al. [57] has even suggested that the Slow SCR reaction shown in (R7) is actually a combination of the production of N_2O as a

combination of NO_2 and NH_3, then a reduction of N_2O with NH_3. Due to the unclear nature of these reaction pathways further experiments have been performed with NH_3, NO_2, and N_2O in the feed gas to quantify the appropriate reaction pathways.

The second experimental study is done to test how steady-state reactions compare to the unsteady operation of the SCR in a LNT-SCR catalyst system. Under steady-state conditions in an SCR, reactions with NH_3 and NO_x occur almost instantaneously, therefore very little NH_3 is present on the catalyst at all times. To account for the unsteady nature of the LNT-SCR system, cycling experiments have been performed to quantify the effect of stored NH_3 on NO_x conversion.

The third and forth experimental studies were performed to find what happens to the chemistry of the SCR catalyst when exposed to rich engine conditions. When the regeneration of the LNT occurs under rich exhaust conditions, H_2O and CO_2 concentrations will increase in the exhaust stream, as well as the possibility for H_2, CO, and HC breakthrough to the SCR. Therefore the third experimental study was performed to study how H_2O and CO_2 concentrations will affect the proposed SCR reactions. The forth experimental study was performed to quantify the effects H_2, CO, and HC will have on the SCR chemistry.

CHAPTER 2

METHODOLOGY

Since the overall goal is to propose the correct chemical reactions and estimate their corresponding kinetic rate forms, a methodology needs to be established. A flow chart for the methodology is shown in Figure 2.1. For model development AVL BOOST is used to solve the conservations equations (mass, species, momentum, energy) with custom defined chemical reactions and kinetic rate forms written by the user. Initially the chemical equations and kinetic rates are developed from literature sources. Experimental data are taken using a bench top reactor, where synthetic gas blends can be made to isolate proposed reactions and vary catalyst temperature and space velocity. Initial kinetic rate equations are commonly based on Arrhenius rate forms as shown in equation (2.1).

$$K = k \cdot \exp^{\left(\frac{-E}{\overline{R} \cdot T}\right)} \prod_{k=1}^{K} [y_k] \tag{2.1}$$

Where the pre-exponential (k) and the activation energy (E), are allowed to be varied using an optimization routine and reapplied to AVL BOOST until the simulations results match experimental data taken on the bench top reactor.

Once simulation results for the proposed kinetic mechanism are statistically significant when compared to experimental results for all reactions, additional simulations are performed and compared to validation data. Validation data can come

from the engine operation with EAS, or different bench top reactor experiments that simulate the LNT-SCR catalyst system.

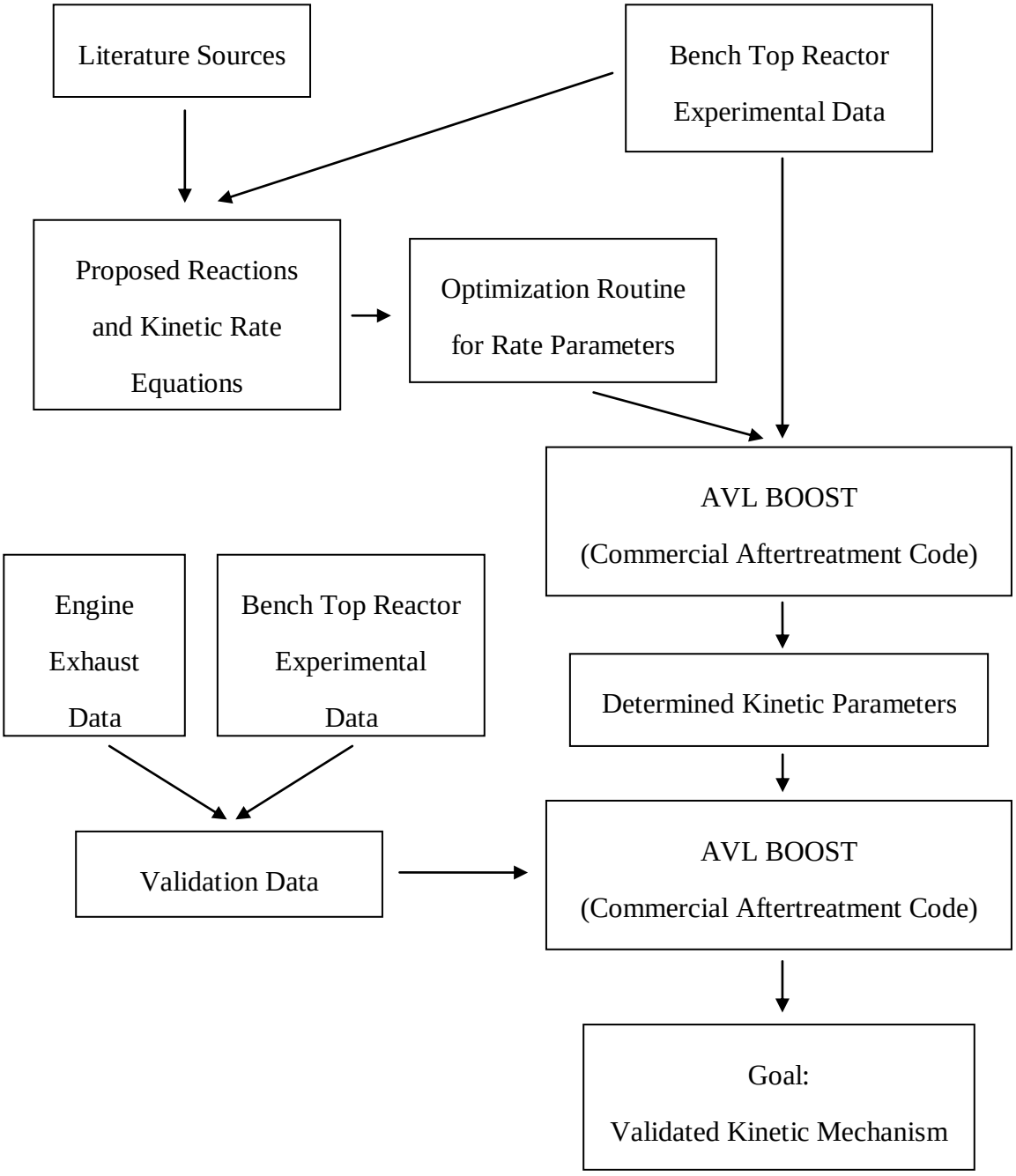

Figure 2.1 – Shows the flow chart for the methodology of determining chemical reaction and kinetic rate equations to be used in a validated kinetic mechanism

2.1 Aftertreatment Modeling

AVL BOOST is used to develop a kinetic mechanism for aftertreatment catalysts. Aftertreatment modeling is usually done as two parts; the first part is developing a solver for the conservation equations that occur during this process. Since many aftertreatment models have been developed, a commercial aftertreatment model (AVL BOOST) is used to solve the conservation equations (mass, momentum, species, and energy). The second part of is the development of the appropriate chemical reactions and kinetic rate forms. AVL BOOST was chosen due to the ability to define chemical reactions with custom kinetic rate forms.

The use of a global kinetic mechanism is suggested since rate parameters must be determined for each reaction. The goal of global kinetics is to use the minimum amount of reactions to characterize the behavior of the catalysts. A simple example of a global reaction for the oxidation of CO to CO_2 is shown in (2.2). It should be noted that the addition of each species exponential increases the amount of detailed reactions required. It can be observed that the detailed approach requires two reactions and four rate constants, while using a global approach requires only one reaction and two rate constants. Since catalyst formulations are always changing and the activity of each catalyst formulation is different, global kinetic models are suggested to reduce the amount of rate parameters to be determined.

$$\begin{array}{r} CO + O \rightarrow CO_2 \\ + \quad \frac{1}{2}\left(O_2 \rightarrow 2O\right) \\ \hline CO + \frac{1}{2}O_2 \rightarrow CO_2 \end{array} \longrightarrow \begin{array}{r} k_1 \exp\left(\frac{-E_2}{\bar{R}T}\right)[y_{CO}][y_O] \\ k_2 \exp\left(\frac{-E_2}{\bar{R}T}\right)\left[y_{O_2}\right] \\ \hline k_{Global} \exp\left(\frac{-E_{Global}}{\bar{R}T}\right)[y_{CO}]\left[y_{O_2}\right] \end{array} \tag{2.2}$$

2.1.1 AVL BOOST Conservation Equations Solver

Catalytic combustion reactors are considered heterogeneous reactors because they contain two phases. (a gas phase (reactants and products) and solid catalyst) Since the catalytic reactions occur on the catalyst, the reactants have to be transported to the external gas-solid interface. Modeling the overall reaction process therefore requires the consideration of both the physical transport and chemical kinetic steps. Figure 2.2 shows the individual steps taking place during a heterogeneous catalytic reaction.

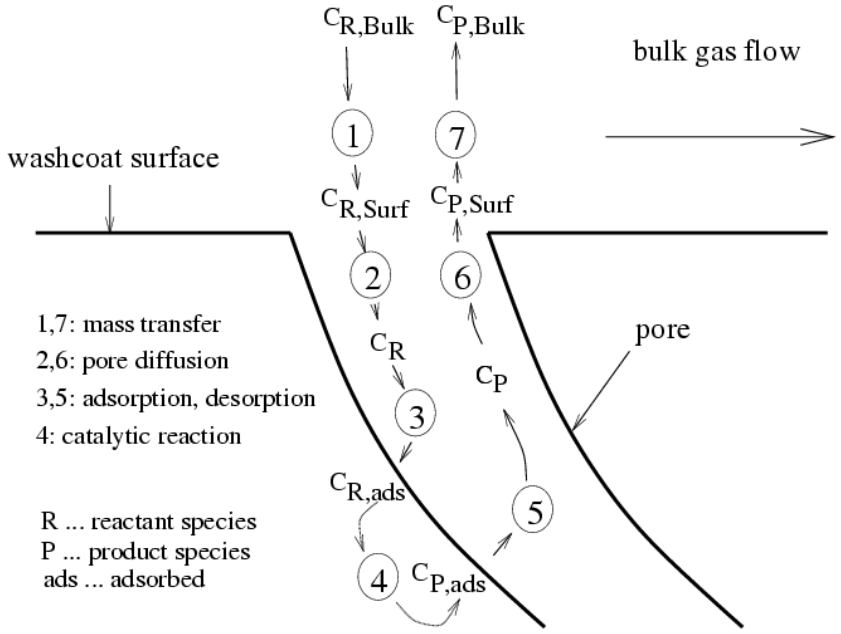

Figure 2.2 − Steps of a Catalytic Reaction where: C_j is concentration of species, P is products, R is reactants, Surf is on the catalyst surface, and Bulk is part of the bulk flow [58].

As discussed by Froment and Bischoff [59] and shown in Figure 2.2, the following steps can be distinguished:

1. Transport of the reactants from the bulk gas phase to the external solid surface across the boundary layer.
2. Diffusion of the reactants into the porous catalyst. Since the main part of the catalyst is located inside the porous material (washcoat) the reactants must diffuse into it.
3. Adsorption of the reactants onto the surface.

4. Catalytic reaction at the surface.
5. Desorption of the products of the reaction.
6. Diffusion of the products to the surface of the catalyst.
7. Transport of the products into the bulk gas phase.

Steps 1, 2, 6 and 7 are mass transport steps while steps 3, 4 and 5 are chemical kinetic steps.

To accomplish the above steps the catalyst structure first needs to be determined. The catalyst structure is determined based on the following known catalyst properties:

- Amount of monoliths in the catalyst
- Length of the catalyst
- Radius of the catalyst
- Size of each monolith
- Monolith Volume
- Open frontal area of the monolith
- Hydraulic area
- Catalyst density
- Catalyst thermal conductivity

From these properties the catalyst geometry as well as thermal properties of any catalyst brick can be determined for use in the conservation equations.

AVL BOOST Conservation Equations

Using the kinetic mechanism created it was assumed that radial transport effects of a honeycomb-type catalytic converter are small compared to the heat transport in axial direction which means that the entire catalyst can be represented by one single channel. The effects taking place in this model are convective, diffusive, and conductive transport in the gas phase; mass and energy transfer through the boundary layer; diffusion and

catalytic conversion in the wash-coat; and conduction in the solid phase. Neglecting the radial effects the continuity equation become equation (2.3).

$$\frac{\partial \rho_g}{\partial t} = \frac{\partial \rho_g \cdot v_g}{\partial z} \tag{2.3}$$

Using the steady – state Darcy equation the momentum equation (2.4) becomes where spatial variation as well as friction from the flow are accounted for.

$$\frac{\partial P_g}{\partial z} = \varphi \cdot \frac{{v_g}^2}{2} \cdot \frac{\rho_g}{d_{hyd}} \cdot \zeta \tag{2.4}$$

The species conservation equation is given by equation (2.5).

$$\varepsilon_g \cdot \frac{\partial \rho_g \cdot w_{k,g}}{\partial t} = \varepsilon_g \cdot \frac{\partial}{\partial z}\left(\rho_g \cdot D_{eff} \cdot \frac{\partial w_{k,g}}{\partial z} \right) + MG_{k,g} \cdot \sum_i^I \nu_{i,k} \cdot \dot{r}\left(c_k^L, T_s \right) \tag{2.5}$$

Viscous flow is neglected because the low velocity of the gas phase therefore the energy equation can be written as equation (2.6) [58].

$$\begin{aligned} &\varepsilon_g \cdot \frac{\partial}{\partial t}\left(\rho_g \cdot \sum_k^K w_{k,g} \cdot h_k \right) = \\ &\varepsilon_g \cdot \frac{\partial}{\partial z}\left(\sum_k^K w_{k,g} \cdot h_k \cdot v_g \right) + \varepsilon_g \cdot \frac{\partial}{\partial z}\left(\lambda_g \cdot \frac{\partial T_g}{\partial z} \right) + \\ &\sum_k^K \varepsilon_g \cdot \left(\rho_g \cdot D_{eff} \cdot \frac{\partial w_{k,g}}{\partial z} \cdot h_k \right) + a_{trans} \cdot k_h \cdot \left(T_s - T_g \right) - \sum_i^I \Delta h_i \cdot \dot{r}\left(c_k^L, T_s \right) \end{aligned} \tag{2.6}$$

The energy from the gas phase is released to the solid phase in the catalyst therefore energy equation for the solid phase of the catalyst becomes equation (2.7).

$$\begin{aligned} &\left(1-\varepsilon_g\right) \cdot \rho_s \cdot \frac{\partial\left(c_{p,s} \cdot T_s \right)}{\partial t} = \\ &\left(1-\varepsilon_g\right) \cdot \frac{\partial}{\partial z}\left(\lambda_s \cdot \frac{\partial T_g}{\partial z} \right) + a_{trans} \cdot k_h \cdot \left(T_S - T_g \right) - \sum_i^I \Delta h_i \cdot \dot{r}\left(c_k^L, T_s \right) + \dot{q}_{rad} \end{aligned} \tag{2.7}$$

Because the gas concentration of a species is different in the bulk flow from the space directly above the catalyst equation (2.8) is used.

$$a_{trans} \cdot k_{k,m} \cdot \left(c_k^L - c_{k,g} \right) = \sum_i^I \dot{r} \left(c_k^L, T_s \right) \tag{2.8}$$

The last conservation equation accounts for the species stored on the surface using equation (2.9).

$$\frac{\partial \theta_k}{\partial t} \left(\Theta \cdot a_{trans} \right) = \dot{r}_k \tag{2.9}$$

Transfer Coefficients

Empirical relationships can be used to calculate the heat and mass transfer coefficients. BOOST uses the Sieder/Tate [60] relationship to define the transfer coefficients as seen in equations (2.10) and (2.11).

$$k_h = \frac{1.86 \cdot \left(\mathrm{Re} \cdot \mathrm{Pr} \cdot \frac{d}{l} \right)^{1/3} \lambda_g}{d_{hyd}} \tag{2.10}$$

$$k_{k,m} = \frac{1.86 \cdot \left(\mathrm{Re} \cdot Sc \cdot \frac{d}{l} \right)^{1/3} D_{k,g}}{d_{hyd}} \tag{2.11}$$

BOOST Enthalpy and Heat Capacity Calculations

Table 2.1 describes the where each of the thermal and fluid properties are defined from their reference sources.

Table 2.1 − Shows where all gas thermal fluid properties are determined

Property	Unit	Reference
Molecular Weight	kmol/kg	Tabulated from literature
Specific Heat	kJ/kg*K	Polynomial fits from Barin [61]
Enthalpy	kJ/kg	Polynomial fits from Barin [61]
Entropy	kJ/kg*K	Polynomial fits from Barin [61]
Thermal Conductivity	W/m*K	Polynomial fits from VDI et al [62], and Reid et al [63]
Viscosity	Pa*s	Polynomial fits from VDI et al [62], and Reid et al [63]
Diffusion Coefficients	m^2/s	Binnary acc. To Fuller et al. [64], mixture acc. To Perry et al. [60](Wilke Method)

Boundary Conditions

Using BOOST to solve the above differential equations requires boundary conditions need to be applied. For the continuity and momentum equations to be solved an outlet pressure and an inlet mass flux need to be applied. For the energy and species equations inlet temperatures and mass fractions need to be applied. Lastly either heat loss boundary conditions need to be applied or the simulation can be run as assuming the catalytic converter is adiabatic

Chemical Reaction Rate Calculations

Chemical reactions can be written in the following form shown in equation (2.12).

$$\sum_{k=1}^{K} \nu'_{ki} \cdot \kappa_k \leftrightarrow \sum_{k=1}^{K} \nu''_{ki} \cdot \kappa_k \tag{2.12}$$

The stoichiometric coefficient for a reaction is defined in equation (2.13).

$$\nu_{ki} = \nu''_{ki} - \nu'_{ki} \tag{2.13}$$

The rate of production of species k is defined by equation (2.14).

$$\dot{r}_i = \sum_{i=1}^{I} \nu_{ki} \cdot \dot{q}_i \tag{2.14}$$

The reaction rate is defined by the difference between the forward and backward reaction rates shown in equation (2.15).

$$\dot{q}_i = K_{fi} \cdot \prod_{k=1}^{K} \left[c_{k,g} \right]^{\nu'_{ki}} - K_{ri} \cdot \prod_{k=1}^{K} \left[c_{k,g} \right]^{\nu''_{ki}} \tag{2.15}$$

The reaction rate coefficients are initially defined by the Arrhenius Rate Law [65] (equation (2.16)) but can be changed as shown later in the document.

$$K = k \cdot T^b \cdot \exp\left(\frac{-E}{\bar{R} \cdot T} \right) \tag{2.16}$$

While using equation (2.15) the concentration can come in two forms one form for gas phase species (equation (2.17)), the second for stored species on a catalyst (equation (2.18)).

$$c_{k,g} = y_{k,g} \cdot \frac{P_g}{\bar{R} \cdot T_g} \tag{2.17}$$

$$c_{k,g} = \theta_k \cdot \Theta \tag{2.18}$$

2.2 Experimental Equipment

A bench top reactor is commonly used for global kinetic model development. The bench top reactor allows for synthetic gas blends to be created that allow the user to isolate reactions on a catalyst. The bench top reactor also allows the user to control the flow rate and temperature of the gas as it reaches the catalysts. This allows the user to further isolate reactions based on temperature and the space velocity exposed to the catalyst. Additionally the developed aftertreatment models can be compared to engine results for validation of the kinetic mechanism. This section will describe the experimental equipment used to generate the data presented in this document.

2.2.1 Bench Top Reactor

The flow reactor was designed and built by Stefan Klinkert. The flow reactor consists of the follow major parts as can be seen in the schematic in Figure 2.3 with further details given in [66].

- Various gas bottle (O_2, CO_2, CO, H_2, NO, NO_2, NH_3, C_3H_6; in nitrogen balance) and liquid nitrogen supply with pressure regulators
- 21 Mass flow Controllers (Brooks)
- 2 Peristaltic Pumps for H_2O delivery(Cole Parmer)
- 2 H_2O Vaporizers (in-house design)
- 2 Tube Furnaces (Lidenberg)
- Heat tapes (Brisk Heat) and solid-state-relay temperature controllers (Watlow)
- Data acquisition (DAQ) hardware and software (NI / Labview)
- Various K-Type Thermocouples (Omega)
- 2 Pressure Transducers (Omega)

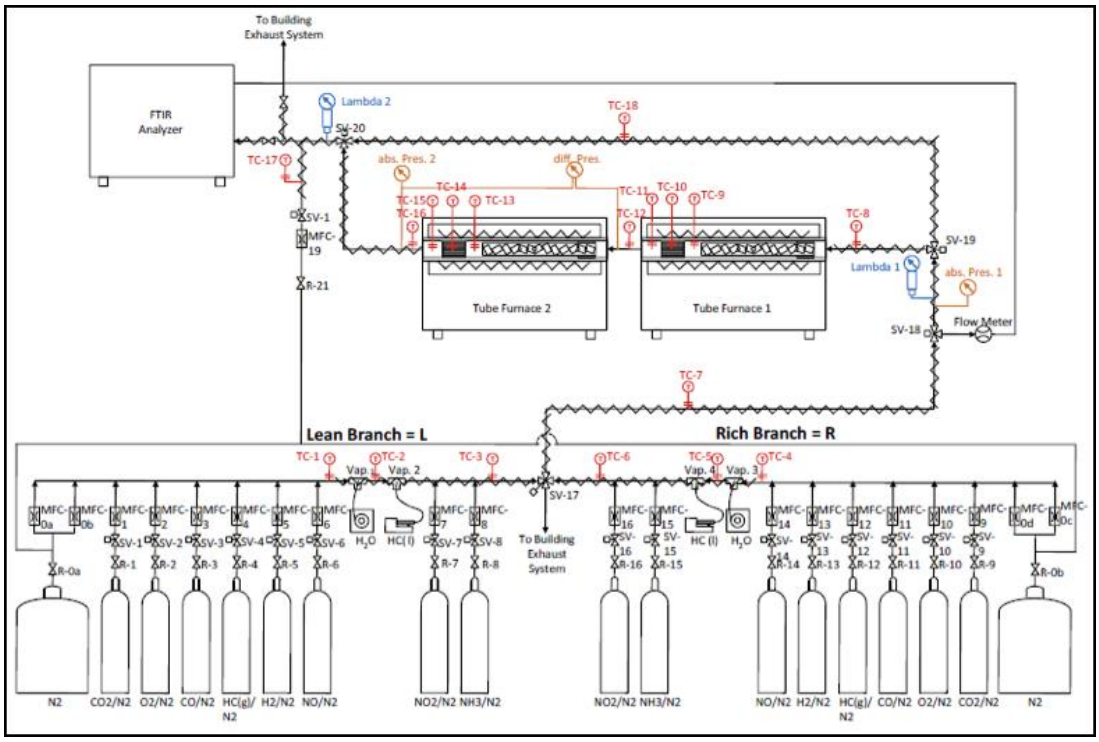

Figure 2.3 − The layout of the synthetic exhaust reactor bench used to obtain experimental data based on work by Klinkert et al. [66].

The reactor is designed to have two synthetic gas mixing sections titled the Lean Branch and the Rich Branch where different gas blends are made. These branches meet at a four way valve controlled by a fast acting solenoid. The four way valve has two inlets and two exits. The inlets are connected to the Lean and Rich Branches. One exit is connected to a vent line, while the other is connected to the tube furnaces where the catalyst temperature can be controlled. The reactor bench has the ability to select different gas concentrations from either the Lean Branch or Rich Branch to flow the tube furnace where the catalyst temperature is being controlled. The outlet of the tube furnaces is connected to a MKS FTIR for emissions measurements, V&F H-Sense for hydrogen measurements, and a Horiba O_2 analyzer for oxygen measurements. The reactor bench contains an additional pathway bypass the tube furnaces directly to emissions analyzers, to measure inlet conditions to the tube furnaces. At the outlet of the tube furnaces an additional MFC is connected to apply dilution N_2 to the reactor flow gas

for faster response of the emissions analyzers. The entire reactor bench is wrapped with heat tapes and controlled to 190°C to avoid H_2O condensation.

Mass Flow Controllers

All MFCs were verified within error using an Omega digital volume flow sensor. The MFC listed error is less than 0.2% of full scale flow. The full scale flow for each MFC, the maximum concentration values for each gas at 50,000 h^{-1} SV (6 L/min total flow for 1 inch catalyst length), and the expected error for each MFC at a 50,000 h^{-1} SV are listed in Table 2.2 for the lean and rich branches [66].

Table 2.2 – Full flow of each MFC and respective concentration of gas cylinder each MFC is connected to.

Gas	Lean Branch			Rich Branch		
	Total Flow	Max Conc.	Expected Error	Total Flow / Error	Max Conc.	Expected Error
	(mL min^{-1}/%)	(ppm)	(ppm)	(mL min^{-1}/%)	(ppm)	(ppm)
N_2	8000/100	Balance	Balance	8000/100	Balance	Balance
CO_2	1200/100	200,000	400	1200/100	200,000	400
O_2	720/1	120,000	240	2000/10	60,000	120
CO	1200/1	2,000	4	1200/7.5	30,000	60
C_3H_6	600/2	2,000	4	1200/10	20,000	40
H_2	600/1	1,000	2	600/100	40,000	80
NO	600/2	2,000	4	600/2	2,000	4
NO_2	600/2	2,000	4	600/2	2,000	4
NH_3	600/2	2,000	4	600/2	2,000	4

Reactor Bench Emissions Analyzers

MKS FTIR

An FTIR analyzer was used to measure the majority of the composition of outflow of the Reactor Bench. The specific instrument used was a 2030-HS Multigas Analyzer manufactured by MKS Instruments Inc. It has the capability to detect species from ppb levels to percent concentration in a gas stream. Identification of specific molecules is accomplished by measuring the absorption spectrum emitted by that species when exposed to an infrared beam in a gas cell. The spectral frequencies and intensities are unique based on the number and strength of chemical bonds among atoms contained in a given molecule. Most gases in engine exhaust are infrared detectable with exception of diatomic gases like O_2, H_2 and N_2. The concentration of gas is determined by comparison of magnitude of the signal compared with pre-loaded calibrations. During the testing, a range of calibrations were loaded into the FT-IR software to look for desired species. The accuracy of MKS FTIR and species measured are shown in Table 2.3 [67].

Table 2.3 – Accuracy of species measureable by the MKS FTIR

Gas	Lowest Detectable Limit
NH_3	0.5 ppm
CO_2	0.2 ppm
CO	1.0 ppm
H_2CO	0.6 ppm
CH_4	1.0 ppm
C_3H_6	1.0 ppm
NO	1.0 ppm
SO_2	1.0 ppm
C_8H_{10}	1.0 ppm
H_2O	100 ppm

V&F H-Sense

H_2 is measured in on Reactor Bench using a sector-field mass spectrometer manufactured by V&F Instruments. The sector field mass spectrometer uses a high speed turbo pump to separate H_2 from the other heavier gases in the exhaust. Then by ionizing and collecting molecules according to charge, the instrument measures the quantity of hydrogen molecules in the gas stream. The V&F H-Sense can be used to measure H_2 concentrations on a wet or dry basis from 1 ppm to 100% [67].

Horriba O_2 Analyzer

A paramagnetic oxygen analyzer is used to determine the amount of oxygen in the exhaust gas sample. This instrument operates by quantifying the magnetic susceptibility of the sample, which is the ability of a molecule to become a temporary magnet when

placed in an oscillating magnetic field. Since oxygen is the only exhaust gas constituent that is strongly paramagnetic, its quantity is readily obtained by using this method. A dumbbell-shaped test body mounted on a quartz fiber is suspended in a nonuniform magnetic field. As the partial pressure of oxygen in the gas sample surroundings the test body changes, the body will rotate. An optical system that senses this rotation causes a voltage to be applied to the test body to maintain it in a stationary position. This voltage is output signal of the amplifier circuit, and is then correlated to the oxygen concentration in the gas sample. The range of 0 – 2% is selected on the O_2 analyzer due to a common dilution ratio of four to one. With the dilution ratio the O_2 Analyzer can operate on a wet basis with up to 2% H_2O. The accuracy of the O_2 analyzer is 1% of the full scale range which yields a value an error value of 200 ppm.

Validation

Validation of the reactor bench was performed by Klinkert et al. [66]. The reactor bench was validated by testing the gas preparation, mixing of the feed gas into the catalyst, and uniform temperature control. The gas preparation was validated by characterizing the command and output concentrations for each gas along with the associated time lag for each species. Glassware to increase turbulence was added to increase mixing of the feed gas, which was validated by commanding concentrations of multiple species in the feed gas. It was found that the addition of the turbulence inducing glassware aided in uniform temperature control, which was validated in the second furnace by finding the temperature distribution in a blank catalyst with seven thermocouples distributed throughout the catalyst.

Catalyst Preparation

The catalyst used in this set of experiments is comprised of 99 channels of a 300 cpsi, Fe-zeolite catalyst core, cut to 19.05 mm diameter and 25.4 mm length. The catalyst was aged for 20 hours in 10% H_2O with a balance of N_2 at 550°C. The wall and washcoat thickness of the catalyst were determined using from digital images taken by a 16-bit Resolution Microscope by the Keyence Corporation (VHX-S50 Serial Num: 5D010002). An example of these images are shown in Figure 2.4

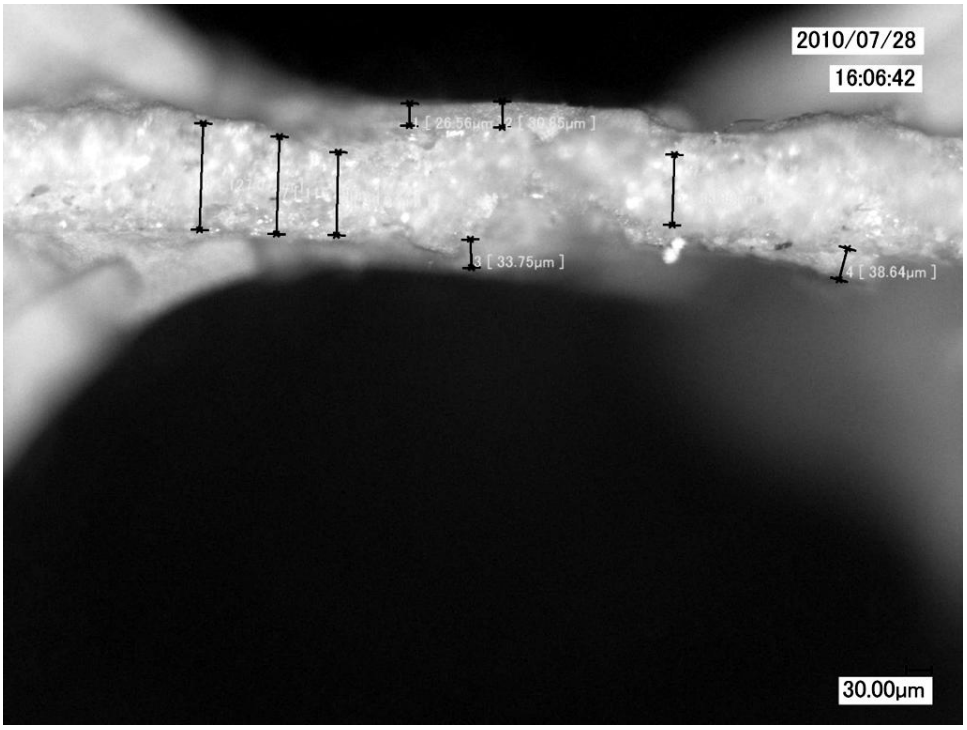

Figure 2.4 – Multiple measurements were taken to get an average wall thickness and washcoat thickness of the SCR catalyst.

2.2.2 Engine Test Cell

The Eaton Aftertreatment System (EAS) shown in Figure 1.1, was configured to operate connected to a 6.4L International Diesel Engine. Emissions were measured before and after the SCR catalyst simultaneously by two MKS FTIRs. Additionally at

the inlet hydrogen measurements were taken with the V&F H-Sense, and oxygen measurements were taken using the AVL CEB II emissions bench. Details of the test cell configuration are as follows in this section.

Engine

The engine used with the EAS is a 6.4 L V-8 direct-injection diesel engine manufactured by the International Truck and Engine Corporation. Known as the Power Stroke, this medium-duty engine is most commonly used in Ford F-series pickup trucks and incorporates advanced technologies to reduce exhaust emissions while maintaining engine performance. Primary engine specifications are shown in Table 2.4.

Table 2.4 – Shows the Engine Specifications for the 6.4L International V8 engine

Engine Type	Diesel, 4 Cycle
Configuration	4 OHV/1 Cam-in-Crankcase-V*
Displacement	6.4 L (390in^3)
Bore and Stroke	98.2 x 105 mm (3.87 x 4.134 in)
Compression Ratio	17.5:1
Aspiration	Series Sequential Turbo/Charge Air Cooler
Rated Power @ RPM	261 kW (350 hp) @ 3000 RPM
Rated Torque @ RPM	881 N-m (650 ft-lb) @ 2000 RPM
Combustion System	High Pressure Common Rail Direct Injection
Total Engine Weight	499 kg (1130 lb)
Coolant Flow	473 L/min (125 gpm) @ 3000 RPM
Air Flow	21.1 m^3/min (744 cfm) @ 3000 RPM
Exhaust Flow	55.6 m^3/min (1962 cfm) @ 3000 rpm
Oil Flow	59 L/min (13 gpm) @ 3000 rpm

The engine is also equipped with an electronically controlled common rail direct injection system. This works by maintaining common lines at high pressures with a central pump. The injectors are then sent an electronic injection signal where fuel is injected. Using this fuel system the engine is capable of multiple injections strategies, meaning there is the ability for multiple pilot, main, and a post injections for every combustion cycle.

AVL Emissions Bench

An AVL Combustion Emissions Bench II (CEB-II) is used to sample condition and measure exhaust gas concentrations. The CEB-II can quantify the amount of CO, CO_2, O_2, total Hydrocarbons (THC), NO and NO_x in the exhaust gases and CO_2 levels from the intake manifold.

THC Analyzer

An ABB Advance Optima Milt-Fid 14 EGA is used to measure the total hydrocarbon emissions. The flame ionization detector (FID) determines the mass fraction of carbon in the sample which is converted to a hydrocarbon-mass basis by assuming a specific carbon to hydrogen ratio recommended for diesel exhaust. A FID uses a burner to combust a stream of hydrogen/helium commonly known as "FID fuel" as diffusion flame in air releasing ions during combustion. The hydrocarbon-containing sample gas is premixed with the fuel and is also consumed in the burner which increases the concentration of ions within the flame. This increase in ionization is directly proportional to the mass flow rate of carbon atoms into the flame. A DC voltage between the burner tip and a collector electrode, which surrounds the flame, collects the ions within the flame causing a current to flow through an electronic circuit which is measured

and associated to total hydrocarbon emissions. The THC Analyzer saves data on a wet basis.

NO_x Analyzer

NO and NO_x emissions are quantified with an Eco-Physics CLD 700 chemiluminescent detector (CLD). This analyzer can only measure the concentration of NO, but incorporates a high-efficiency converter to change any NO_2 present to NO to determine the total NO_x emissions. Light is emitted from the chemiluminescent reaction of NO and ozone (O_3) and when excess O_3 is present, the amount of light emitted is proportional to the concentration of NO. This light is detected by an optical filter-photomultiplier combination that produces an output that is linear to the concentration of NO in the sample. The NO_x Analyzer saves data on a wet basis.

CO and CO_2 Analyzer

Two ABB Advance Optima URAS 14 EGA non-dispersive infrared analyzers (NDIR) are used to determine the amount of CO and CO_2 in the samples. One will measures the amount of CO and CO_2 in the exhaust stream, and the other is used to measure the amount of CO_2 in the intake manifold which is related to the amount of EGR in the system.

The NDIR analyzers detect the infrared energy absorption differential between two gas-filled columns, one sample column and one reference column. Infrared radiation is passed through the sample and reference columns into a detector that has two cells which are filled with gas and physically separated by a flexible metal diaphragm. The infrared radiation collected by each cell heats up its gas and increases the cell pressure. When a sample gas passes through the sample column, some of the infrared energy is absorbed by the gas and less energy will arrive at the sample cell side of the detector due

to the presence of CO and CO_2 in the column resulting in a lower temperature in the sample column. From the ideal gas law it is seen that when the temperature decreases the pressure will decrease. The pressure difference causes a deflection in the metal diaphragm, which is used as one plate of a variable plate capacitor in an electric circuit. The detector output is generated by measuring the amplitude of the oscillating electric current caused the diaphragm, which can be correlated to the amount of CO and CO_2. The CO/CO_2 Analyzer saves data on a dry basis.

O_2 Analyzer

An AB Advance Optima Mangos 16 paramagnetic oxygen analyzer is used to determine the amount of oxygen in the exhaust gas sample. This instrument operates by quantifying the magnetic susceptibility of the sample, which is the ability of a molecule to become a temporary magnet when place in a magnetic field. Since oxygen is the only exhaust gas constituent that is strongly paramagnetic, its quantity is readily obtained by using this method. A dumbbell-shaped test body mounted on a quartz fiber is suspended in a nonuniform magnetic field. As the partial pressure of oxygen in the gas sample surroundings the test body changes, the body will rotate. An optical system that senses this rotation causes a voltage to be applied to the test body to maintain it in a stationary position. This voltage is output signal of the amplifier circuit, and is then correlated to the oxygen concentration in the gas sample. The O_2 Analyzer saves data on a dry basis.

Emissions Error Summary

All analyzers listed above are calibrated with calibration gases. The analyzers are also linearized yearly with a gas divider to make higher order polynomials for the analyzers. Below in Table 2.5 is a list of the associated error for the readings for the above analyzers.

Table 2.5 − Shows the error associated with the AVL CEB II Emissions bench readings based on instrument specifications

Species	Range	Error From Analyzers
THC	10 ppm – 5%	±1 ppm
CO	Low: 50 – 2500 High: 0.5 – 10%	±2 ppm ±100 ppm
CO_2	0.5 – 20%	±100 ppm
NO / NO_x	Low: 30 – 5000 ppm High: 50 – 10000 ppm	±1 ppm ±2 ppm

Dynamometer

A dynamometer is a device that absorbs the rotational energy from an engine and determines the output power by measuring the engine's speed and torque. The dynamometer used in this experimental effort is an AVL ELIN series 100 APA Asynchronous Dynamometer. Table 2.6 shows dynamometer performance specifications [68].

Table 2.6 – Shows the specifications for the AVL ELIN series 100 APA Asynchronous Dynamometer

Speed Range	±8000 RPM
Torque Range	-1273 to +1400 N*m
Power (Absorbing)	330 kW
Power (Motoring)	300 kW
Power Consumption	400 Amps @ 400 Volts

The dynamometer is essentially a highly controllable electric motor/generator. It has a rotor that is connected to the engine via a driveshaft and a stationary stator. When the rotor turns, an electric field is transmitted from the rotor to the stator resulting in a torque as mechanical power is transferred into electrical power. This torque is generated by the moving of magnetic fields between the rotor and stator. The torque on the stator is equal in magnitude and opposite in direction of the engine torque and is resisted by a bending beam mechanism that deflects under load. The deflection of the bending beam is measured with a strain gage and is related to the torque through geometrical and material properties of the beam. Accuracy of dynamometer torque measurements are within ±0.3% of actual values. Rotational speed is obtained from an encoder mounted on the dynamometer's shaft. The encoder measures the frequency of a pulse generated in the encoder by the rotation of the shaft.

Measurements and Calculations

The following states how measurements were taken for input into the BOOST aftertreatment model

Air Mass Flow Measurement

Air coming into the engine first passes through the intake system, where the air is filtered, measured, and then directed into the engine. The flow is measured using a laminar flow element (LFE) that works by slowing the flow through multiple small channels and measuring the small pressure drop across these channels. Other readings needed for these calculations are intake temperature, relative humidity, and barometric pressure. The mass flow rate through the laminar flow element is calculated using equation (2.19).

$$\dot{m} = 7.55987 \rho_{std} \left[B(DP) \cdot C(DP)^2 \right] \left(\frac{\mu_{std}}{u_f} \right) \left(\frac{T_{std}}{T_f} \right) \left(\frac{P_f}{P_{std}} \right) \left(\frac{\rho_{wet}}{\rho_{dry}} \right) \tag{2.19}$$

Table 2.7 shows a list of error for the calculation of air mass flow rate shown in equation (2.19) with the mass flow rate percentage calculated based on the root mean square method.

Table 2.7 – Shows the error associated with intake air mass flow rate readings

Parameter	**Error**
DP	0.1 in H_2O
T_f	0.6°K
P_f	0.05 kPa
Relative Humidity	2.5% RH

The error for the mass flow rate was determined by using the root mean square (RMS) error analysis and is approximately 3% for the range of the engine.

Fuel Mass Flow Measurement

The fuel flow rate is measured by a Micro Motion coriolis flow meter CMF025 model which provides mass flow rate measurements independent of fluid temperature or

composition. This is accomplished by measuring a volumetric flow rate and using a tuning fork to measure the density of the liquid that is traveling through the fuel system. The accuracy of this meter is 0.5% of the flow rate. From the above information the error in total mass flow from the engine can then be calculated as approximately 3% of the total mass flow rate.

2.3 Error Analysis

Error analysis for all modeling and experimental results is performed using the Root Mean Squares method. The error for each measurement is defined as the square root of the sum of the square of the resolution error plus the square of two times the standard deviation as shown in equation (2.20).

$$e_A = \sqrt{e_{resolution}^2 + (2\sigma)^2} \tag{2.20}$$

For calculations performed equations (2.21) – (2.24) can be used to determine the error in the readings

Addition

$$A + B \pm \sqrt{e_A{}^2 + e_B{}^2} \tag{2.21}$$

Subtraction

$$A - B \pm \sqrt{e_A{}^2 + e_B{}^2} \tag{2.22}$$

Multiplication

$$A \cdot B \pm \sqrt{e_A{}^2 \cdot B^2 + e_B{}^2 \cdot A^2} \tag{2.23}$$

Division

$$\frac{A}{B} \pm \frac{A}{B}\sqrt{\left(\frac{e_A}{A^2}\right)^2 + \left(\frac{e_B}{B^2}\right)^2} \tag{2.24}$$

CHAPTER 3

LEAN SCR KINETIC MECHANISM

This chapter details the process to generate a lean SCR kinetic mechanism. The kinetic mechanism is based on literature sources [45, 47, 48] for proposed reaction and kinetic rate forms. The effect of oxygen concentration is focused on specifically due to account for NO_x regeneration in a LNT-SCR aftertreatment system. The results in this chapter detail all pertinent reactions from literature resources for steady state conditions on an iron based SCR catalyst with varying oxygen concentrations. The results were then applied to validation data from the EAS system on an engine as well as further reactor bench experiments.

3.1 NO Oxidation

The oxidation of NO to NO_2 as shown in equation (3.1) can be found on most types of aftertreatment catalysts [45, 69-72]. The oxidation of NO to NO_2 was first theorized for the SCR process in 1980 by Kiovsky et al. [73]. In the early work involving NO decomposition over Zeolite catalysts, it was inferred that the O_2 liberated from the surface during decomposition reacts with the inlet NO to form NO_2 [74].

$$NO + \tfrac{1}{2} O_2 \leftrightarrow NO_2 \tag{3.1}$$

The oxidation of NO is equilibrium limited and subject to the temperature conditions of the monolith. It was later determined to be an important precursor step to

NO_x reduction in the ammonia and HC SCR processes over a zeolite material [75-78]. This was because experiments illustrate that the temperature required for total conversion to nitrogen can be lower when NO_2 is present. The equilibrium basis in the NO oxidation reaction can be seen in Figure 3.1 where the temperature can be determined where the onset of equilibrium kinetics occurs.

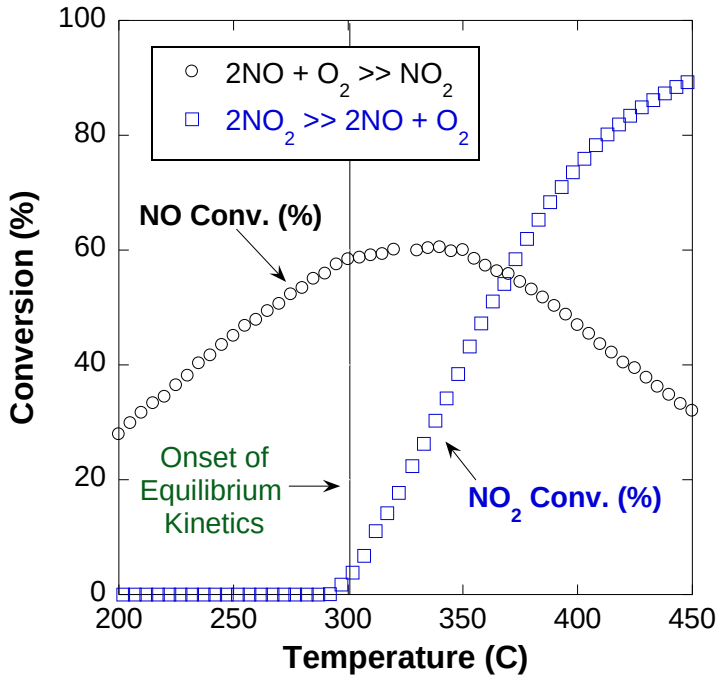

Figure 3.1 − The oxidation of NO to NO_2 is a reversible reaction with the onset of equilibrium chemistry to convert NO_2 to NO and O_2 at higher temperature. Results are shown in temperature ramp experiments with stoichiometric ratios of feed gas with 0% H_2O and 0% CO_2 in the feed gas.

3.1.1 Experimental Results

Experimental data for the NO oxidation reaction when using a bench-top style reactor is collected using constant inlet concentrations and varying temperature in a constant upward or downward ramp rate up to 5°C/min. Experimental results are then compiled to show a conversion percentage vs. temperature profile.

NO Oxidation Effect of Varying O_2 Concentration

By examining the reaction in equation (3.1), it can be predicted that oxygen concentration has a large effect when oxidizing NO to NO_2. NO conversion is defined as the disappearance of NO as seen in equation (3.2), similarly NO_2 conversion is defined in equation (3.3).

$$\eta_{NO} = \left(\frac{c_{NO\_IN} - c_{NO\_OUT}}{c_{NO\_IN}} \right) \cdot 100 \tag{3.2}$$

$$\eta_{NO_2} = \left(\frac{c_{NO_2\_IN} - c_{NO_2\_OUT}}{c_{NO_2\_IN}} \right) \cdot 100 \tag{3.3}$$

Figure 3.2 shows that increasing oxygen concentration will increase the conversion of NO to NO_2.

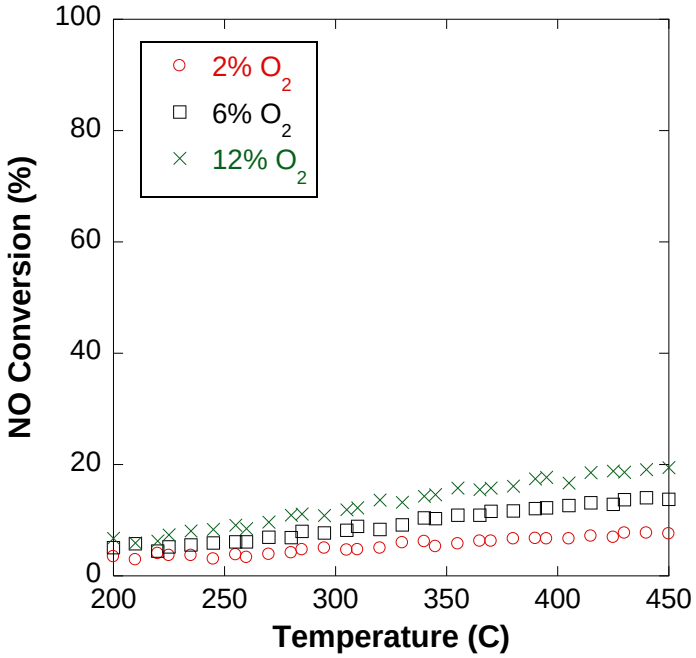

Figure 3.2 − The oxidation of NO to NO_2 is dependent on O_2 concentration in the feed gas, all experiments were performed as a temperature ramp with 6% H_2O, 6% CO_2, and 1000 ppm NO in the feed gas

From the experimental results shown in Figure 3.2 the dependence on oxygen concentration can be determined by the following method. NO conversion efficiency

(η_{NO}) can be defined as proportional to the oxygen concentration to some power (γ) as seen in equation (3.4).

$$\eta_{NO} \propto [O_2]^{\gamma} \tag{3.4}$$

By using the proportionality shown in equation (3.4) the NO conversion efficiency for the experiments for 2% O_2 concentration and 12.0% O_2 concentration can be compared as shown in equation (3.5).

$$\frac{\eta_{NO=12.0\%O_2}}{\eta_{NO=2.0\%O_2}} \propto \frac{[O_2 = 12.0\%]^{\gamma}}{[O_2 = 2.0\%]^{\gamma}} = \left(\frac{[O_2 = 12.0\%]}{[O_2 = 2.0\%]}\right)^{\gamma} \tag{3.5}$$

The log of each side of the proportionality can then be taken (3.6) to find the dependence on O_2 concentration as shown in equation (3.7).

$$\log\left(\frac{\eta_{NO=12.0\%O_2}}{\eta_{NO=2.0\%O_2}}\right) \propto \gamma \log\left(\frac{[O_2 = 12.0\%]}{[O_2 = 2.0\%]}\right) \tag{3.6}$$

$$\gamma \propto \frac{\log\left(\frac{\eta_{NO=12.0\%O_2}}{\eta_{NO=2.0\%O_2}}\right)}{\log\left(\frac{[O_2 = 12.0\%]}{[O_2 = 2.0\%]}\right)} \tag{3.7}$$

The results from this approximation are shown in Figure 3.3, where it can be determined that the average dependence shows conversion at most temperatures to an oxygen dependence of 0.49, which is within error of the proposed kinetic oxygen dependence of 0.5. It should also be noted that the comparison of the 12% O_2 concentration experiment and 6% O_2 concentration yielded similar results.

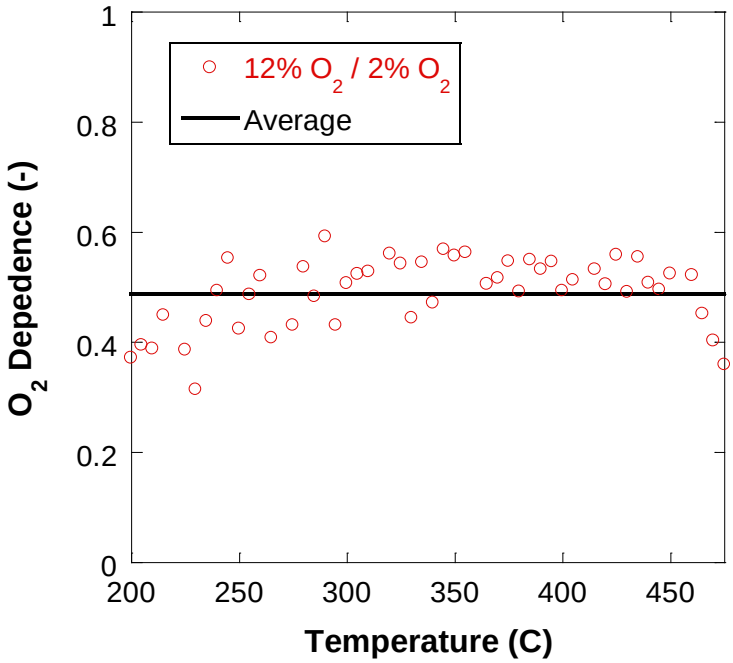

Figure 3.3 − Experimental data matches a half order oxygen dependence for the oxidation of NO to NO_2, all experiments were performed as a temperature ramp with 6% H_2O, 6% CO_2, and 1000 ppm NO in the feed gas.

Figure 3.4 shows the reverse direction of the NO oxidation reaction in equation (3.1) will decrease conversion of NO_2 to NO as oxygen concentration increases. The effect of oxygen concentration is negligible for the reverse rate which is dominated by the equilibrium kinetics shown in Figure 3.1.

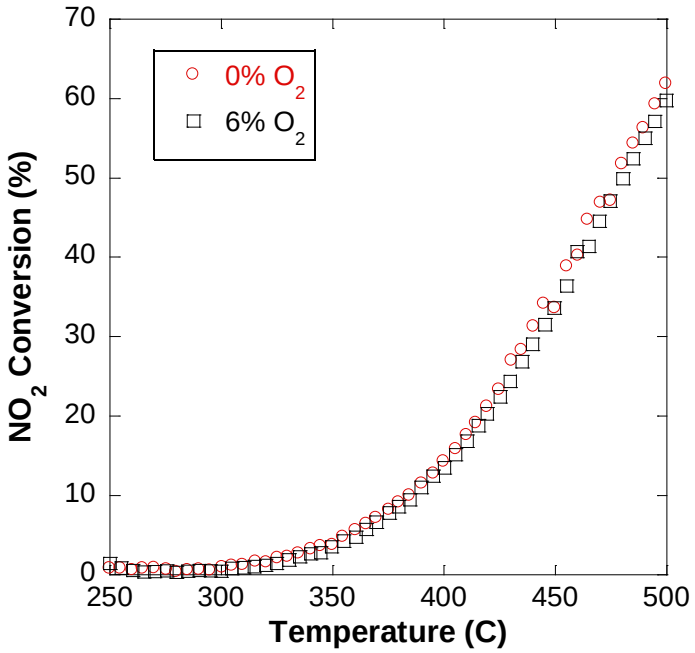

Figure 3.4 – O_2 concentration has negligible effects on NO_2 conversion to NO. All experiments were performed as a temperature ramp with 6% H_2O, 6% CO_2, and 1000 ppm NO_2 in the feed gas.

NO Oxidation Effect with varying H_2O and CO_2 concentration

While it is widely acknowledged that increases in H_2O concentration will decrease NO oxidation to NO_2, the magnitude of this effect will differ among types of SCR catalysts [79, 80]. It was found by Petunchi and Hall [78] that water strongly inhibits the oxidation of NO to the point of complete suppression, however small amounts of NO_2 can still be stored in the presence of this water. It is assumed that CO_2 has very little effect on the NO oxidation process [81]. As a result it was theorized that nitrogen dioxide is the principal component of the NO_x in contact with the catalyst and available for the SCR process [82]. With respect to zeolite catalysts, copper ion-exchanged zeolites are more active then iron ion-exchanged zeolite catalysts for oxidation of NO to NO_2 [42]. While there was still some questions with respect to this being the initial step in the reaction mechanism [83], most authors agree that the copper is desired to activate the NO to form NO_2 to enhance conversion for lean SCR operation

[81, 84]. Eventually, it was determined that this NO oxidation reaction is the rate determining step over a H-ZSM-5 catalyst [85-89]. Recent papers have illustrated that this result can be generalized to the zeolite materials for the SCR process [90-93].

In the experiments shown in Figure 3.5, the oxidation of NO to NO_2 is a dominant effect when H_2O is not present in the feed gas; however in experiments with H_2O present there are only negligible differences in conversion efficiencies. The same effect is seen in the experiments shown in Figure 3.6 where NO_2 conversion to NO is a more dominant effect when H_2O is not present, but when H_2O is present there are only negligible differences. Figure 3.5 and Figure 3.6 show a saturation effect of H_2O inhibition, where saturation effects commonly occur due to species with concentrations above 1% [80].

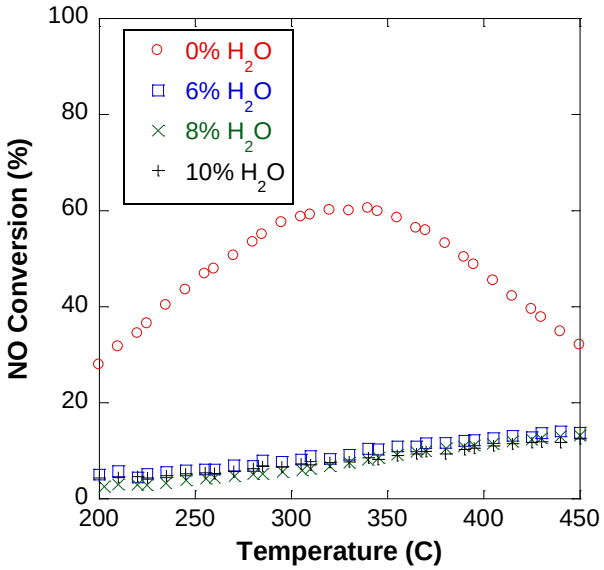

Figure 3.5 − From 0 – 6% water concentration in the feed gas can have large effects on the oxidation of NO to NO_2, while there is little effect on the oxidation of NO to NO_2 when comparing H_2O concentration from 6 – 10%, all experiments were performed with 6% O_2, and 1000 ppm NO.

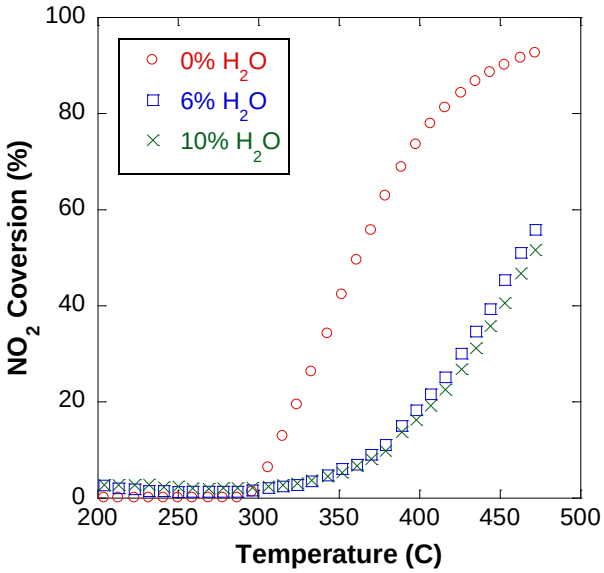

Figure 3.6 − From 0 – 6% water concentration in the feed gas can have large effects in the reduction of NO_2 to NO, while there is little effect in the reduction of NO_2 to NO when comparing H_2O concentration from 6 – 10%, all experiments were performed with 6% O_2, and 1000 ppm NO.

3.1.2 NO Oxidation Modeling Results

To determine the kinetic rate expression for the NO oxidation reaction shown in equation (3.1), a survey of the literature is performed to illustrate a number of important points regarding the different chemical species and their adsorption properties on the surface:

- Water is weakly adsorbed [80], CO_2 is not adsorbed and CO adsorption is negligible.
- Nitrates formed on surface are thermally stable even at conditions in which SCR proceeds with a high rate [81].
- CO adsorption is greater than NO adsorption [81, 94], however there is little to no NO adsorption [95].
- Zeolites absorb mainly NO_2 and only a small amount of NO [78, 96].
- Ammonia hinders oxidation of NO to NO_2 [87].

The original kinetic expression for this reaction over a zeolite comes from a paper based on work by Marangozis [97] and is based on a Langmuir-type isotherm as illustrated in equation (3.8) . Because of the much weaker adsorption properties of NO than O_2, Marangozis converted the rate equation into a power-law format as shown in equation (3.9). However, this form of the equation does not account for the equilibrium limitation of the reaction as shown in Figure 3.1. Recent literature work by Brosius et al. has formulated a reaction rate expression for this reaction over an iron-zeolite catalyst [98]. They generated three different Langmuir-Hinshelwood type of mechanisms as described in equations (3.10), (3.11), and (3.12). In their work, they found that the kinetic rate used in equation (3.12) was more accurate than equation (3.11), while predictions of kinetic rate in equation (3.10) appeared to be poor. It is interesting to note that the Marangozis mechanism in equation (3.8) and the kinetic rate from Brosius et al. in equations (3.10), (3.11), and (3.12) all include the negative half-order dependence on oxygen as found for the NO decomposition reaction which can be validated from experimental data shown in Figure 3.3.

$$R = \frac{kK_{NO}K_{O_2}^{0.5}y_{NO}y_{O_2}^{0.5}}{\left(1+K_{NO}y_{NO}+K_{O_2}^{0.5}y_{O_2}^{0.5}\right)^2} \tag{3.8}$$

$$R = kK_{NO}K_{O_2}^{0.5}y_{NO}y_{O_2}^{m} \tag{3.9}$$

$$R = \frac{k\left(y_{NO}y_{O_2}^{0.5}-\frac{y_{NO_2}}{K_{eq}}\right)}{1+K_A y_{NO}+K_C y_{NO_2}+K_D y_{H_2O}} \tag{3.10}$$

$$R = \frac{k\left(y_{NO}y_{O_2}^{0.5}-\frac{y_{NO_2}}{K_{eq}}\right)}{\left(1+K_{A\,NO}+\sqrt{K_B y_{O_2}}+K_C y_{NO_2}+K_D y_{H_2O}\right)^2} \tag{3.11}$$

$$R = \frac{k\left(y_{NO}^2 y_{O_2}^{0.5} - \frac{y_{NO_2}^2}{K_{eq}^2} \right)}{\left(1 + K_A y_{NO} + K_B y_{O_2} + K_C y_{NO_2} + K_D y_{H_2O}\right)^3} \tag{3.12}$$

Due to equilibrium effects shown in Figure 3.1, the kinetic rate forms listed in equations (3.8) and (3.9) can be eliminated. When evaluating the kinetic rate forms in equations (3.10), (3.11), and (3.12) each contains an equilibrium term for the reverse rate, and a half order dependence on oxygen concentration. Since pressure changes are negligible due to the location of the EAS in exhaust stream, the equilibrium constant can be determined as a function of temperature by fitting equation (3.13) [99] from experimental data published in the JANAF tables [100].

$$K_{eq} = C_1 + C_2\left(\frac{1000}{T}\right) + C_3\left(\frac{T}{1000}\right) + C_4\left(\frac{T}{1000}\right)^2 + C_5 \log\left(\frac{T}{1000}\right) \tag{3.13}$$

Additionally while each kinetic rate form contains an inhibition term for NO, O_2 and NO_2 present in the denominator the dependence on this inhibition changes. Each inhibition term represents adsorption on the catalyst and can change the reaction rate for the NO oxidation reaction shown in equation (3.1).

From literature it can be assumed that NO and O_2 adsorption is negligible [95]. Experimentally by performing a Temperature Programmed Desorption experiment, which will be described in greater detail in Section 3.2 (NH_3 Storage), with NO_2 in the feed gas as shown in Figure 3.7. It can be determined that only a negligible amount of NO_2 will store on the catalyst, which rapidly thermally decomposes to become NO. The effect of H_2O inhibition can be determined from experiments shown in Figure 3.5 and Figure 3.6 which are consistent with results by Kijlstra et al. with H_2O levels saturating the catalyst through the entire expected operational range of 6 – 12% H_2O [80], it can be assumed that H_2O concentration will have negligible effects on NO oxidation. Due to low adsorption of NO, O_2 and NO_2, and the saturation effect of H_2O on the catalyst all

the inhibition terms can be neglected which became evident from further evaluation of kinetics, where all inhibition terms optimized to extremely low values and therefore can be neglected. This yields the kinetic rate form shown in equation (3.14) which is consistent with kinetic models for copper based zeolite catalysts from Olsson et al. [45] and Kim et al. [47].

$$\mathbf{R_1} = k_1 \exp^{\left(-\frac{E_1}{R_u T_m}\right)} \left(y_{NO} y_{O_2}^{0.5} - \frac{y_{NO_2}}{K_{eq}} \right) \tag{3.14}$$

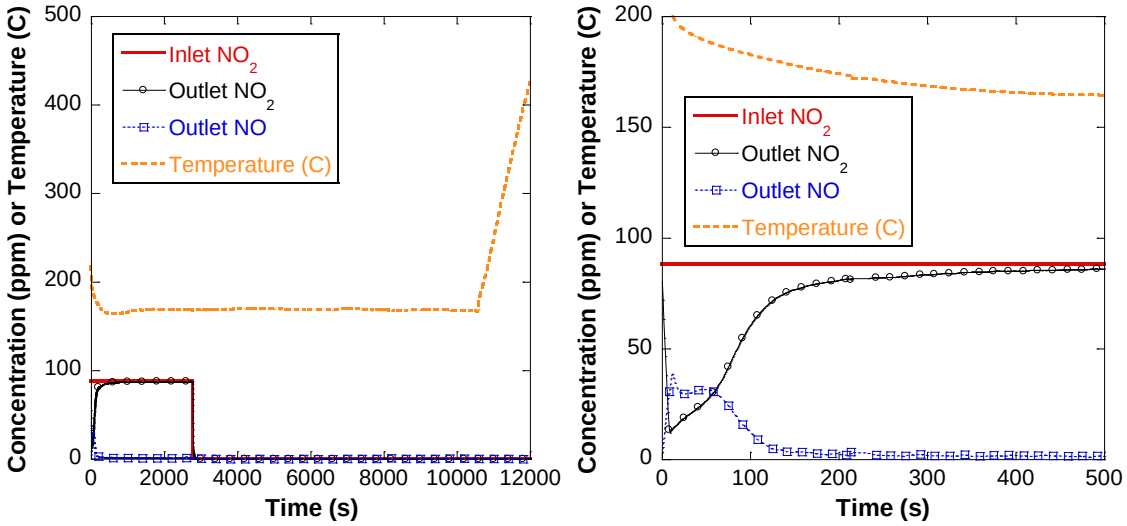

Figure 3.7 − Negligible amounts of NO_2 storage capacity when performing a Temperature Programmed Desorption (TPD) experiment (left). NO_2 that does adsorb rapidly converts to NO and does not store on the catalyst (right). The TPD experiment was performed with a background of 8% H_2O and 8% CO_2.

One issue with the kinetic model shown in equation (3.14) is that it does not take into account the presence of ammonia hindering the reaction. Due to the ability of NH_3 to convert NO to N_2 this is difficult to determine experimentally, while Wurzenberger et al. [48] has proposed the kinetic rate form shown in equation (3.15), which is similar to the kinetic rate shown in equation (3.14) but includes a surface coverage dependence for free catalytic sites (θ_Z) that reduce as NH_3 stores on the catalyst.

$$\mathbf{R_1} = k_1 \exp^{\left(-\frac{E_1}{R_u T_m}\right)} \left(y_{NO} y_{O_2}^{0.5} - \frac{y_{NO_2}}{K_{eq}} \right) \theta_Z \tag{3.15}$$

While equation (3.14) and (3.15) will yield the same modeling results for the experimental data due to all available sites being free (i.e. $\theta_Z = 1$), there is no proof that the oxidation of NO to NO_2 occurs on the same catalytic site as NH_3 storage therefore the kinetic rate form shown in equation (3.14) is used for the global mechanism. The results are shown in Figure 3.8 where the average error for the model is less than 2.0 ppm for the entire experiment, thus the use of the kinetic rate shown in equation (3.14) is corroborated.

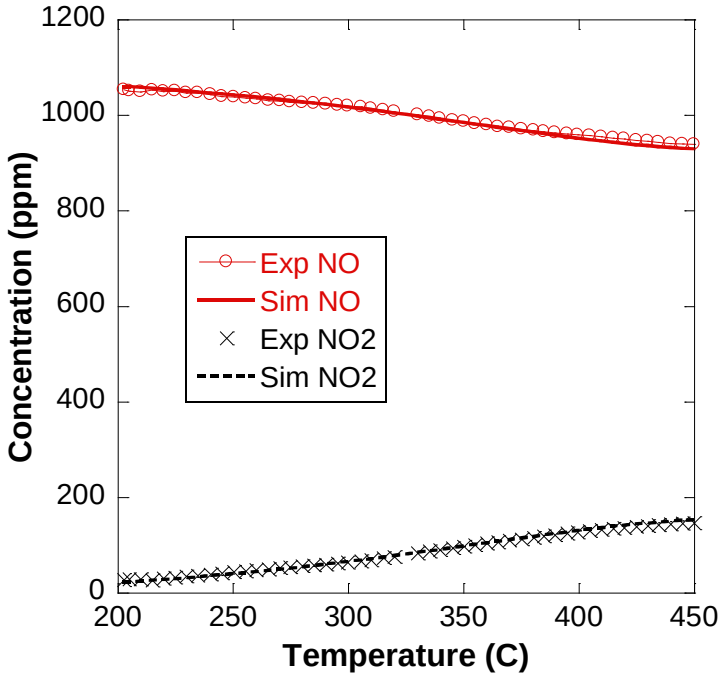

Figure 3.8 − Modeling results show good agreement for oxidation of NO to NO_2, modeling experiments were calibrated against a temperature ramp experiment with 8% H_2O, 8% CO_2, 6% O_2, and 1000 ppm NO.

3.2 NH_3 Storage

NH_3 storage can commonly be written as the difference in NH_3 adsorption and NH_3 desorption which is shown as a reversible reaction in equation (3.16). NH_3 storage

is the rate limiting step in SCR NO_x conversion and therefore the most important reaction when modeling a kinetic mechanism. While there are three possible ammonia storage sites on a zeolite, this section is concerned primarily with the strongly chemisorbed state (Brønsted and Lewis acid sites) [46], which literature suggests has a much larger influence than the weakly adsorbed or chemisorbed states [45, 101]. Experimentally, multiple storage sites would be seen if there are multiple peaks during desorption or multiple shoulders during adsorption which correspond to different bonding strengths from multiple storage sites. These were not present in any TPD experiment performed on this catalyst. Because of the literature sources stated above and experimental results, a simplification can be made by writing a generalized storage mechanism with only one storage site as seen in equation (3.16):

$$NH_3 + Z \underset{\dot{r}_{1r}}{\overset{\dot{r}_{1f}}{\rightleftarrows}} Z\left(NH_3\right) \tag{3.16}$$

where Z represents a free storage site that is active for stored ammonia on the zeolite. This mechanism should perform well during steady-state storage events when there is time for ammonia to bond to these strong sites due to the strongly bound chemisorbed site being dominant in NH_3 storage [45].

3.2.1 NH_3 Storage Experimental Results

Commonly, a Temperature Programmed Desorption (TPD) experiment is performed when using a bench-top style reactor to study effective storage of a species on a catalyst.

Temperature Programmed Desorption (TPD)

In the early history of the zeolite catalyst, researchers wanted to know its acidic properties because it led to a direct understanding of the heterogeneous catalysis that

occurs on the surface [102, 103]. One method often used was a Temperature-Programmed Desorption (TPD) in order to determine the strength of the adsorbate-adsorbent interaction and hence its "acidity strength" [104-110]. Ammonia was often used during this process because it is small enough to enter all of the zeolite pores and react with both Brønsted and Lewis acid sites [108]. During these experiments, up to three different sites/types of ammonia storage took place with varying levels of potency. The three types of ammonia storage are weakly adsorbed, chemisorbed, or strongly chemisorbed states [109]. The strongly chemisorbed state is associated with structural Brønsted hydroxyl groups and strong Lewis acidic sites [91, 104, 109]. The primary advantage of zeolite-based catalysts for diesel NO_x SCR is its ability to utilize these Brønsted and Lewis sites [111].

To determine the role of the three different types of storage sites on the iron based zeolite SCR catalyst in the EAS, multiple TPD experiments were performed to determine the storage capacity of NH_3. In Figure 3.9 it can be seen that there is a single desorption peak indicating that we are primarily concerned with only the strongly chemisorbed state for NH_3 storage. Therefore, the storage capacity is defined as the total amount of NH_3 stored on the entire catalyst in both Brønsted and Lewis sites. Experiments were conducted in a test matrix with different initial storage temperatures (200°C – 475°C) and different CO_2 and H_2O levels (0% – 10%). The space velocity was held constant at 33k hr^{-1}, which corresponded to a total flow of 4 L/min. The experimental methodology is as follows and is illustrated in Figure 3.9:

1. The TPD starts with the SCR inlet flow set at a constant NH_3 concentration and temperature and continues until catalyst outlet concentration rises to equal the inlet concentration. For this experiment, the inlet NH_3 concentration is set at 250 ppm.

2. Once the catalyst is filled (i.e. constant outlet NH_3 concentration), the controls shut off the inlet feed of NH_3 and hold a constant temperature until the outlet NH_3 concentration coming from the catalyst approaches zero.
3. Temperature is ramped at 5°C/min until it reaches peak normal operating temperature for the catalyst system. For this experiment, this value is 500°C and once this temperature is reached, it is held for 5 minutes.
4. Lastly, cleaning of the catalyst follows utilizing an O_2 and N_2 mixture (not shown in Figure 3.9). This allows the model to start with the assumption that the surface is completely clear of absorbed species. At high temperatures, oxidation of NH_3 becomes a more dominant effect, which is the process that cleans the catalyst [45, 79, 112]. This held the O_2 and N_2 mixture for 15 minutes above 500°C. Due to repeatability in experiments, it can be assumed this cleaning process is sufficient.
5. This procedure was repeated for different storage temperatures in order to obtain a temperature dependence on storage capacity.

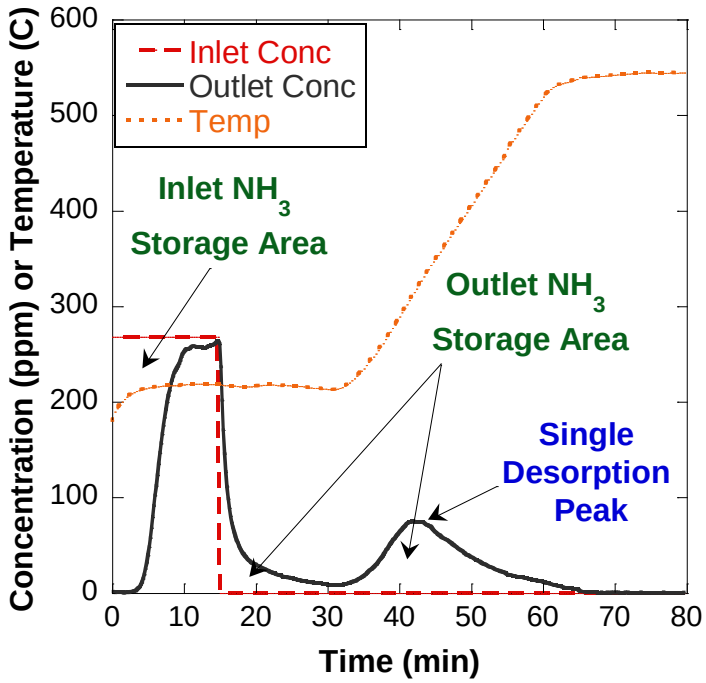

Figure 3.9 – TPD experiment highlighting the Inlet and Outlet NH_3 storage area and an experimentally determined single desorption peak. The TPD experiment was performed with an inlet flow of 250 ppm NH_3, 0% H_2O, 0% CO_2 in balance N_2.

The total NH_3 storage capacity of the catalyst can be calculated by taking the integral of the difference between the inlet and the outlet molecular flow rates of NH_3. This calculation can be done at two locations (Inlet NH_3 Storage Area and Outlet NH_3 Storage Area) during this experiment which yield equal NH_3 storage capacities. Examples of both locations are shown in Figure 3.9. The Inlet NH_3 Storage is calculated during step 1 listed above (where there is constant inlet flow of NH_3 and the adsorption of NH_3 is calculated), while the Outlet NH_3 Storage area is calculated during steps 2 and 3 (where the desorption of NH_3 is calculated).

3.2.2 NH_3 Storage Effects with Temperature

By integrating the NH_3 Inlet Storage area as shown in Figure 3.9 it can be seen in Figure 3.10 that NH_3 Storage capacity will decrease as temperature increases. The ideal results for using the one site reaction listed in equation (3.16) are also shown in Figure

3.10. Due to experimental results deviating from the single storage site approximation, it becomes apparent that there is a possibility of multiple storage sites present on the Fe-zeolite based SCR catalyst used in the EAS. Since a non-analysis agreement has been made evaluation of the strength of the different catalytic sites is not possible. However, as shown in Figure 3.9 all NH_3 is released in a single desorption peak which translates to a similar bonding strength for all active sites, which allows for us to use the single site approximation (equation (3.16)) in the global SCR kinetic model.

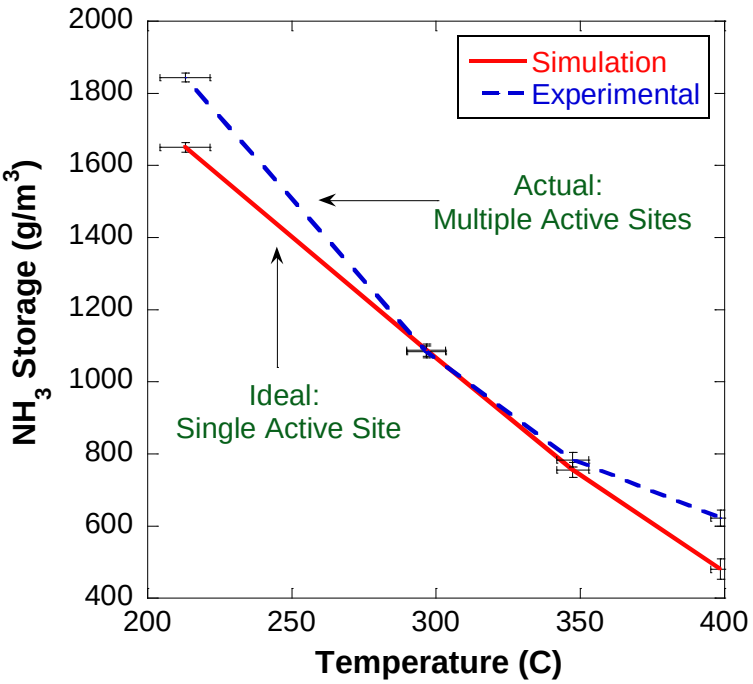

Figure 3.10 − Shows the integral NH_3 storage capacity for the same brick, calculated by integrating the storage capacity of TPD experiments performed at 225°C, 300°C, 350°C, and 400°C. Each experiment had the same inlet gas concentrations of 250 ppm NH_3, 0% H_2O, and 0% CO_2.

3.2.3 NH_3 Storage Kinetic Modeling

Once it has been established that the single storage reaction shown in equation (3.16) can be used, common Arrhenius rate forms for surface chemistry can be used to define the reaction with the forward rate expression as shown in equation (3.17).

$$\dot{r}_{1f} = k_{1f} \exp\left(-\frac{E_{1f}}{R_u T_m}\right) y_{NH_3} \theta_Z \tag{3.17}$$

where θ_Z is the fraction of the surface that is available to store ammonia (i.e. free sites), k is the pre-exponential in the rate form, E is the activation energy, y_i is the mole fraction of species i at the reaction layer on the surface of the catalyst, R_u is the universal gas constant, and T_m is the brick temperature. Commonly, in TPD experiments for SCR catalysts, adsorption of ammonia occurs quickly [106], which results in a negligible NH_3 adsorption activation energy from the gas to surface for a one site storage mechanism [108]. The activation energy being small is consistent with vanadium-based SCR modeling efforts, which shows little or no activation energy required for this forward rate expression due to the gas-to-surface interaction [113].

The reverse direction kinetics for equation (3.16) are commonly written as a function of the temperature of the monolith and the ammonia storage density on the surface. A review of the literature did not identify any species that were active in desorption of ammonia from the surface at standard diesel exhaust conditions. Only increasing the temperature above 573 K triggers the desorption process of the strongly chemisorbed ammonia [48, 91, 109, 114-116]. The rate form for the reverse kinetics was initially written in standard rate law form, which can be seen in equation (3.18) [45].

$$\dot{r}_{1r} = k_{1r} \exp\left(-\frac{E_{1r}}{R_u T_m}\right) \theta_{Z(NH_3)} \tag{3.18}$$

where $\theta_{Z(NH_3)}$ is the surface coverage fraction of stored NH_3. However, the reverse direction rate for equation (3.18) has been changed to make the activation energy a fractional NH_3 surface coverage term based on a Tempkin isotherm [47, 48], which can be seen in equation (3.19).

$$\dot{r}_{1r} = k_{1r} \exp\left(-\frac{E_{1r}}{R_u T_m} - \lambda \theta_{Z(NH_3)}\right) \theta_{Z(NH_3)} \tag{3.19}$$

where λ is a constant to multiply with the surface coverage of NH_3. The Tempkin isotherm reverse rate form shown in equation (3.19) was used, because the Tempkin isotherm rate form increased the accuracy of the model for the TPD experiments when compared to the standard reverse rate form (equation (3.18)). Modeling results showing the comparison for these two reverse kinetic rate forms are shown in Figure 3.11.

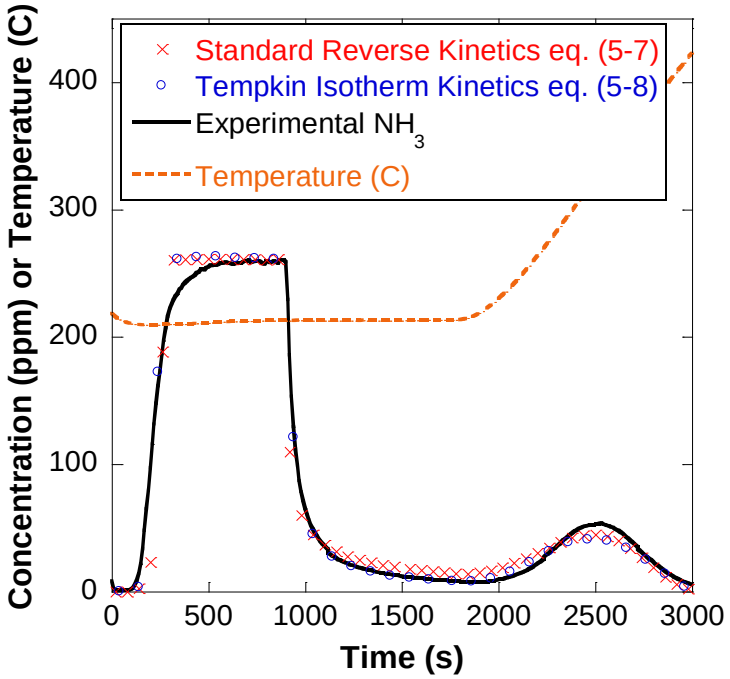

Figure 3.11 − Shows a slight increase in modeling accuracy when using the Tempkin Isotherm Kinetics listed in equation (5-8). The modeling experiment was performed with an inlet gas feed of 250 ppm NH_3, 8% H_2O, and 8% CO_2 with an initial storage temperature of 200°C

3.3 Selective Catalytic Oxidation of NH_3

One advantage of zeolite catalysts is that they have a wider operating temperature window than vanadium-based catalysts because of larger conversion rates at the higher temperatures [15, 92, 116-118]. This conversion relates directly to the selective catalytic oxidation (SCO) of ammonia which was found by Amiridis et al. over a Fe-Y zeolite when the excess ammonia consumption during the SCR process corresponded to the hypothesis that ammonia oxidation was occurring [119]; later corroborated by Stevenson

et al. over an H-ZSM-5 catalyst [88]. As a result, the SCO reaction is important to model, as it becomes the upper bounds of SCR based activity.

Literature research into zeolite catalysts illustrates that Fe-ZSM-5 is a good catalyst for the SCO process [120]. It can be significant for H-zeolite catalysts [88] whereas Cu-ZSM-5 had the lowest instance of SCO in comparison [92]. Centi and Perathoner reasoned that this limitation occurs in catalysts like Cu-ZSM-5 because they form stronger nitrosyl species which inhibit the dissociative chemisorption of ammonia which is the first step in oxidation to N_2 [42]. The preparation of the catalyst is also important because it can lead to extra framework cations and metal oxide clusters which are too active for NH_3 oxidation [92].

The oxidation of ammonia is commonly the weak point of global SCR kinetic models due to a number of theorized ammonia oxidation reactions that can occur [121]. Bodenstein et al. [122] suggested a detailed mechanism listed in equations (3.20) - (3.23) for the oxidation of NH_3 with on a platinum wire.

$$NH_3 + O \rightarrow NH_3O \tag{3.20}$$

$$NH_3O + O \rightarrow HNO + H_2O \tag{3.21}$$

$$NH_3O + HNO \rightarrow N_2 + H_2O \tag{3.22}$$

$$HNO + HNO \rightarrow N_2O + H_2O \tag{3.23}$$

It was also found that catalysts known to be active for NH_3 oxidation (Pt/Pd/Rh-ZSM-5) producing partial reduction of NH_3 yielding NO and N_2O as by-products [47, 48, 123] listed in equations (3.24) and (3.25) as well as complete reduction to N_2 and H_2O [45, 79] as shown in equation (3.26) . Commonly all ammonia oxidation reactions are written as surface reactions due to the strong bond of NH_3 to the catalyst surface,

although Wurzenberger [48] suggests there is a possibility of NH_3 oxidizing to complete reduction in the gas phase as shown in equation (3.27).

$$4Z\left(NH_3\right)+4O_2 \rightarrow Z+N_2+2NO+6H_2O \tag{3.24}$$

$$4Z\left(NH_3\right)+5O_2 \rightarrow Z+2N_2O+6H_2O \tag{3.25}$$

$$4Z\left(NH_3\right)+3O_2 \rightarrow 4Z+2N_2+6H_2O \tag{3.26}$$

$$4NH_3+3O_2 \rightarrow 2N_2+6H_2O \tag{3.27}$$

Over a Cu-ZSM-5 catalyst, it was found by Komatsu et al. [124] that NO and N_2O yields were less than 1% during ammonia oxidation experiments. In addition, the full conversion of ammonia to N_2 occurs at lower temperatures than the conversion to NO [125]; which was also found over Cu-FAU catalyst [126]. Over a H-ZSM-5 catalyst [88], the majority of the ammonia oxidized appears to be converted directly to N_2 and not just to NO. These results were further corroborated by Sjövall et al. [46] on Fe based zeolite SCR catalysts. Figure 3.12 below shows concentrations on a temperature basis for an ammonia oxidation experiment performed on the Fe based zeolite used in the EAS. From these results it can be seen that only negligible values of NO and N_2O are present during the entire temperature range which corroborates Sjövall findings for a different iron based zeolite SCR catalyst. Based on the experimental data shown in Figure 3.12 and the above references, only the stoichiometric reaction to complete products is needed in a global kinetic model.

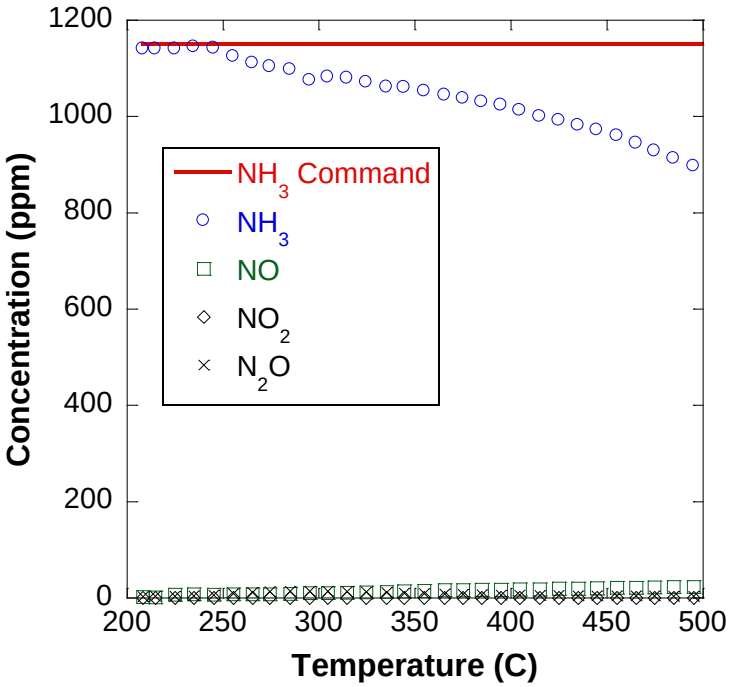

Figure 3.12 − NH_3 oxidation temperature ramp experiment with an inlet feed gas of 6% O_2, 8% H_2O, 8% CO_2, and 1150 ppm NH_3; yielded only negligible values of NO and N_2O for entire temperature range.

It is important to mention that the SCO of ammonia is not necessarily a negative reaction as it can abate the ammonia slip after the SCR reactors without introducing other reactants in the gas mixture and producing further pollutants [125]. This SCO process is the basis for ammonia slip catalysts present in some SCR aftertreatment systems [127].

3.3.1 NH_3 Oxidation Experimental Results

Experimental data for the ammonia oxidation reaction when using a bench-top style reactor are collected using constant inlet concentrations and varying temperature in a constant upward or downward ramp rate up to 5°C/min. Experimental results are then compiled to show a conversion percentage vs. temperature profile.

NH_3 Oxidation Effect of varying O_2 concentration

It is commonly accepted that the SCO reactions are dependent on oxygen concentrations. Kim et al. [47] suggests that for the oxidation of NH_3 on a SCR catalyst is subject to catalytic saturation of oxygen content. This means that there will be a law of diminishing returns for the conversion of NH_3 as O_2 concentration increases. This can be seen in Figure 3.13 where the NH_3 conversion is shown as a function of temperature and O_2 concentration. NH_3 conversion is defined in equation (3.28).

$$\eta_{NH_3} = \left(\frac{c_{NH_3\_IN} - c_{NH_3\_OUT}}{c_{NH_3\_IN}} \right) \cdot 100 \tag{3.28}$$

From Figure 3.13 it can be seen that NH_3 conversion increases the most when O_2 concentration increases from 0.5% to 2.0%. While there is in increase from 2.0% O_2 to 6.0% O_2 in the inlet feed gas, it is not as large as the change from 0.5% to 2.0%.

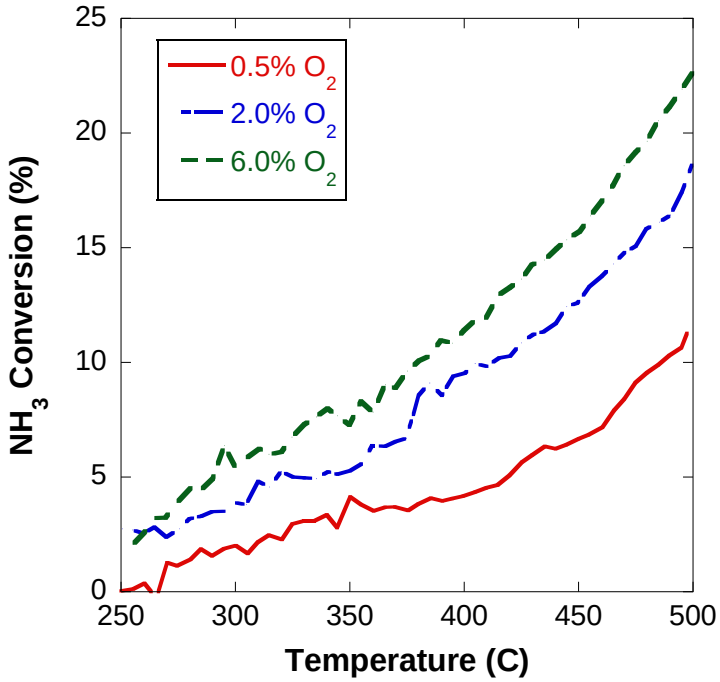

Figure 3.13 − The conversion of NH_3 due to oxidation increases as O_2 levels in the feed gas increase, with saturation effects shown when O_2 concentration are greater than 2%.

3.3.2 Selective Catalytic Oxidation of NH_3 Modeling Results

The SCO of NH_3 was originally proposed by Stevenson et al. over a H-ZSM-5 [86, 88] as a Langmuir-Hinshelwood mechanism, where they assumed the rate of ammonia oxidation is a function of the ammonia coverage and is zero order in oxygen concentration as shown in equation (3.29).

$$R = \frac{k_{ox} K_a \left[\mathrm{NH_3}\right]}{1 + K_a \left[\mathrm{NH_3}\right]} \tag{3.29}$$

where ammonia inhibition of the process is accounted by using the ammonia adsorption constant K_a.

This rate form was determined from experiments with only 0.5% to 2.0% O_2 in the feed gas. This zero order functionality with respect to oxygen is hard to reason considering that the stoichiometric reaction is a function of oxygen; it may be the result of a relatively small sample of oxygen concentrations. As a result Olsson et al. [45], Sjövall et al. [46], and Wurzenberger [48] all proposed a kinetic rate form as a first order function of oxygen as shown in equation. As a result, the reaction mechanism includes first-order dependence in the local coverage fraction of ammonia and oxygen levels:

$$\mathbf{R}_2 = k_2 \exp^{\left(-\frac{E_2}{R_u T_m}\right)} \theta_{Z(\mathrm{NH_3})} y_{\mathrm{O_2}} \tag{3.30}$$

While the kinetic rate form shown in equation (3.31), is commonly used when describing the stoichiometric NH_3 oxidation reaction shown in equation (3.26), Kim et al. [47] suggests using a saturation effect which changes the kinetic rate equation from a first order function of oxygen to a kinetic function based on a saturation effect of oxygen as shown in equation (3.31).

$$\mathbf{R}_2 = k_2 \exp^{\left(-\frac{E_2}{R_u T_m}\right)} \theta_{Z(\mathrm{NH_3})} \left(y_{\mathrm{O_2}}\right)^{\gamma} \tag{3.31}$$

From the experimental results shown in Figure 3.13 the dependence on oxygen concentration can be determined for the kinetic rate shown in equation (3.31) by the following method. NH_3 conversion efficiency $\left(\eta_{NH_3}\right)$ can be defined as proportional to the oxygen concentration to some power (γ) as seen in equation (3.32).

$$\eta_{NH_3} \propto \left[O_2\right]^{\gamma} \tag{3.32}$$

By using the proportionality shown in equation (3.32) the NH_3 conversion efficiency for the experiments for 0.5% O_2 concentration and 6.0% O_2 concentration can be compared as shown in equation (3.33).

$$\frac{\eta_{NH_3=6.0\%O_2}}{\eta_{NH_3=0.5\%O_2}} \propto \frac{\left[O_2=6.0\%\right]^{\gamma}}{\left[O_2=0.5\%\right]^{\gamma}} = \left(\frac{\left[O_2=6.0\%\right]}{\left[O_2=0.5\%\right]}\right)^{\gamma} \tag{3.33}$$

The log of each side of the proportionality can then be taken (3.34) to find the dependence on O_2 concentration as shown in equation (3.35).

$$\log\left(\frac{\eta_{NH_3=6.0\%O_2}}{\eta_{NH_3=0.5\%O_2}}\right) \propto \gamma \log\left(\frac{\left[O_2=6.0\%\right]}{\left[O_2=0.5\%\right]}\right) \tag{3.34}$$

$$\gamma \propto \frac{\log\left(\frac{\eta_{NH_3=6.0\%O_2}}{\eta_{NH_3=0.5\%O_2}}\right)}{\log\left(\frac{\left[O_2=6.0\%\right]}{\left[O_2=0.5\%\right]}\right)} \tag{3.35}$$

The results from this approximation are shown in Figure 3.13; all cases can be averaged to find that the predicted oxygen dependence for all cases is 0.33. However, unlike with the oxygen dependence on the NO oxidation reaction the average for each comparison of NH_3 oxidation varied from 0.2 to 0.4. Therefore it can be determined that there is an oxygen dependence, however the exact value could not be determined for the kinetic rate development but a range can be determined to approach for optimization purposes.

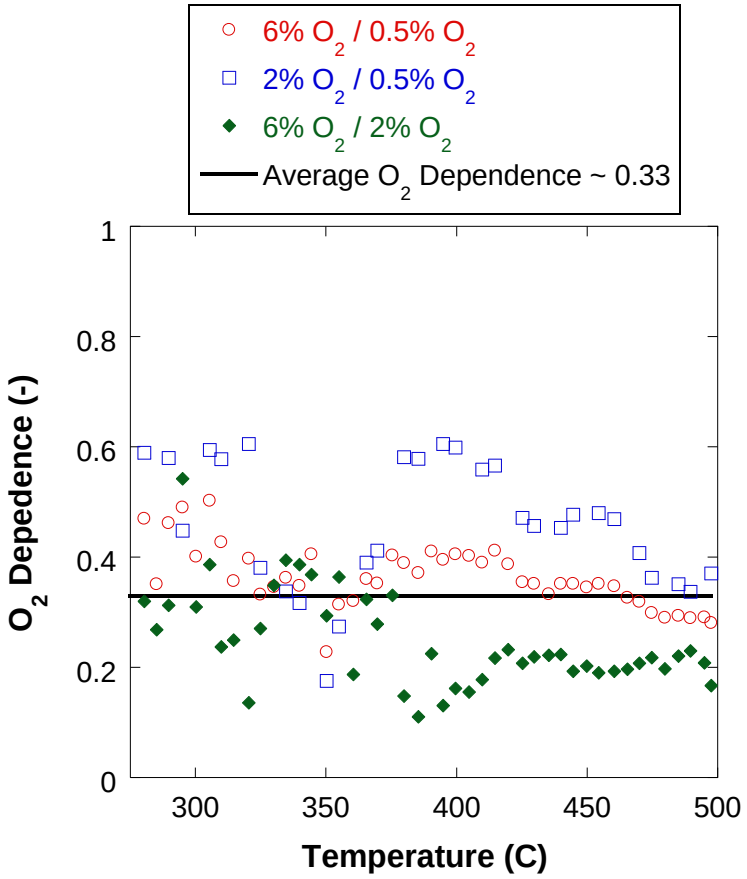

Figure 3.14 – The average dependence of O_2 on NH_3 oxidation for all cases is 0.33, while the average oxygen dependence for each individual case varies from 0.2 – 0.4.

From these results two kinetic models were developed to compare accuracy in the two approaches. The first kinetic model was developed using the first order oxygen kinetics proposed by Olsson et al. [45], Sjövall et al. [46], and Wurzenberger [48] as shown in equation (3.30). The second kinetic model was accomplished by using Kim et al. [47] saturation of O_2 as shown in equation (3.31). Each kinetic model was developed to compare with data from a temperature ramp experiment with 8% H_2O, 8% CO_2, 1000 ppm NH_3, and 6% O_2. A downhill simplex optimize was used to find the fit parameters for each kinetic rate equation. In Figure 3.15 in can be seen that when only comparing at a constant level of O_2 either kinetic rate form is acceptable, however it would be preferred to use less fit parameters so the first order oxygen kinetic approximation shown in equation (3.30) would be used.

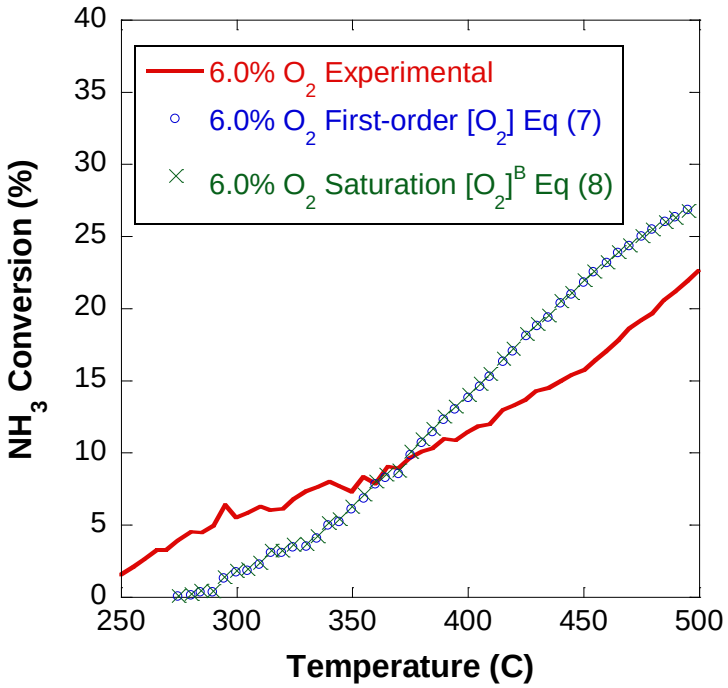

Figure 3.15 – Shows no discernable difference in modeling results for both kinetic rate forms when compared with experimental data from a temperature ramp experiment with a feed gas of 8% H_2O, 8% CO_2, 6% O_2, and 1000 ppm NH_3.

Due to the operation of rich and lean conditions in the EAS, different O_2 concentrations need to be evaluated for a more comprehensive kinetic mechanism. To evaluate the different rate forms it is important to compare the accuracy when O_2 levels change in the feed gas. From Figure 3.16 and Figure 3.17 it can be seen that the saturation kinetic rate form shown in equation (3.31) increases the accuracy when O_2 concentration is 2% and 0.5% respectively, therefore it is important to use saturation kinetics when O_2 concentration will vary by large amounts as seen in the EAS.

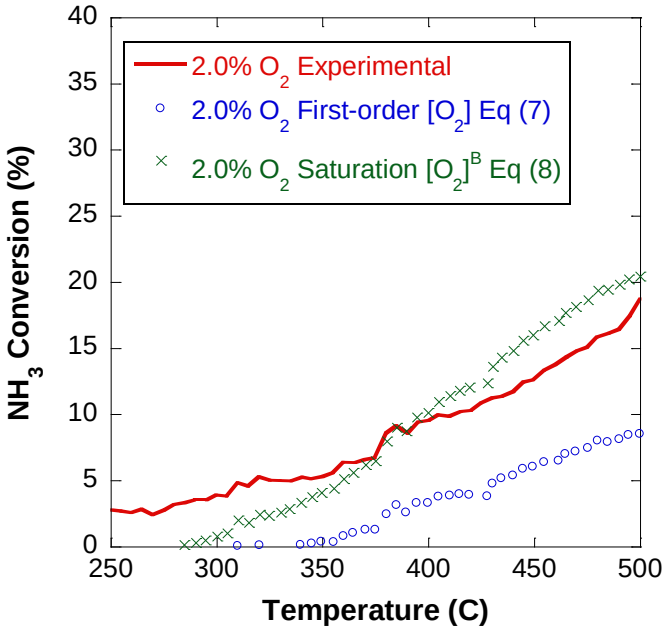

Figure 3.16 – Shows variation when comparing the kinetic rate forms with the saturation kinetic model yielding higher accuracy when compared with experimental data from a temperature ramp experiment with a feed gas of 8% H_2O, 8% CO_2, 2% O_2, and 1000 ppm NH_3.

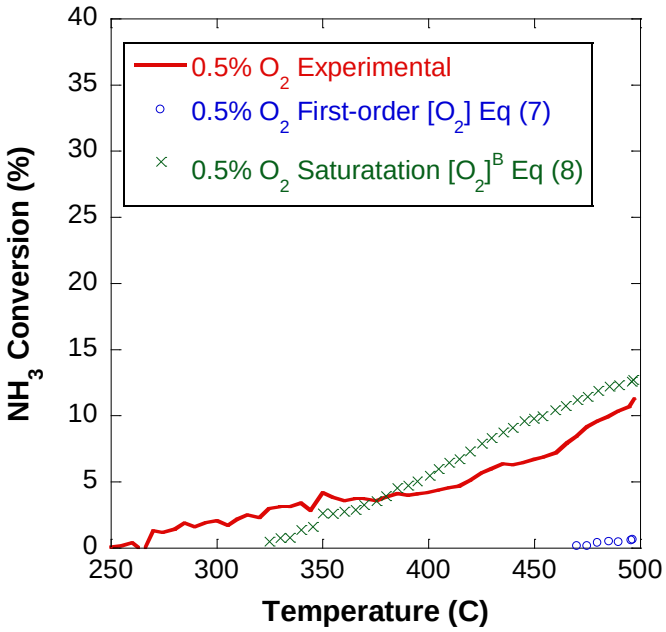

Figure 3.17 – Shows variation when comparing the kinetic rate forms with the saturation kinetic model yielding higher accuracy when compared with experimental data from a temperature ramp experiment with a feed gas of 8% H_2O, 8% CO_2, 0.5% O_2, and 1000 ppm NH_3.

3.4 NO_x Reduction with NH_3

NO_x reduction is defined as the conversion of NO and NO_2 from the feed gas through the catalyst into environmentally benign compounds such as N_2 as shown in (3.36). NH_3 SCR catalysts store NH_3 on the surface which reacts with NO_x and O_2 in the feed gas to from N_2 and H_2O.

$$\eta_{NO_x} = \left(\frac{\left(c_{NO\_in} + c_{NO_2\_in}\right) - \left(c_{NO\_out} + c_{NO_2\_out}\right)}{\left(c_{NO\_in} + c_{NO_2\_in}\right)} \right) \cdot 100 \tag{3.36}$$

3.4.1 Background

NO_x reduction on an SCR catalyst is commonly thought of to occur as the results of three simultaneous reactions shown in equations (3.37), (3.38), and (3.39) commonly labeled as the Standard SCR reaction, the Fast SCR reaction, and the Slow SCR reaction respectively [2, 3, 45-48, 128].

$$4NH_3 + 4NO + O_2 \rightarrow 4N_2 + 6H_2O \tag{3.37}$$

$$2NH_3 + NO + NO_2 \rightarrow 2N_2 + 3H_2O \tag{3.38}$$

$$8NH_3 + 6NO_2 \rightarrow 7N_2 + 12H_2O \tag{3.39}$$

The SCR NO_x reduction reactions listed in equations (3.37), (3.38), and (3.39) are assumed to contribute to NO_x reduction simultaneously, as seen from previous results it was concluded the SCR catalyst can oxidize NO to NO_2 as well as thermally decompose NO_2 to NO. Due to the nature of these simultaneous NO_x reduction reactions with NH_3, experimentally it can be determined that NO_x reduction is highly dependent on catalyst temperature and the NO to NO_x ratio ($NO:NO_x$), as illustrated in Figure 3.18.

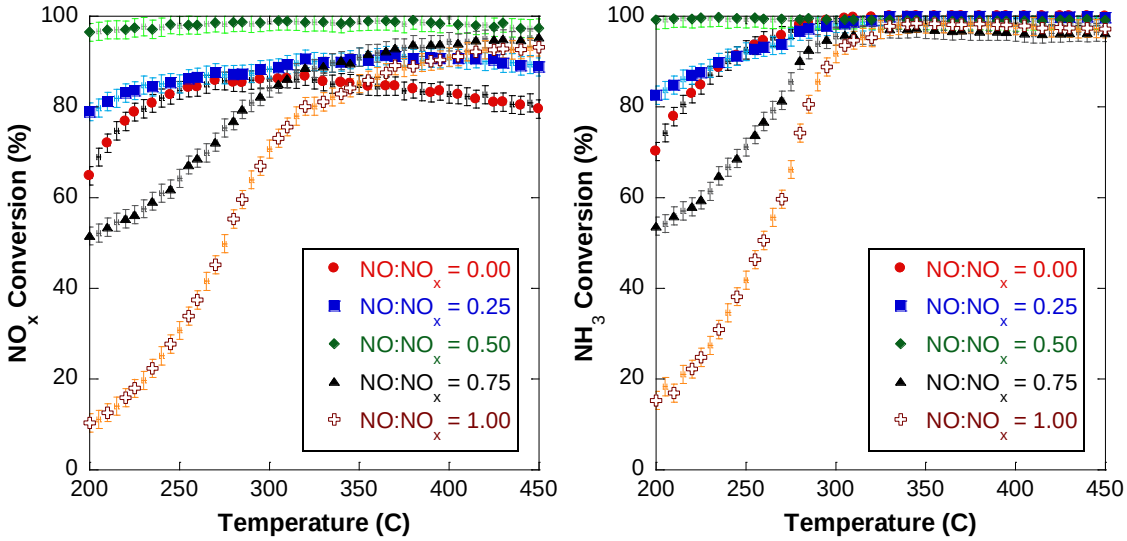

Figure 3.18 – NO_x conversion is highly dependent on the $NO:NO_x$ ratio in the feed gas when comparing experiments performed with a feed gas of 6% H_2O, 6% CO_2, 6% O_2, 400 ppm NH_3, 400 ppm NO_x.

Standard SCR Reaction

Lyon was one of the first to study the reaction between NH_3, NO, and O_2 on a platinum catalyst. From Lyon's observations the reaction with NH_3 and NO without O_2 present was trivial. Lyon then proposed a detailed mechanism to model the results from NH_3, NO, and O_2 as seen in equations (3.40) - (3.45) [129].

$$NH_2 + NO \rightarrow N_2 + H + OH \tag{3.40}$$

$$NH_2 + NO \rightarrow N_2 + H_2O \tag{3.41}$$

$$H + O_2 \rightarrow OH + O \tag{3.42}$$

$$8NH_3 + O \rightarrow OH + NH_2 \tag{3.43}$$

$$NH_3 + OH \rightarrow NH_2 + H_2O \tag{3.44}$$

$$NH_3 + H \rightarrow H_2 + NH_2 \tag{3.45}$$

The reactions in equations (3.40) - (3.45) are all two body reactions that demonstrate the detailed reduction of NO with NH_3 in the presence of O_2 as gas phase reactions. Byrne et al. [29] combines these reactions to form one global three body reaction as shown in equation (3.37).

$$4NH_3 + 4NO + O_2 \rightarrow 4N_2 + 6H_2O \tag{3.37}$$

Fast SCR Reaction

The reduction of NO_2 with NH_3 was initially neglected because engine exhaust composition heavily favored NO with at least 95% of the NO_x composition [30, 130-133]. It was later discovered by Kato et al. that NO_x reduction with NH_3 increases dramatically if equal parts of NO and NO_2 were present in the feed gas to the catalyst [122]. Kato et al. proposed the following detailed reaction mechanism shown in equations (3.46) - (3.50) for NO_x conversion with NH_3 when there is an equal ratio of NO to NO_2 in the feed gas to the catalyst.

$$Z + NH_3 \leftrightarrow Z\left(NH_3\right) \tag{3.46}$$

$$Z\left(NH_3\right) + NO \rightarrow Z\left(NH_3\right)NO \tag{3.47}$$

$$Z\left(NH_3\right)NO \rightarrow Z\left(H\right) + N_2 + H_2O \tag{3.48}$$

$$Z\left(H\right) + NO_2 \rightarrow Z + HONO \tag{3.49}$$

$$Z\left(H\right) + HONO \rightarrow Z\left(H_2ONO\right) \rightarrow Z + H_2O + NO \tag{3.50}$$

Due to the high reaction from experimental data, Kato et al. then proposed the global reaction shown in equation (3.38) as a global reaction to describe the detailed mechanism in equations (3.46) - (3.50).

$$2NH_3 + NO + NO_2 \rightarrow 2N_2 + 3H_2O \quad (3.38)$$

Nova et al. [44] and Grossale et al. [134] investigated the surface nitrate formation in the reduction of NO_2 and NO with NH_3 by performing experiments at low temperatures and proposed the following reactions in equations (3.51) – (3.53) for vanadium based SCR catalysts and iron based zeolite SCR catalysts respectively. Their work elaborates on Kato's reaction scheme by combining NO_2 and NH_3 to form ammonium nitrate on the surface of the catalyst as a precursor to the Fast SCR reaction.

$$2NH_3 + 2NO_2 \rightarrow N_2 + NH_4NO_3 + H_2O \quad (3.51)$$

$$NH_4NO_3 + NO \rightarrow NO_2 + N_2 + H_2O \quad (3.52)$$

$$NH_4NO_3 + 2NO + 2NH_3 \rightarrow 3N_2 + 5H_2O \quad (3.53)$$

Nova [44] and Grossale [134] state their reaction scheme is important when considering low temperature operation of a SCR catalyst due to the inhibition effects of NH_3 at low temperatures (Temperature < 200°C). Nova and Grossale also note that the combination of the reactions shown in equations (3.51) – (3.53) can be combined to form the global Fast SCR reaction shown in equation (3.38). To simplify the kinetics for the development of the model, the SCR temperature will be investigated above 200°C where the global Fast SCR reaction (equation (3.38)) can be used.

Slow SCR Reaction

Kato et al. [122] suggested that NO_2 reduction with NH_3 should show a similar detailed reaction mechanism as the oxidation of NH_3 as seen in equations (3.20) - (3.23), however O_2 should be replaced with NO_2. Thus yielding the following reactions listed in equations (3.54) – (3.58).

$$NH_3 + NO_2 \rightarrow NH_3O + NO \quad (3.54)$$

$$NO + O \leftrightarrow NO_2 \quad (3.55)$$

$$NH_3O + O \rightarrow HNO + H_2O \quad (3.56)$$

$$NH_3O + HNO \rightarrow N_2 + H_2O \quad (3.57)$$

$$HNO + HNO \rightarrow N_2O + H_2O \quad (3.58)$$

Due to absence of intermediates in experimental results Kato et al. [122] suggested equation (3.39) as the global reaction for NO_2 reduction with NH_3.

$$8NH_3 + 6NO_2 \rightarrow 7N_2 + 12H_2O \quad (3.39)$$

Ciardelli et al. [135] studied the NH_3-NO_2 reaction and published a modification to Kato's detailed reduction pathway as shown in equations (3.59) – (3.66).

$$2NO_2 \leftrightarrow N_2O_4 \quad (3.59)$$

$$N_2O_4 + H_2O \leftrightarrow HONO + HNO_3 \quad (3.60)$$

$$HONO + NH_3 \leftrightarrow NH_4NO_2 \quad (3.61)$$

$$NH_4NO_2 \rightarrow N_2 + 2H_2O \quad (3.62)$$

$$NH_3 + HNO_3 \leftrightarrow NH_4NO_3 \quad (3.63)$$

$$NH_4NO_3 \leftrightarrow N_2O + 2H_2O \quad (3.64)$$

$$NO_2 \leftrightarrow NO + O \quad (3.65)$$

$$NH_4NO_3 + 2NO + 2NH_3 \rightarrow 3N_2 + 5H_2O \quad (3.66)$$

Ciardelli points out that the detailed mechanism combines to form the two global reactions for NO_x reduction and for N_2O production as shown in equations (3.39) and (3.67) respectively. A similar reaction for N_2O production is also proposed by Kim et al. [47] and Olsson et al. [45].

$$8NH_3 + 6NO_2 \rightarrow 7N_2 + 12H_2O \quad (3.39)$$

$$2NH_3 + 2NO_2 \rightarrow N_2 + N_2O + 3H_2O \quad (3.67)$$

3.4.2 Experimental Results

Experimental data for the NO_x reduction with NH_3 while using a bench-top style reactor was collected using a variety of experiments. Steady state data was taken in the form of temperature ramp experiments, which consist of constant inlet concentrations and varying temperature in a constant upward or downward ramp rate up to 5°C/min. Experiments were also performed while switching from lean to rich exhaust to replicate conditions behind a LNT catalyst. During these switching experiments NH_3 is present while rich feed gas is flowing across the catalyst, and oxygen and NO_x are present while the lean feed gas is flowing across the catalyst.

Effect of NH_3 to NO_x Ratio

It was already shown in Figure 3.18 that the NO to NO_x ratio is important in determining the NO_x conversion capabilities of the SCR catalyst. It is also important to consider NH_3 to NO_x ratio when predicting NO_x conversion with NH_3, due to the highly reactive nature of NH_3 on a SCR catalyst. Increasing the NH_3 to NO_x ratio will increase the NO_x conversion while lowering NH_3 conversion which is confirmed in Figure 3.19.

It should be noted that NH_3 is also a regulated tailpipe emission, and therefore the limiting factor in the max NH_3 to NO_x ratio that can be used. Figure 3.19 can be used to confirm the stoichiometric ratios of NH_3 to NO_x for the three global NO_x reduction reactions listed in equations (3.37), (3.38), and (3.39) by maximizing both NO_x conversion and NH_3 conversion for a set of NH_3 to NO_x ratios. From Figure 3.19 it can be confirmed that the stoichiometric NH_3 to NO_x ratio is 1.0 for the Standard SCR reaction (equation (3.37)) and the Fast SCR reaction (equation (3.38)), and an NH_3 to NO_x ratio of 1.3 for the Slow SCR reaction (equation (3.39)).

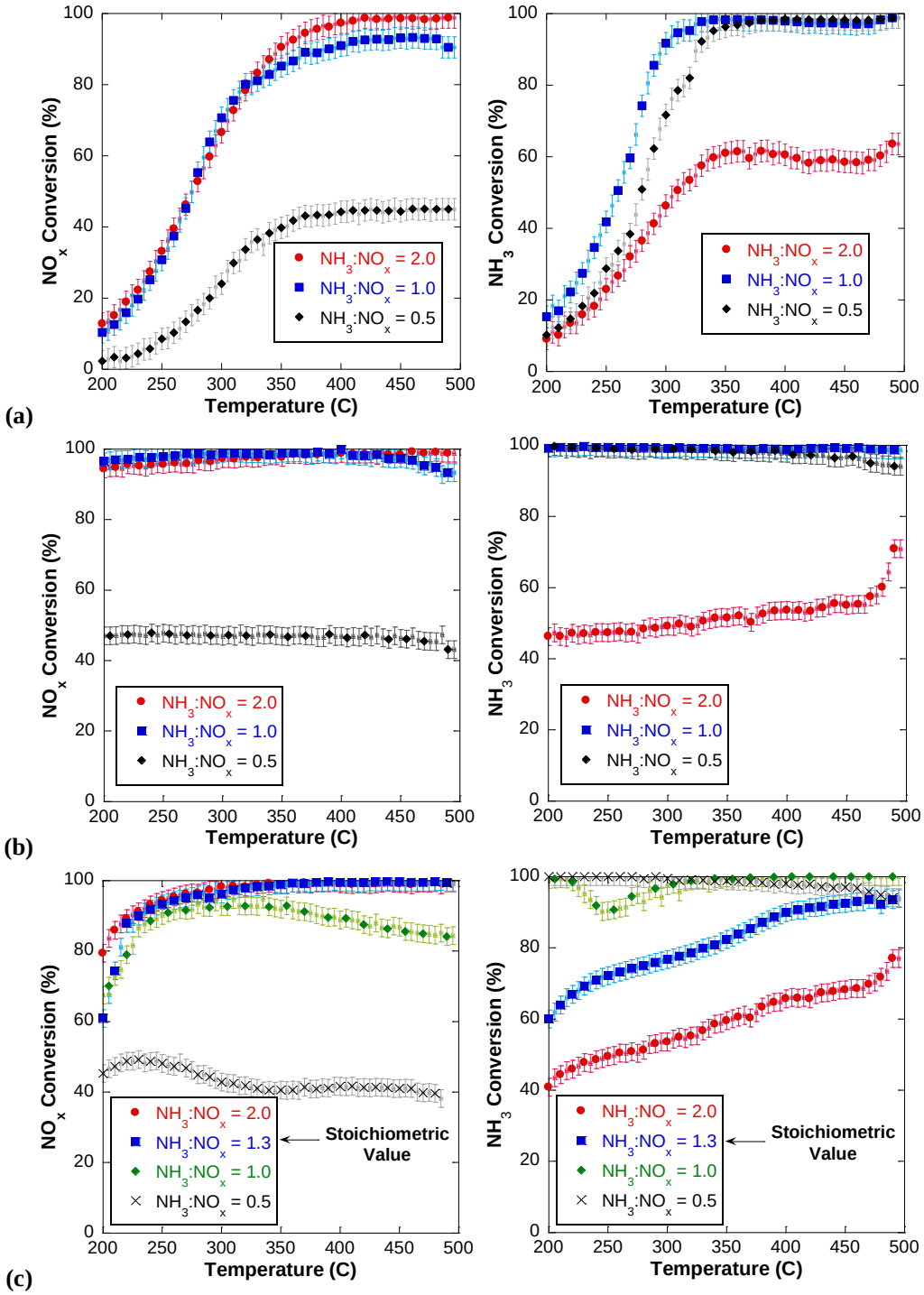

Figure 3.19 – Increasing the NH_3 to NO_x ratio increases NO_x conversion while lowering NH_3 conversion which increases the amount of NH_3 slip. All experiments are performed as a temperature ramp with a feed gas of 6% H_2O, 6% CO_2, 6% O_2, 400 ppm NO_x, varying NH_3 concentration (a) NO:NO_x = 1.0, (a) NO:NO_x = 0.5, (c) NO:NO_x = 0.0.

Effect of O_2 Concentration

By observing the reactions listed in equations (3.37), (3.38), and (3.39); it becomes apparent that O_2 only has an effect on the conversion of NO with NH_3, where it was first observed by Lyon [129] that NO conversion with NH_3 is strongly enhanced in the presence of oxygen. In Figure 3.20 it can be seen there is negligible effect due to O_2 concentration on NO_x conversion when the NO to NO_x ratio is 0.5 or 0.0, however there is a distinct increase in NO_x conversion as O_2 concentration increases when the NO to NO_x ratio is 1.0 which is studied further in the next section.

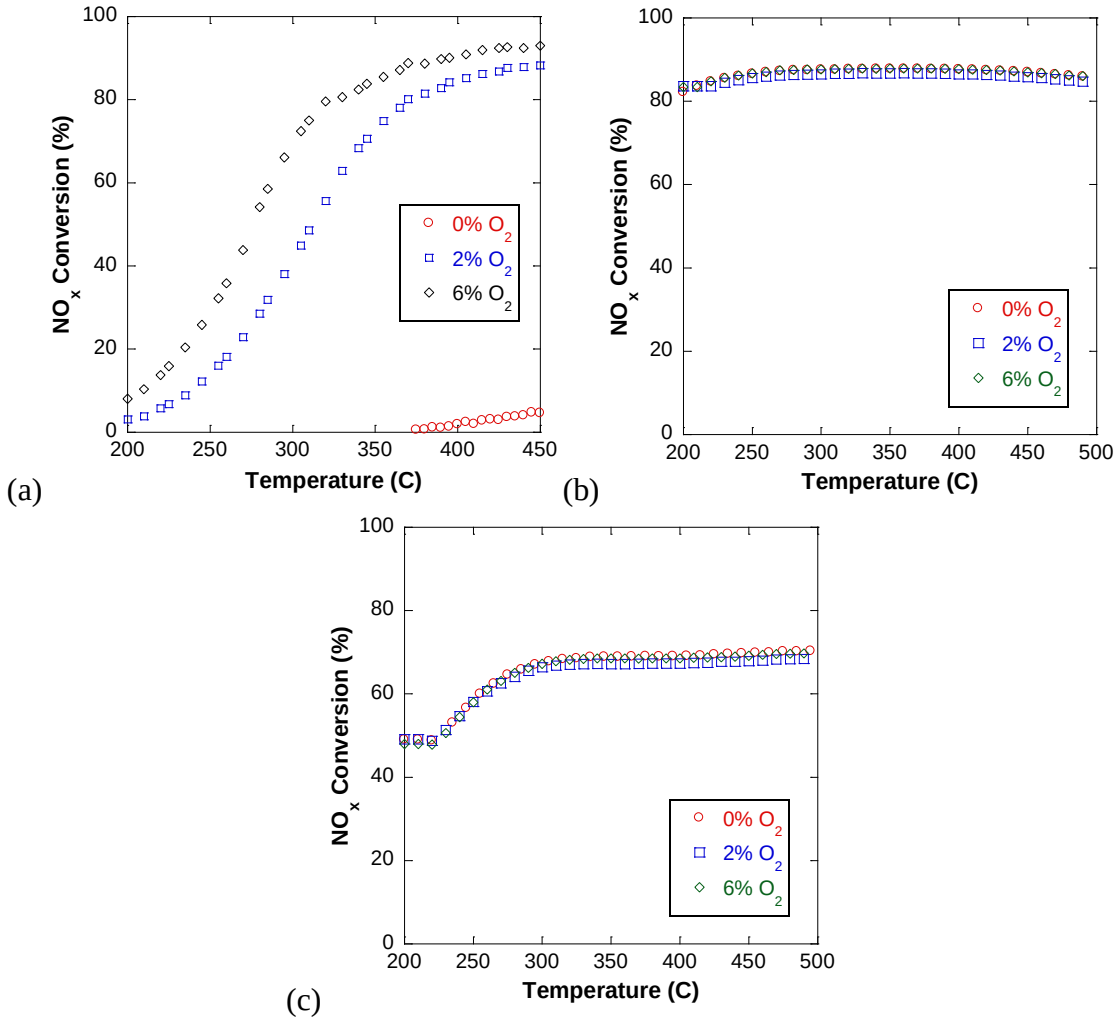

Figure 3.20 – NO_x conversion is a strong function of O_2 concentration only when the composition of NO_x in the feed gas favors NO. The experiments were performed with a feed gas composition of 8% H_2O, 8% CO_2, 1000 ppm NH_3, 1000 ppm NOx, varying O_2 concentration (a) NO:NO_x = 1.0, (b) NO:NO_x = 0.5, (c) NO:NO_x = 0.0

O_2 Effect on the Standard SCR Reaction

As discussed earlier it was found by Lyon [129] that NH_3 will have a strong reaction with NO in the presence of O_2 on a platinum based catalyst. Lyon also found there is a reaction with NH_3 and NO without O_2 but it is much lower than with O_2 present [129]. Similarly in Figure 3.21 it can be seen that NO reduction with NH_3 without O_2 still exists but is small in comparison to when O_2 is present.

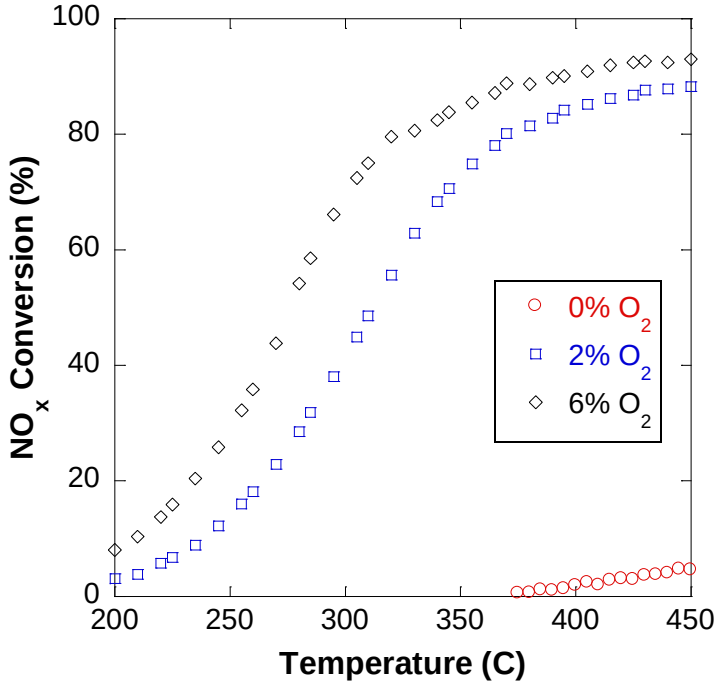

Figure 3.21 – NO_x conversion is a strong function of O_2 concentration for all experiments performed with a feed gas composition of 8% H_2O, 8% CO_2, 400 ppm NH_3, 400 ppm NO_x, varying O_2 concentration

An additional reaction can be added for conversion of NO with NH_3 without O_2 as seen in equation (3.68) commonly called the Rich Standard SCR reaction.

$$4NH_3 + 6NO \rightarrow 5N_2 + 6H_2O \tag{3.68}$$

It should be noted that due to the low conversion of NO with NH_3 without O_2 the reaction listed in equation (3.68) is removed from most literature models since their kinetic mechanisms are going to be used for lean exhaust conditions.

By confirming NO_x conversion for the Standard SCR reaction is dependent on oxygen concentration from Figure 3.21, as seen previously equation (3.69) can be formed by assuming the NO_x conversion efficiency $\left(\eta_{NO_x}\right)$ is proportional to the oxygen concentration to some power (γ).

$$\eta_{NO_x} \propto [O_2]^{\gamma} \tag{3.69}$$

By using the proportionality shown in equation (3.69) the experiments for 2% O_2 concentration and 6.0% O_2 concentration can be compared as shown in equation (3.70).

$$\frac{\eta_{NO_x=6.0\%O_2}}{\eta_{NO_x=2.0\%O_2}} \propto \frac{[O_2=6.0\%]^{\gamma}}{[O_2=2.0\%]^{\gamma}} = \left(\frac{[O_2=6.0\%]}{[O_2=2.0\%]}\right)^{\gamma} \tag{3.70}$$

The log of each side of the proportionality can then be taken (3.71) to find the dependence on O_2 concentration as shown in equation (3.72).

$$\log\left(\frac{\eta_{NO_x=6.0\%O_2}}{\eta_{NO_x=2.0\%O_2}}\right) \propto \gamma \log\left(\frac{[O_2=6.0\%]}{[O_2=2.0\%]}\right) \tag{3.71}$$

$$\gamma \propto \frac{\log\left(\frac{\eta_{NO_x=6.0\%O_2}}{\eta_{NO_x=2.0\%O_2}}\right)}{\log\left(\frac{[O_2=6.0\%]}{[O_2=2.0\%]}\right)} \tag{3.72}$$

Figure 3.22 shows the O_2 dependence as a function of temperature. A strong dependence on O_2 concentration would signify a straight line at each temperature. Due to minimal conversion of NO with NH_3 in experiments without oxygen, it is important to include the oxygen concentration term in the kinetic rate for the Standard SCR reaction. The dependence on O_2 concentration for the NO Oxidation reaction could be determined using this method because it is the only reaction occurring on the catalyst; while the Standard SCR reaction yields inconclusive results due to the simultaneous reactions of NH_3 oxidation, NO oxidation, the Standard SCR reaction, the Fast SCR reaction, and the

Slow SCR reaction taking place on the catalyst surface at the same time. Due to the simultaneous nature of the NO_x reduction reactions it can be concluded that O_2 dependence is not constant, but a strong function of temperature through the tested temperature range.

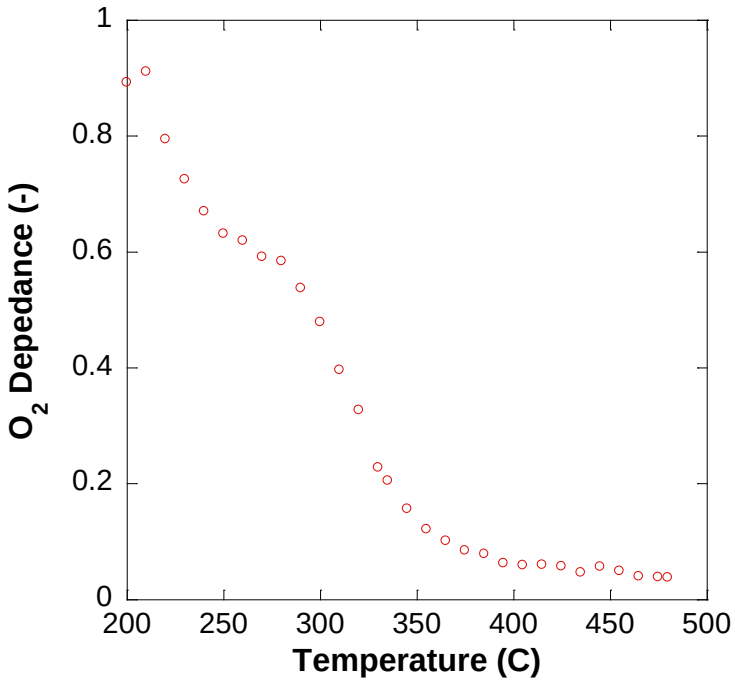

Figure 3.22 – The dependence on O_2 is not constant and therefore is not independent of temperature.

Effect of NH_3 Storage on NO_x Conversion

Experiments from this section are performed to study the effect of stored NH_3 on NO_x conversion capabilities for the iron based zeolite SCR catalyst in the EAS. Under steady state conditions NH_3 levels react instantly with NO_x on the catalyst to form N_2 and H_2O. In an LNT SCR aftertreatment system, NO_x is stored on the LNT during lean exhaust operation. NH_3 is produced as a byproduct as of NO_x reduction with H_2 during a rich regeneration of the LNT catalyst. The SCR in the EAS operates by storing the NH_3 from the rich regeneration to react with any NO_x that slips during lean operation. An

example of a catalyst bench experiment replicating these conditions is shown in Figure 3.23.

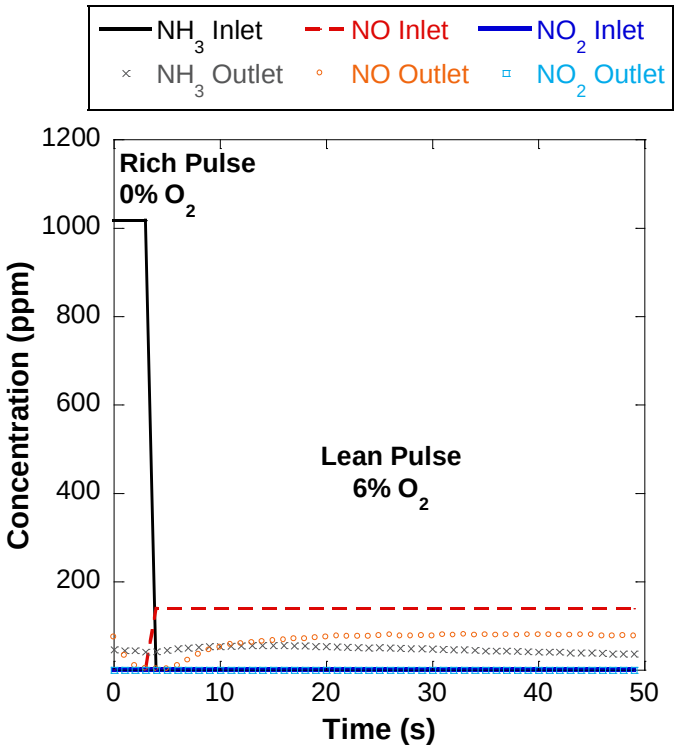

Figure 3.23 – NH_3 stores on catalyst during rich pulse, NO_x reacts with stored NH_3 on lean pulse. The experiment was performed as a lean rich cycling bench experiment for 50 sec cycle length at constant temperature of 250°C and a feed gas with 8% H_2O, and 8% CO_2.

From Figure 3.23 it can be seen that NH_3 will store on the catalyst during the rich pulse, and then will either react with NO_x or O_2 during the lean pulse or it will desorb off the catalyst. Instantaneous NO_x conversion for a switching experiment as previously defined in equation (3.36), is not a good measurement of catalyst activity. Instead integral NO_x conversion is defined in equation (3.73) and provides measurement of catalyst activity throughout a rich lean cycle.

$$\eta_{Int,NO_x} = \int_{Cycle} \left(\left[\frac{\left(y_{NO,in} + y_{NO_2,in}\right) - \left(y_{NO,out} + y_{NO_2,out}\right)}{\left(y_{NO,in} + y_{NO_2,in}\right)} \right] \cdot \left[\frac{P\dot{V}}{\bar{R}T} \right] dt \right) \tag{3.73}$$

Figure 3.24 summarizes the integral NO_x conversion, for switching experiments with six consecutive cycles at six different catalyst temperatures. Error analysis is performed as the RMS value of the standard deviation of integral NO_x conversion for the six consecutive cycles and the measurement error from the bench top reactor used in the experiments. When comparing the switching experiments with steady state experiments shown in Figure 3.18, it can be seen that steady experiments approach 90% conversion efficiency above 350°C, it can be seen that at temperatures above 375°C the integral NO_x conversion becomes limited by the amount of NH_3 the catalyst can store.

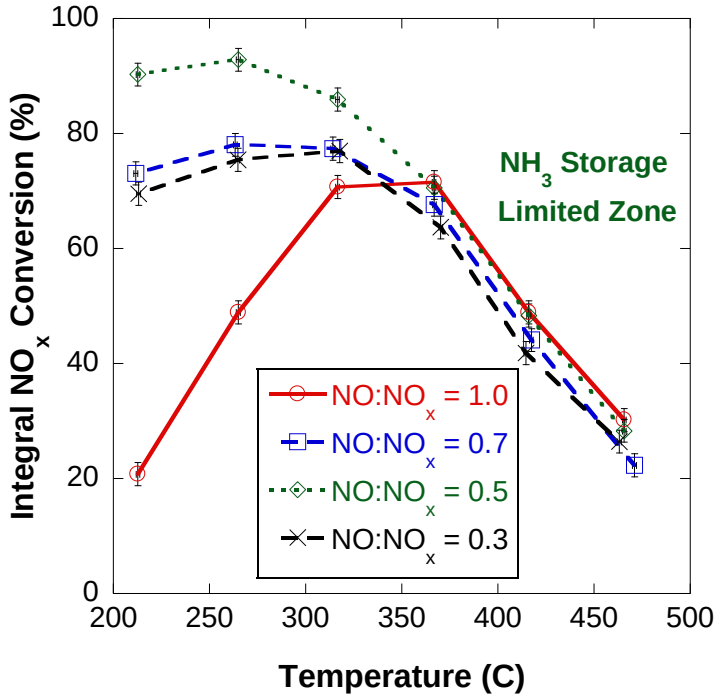

Figure 3.24 – Integral NO_x conversion decreases as temperature increase above 300°C, due to the limited ability to store NH_3 at high temperatures in switching experiments. All experiments are performed with a rich pulse of 8% H_2O, 8% CO_2, 1000 ppm NH_3; and a lean pulse of 8% H_2O, 8% CO_2, 150 ppm NO_x, with varying NO to NO_x ratios.

From the results shown in Figure 3.24 it can be seen that stored NH_3 on the catalyst is used to convert NO_x in the feed gas, therefore the gas phase NO_x reduction reactions shown in equations (3.37), (3.38), (3.39), (3.68), and (3.67) can be rewritten as the NH_3 storage reactions shown in equations (3.74), (3.75), (3.76), (3.77), and (3.78)

respectively which confirms results by Kim et al. [47], Olsson et al. [45], and Wurzenberger et al. [48].

$$4Z\left(NH_3\right)+4NO+O_2 \rightarrow 4Z+4N_2+6H_2O \tag{3.74}$$

$$2Z\left(NH_3\right)+NO+NO_2 \rightarrow 2Z+2N_2+3H_2O \tag{3.75}$$

$$8Z\left(NH_3\right)+6NO_2 \rightarrow 8Z+7N_2+12H_2O \tag{3.76}$$

$$4Z\left(NH_3\right)+6NO \rightarrow 4Z+5N_2+6H_2O \tag{3.77}$$

$$2Z\left(NH_3\right)+2NO_2 \rightarrow 2Z+N_2+N_2O+3H_2O \tag{3.78}$$

Temperature Effects

Due to the dependence of temperature on the storage of NH_3 on the catalyst a possibility exists for a hysteresis where NO_x will differ depending on the direction of the temperature ramp in an experiment [136]. Figure 3.25, Figure 3.26, and Figure 3.27 show experiments performed with a constant feed gas where temperature was ramped upwards at 5°C/min from 200°C to 500°C then temperature was ramped downward at 5°C/min from 500°C to 200°C. From these experiments a small hysteresis effects is seen where NO_x conversion is lower during the downward ramp due to less NH_3 being available on the catalyst. Additionally, in Figure 3.25, Figure 3.26, and Figure 3.27 it can be seen that at lower temperatures ($T \approx 200°C$) the onset of nitrate formation can be seen from the experimental data. Nitrate formation can occur as low as 150°C where NO_2 formed at the catalyst surface can combine with H_2O to inhibit NO_x conversion with NH_3 on the catalyst. It was found by Despres et al. [137], Nova et al. [44], and Ciardelli et al. [135] that nitrates once formed can be removed at low temperature by NO, or by increasing temperature on the catalyst.

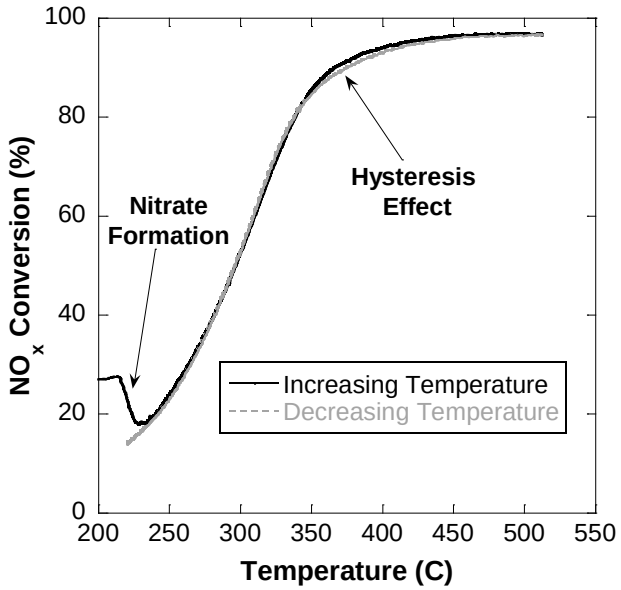

Figure 3.25 – Upward and downward temperature ramps differ with a small hysteresis effect between 350–450°C, additionally NO_x conversion changes differ at low temperatures due to the onset of nitrate formation. The experiment was performed as an upward and then downward temperature ramp with a feed gas of 6% H_2O, 6% CO_2, 6% O_2, 1000 ppm NH_3, and 1000 ppm NO.

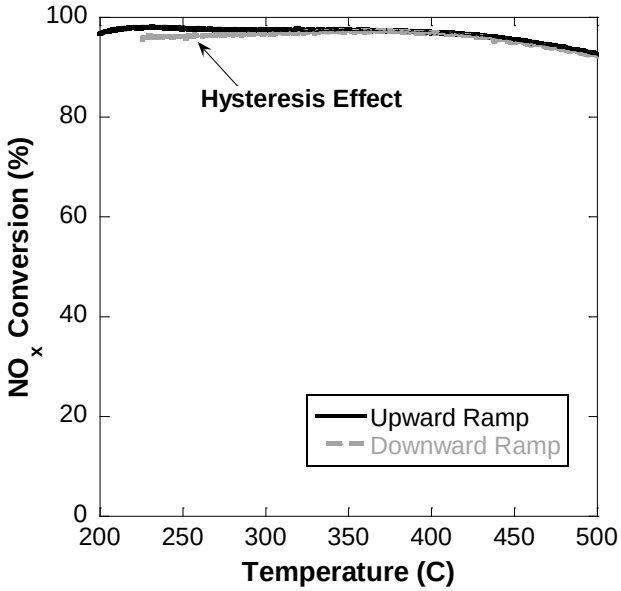

Figure 3.26 – Negligible hysteresis effect on NOx conversion for Fast SCR reaction. The experiment was performed as an upward and downward temperature ramp with 6% H_2O, 6% CO_2, 0% O_2, 1000 ppm NH_3, 500 ppm NO, 500 ppm NO_2.

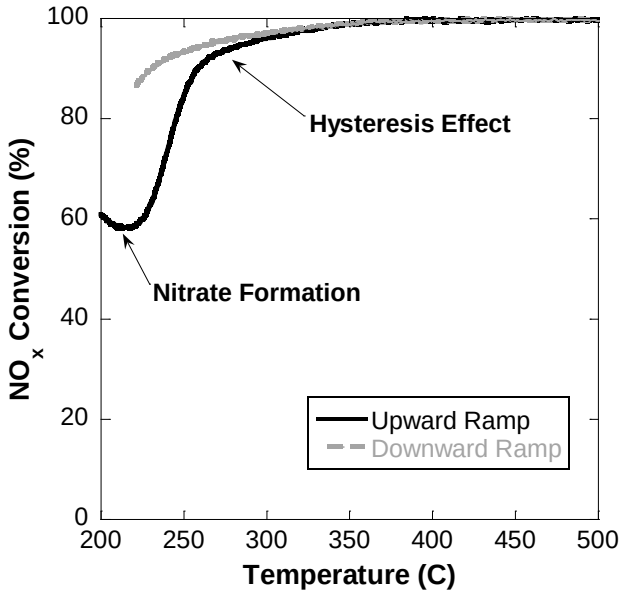

Figure 3.27 – Large hysteresis effect in NO_x conversion for Slow SCR reaction at low temperatures due to the nitrate formation on the catalyst. The experiment was performed as an upward and downward temperature ramp with 6% H_2O, 6% CO_2, 0% O_2, 1000 ppm NH_3, 750 ppm NO_2.

3.4.3 NO_x Reduction with NH_3 Modeling Approach

The modeling approach for NO_x reduction with NH_3 is accomplished by simultaneously determining the kinetic rate parameters of the four reactions shown (3.74), (3.75), (3.76), and (3.78). However, the kinetic parameters for the Rich Standard SCR reaction where the reaction shows reduction of NO with NH_3 when O_2 is not present in the feed gas (equation (3.77)) can be determined independently of the other NO_x reduction reactions.

Rich Standard SCR (O_2 = 0%)

The Rich SCR reaction shown in equation (3.77) shows the reduction pathway of NO with NH_3 when O_2 is not present in the feed gas. The kinetic rate form shown in equation (3.79) is developed from standard surface species reactions shown in Chapter 2.

$$4Z\left(NH_3\right)+6NO\rightarrow 4Z+5N_2+6H_2O \tag{3.77}$$

$$R=k\exp^{\left(\frac{-E}{\bar{R}\cdot T}\right)}y_{NO}\theta_{Z(NH_3)} \tag{3.79}$$

Figure 3.28 shows acceptable agreement in concentration values for experimental results compared to modeling results using the reaction shown in equation (3.77) with the standard kinetic rate form show in equation (3.79). While Figure 3.29 shows expected conversion levels for this reaction when comparing experimental and modeling results.

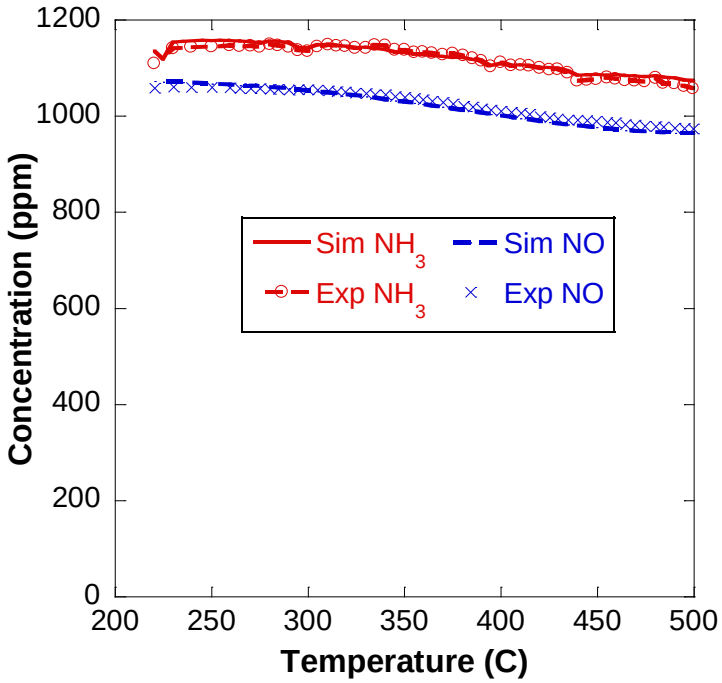

Figure 3.28 – The model for the Rich Standard SCR reaction accurately predicts the NH_3 and NO concentrations for a temperature ramp experiment with feed gas of 8% H_2O, 8% CO_2, 0% O_2, 1000 ppm NH_3, 1000 ppm NO

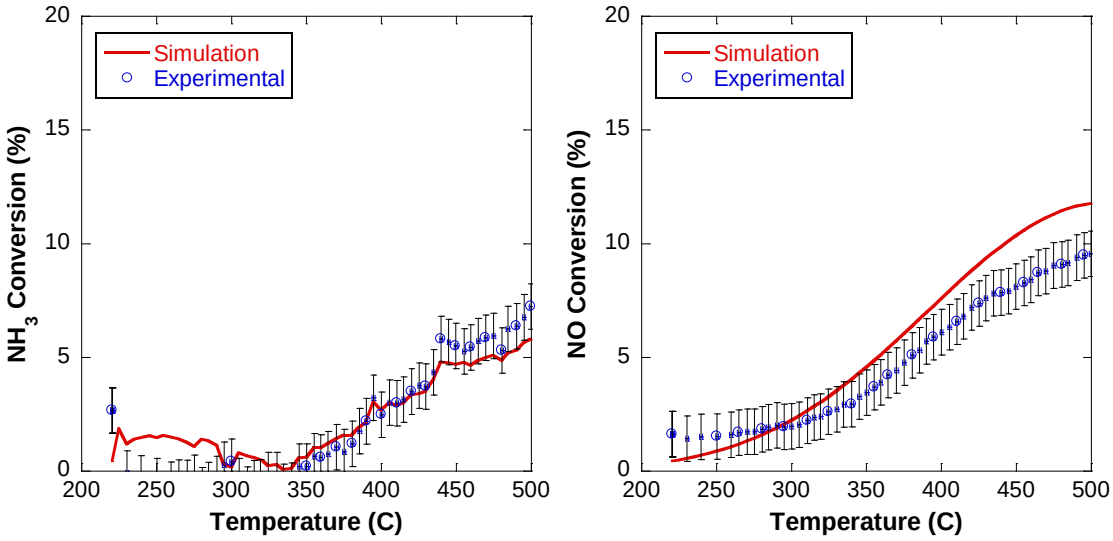

Figure 3.29 – NO Conversion is low without O_2 present in feed gas, standard Arrhenius rate kinetics capture this effect well.

Standard SCR (O_2 > 0%)

The Standard SCR reaction is the reduction of NO with NH_3 in the presence of O_2. In the early days of SCR modeling, quite often the only reaction used was a gas phase standard SCR reaction shown in equation (3.37). This assumption was made since NO_x in engine exhaust is approximately greater than 95% NO [4].

$$4NH_3 + 4NO + O_2 \rightarrow 4N_2 + 6H_2O \tag{3.37}$$

A common thought was that for many catalysts different SCR surfaces the kinetics of SCR can be modeled with simple power-law kinetics as shown in equation (3.80) [125, 130-133, 138].

$$R_{SCR} = k_{SCR}\left[NH_3\right]^{\alpha}\left[NO\right]^{\beta}\left[O_2\right]^{\delta} \tag{3.80}$$

While power-law kinetics are feasible, it is generally accepted that the rate of the SCR of NO by NH_3 obeys a Langmuir-Hinshelwood type mechanism involving reaction on copper-containing sites of an adsorbed species derived from NO with a different adsorbed species derived from NH_3 with a stronger adsorption of NH_3 than NO [41]. A

Langmuir-Hinshelwood type mechanism would also allow a pathway for results found by Stevenson et al. [130] and Eng and Bartholomew [132], where high levels of ammonia can inhibit the SCR reaction by replacing the available nitrate sites as shown in equation (3.81).

$$R_{SCR} = \frac{k_{SCR}[\mathrm{NO}][\mathrm{O_2}]}{1 + K_a[\mathrm{NH_3}]} \tag{3.81}$$

From current kinetic mechanisms for SCR catalysts where more than one NO_x reduction pathway exists, it is assumed that NO_x will only react with NH_3 stored on the catalyst surface and the reaction will written according to equation (3.74) [45-48, 128].

$$4Z(NH_3) + 4NO + O_2 \rightarrow Z + 4N_2 + 6H_2O \tag{3.74}$$

Sjövall et al. [46], Olsson et al. [45], Narayanaswamy and He [128], and Wurzenberger [48], all suggest that a kinetic rate in equation (3.82) with first order dependence on oxygen concentration be used to describe the standard SCR reaction in equation (3.74).

$$R = k \exp^{\left(\frac{-E}{\bar{R}\cdot T}\right)} y_{NO} y_{O_2} \theta_{Z(NH_3)} \tag{3.82}$$

While Kim et al. [47] suggest that the kinetic rate form should have an oxygen dependence (γ) for saturation effects of oxygen as shown in equation (3.83).

$$R = k \exp^{\left(\frac{-E}{\bar{R}\cdot T}\right)} y_{NO} \left(y_{O_2}\right)^{\gamma} \theta_{Z(NH_3)} \tag{3.83}$$

From earlier results it can be seen that it is important to keep oxygen concentration in the kinetic rate but the power dependence on oxygen concentration could not be determined (Figure 3.22). Therefore, the kinetic rates from equations (3.82) and (3.83) were both fit to using a downhill simplex optimizer to data from a temperature ramp experiment with a feed gas composition of 8% H_2O, 8% CO_2, 6% O_2, 1000 ppm

NH_3, and 1000 ppm NO. The results were then compared to a similar experiment with 2% O_2. Figure 3.30 shows how both kinetic rate forms compare to experimental results. Each kinetic rate yields the same result for the 6% O_2 experiment. The standard kinetic rate form in equation (3.82) yielded more accurate NH_3 concentration results for the 2% O_2 case, while the oxygen dependent rate form shown in equation (3.83) yielded more accurate NO conversion results. Due acceptable accuracy with each kinetic rate, it can be assumed that either rate for could be used, however due to less rate parameters being present in the standard rate form shown in equation (3.82) is suggested to be used.

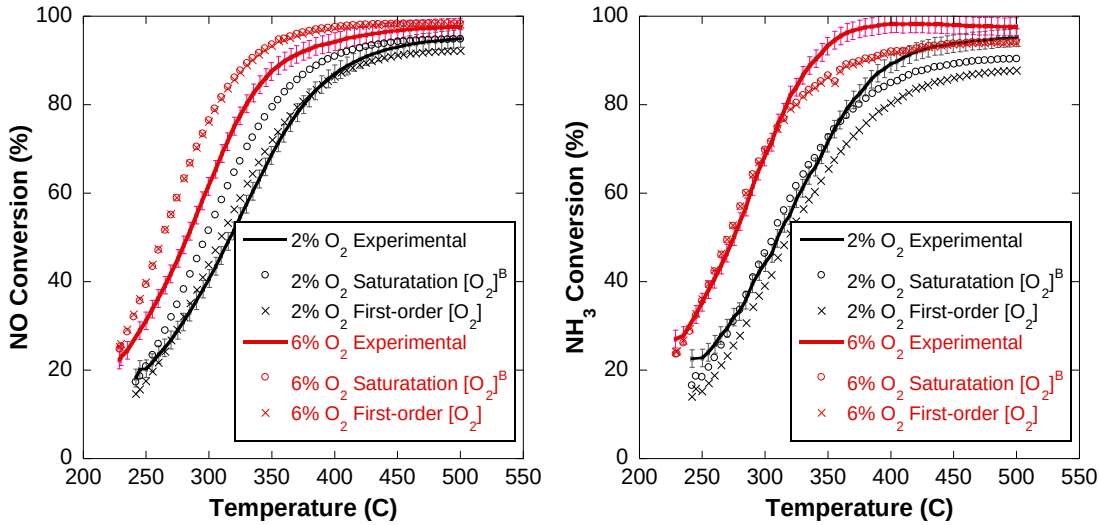

Figure 3.30 – The first order kinetic O_2 approximation is more accurate for NO predictions while the saturation kinetic O_2 approximation is more accurate for NH_3 predictions. Each experiment was performed as a temperature ramp experiment with feed gas of 8% H_2O, 8% CO_2, 1000 ppm NH_3, 1000 ppm NO, with O_2 concentration as listed

Fast SCR

The Fast SCR reaction shown in equation (3.75) has commonly been modeled with two methods, the first approach is a more detailed approach where NO_2 and NH_3 will form a ammonia nitrate on the catalyst surface which can then be reduced by NO as shown in equations (3.46) - (3.50). While the second approach models the global Fast SCR reaction using a standard Arrhenius rate form shown in equation (3.84).

$$2Z\left(NH_3\right)+NO+NO_2 \rightarrow 2Z+2N_2+3H_2O \tag{3.75}$$

$$R = k\exp^{\left(\frac{-E}{\bar{R}\cdot T}\right)} y_{NO}y_{NO_2}\theta_{Z(NH_3)} \tag{3.84}$$

Due to the temperature range expected the global reaction approach is used with the results shown in Figure 3.31. From the modeling results it can be seen that simulation predictions are statistically significant when the catalyst temperature is between 200°C – 450°C, while at temperatures above 450°C the model under predicts NO_x conversion.

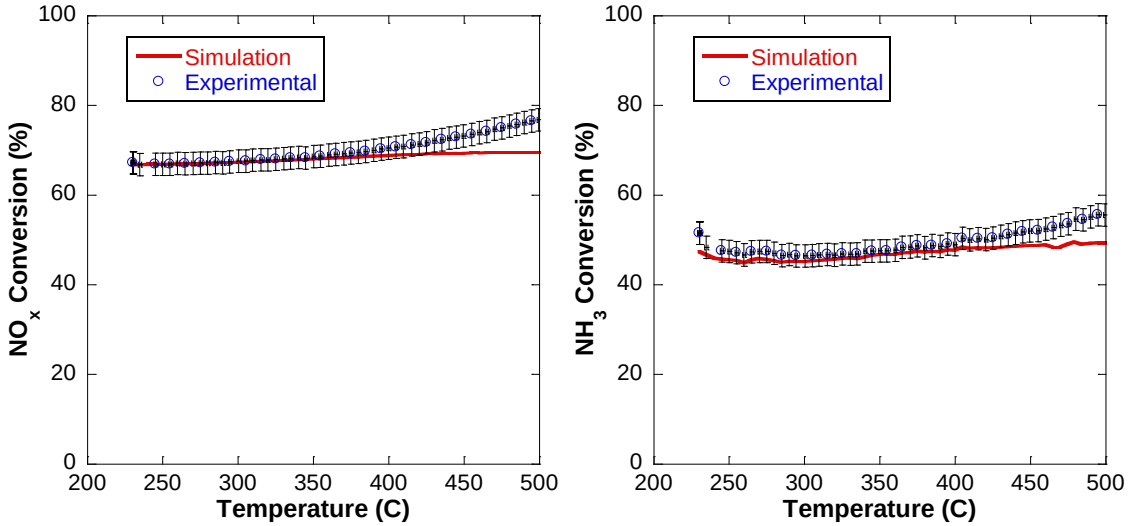

Figure 3.31 – Simulation prediction for NO_x conversion and NH_3 conversion is within error for 200°C – 450°C. The experiment was performed as a temperature ramp with 8% H_2O, 8% CO_2, 0% O_2, 1140 ppm NH_3, 540 ppm NO, 268 ppm NO_2.

Slow SCR

The global Slow SCR reaction shown in equation (3.76) is similar to the global fast SCR reaction, in that it can be modeled by two methods, the first approach is a more detailed approach where NO_2 and NH_3 will form a ammonia nitrate on the catalyst surface which can then be reduced by thermal decomposition of NO_2 to NO or by reduction of nitrate formation with HONO as shown in equations (3.59) – (3.66). The

second approach is to use an Arrhenius rate form for the global reaction shown in equation (3.85).

$$8Z\left(NH_3\right)+6NO_2 \rightarrow 8Z+7N_2+12H_2O \tag{3.76}$$

$$R = k\exp^{\left(\frac{-E}{\bar{R}\cdot T}\right)} y_{NO_2}\theta_{Z(NH_3)} \tag{3.85}$$

Due to the temperature range expected the global reaction approach is used with the results shown in Figure 3.32. From the modeling results it can be seen that simulation predictions are statistically significant for the tested temperature range.

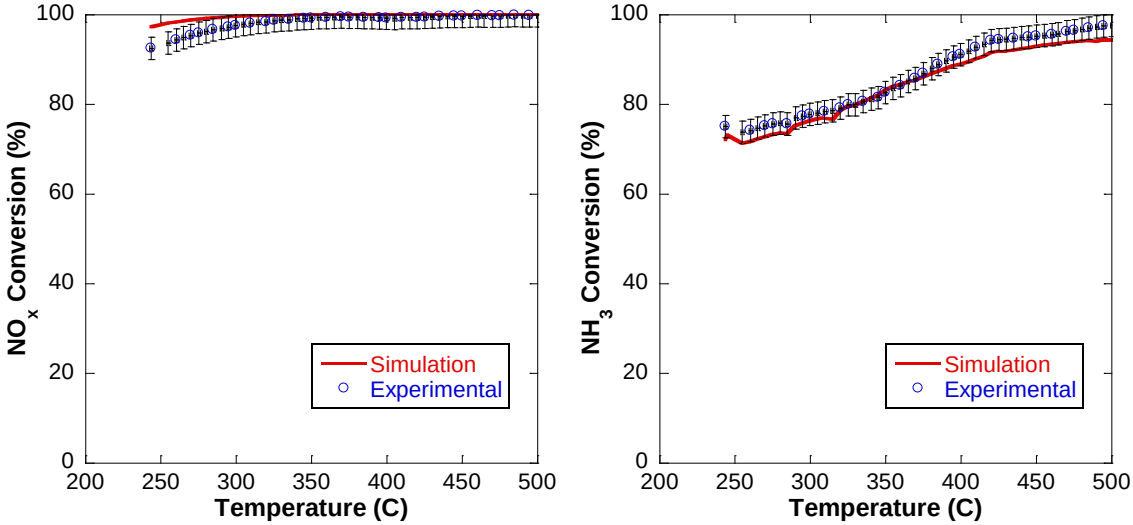

Figure 3.32 – Simulation predicts NO_x and NH_3 conversion within error NO_2 conversion with NH_3. The experiment was performed as a temperature ramp with 8% H_2O, 8% CO2, 0% O_2, 1110 ppm NH_3, 800 ppm NO_2.

3.5 Model Validation

Validation of a kinetic mechanism is done by comparing simulation results with experimental results not used for determining kinetic parameters. If simulation results are within experimental error, that model is validated to the accuracy the validation experiment.

3.5.1 Summary of Global SCR Mechanism

From the previous sections the following lean mechanism has been established as a starting point for developing a kinetic mechanism for the SCR catalyst in the EAS. A summary of the reactions and rate forms are listed in Table 3.1, while Table 3.2 lists corresponding parameters for the listed kinetic rates listed in Table 3.1.

Table 3.1 − Summary of chemical reaction and kinetic rates for lean SCR model

	Chemical Reaction	**Kinetics Rate Form**
(R1)	$NO + \frac{1}{2}O_2 \leftrightarrow NO_2$	$R_1 = k_1 \exp^{\left(\frac{-E_1}{RT}\right)} \left(y_{NO}\sqrt{y_{O_2}} - \frac{y_{NO_2}}{K_{eq}} \right)$
(R2)	$Z + NH_3 \leftrightarrow Z(NH_3)$	$R_2 = k_{2f} y_{NH_3} \theta_Z - k_{2r} \exp^{\left(\frac{-E_{2r}}{RT} - \lambda_{2r}\theta_{Z(NH_3)}\right)} \theta_{Z(NH_3)}$
(R3)	$4Z(NH_3) + 3O_2 \rightarrow 4Z + 2N_2 + 6H_2O$	$R_3 = k_3 \exp^{\left(\frac{-E_3}{RT}\right)} \left(y_{O_2}\right)^{\gamma_3} \theta_{Z(NH_3)}$
(R4)	$4Z(NH_3) + 6NO \rightarrow 4Z + 5N_2 + 6H_2O$	$R_4 = k_4 \exp^{\left(\frac{-E_4}{RT}\right)} y_{NO}\theta_{Z(NH_3)}$
(R5)	$4Z(NH_3) + 4NO + O_2 \rightarrow 4Z + 4N_2 + 6H_2O$	$R_5 = k_5 \exp^{\left(\frac{-E_5}{RT}\right)} y_{NO}y_{O_2}\theta_{Z(NH_3)}$
(R6)	$2Z(NH_3) + NO + NO_2 \rightarrow 2Z + 2N_2 + 3H_2O$	$R_6 = k_6 \exp^{\left(\frac{-E_6}{RT}\right)} y_{NO}y_{NO_2}\theta_{Z(NH_3)}$
(R7)	$8Z(NH_3) + 6NO_2 \rightarrow 8Z + 7N_2 + 12H_2O$	$R_7 = k_7 \exp^{\left(\frac{-E_7}{RT}\right)} y_{NO_2}\theta_{Z(NH_3)}$
(R8)	$2Z(NH_3) + 2NO_2 \rightarrow 2Z + N_2 + N_2O + 3H_2O$	$R_8 = k_8 \exp^{\left(\frac{-E_8}{RT}\right)} y_{NO_2}\theta_{Z(NH_3)}$

Table 3.2 − Summary of kinetic parameters used in the lean SCR model kinetic model

Parameter	**Value**	**Units**
Site density	1.13×10^{-2}	[kmol m^{-2}]
k_1	1.06×10^{0}	[kmol m^{-3} s^{-1}]
E_1	24.64	[kJ mol^{-1}]
k_{2f}	7.99×10^{-2}	[kmol m^{-2} s^{-1} $mole_{NH3}^{-1}$]
k_{2r}	1.29×10^{7}	[kmol m^{-2} s^{-1}]
E_{2r}	98.00	[kJ mol^{-1}]
λ_{2r}	0.2894	[-]
k_3	1.31×10^{1}	[kmol m^{-2} s^{-1} $mole_{O2}^{-1}$]
E_3	66.79	[kJ mol^{-1}]
γ_3	0.2585	[-]
k_4	3.63×10^{3}	[kmol m^{-2} s^{-1} $mole_{NO}^{-1}$]
E_4	57.94	[kJ mol^{-1}]
k_5	2.6×10^{7}	[kmol m^{-2} s^{-1} $mole_{NO}^{-1}$ $mole_{O2}^{-1}$]
E_5	76.29	[kJ mol^{-1}]
k_6	5.41×10^{9}	[kmol m^{-2} s^{-1} $mole_{NO}^{-1}$ $mole_{NO2}^{-1}$]
E_6	0.46	[kJ mol^{-1}]
k_7	1.06×10^{9}	[kmol m^{-2} s^{-1} $mole_{NO2}^{-1}$]
E_7	104.45	[kJ mol^{-1}]
k_8	7.99×10^{2}	[kmol m^{-2} s^{-1} $mole_{NO2}^{-1}$]
E_8	0.00	[kJ mol^{-1}]

Experiments were done to validate the kinetic mechanism using the synthetic gas bench and measurements on an International 6.4L engine using the EAS for emissions control. The following sections discuss the experimental and simulation results from the two sources.

3.5.2 Engine Validation

In this section the model is first compared to engine data taken with the EAS attached to a 6.4 L International diesel engine. Emissions data were taken simultaneously at the inlet and outlet of the SCR catalyst. At the inlet the AVL CEB II emissions bench is used for oxygen measurements, along with the H-Sense for hydrogen measurement, and an MKS FTIR measurement for all other species in the exhaust. For 1-D simulation the catalyst temperature is assumed to be constant which is determined by two thermocouples mounted in the front and back of the catalyst brick. The temperature of each thermocouple differed by an average of 10°C. The average temperature is shown in Figure 3.33 where the average SCR temperature increases to 420°C during the LNT regeneration of the EAS and cools to 370°C during normal operation.

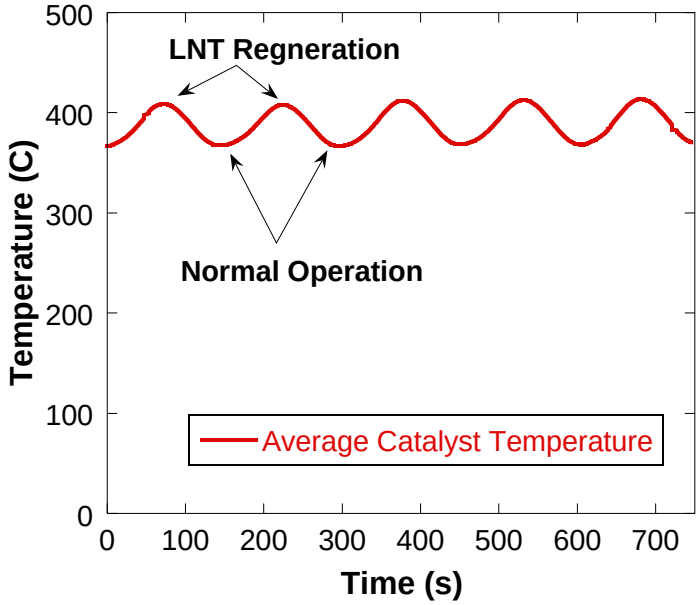

Figure 3.33 – The average SCR catalyst temperature varies from 370°C to 420°C during regeneration cycling of the EAS.

The EAS did not produce large amounts of NH_3 at the SCR inlet of the original design target during engine operation with the calibration of engine and EAS used in these experiments. Therefore, NO_x conversion for the SCR is moderate. Figure 3.34 shows agreement in inflection points between simulation predictions and experimental

results. However, it was determined that the model commonly over predicted the conversion NO_x, but all reactions with H_2, CO, and HC shown in Figure 3.35 are not included in the kinetic mechanism listed in Table 3.1 but will be discussed later in chapter 9.

The simulation error for each species was determined as the average absolute difference between experimental results and simulation results for each species. The average error for NO is 31.9 ppm, the average error for NO_2 is 18.2, and the average error for NH_3 is 2.2 ppm.

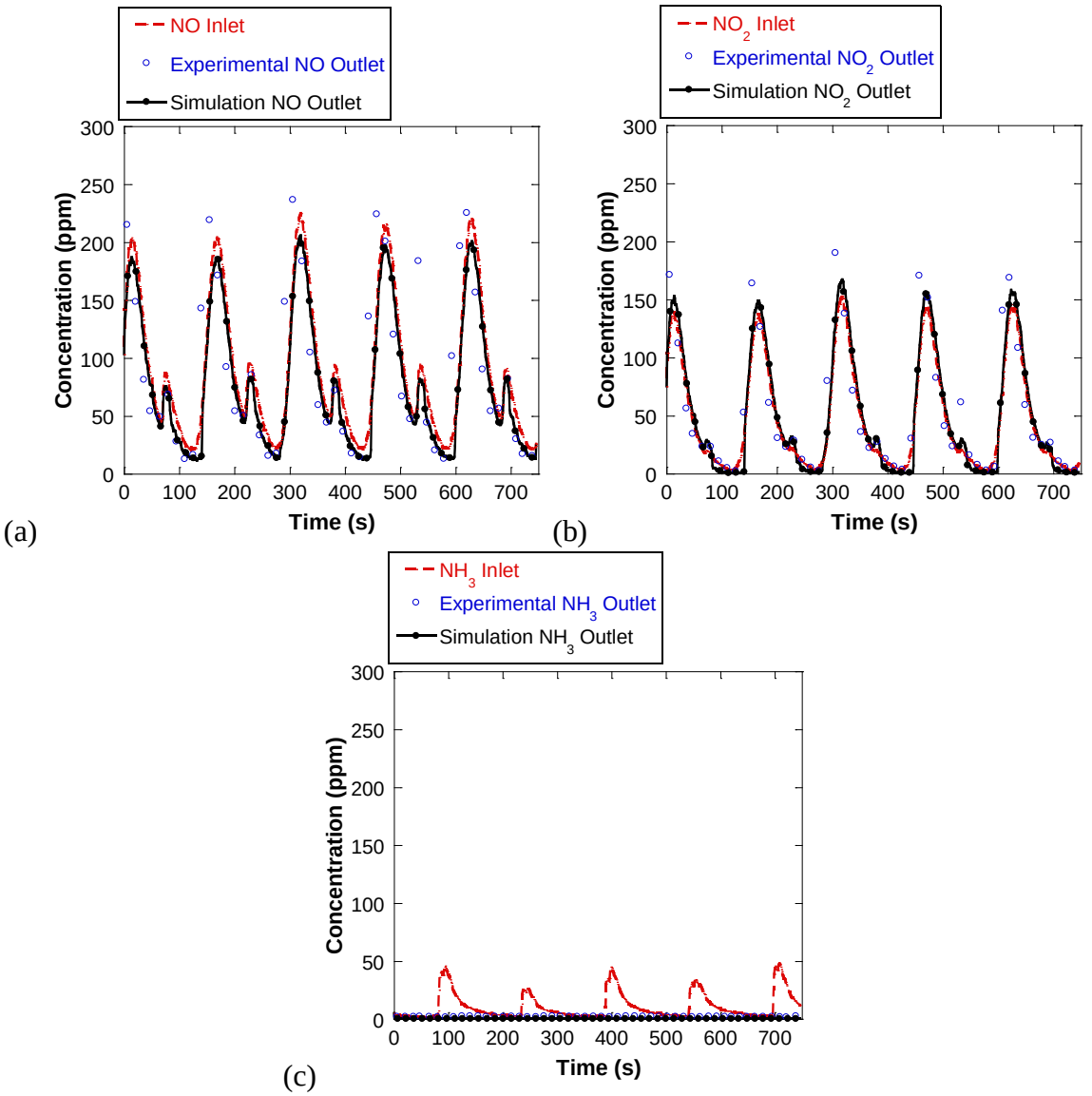

Figure 3.34 – Experimental and Simulation outlet species show acceptable agreement for (a) NO, (b) NO_2, and (c) NH_3.

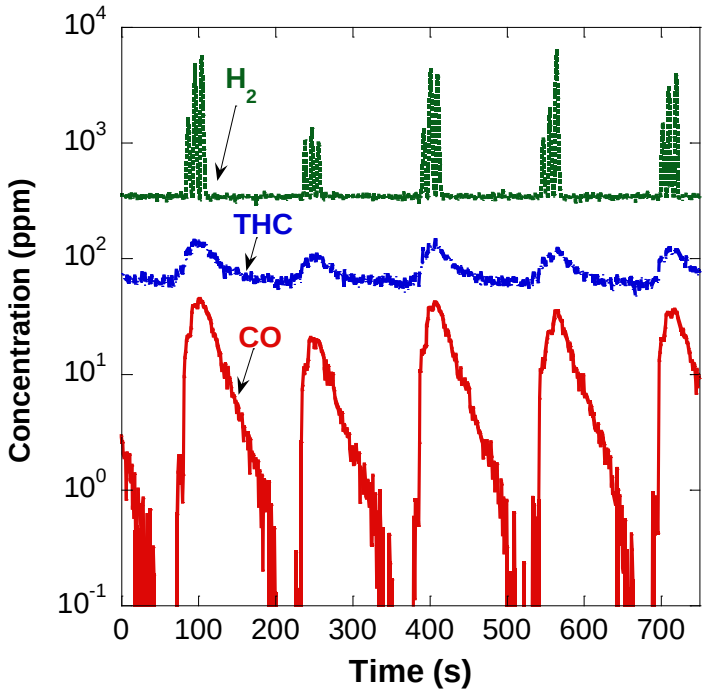

Figure 3.35 – Low levels of H_2, THC, and CO were present at the inlet of the SCR when engine validation data was measured.

3.5.3 Synthetic Gas Bench Validation

Further experiments were performed on the synthetic gas bench to replicate conditions for the SCR in the EAS. The SCR in the EAS ideally operates by storing the NH_3 from the rich regeneration to react with any NO_x that slips during lean operation. Using the synthetic gas bench an example of ideal operation of the EAS is shown in Figure 3.23, where a rich pulse where the feed gas has 0% O_2 and 1000 ppm NH_3 for five seconds followed by a lean pulse of 6% O_2 and 150 ppm NO_x for forty-five seconds.

The average integral NO_x conversion is then determine by averaging all six cycles at each temperature. The error for the experimental and simulation data is determined as standard deviation of the average integral NO_x conversion at each temperature. The simulation and experimental integral NO_x conversion results are shown in Figure 3.36, where it can be determined that the kinetic model results are statistically significant above 350°C, while below 350°C the model will under predict when the NO to NO_x ratio

equals 1.0, or over predict integral NO_x conversion when the integral NO_x conversion is equal to 0.5.

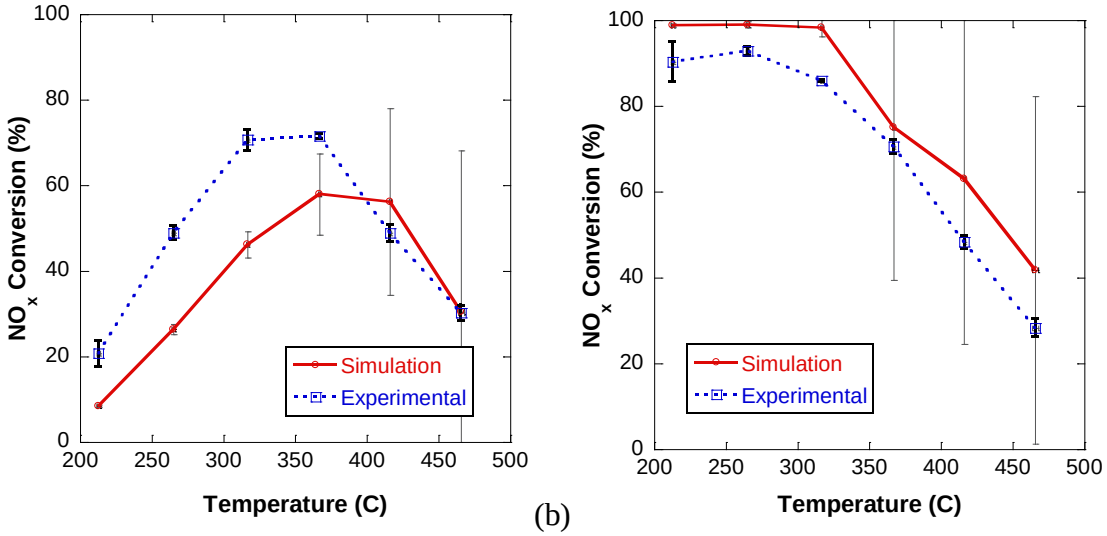

Figure 3.36 – Simulation data under predicts integral NOx conversion under 400°C when compared to the Experimental data when (a) NO:NOx = 1.0; while simulation data over predicts integral NOx conversion under 350°C when compared to the experimental data for (b) NO:NOx = 0.5 .

In Figure 3.36 it has been observed that the simulation predictions for integral NO_x conversion predictions match inflection points with the experimental data, but do not predict the right magnitude for the integral NO_x conversion. Figure 3.37 shows a comparison of simulation concentration values with experimental values for NO and NO_2. In all of the experiments there is a large amount of NO_x reduction after the rich pulse, then asymptotes to a minimum NO_x conversion during the lean pulse for the experimental data. However, since the NO_x reduction reactions (Reactions (4) – (8) in Table 3.1) are based linearly on the surface coverage fraction of NH_3 in the kinetic mechanism $\left(\theta_{Z(NH_3)}\right)$, the simulation predicted NO_x conversion will continue linearly throughout the lean pulse of the cycle until the predicted NH_3 on the catalyst is equal to zero. Therefore it can be determined that NO_x conversion is highly dependent on the amount of NH_3 on the surface of the catalyst.

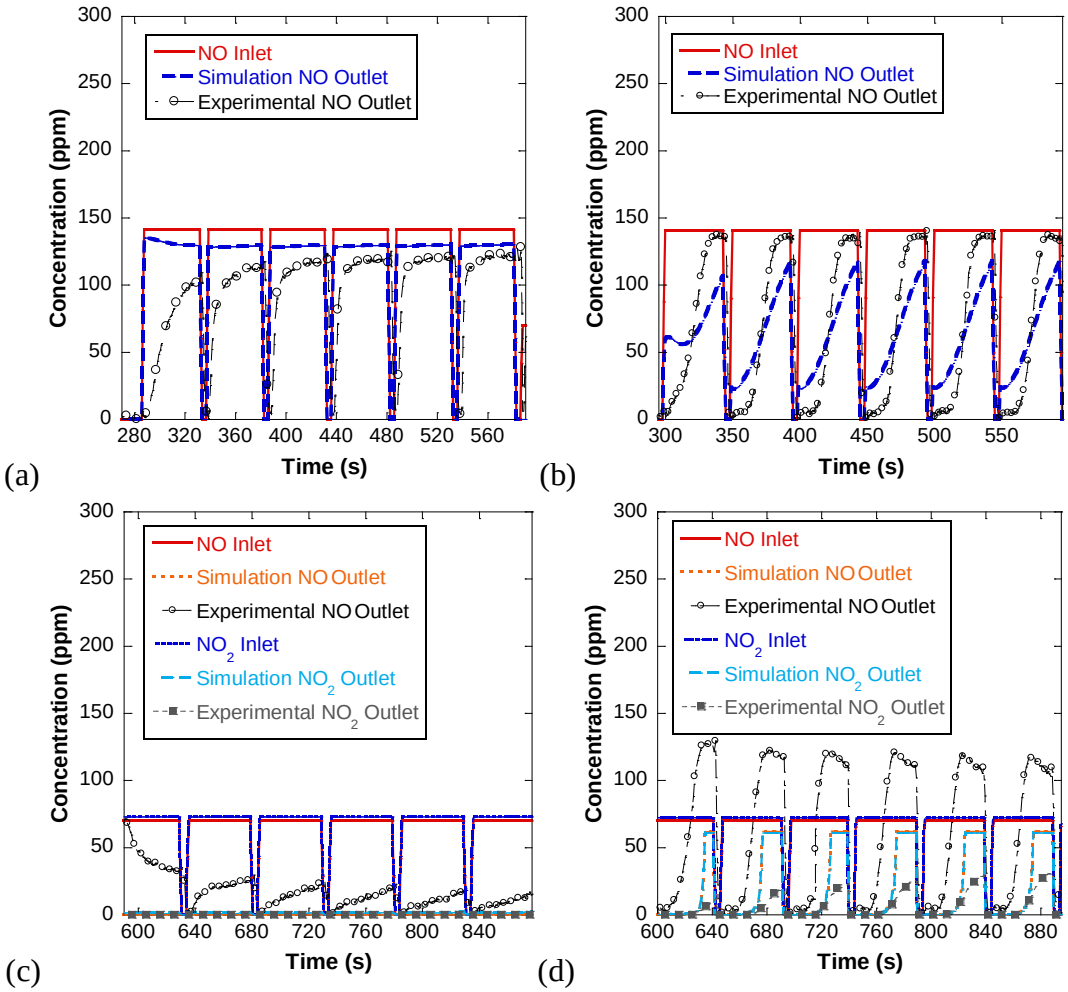

Figure 3.37 – The amount of stored NH_3 on the catalyst plays are large role in NO_x reduction capabilities during lean rich cycling experiments for (a) NO:NO_x = 1.0, Temperature =200°C, (b) NO:NO_x = 1.0, Temperature =400°C, (c) NO:NO_x = 0.5, Temperature =200°C, (d) NO:NO_x = 1.0, Temperature =400°C

3.6 Conclusions

The following conclusions can be made based on experimental and simulation results shown in this chapter.

3.6.1 NO Oxidation Conclusions

From the experimental data shown Figure 3.1 it can be concluded that the oxidation of NO to NO_2 is a reversible reaction with NO_2 experiencing thermal decomposition at temperatures above 300°C.

From experimental data in Figure 3.2 it can be determined that the oxidation of NO to NO_2 is dependent on O_2 concentration by a half order effect as seen in Figure 3.3, while from Figure 3.4 it can be determined that O_2 concentration has negligible effects on NO_2 thermal decomposition to NO and O_2.

Further experimental results shown in Figure 3.5 and Figure 3.6 show that a feed gas that includes H_2O and CO_2 will inhibit the oxidation of NO to NO_2 as well as the thermal decomposition of NO_2 to NO and O_2. However, this effect is negligible in the expected concentration range.

From the storage experiment shown in Figure 3.7 it can be determined that NO_2 adsorption is small with any adsorbed NO_2 thermally decomposing to NO making NO_2 adsorption negligible for kinetic modeling of the NO oxidation reaction.

From the experimental results it has been proven that the NO oxidation reaction is not inhibited by NO_2 and H_2O, and assuming NO and O_2 storage is negligible the kinetic rate in equation (3.14) is determined, which yields an accurate agreement between experimental and modeling results as shown in Figure 3.8.

3.6.2 NH_3 Storage Conclusions

It has been determined that a single site global approximation can be used to model the storage of NH_3 due to the presence of a single desorption peak in Figure 3.9. When NH_3 storage capacity for the simulation is compared to experimentally determined values it can be seen that multiple catalytic sites are used to store NH_3 due to non linearity in shape of the experimental data as seen in Figure 3.10. In Figure 3.11 it can be

seen that a slight accuracy increase can be made when using a Tempkin isotherm kinetic rate for the ammonia storage reaction.

3.6.3 NH_3 Oxidation Conclusions

As shown from experimental data in Figure 3.12 only negligible amounts of NO and N_2O formed when oxidizing NH_3 on the SCR catalyst. It is therefore only important to model the stoichiometric reaction for ammonia oxidation to complete combustion products as shown in equation (3.26). It has been determined experimentally that increasing O_2 concentration will increase ammonia conversion during ammonia oxidation, although it is not a linear effect between 0.5% and 6% O_2 concentration in the feed gas as seen in Figure 3.14. Lastly, it was found that to account for ammonia oxidation in a kinetic model where O_2 concentration can drastically vary, such as in the EAS, that a saturation kinetic reaction rate needs to be used to increase the accuracy of the model.

3.6.4 NO_x Reduction with NH_3 Conclusions

It can be concluded that the NO to NO_x ratio is an important determining characteristic of the feed gas when predicting NO_x conversion with NH_3 with max conversion of NO_x occurring when the feed gas contains equal amounts of NO and NO_2 as seen in Figure 3.18. It can also be determined from Figure 3.18 that NO_x reduction with NH_3 occurs due to three simultaneous global reactions shown in equations (3.37), (3.38), and (3.39). The stoichiometric ratios for the three reactions in equations (3.37), (3.38), and (3.39) are confirmed by varying the NH_3 to NO_x ratio to maximize NO_x and NH_3 conversion for the purposed NO to NO_x ratios as seen in Figure 3.19. Experimental results with varying oxygen concentration as shown in Figure 3.20 have shown that only NO reduction with NH_3 is dependent on oxygen concentration. Due the ability for NO_x

conversion with NH_3 during cycling experiments shown in Figure 3.23; where NH_3 is present in the rich pulse while NO_x is present in the lean pulse, the simultaneous NO_x conversion with NH_3 reactions shown in equations (3.37), (3.38), (3.39), (3.68), and (3.67) can be rewritten as reaction that take place with NH_3 stored on the surface of the catalyst as shown in equations (3.74), (3.75), (3.76), (3.77), and (3.78) respectively.

It has been determined that the reduction of NO with NH_3 when oxygen is not present is small but can be accounted for using standard kinetic rate expressions as seen in (3.77). It can be seen that when oxygen is present NO conversion with NH_3 is strongly dependent on temperature as seen in Figure 3.21. A method to determine the oxygen dependence for this reaction was used which yielded results that show that the oxygen dependence is also a function of temperature as seen in Figure 3.22. It is proposed that this is due to the effect of simultaneous nature of the NO Oxidation, NH_3 Oxidation, Fast SCR, and Slow SCR reactions on the catalyst.

From the Fast SCR reaction as shown in equation (3.75) it was determined that the Fast SCR reaction can be modeled as a global reaction with a standard Arrhenius kinetic rate for the 200°C – 450°C temperature range as seen in Figure 3.31.

The Slow SCR reaction as shown in equation (3.76) was determined to have the largest hysteresis effect at low temperatures; primarily due to the formation of ammonium nitrate at low temperatures on the catalyst surface. The global Slow SCR reaction with a standard Arrhenius rate simulation was shown to be within error and is therefore considered adequate when predicting NH_3 and NO_x conversion for the entire temperature range tested as shown in Figure 3.32.

3.6.5 Model Validation Conclusions

It was observed in Figure 3.34 that simulation predictions align within 15% of experimental engine data. However, it should be noted that during validation testing of

the EAS and engine, the NH_3 levels at the SCR inlet were low which correlates to low activity of the SCR catalyst. Therefore further validation experiments were required.

The synthetic gas bench was then used for further validation of the kinetic mechanism. Cycling experiments were designed as shown in Figure 3.23, where 1000 ppm of NH_3 was stored on the catalyst during a five second rich pulse to reduce NO_x present in the forty-five second lean pulse. Simulation predictions were compared to varying the NO to NO_x ratios in the lean pulse, where it was observed that the kinetic model under predicts integral NO_x conversion when the NO to NO_x ratio favors NO, and over predicts integral NO_x conversion when the NO to NO_x ratio favors an equal mixture as seen in Figure 3.36. It is determined that the NO_x conversion is a strong function of stored NH_3 on the catalyst, which is determined to be the weak point in the current kinetic model.

CHAPTER 4

N_2O PRODUCTION AND REACTIONS

With increasing emphasis on greenhouse gases, nitrous oxide (N_2O) emissions from automobiles are coming under increasing scrutiny [139-142]. N_2O is an absorber of infrared radiation and contributes around 8% to the "greenhouse effect" in the troposphere [143]. N_2O is a stable molecule with a lifetime of 170 years, and can diffuse into the stratosphere causing ozone layer depletion [144-146]. This chapter will discuss the potential for production of N_2O on the SCR catalyst used in the EAS, as well a suggested modeling approach to account for the reduction of N_2O with NH_3.

4.1 Background

Previous research regarding N_2O over zeolite-based catalysts has shown that it can be formed when either NO or NO_2 is in the inlet mixture [87, 92, 116, 117, 119, 147-149]. Research has shown that Cu-containing zeolites clearly formed larger amounts of N_2O than Fe-containing zeolites [92]. Ciardelli et al. [135] has suggested from work on vanadium and iron based zeolite catalyst that NH_3 and NO_2 will form ammonium nitrate as the precursor to all reactions with NH_3 and NO_2 as seen in equation (4.1). Ciardelli then suggests ammonium nitrate can be reduced with NO as seen in equation (4.2), or form N_2O due to thermal breakdown as seen in equation (4.3).

$$2NH_3 + 2NO_2 \rightarrow NH_4NO_3 + N_2 + H_2O \quad (4.1)$$

$$NH_4NO_3 + NO \rightarrow NO_2 + N_2 + 2H_2O \quad (4.2)$$

$$NH_4NO_3 \rightarrow N_2O + 2H_2O \quad (4.3)$$

This is corroborated in experimental tests over a H-ZSM-5 catalyst [87, 149] and a copper-zeolite catalyst [116] where the selectivity to N_2O is highest in the case of 100% NO_2.

Kim et al. [47] has summarized three possible reaction pathways for N_2O production shown in equations (4.4) – (4.6) where N_2O can be formed as a product of NH_3 and O_2, NO, or NO_2 respectively. Kim et al. suggests any N_2O production reaction can be neglected based on experimental data.

$$4NH_3 + 4O_2 \rightarrow 2N_2O + 6H_2O \quad (4.4)$$

$$4NH_3 + 4NO_2 + 3O_2 \rightarrow 4N_2O + 6H_2O \quad (4.5)$$

$$4NH_3 + 2NO_2 \rightarrow N_2 + N_2O + 3H_2O \quad (4.6)$$

Epling et al. [57] found that N_2O formation only occurs when NO_2 concentration is higher than NO concentration in the feed gas in experiments performed on a iron based zeolite SCR catalyst. Epling et al. performed spatial analysis experiments for the reduction of NO_2 with NH_3. When the maximum catalyst length was used in the spatial study large amounts of NO_2 and NH_3 were converted to N_2 and H_2O. However, the spatial analysis yielded large quantities of N_2O formation as less catalyst length is used. From these results Epling suggested a two reaction mechanism for NO_2 reduction with NH_3, where NO_2 and NH_3 first react to form N_2O as seen in equation (4.6), and then N_2O will be converted by NH_3 as seen in equation (4.7). N_2O reduction with NH_3 is consistent

with results by Mauvezin et al. [150] on an Fe-exchanged zeolite SCR catalyst. It should be noted that the combination of the reactions shown in equations (4.6) and (4.7) yield the global Slow SCR reaction for NO_2 reduction with NH_3 as seen in equation (4.8).

$$2NH_3 + 3N_2O \rightarrow 4N_2 + 3H_2O \quad (4.7)$$

$$8NH_3 + 6NO_2 \rightarrow 7N_2 + 12H_2O \quad (4.8)$$

4.2 Experimental Results

Experimental data for the N_2O production and reduction reactions when using a bench-top style reactor are collected using temperature ramp experiments which consist of constant inlet concentrations and varying temperature in a constant upward or downward ramp rate up to 5°C/min. The data presented by Epling et al. suggests space velocity is important when determining the reduction pathways of NO_2 and N_2O with NH_3 all experiments were run at a low space velocity so diffusion effects are minimized to determine the proper reduction pathway.

4.2.1 N_2O Production

Kim et al. [47] has suggested secondary pathways where N_2O production can exist during the reaction of NH_3 and NO or NO_2 on a copper based zeolite SCR catalyst. Since it was already experimentally determined in the last chapter that NH_3 and O_2 do not form N_2O on this catalyst, the reaction in equation (4.4) can be neglected. The N_2O generation reactions are shown in equations (4.5) and (4.6).

$$4NH_3 + 4NO + 3O_2 \rightarrow 4N_2O + 6H_2O \quad (4.5)$$

$$2NH_3 + 2NO_2 \rightarrow N_2 + N_2O + 3H_2O \quad (4.6)$$

Figure 4.1 shows the concentrations of NO, NO_2, N_2O, NH_3 on a temperature basis for five different experiments performed with different NO to NO_x ratios. By examining the levels of N_2O in these experiments it can be seen that N_2O formation is negligible when the NO to NO_x ratio is between 1.0 and 0.5; however when the NO to NO_x ratio is between 0.5 and 0.0, N_2O concentrations are considerable. When examining the NO_x N_2O pathways it can be seen that the reaction with NH_3 and NO to form N_2O shown in equation (4.5) can be neglected, while the reaction with NO_2 and NH_3 shown in equation (4.6) remains as the only N_2O pathway.

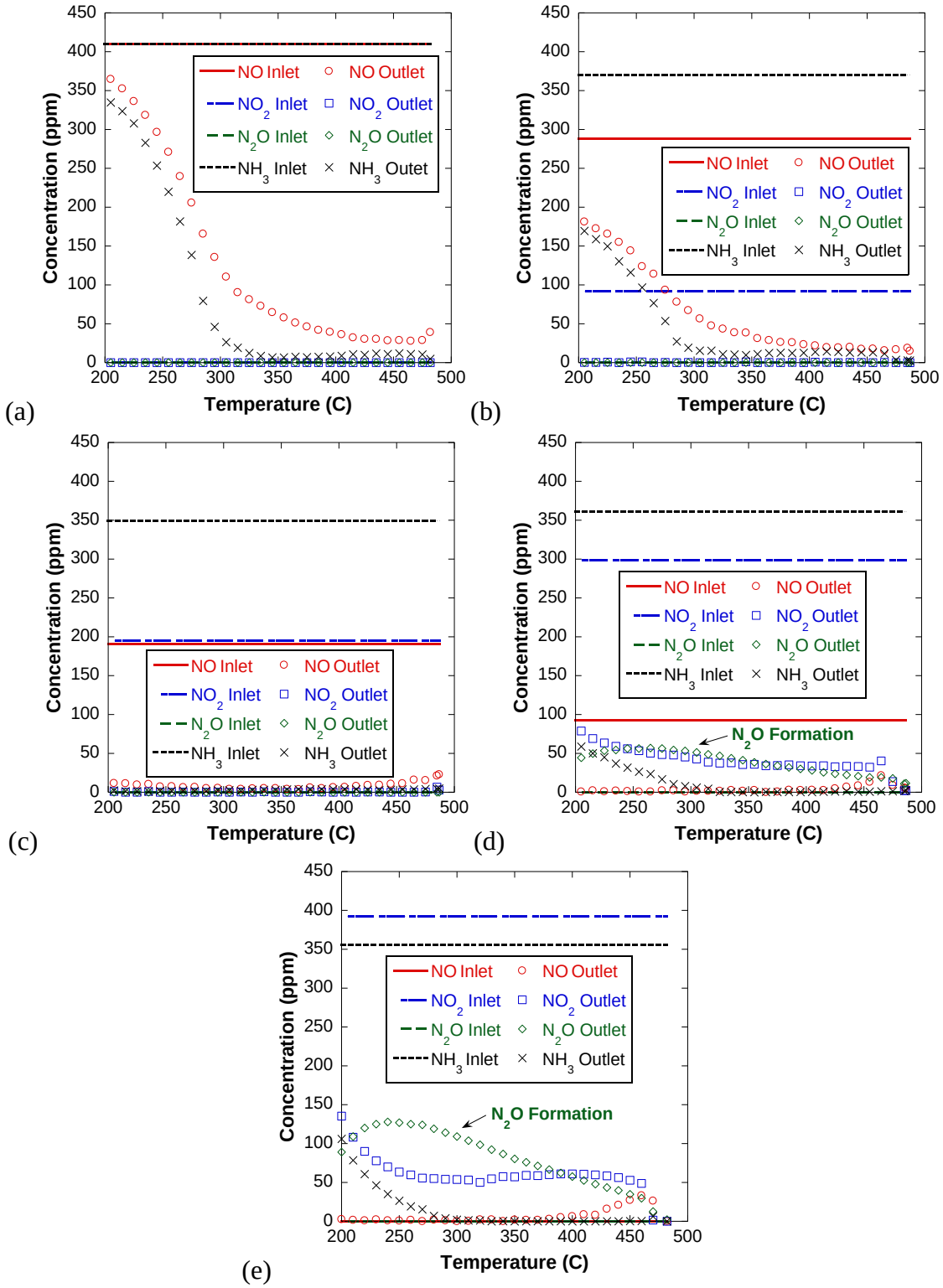

Figure 4.1 – Significant N_2O levels are seen when the NO to NO_x ratio favors NO_2, All experiments are performed as a temperature ramp with feed gas composition of 6% H_2O, 6% CO_2, 6% O_2, 400 ppm NH_3, 400 ppm NO_x, with an NO to NO_x ratio equal to (a) 1.0, (b) 0.75, (c) 0.5 (d) 0.25, and (e) 0.0.

4.2.2 Effect of NH_3 to NO_2 Ratio on N_2O Production

Since it has been determined that N_2O production is due to NH_3 reaction with NO_2, the conversion of NO_2 to N_2O is defined in equation (4.9) based on the stoichiometric values from equation (4.6) where two NO_2 molecules will combine with two NH_3 molecules to form one N_2O molecule.

$$\eta_{NO_2\_to\_N_2O} = \left(\frac{2 \cdot y_{N_2O\_out}}{y_{NO_2\_in}} \right) \cdot 100 \tag{4.9}$$

A series of experiments is then performed test the N_2O production for different NH_3 to NO_2 ratios in the feed gas. From the N_2O production reaction with NH_3 and NO_2 listed in equation (4.6) it can be seen that the stoichiometric ratio of NH_3 to NO_2 for N_2O production is 1.0 due to the highest value of NO_2 conversion to N_2O over the entire temperature range.

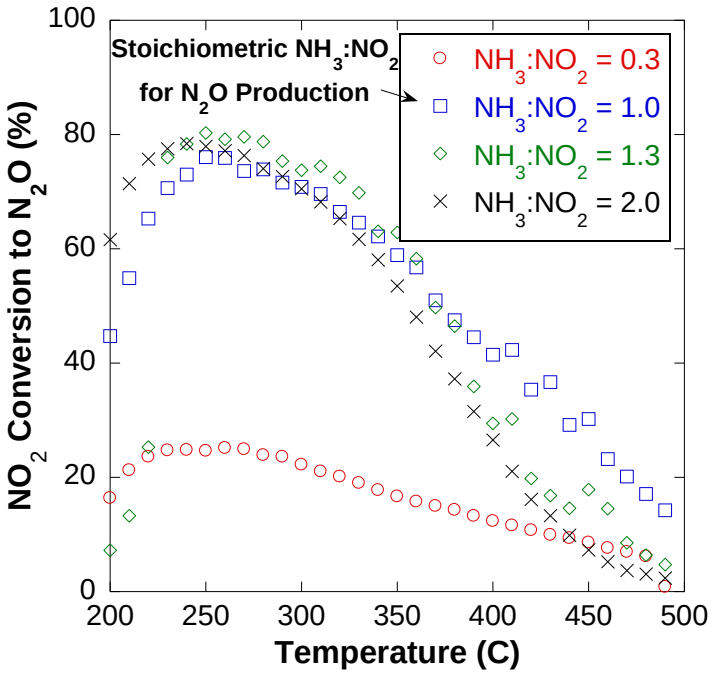

Figure 4.2 – N_2O production is the highest when there is an equal amount of NH_3 and NO_2 in the feed gas. The experiments were performed as a temperature ramp with 6% H2O, 6% CO_2, 0% O_2, 400 ppm NO_x, and varying NH_3 concentration in the feed gas.

4.2.3 N_2O Reaction with NH_3

Due to significant formation of N_2O when reducing NO_2 with NH_3, temperature ramp experiments were performed with N_2O and NH_3 in the feed gas. In Figure 4.2 it was observed that NO_2 conversion to N_2O reaches a maximum of 80% when varying temperature and the NH_3 to NO_2 ratio. According to the reaction scheme proposed by Epling et al. [57], the reaction of N_2O with NH_3 is expected in the entire temperature range. Figure 4.3 shows a temperature ramp experiment measuring the N_2O conversion due to a reaction with NH_3. From these experiments it was found that N_2O conversion with NH_3 is negligible below 350°C but steadily increases at temperatures above 350°C.

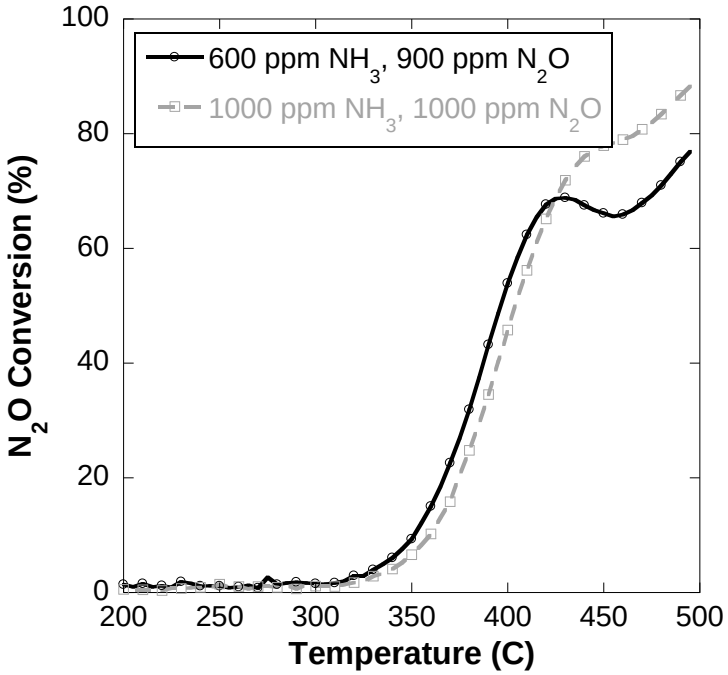

Figure 4.3 − N_2O conversion with NH_3 is negligible below 350°C. The experiment was performed as a temperature ramp with 6% H_2O, 6% CO_2 and listed NH_3 and N_2O concentrations in the feed gas.

4.2.4 N_2O Conversion in Fast SCR Reaction

Due to the high rate of conversion of NO_2 and NH_3 to N_2O, it is important to test if this occurs simultaneously with the Fast SCR reaction. By combing the Fast SCR

reaction in equation (4.10) with the N_2O production reaction from NH_3 and NO_2 shown in equation (4.6); the reduction of NO and N_2O by NH_3 reaction can be defined in equation (4.11). If experimental data proves this is indeed the precursor to these steps the reduction of NO and N_2O by NH_3 reaction (4.11) can be substituted for the Fast SCR reaction (4.10).

$$2NH_3 + NO + NO_2 \rightarrow 2N_2 + 3H_2O \tag{4.10}$$

$$2NH_3 + 2NO_2 \rightarrow N_2 + N_2O + 3H_2O \tag{4.6}$$

$$2NH_3 + 2NO + N_2O \rightarrow 3N_2 + 3H_2O \tag{4.11}$$

To measure total conversion of NO, NO_2, and N_2O with NH_3 during these experiments, NO_y conversion is defined according to equation (4.12).

$$\eta_{NO_y} = \left(\frac{\left(y_{NO\_in} + y_{NO_2\_in} + y_{N_2O\_in}\right) - \left(y_{NO\_out} + y_{NO_2\_out} + y_{N_2O\_out}\right)}{\left(y_{NO\_in} + y_{NO_2\_in} + y_{N_2O\_in}\right)} \right) \cdot 100 \tag{4.12}$$

An experiment is designed by combining NO, N_2O, and NH_3 in feed gas for a temperature ramp. If N_2O is a precursor in the Fast SCR experiment NO_y conversion would approach 95% conversion. From Figure 4.4 it can be seen that the conversion of NO and N_2O by NH_3 follows the same trend as the N_2O reduction with NH_3 as shown in Figure 4.4, where conversion is minimal below 350°C, but steadily increases as the temperature increases above 350°C. Therefore, the Fast SCR reaction shown in equation (4.10) cannot be substituted for the NO and N_2O reduction with NH_3 reaction shown in equation (4.11).

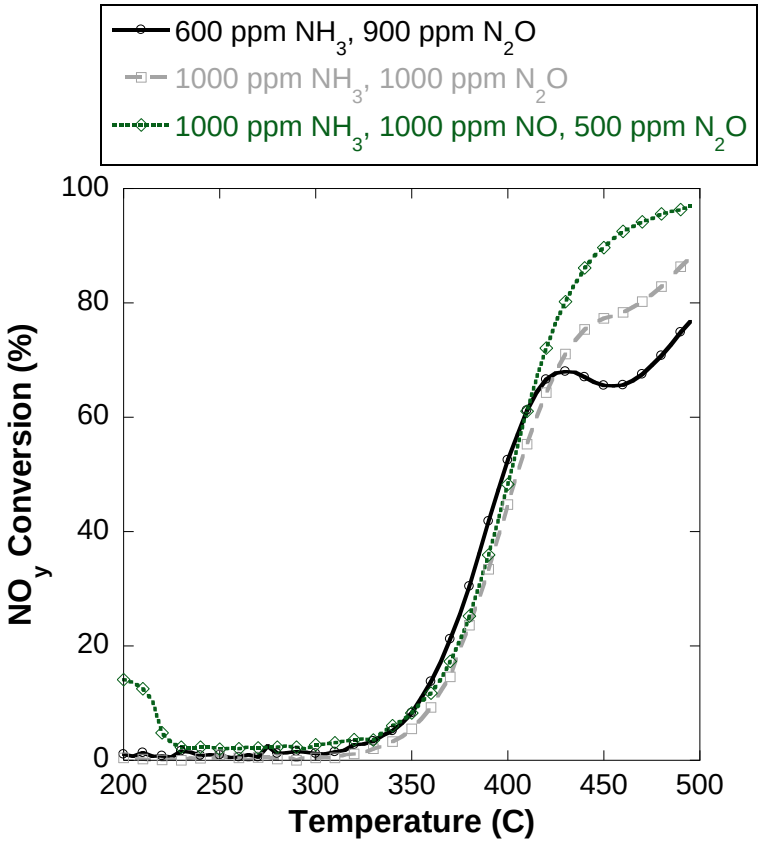

Figure 4.4 − The addition of NO in the feed gas of NH_3 and N_2O does not increase the conversion of NO_y. The experiments were performed as a temperature ramp with 6% H_2O, 6% CO_2, and listed values of NH_3, NO, and N_2O.

4.3 N_2O Production Effect on NO_2 Reduction with NH_3

From Figure 4.1 it was determined that N_2O production is significant when the NO to NO_x favors NO_2 with N_2O production being the highest when only NO_2 and NH_3 are in the feed gas. Therefore it can be determined that NO_x reduction with NH_3 is a combination of at least the four reactions shown in equations (4.13), (4.14), (4.15), and (4.16).

$$4NH_3 + 4NO + O_2 \rightarrow 4N_2 + 6H_2O \tag{4.13}$$

$$2NH_3 + NO + NO_2 \rightarrow 2N_2 + 3H_2O \tag{4.14}$$

$$6NH_3 + 8NO_2 \rightarrow 7N_2 + 12H_2O \quad (4.15)$$

$$2NH_3 + 2NO_2 \rightarrow N_2 + N_2O + 3H_2O \quad (4.16)$$

Epling et al. [57] has suggested that since N_2O production only occurs as a reaction with NH_3 and NO_2, equation (4.15) can be replaced with equation (4.17) if the N_2O production reaction is included as seen in equation (4.16).

$$2NH_3 + 3N_2O \rightarrow 4N_2 + 3H_2O \quad (4.17)$$

To test this theory by Epling et al. the NO_x conversion, the NO_2 conversion to N_2O, N_2O conversion with NH_3, and the NO_2 conversion due to thermal decomposition are plotted based on temperature as seen in Figure 4.5. It should be noted that the N_2O conversion with NH_3 and the NO_2 conversion due to thermal decomposition are from separate experiments shown earlier in Figure 4.3 and Figure 3.6 respectively. In Figure 4.5 it can be seen that most of the NO_x conversion from the reaction of NO_2 and NH_3 is initially due to NO_2 conversion to N_2O. However, as the temperature increases NO_2 conversion to N_2O decreases due to possible reactions with N_2O and NH_3 or by the enacting the Fast SCR reaction by thermally decomposition of NO_2 to NO.

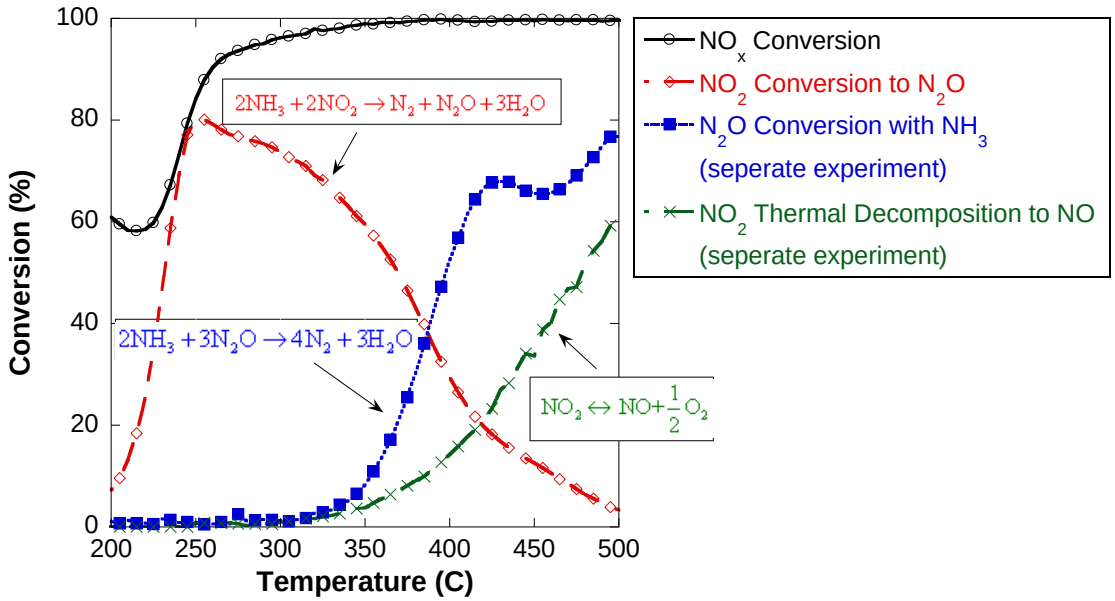

Figure 4.5 – Summary of NO_x conversion pathways for reactions with NO_2 and NH_3. The experiment was performed as a temperature ramp with 6% H_2O, 6% CO_2, 1000 ppm NH_3, and 750 ppm NO_2, in the feed gas.

From the conversions results shown in Figure 4.5, the conversion of NO_2 to N_2O $\left(\eta_{NO_2\_to\_N_2O}\right)$ and the N_2O conversion with NH_3 $\left(\eta_{N_2O}\right)$ are combined to see if their values equal the NO_x conversion values for the stoichiometric experiment. This is done to test the proposed reaction scheme by Epling et al. [57] as shown in equation (4.18).

$$\begin{array}{r} 2NH_3 + 2NO_2 \rightarrow N_2 + N_2O + 3H_2O \\ + \quad 2NH_3 + 3N_2O \rightarrow 4N_2 + 3H_2O \\ \hline 8NH_3 + 6NO_2 \rightarrow 7N_2 + 12H_2O \end{array} \approx \begin{array}{r} \eta_{NO_2\_to\_N_2O} \\ + \quad \eta_{N_2O} \\ \hline \eta_{NO_x} \end{array} \tag{4.18}$$

When comparing the method shown in equation (4.18) it can be seen in Figure 4.6 that a significant amount of NO_x conversion is unaccounted for, therefore it is important to test Epling et al. approximation by including the Fast SCR reaction from equation (4.10). The Fast SCR reaction is added by adding the NO_2 conversion due to thermal decomposition is assuming NO formed due to thermal decomposition $\left(\eta_{NO_2}\right)$ enacts the Fast SCR reaction which is the dominant reaction for NO_x reduction with NH_3. Since oxygen is not present in these experiments, the Standard SCR reaction as seen in equation

(4.13) is ignored. The combination of the Fast SCR reaction and N_2O pathways for NO_x reduction is shown mathematically in equation (4.19) with maximum predicted NO_x conversion based on these reactions is set to 100% conversion.

$$\begin{array}{l} 2NH_3 + 2NO_2 \rightarrow N_2 + N_2O + 3H_2O \\ + \quad 2NH_3 + 3N_2O \rightarrow 4N_2 + 3H_2O \\ + \quad NO_2 \leftrightarrow NO + \frac{1}{2}O_2 \\ + \quad 2NH_3 + NO + NO_2 \rightarrow 2N_2 + 3H_2O \\ \hline \eta_{NO_x} \end{array} \approx \min\left(\begin{bmatrix} \eta_{NO_2\_to\_N_2O} \\ \eta_{N_2O} \\ \eta_{NO_2} \\ + \\ \eta_{NO_x} \end{bmatrix} \; or \; [100]\right) \qquad (4.19)$$

A comparison of NO_x conversion from the experiment versus predicted values using the reaction pathways suggested by Epling et al. [57] are shown in Figure 4.6. From these results it can be seen that neither combination will account for the entire conversion of NO_x from the experimental data. It can therefore be concluded that the global Slow SCR reaction cannot be neglected in the reaction mechanism, but the additional pathway for N_2O conversion with NH_3 proposed by Epling et al. needs to be included.

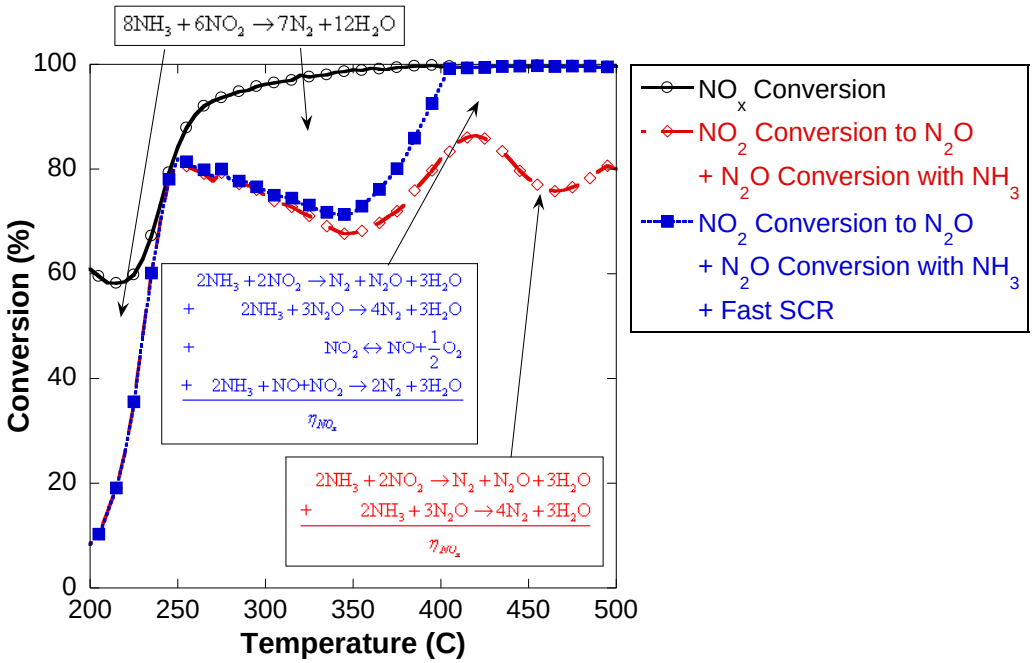

Figure 4.6 − The Slow SCR reaction cannot be neglected due the combination of other reactions not equaling the conversion of NO_x for NO_2 reduction with NH_3. The experiment was performed as a temperature ramp with 6% H_2O, 6% CO_2, 1000 ppm NH_3, and 750 ppm NO_2, in the feed gas.

4.4 Suggested Modeling Approach

In the detailed reactions shown in equations (4.1) – (4.3) there is no reaction pathway for the reduction of N_2O with NH_3. Due to the inability to test N_2O reactions with ammonium nitrate, a global mechanism is proposed to account for the results shown in Figure 4.6. From the last chapter it was determined that all the NO_x reduction with NH_3 reactions take place with NH_3 stored on the surface of the catalyst. Therefore, the proposed modeling global reactions for NO_x reduction with NH_3 are shown in equations (4.20) – (4.25).

$$4Z(NH_3) + 6NO \rightarrow 4Z + 5N_2 + 12H_2O \tag{4.20}$$

$$4Z(NH_3) + 4NO + O_2 \rightarrow 4Z + 4N_2 + 6H_2O \tag{4.21}$$

$$2Z(NH_3) + NO + NO_2 \rightarrow 2Z + 2N_2 + 3H_2O \quad (4.22)$$

$$6Z(NH_3) + 8NO_2 \rightarrow 6Z + 7N_2 + 12H_2O \quad (4.23)$$

$$2Z(NH_3) + 2NO_2 \rightarrow 2Z + N_2 + N_2O + 3H_2O \quad (4.24)$$

$$2Z(NH_3) + 3N_2O \rightarrow 2Z + 4N_2 + 3H_2O \quad (4.25)$$

While the kinetics for each reaction can be modeled as an Arrhenius rate as shown in equation (4.26). The pre-exponential (k) and the activation energy (E) from the Rich Standard SCR reaction (equation (4.20)) and the N_2O reduction with NH_3 reaction (equation (4.25)) can be determined based on separately based on their respective individual experiments. The pre-exponential and activation energy will need to be determined simultaneously for the remaining reactions from multiple experiments.

$$R = k \exp^{\left(\frac{-E}{RT}\right)} \theta_{Z(NH_3)} \prod_{i=\text{Inlet Species}} y_i \quad (4.26)$$

4.5 Conclusions

It has been determined that significant amounts of N_2O are produced simultaneously during the reduction of NO_x with NH_3 when the NO to NO_x ratio favors NO_2 as seen in Figure 4.1. It has been determined that up to 80% of NO_2 can be converted to N_2O when reacting with NH_3 as seen in Figure 4.2. From Figure 4.3 it was determined that NH_3 can be used to in the reduction of N_2O, but the reaction does not start until the catalyst temperature is above 350°C. It was determined that N_2O is not the critical pathway for NO_2 for the Fast SCR reaction because NO does not increase the conversion of N_2O with NH_3 below 350°C as seen in Figure 4.4. Lastly, it was determined that combining the NO_2 conversion to NO, N_2O conversion with NH_3, and

the NO_2 conversion due to thermal decomposition, a NO_x conversion estimate can be formed for the simultaneous NO_x reduction reactions. From these results it was seen that the Slow SCR reaction (equation (4.23)) cannot be neglected, as well as the N_2O production reaction from NO_2 and NH_3 (equation (4.24)) and the reduction of N_2O with NH_3 reaction (equation (4.25)) need to be included in the kinetic mechanism.

CHAPTER 5

EFFECT OF NH_3 STORAGE ON NO_X REDUCTION

One major weak point of the current kinetic mechanism is NO_x conversion predictions as NH_3 concentration varies. This is due to instantaneous reactions between NO, NO_2, and NH_3 during steady state operation. This chapter provides experimental studies of NO_x conversion dependence on NH_3 concentration on the catalyst as well as a proposal for modifications to the current kinetic rate form equations.

5.1 Model Validation Results

The current proposed global reactions and their corresponding kinetic rate forms are shown in Table 5.1. From Table 5.1 it can be seen that every reaction that includes NH_3 in its reactants includes surface coverage fraction of $NH_3\left(\theta_{Z(NH_3)}\right)$. The surface coverage fraction of NH_3 is a non-dimensional number from 0 to 1 that represents the amount of NH_3 stored on the catalyst compared to maximum amount of NH_3 able to store on the catalyst. When reviewing the kinetic rate equations for all reactions with NH_3 in the reactants in Table 5.1, it can be seen that each kinetic rate form is based on a linear dependence on the surface coverage fraction of NH_3.

Table 5.1 − Summary of chemical reaction and kinetic rates for lean SCR model from literature and experimental sources.

	Chemical Reaction	**Kinetics Rate Form**
(R1)	$NO + \frac{1}{2}O_2 \leftrightarrow NO_2$	$R_1 = k_1 \exp^{\left(\frac{-E_1}{RT}\right)} \left(y_{NO}\sqrt{y_{O_2}} - \frac{y_{NO_2}}{K_{eq}} \right)$
(R2)	$Z + NH_3 \leftrightarrow Z(NH_3)$	$R_2 = k_{2f} y_{NH_3} \theta_Z - k_{2r} \exp^{\left(\frac{-E_{2r}}{RT} - \lambda_{2r}\theta_{Z(NH_3)}\right)} \theta_{Z(NH_3)}$
(R3)	$4Z(NH_3) + 3O_2 \rightarrow 4Z + 2N_2 + 6H_2O$	$R_3 = k_3 \exp^{\left(\frac{-E_3}{RT}\right)} \left(y_{O_2}\right)^{\gamma_3} \theta_{Z(NH_3)}$
(R4)	$4Z(NH_3) + 6NO \rightarrow 4Z + 5N_2 + 6H_2O$	$R_4 = k_4 \exp^{\left(\frac{-E_4}{RT}\right)} y_{NO}\theta_{Z(NH_3)}$
(R5)	$4Z(NH_3) + 4NO + O_2 \rightarrow 4Z + 4N_2 + 6H_2O$	$R_5 = k_5 \exp^{\left(\frac{-E_5}{RT}\right)} y_{NO}y_{O_2}\theta_{Z(NH_3)}$
(R6)	$2Z(NH_3) + NO + NO_2 \rightarrow 2Z + 2N_2 + 3H_2O$	$R_6 = k_6 \exp^{\left(\frac{-E_6}{RT}\right)} y_{NO}y_{NO_2}\theta_{Z(NH_3)}$
(R7)	$8Z(NH_3) + 6NO_2 \rightarrow 8Z + 7N_2 + 12H_2O$	$R_7 = k_7 \exp^{\left(\frac{-E_7}{RT}\right)} y_{NO_2}\theta_{Z(NH_3)}$
(R8)	$2Z(NH_3) + 2NO_2 \rightarrow 2Z + N_2 + N_2O + 3H_2O$	$R_8 = k_8 \exp^{\left(\frac{-E_8}{RT}\right)} y_{NO_2}\theta_{Z(NH_3)}$
(R9)	$2Z(NH_3) + 3N_2O \rightarrow 2Z + 4N_2 + 3H_2O$	$R_9 = k_9 \exp^{\left(\frac{-E_9}{RT}\right)} y_{N_2O}\theta_{Z(NH_3)}$

From Table 5.1 the reactions listed in (R1) – (R8) were compared to lean/rich or lean-rich cycling experiments to validate the kinetic mechanism as shown in Figure 5.1. From these results it was shown that the SCR kinetic mechanism will under predict integral NO_x conversion below 400°C, while at or above 400°C the model prediction is statistically significant for the experimental results for an NO to NO_x ratio equal to 1.0 in the lean pulse. The kinetic mechanism will over predict integral NO_x conversion for the entire temperature range, however at or above 350°C the simulation predictions are statistically significant when compared to the experimental results for an NO to NO_x ratio equal to 0.5 in the lean pulse.

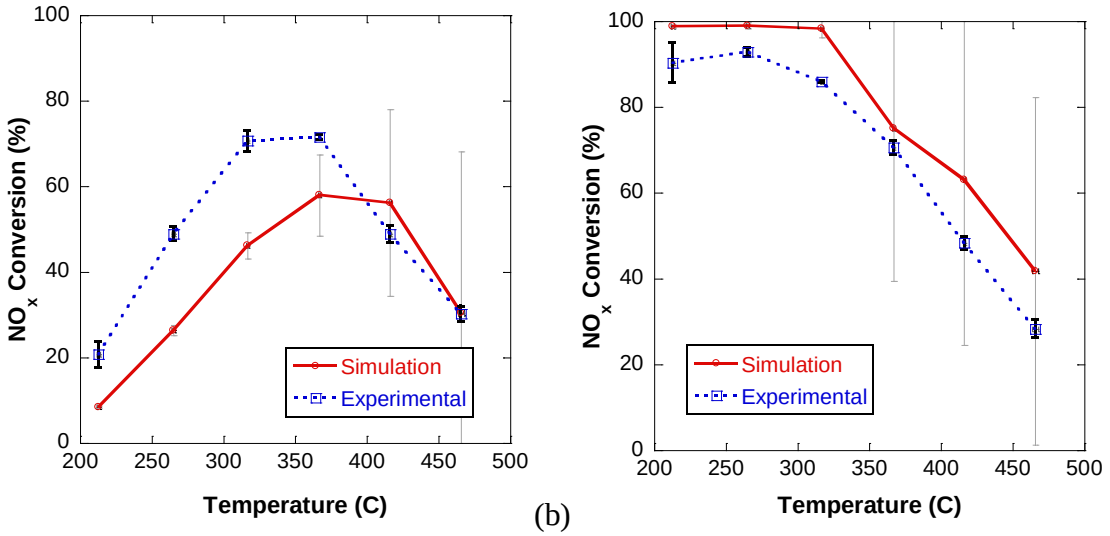

Figure 5.1 – Simulation data under predicts integral NO_x conversion under 400°C when compared to the Experimental data when (a) NO:NO_x = 1.0; while simulation data over predicts integral NO_x conversion under 350°C when compared to the experimental data for (b) NO:NO_x = 0.5.

When examining the common Arrhenius kinetic rate form for NH_3 based reactions shown in (5.1), it can be seen that at constant temperature and inlet composition that most of the kinetic rate form can be approximated as constant as seen in (5.2). The kinetic rate form is approximately constant. Due to the reduction of NO, NO_2, N_2O, or O_2 from the reactions, the mole fraction at the catalyst surface will see slight changes in composition.

$$R = k\exp^{\left(\frac{-E}{\bar{R}\cdot T}\right)}\left(\prod_{i=\text{reactants}} y_i\right)\theta_{Z(NH_3)} \tag{5.1}$$

$$k\exp^{\left(\frac{-E}{\bar{R}\cdot T}\right)}\left(\prod_{i=\text{reactants}} y_i\right) \approx const. \tag{5.2}$$

It can therefore be determined that NO_x reduction with the current kinetic mechanism shown in Table 5.1 is approximately linearly proportional to the surface coverage fraction of NH_3. Figure 5.2 shows the simulation and experimental NO concentrations from a lean pulse of one cycle where integral NO_x conversion values are statistically significant at 400°C in Figure 5.1 (a). In Figure 5.2 it can be seen that the

simulation using the kinetic mechanism predicts NO concentrations corresponding to linear reduction of NH_3 stored on the catalyst, while the experimental results shows definitively that NO concentration is not linearly reduced during the lean pulse. Upon further investigations a similar effect could be derived due to pressure pulsations however, since exhaust pressure is held constant on an engine by a variable geometry turbocharger aftertreatment catalysts pressure is assumed constant. Therefore, pressure was held constant for the rich and lean pulse in the reactor bench experiments. It can therefore be concluded that NO_x conversion is a strong function of the amount of NH_3 on the catalyst. For these experimental results the FTIR readings were offset based experimental data taken that bypassed the catalyst. It is possible that the time constant of the FTIR readings will filter the experimental data in these experiments, however since data is recorded at 1 Hz this will not affect the trend seen where approximately 15 seconds pass before NO breakthrough occurs in Figure 5.2.

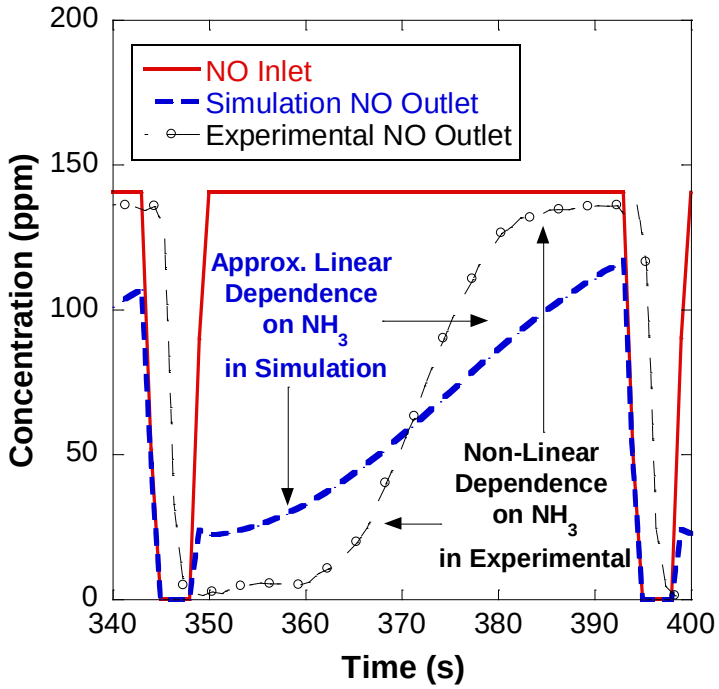

Figure 5.2 – The amount of stored NH_3 on the catalyst plays are large role in NO_x reduction capabilities during lean rich cycling experiments for NO:NO_x = 1.0, Temperature =400°C.

5.2 Experimental Results

Experiments from this section are performed to study the effect of stored NH_3 on NO_x conversion capabilities for the iron based zeolite SCR catalyst in the EAS. As stated earlier, under steady state conditions NH_3 levels react instantly with NO_x on the catalyst to form complete products (N_2 and H_2O). In an LNT-SCR aftertreatment system, NO_x is stored on the LNT during lean exhaust operation. NH_3 is produced as a byproduct of NO_x reduction with H_2 during a rich regeneration of the LNT catalyst. The SCR in the EAS operates by storing the NH_3 from the rich regeneration to react with any NO_x that slips during lean operation. An example of a catalyst bench experiment replicating these conditions is shown in Figure 5.3.

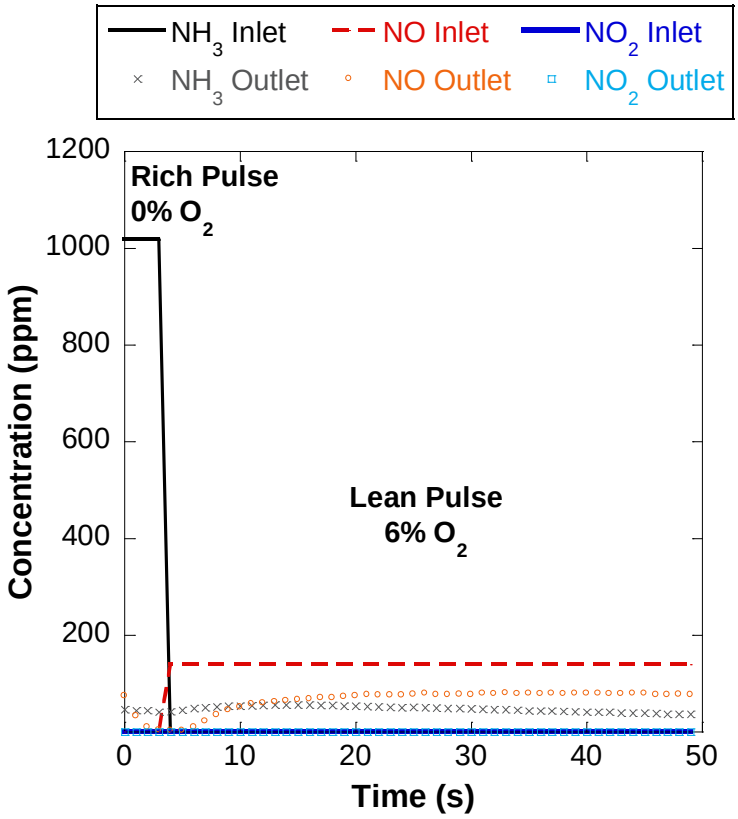

Figure 5.3 – NH_3 stores on catalyst during rich pulse, NO_x reacts with stored NH_3 on lean pulse. The experiment was performed as a lean rich cycling bench experiment for 50 sec cycle length at constant temperature of 250°C and a feed gas with 8% H_2O, and 8% CO_2.

Since NH_3 will store during the rich phase of the cycle, but NO_x conversion will only happen during the lean phase, it is important to study the effect of NH_3 storage on NO_x conversion across the SCR catalyst. An experiment is designed where temperature, CO_2 concentration, and H_2O concentration are held constant, for a much longer cycle than shown in Figure 5.3. The long cycle switching experiment is designed in two steps, with the first step designed to saturate the catalyst with NH_3 in the rich phase by dosing the catalyst with 1000 ppm NH_3, 0% O_2, 6% H_2O, and 6% CO_2 for 2 minutes. The second step will react NO, NO_2, and O_2 with NH_3 stored on the catalyst during an 8 minute dose of 400 ppm NO_x, 6% O_2, 6% H_2O, and 6% CO_2. This process was repeated for 10 cycles at seven temperatures (175°C, 225°C, 275°C, 325°C, 375°C, 425°C, 475°C) and three NO to NO_x ratios (0.0, 0.5, 1.0). An example of the long switching experiment at constant temperature of 275°C with the NO to NO_x ratio equal to 1.0 is shown in Figure 5.4

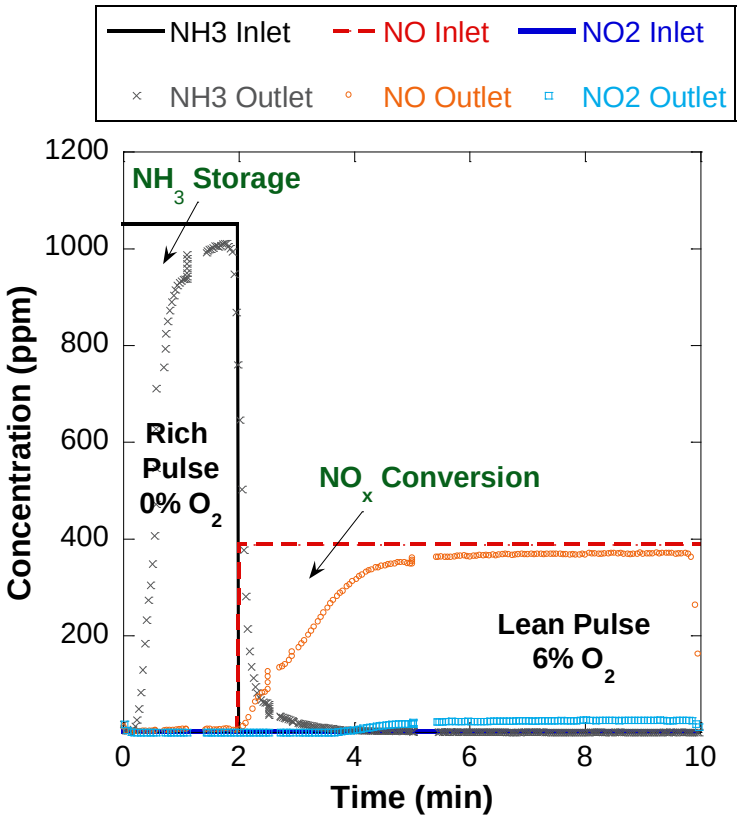

Figure 5.4 – Example of a long switching experiment where the catalyst will saturate with NH_3 during a 2 minute rich pulse, then measure the conversion of NO_x from the feed gas during the 8 minute lean pulse.

5.3 Analysis and Results of Long Cycling Experiments

From the long switching experiments the NO_x conversion as a function of the surface coverage fraction of NH_3 can be determined. The surface coverage fraction of NH_3 $\left(\theta_{Z(NH_3)}\right)$ is defined as the fraction of the amount of stored NH_3 on the catalyst surface over the total amount of NH_3 that can be stored on the catalyst surface. The total amount of stored NH_3 that can be stored on the catalyst was determined from the TPD experiments with NH_3 shown in Chapter 3. The surface coverage fraction of NH_3 from the long switching experiments can be calculated based on experimental measurements as shown in equation (5.3). Where the amount of NH_3 on the catalyst $\left(y_{NH_3,cat}\right)$ in equation (5.3), is based on the stoichiometric NH_3 values of the NH_3 Storage reaction (R1), the

Standard SCR reaction (R5) the Fast SCR reaction (R6), the Slow SCR reaction (R7), and the N_2O Production reaction as seen in (5.4). It should be noted that since the reactor bench using N_2 as the carrier gas, NH_3 loss to oxidation cannot be measured. However, NH_3 oxidation effects can be ignored in the calculation of the surface coverage fraction of NH_3 because it is much smaller then NO_x conversion effects with NH_3 in the investigated temperature range.

$$\theta_{(NH_3)} = \frac{1}{Q_{NH_3,stored,\max} \cdot V_{Cat}} \int_{Cycle} \left(\left(y_{NH_3,cat} \right) \left(\frac{P\dot{V}}{\bar{R}T} \right) \right) dt \tag{5.3}$$

$$y_{NH_3,cat} = \underbrace{\left(y_{NH_3,in} - y_{NH_3,out} \right)}_{NH_3 \text{ Storage}} + \underbrace{\left(y_{NO,in} - y_{NO,out} \right) + \left(y_{NO_2,in} - y_{NO_2,out} \right)}_{\text{Standard and Fast SCR}} + \underbrace{2\left(y_{N_2O,out} \right)}_{N_2O \text{ Production}}$$

$$\max \left\{ \underbrace{\frac{1}{3} \left(\left(y_{NO_2,in} - y_{NO_2,out} \right) - \overbrace{\left(y_{NO,in} - y_{NO,out} \right)}^{\text{Fast SCR Correction}} - \overbrace{2\left(y_{N_2O,out} \right)}^{N_2O \text{ Production Correction}} \right)}_{\text{Slow SCR}}, 0 \right\} \tag{5.4}$$

$$\eta_{NO_x} = \left(\frac{\left(y_{NO,in} - y_{NO_2,in} \right) + \left(y_{NO,out} + y_{NO_2,out} \right)}{\left(y_{NO,in} - y_{NO_2,in} \right)} \right) \cdot 100 \tag{5.5}$$

For each experiment the surface coverage fraction of NH_3 (equation (5.3)) was plotted against the instantaneous NO_x conversion (equation (5.5)) for ten consecutive cycles. Since the comparison of surface coverage fraction of NH_3 and instantaneous NO_x conversion are non-dimensionalized terms, all ten cycles at each NO to NO_x ratio for each temperature were overlapped as seen in Figure 5.5. When examining the trendlines it was observed that all data had collapsed creating a single trend line for each temperature and at a given NO to NO_x ratio.

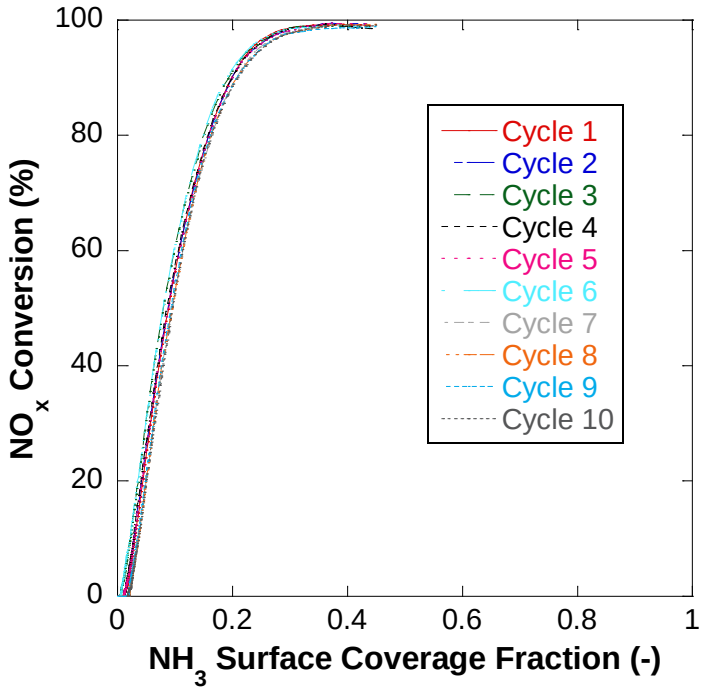

Figure 5.5 – By non-dimensionalizing NO_x conversion vs. the surface coverage fraction of NH_3, all 10 cycles can be collapsed to form one trendline to characterize the effect of stored NH_3 on NO_x conversion. Each cycle was performed with a rich pulse of 2 minutes with 1000 ppm NH_3, 6% H_2O, and 6% CO_2, and a lean pulse of 8 minutes with 400 ppm NO_2, 6% O_2, 6% H_2O, and 6% CO_2 in the feed gas at a constant temperature of 325°C.

The results are shown in Figure 5.6, where it can be seen that instantaneous NO_x conversion is highly dependent on the surface coverage fraction of NH_3. In Figure 5.6 it can be seen that at 275°C and below for the NO to NO_x ratio equal to zero (Figure 5.6 (a)), NO_x conversion is linearly dependant on the surface coverage fraction of NH_3. This linear dependence of NO_x conversion on the surface coverage fraction of NH_3 for the all NO_2 NO_x composition is due to existence of two simultaneous reactions competing for the reduction of NO_2 with NH_3 as shown in (R7) and (R8) from Table 5.1. In all other cases NO_x conversion below the threshold surface coverage fraction for each temperature is negligible. This behavior implies that there are multiple surface sites that can store NH_3, but not all of the sites will contribute to the reduction of NO_x with NH_3. This is different than results shown in Chapter 3, where NH_3 storage is modeled on a single

catalytic sited due to the presence of a single desorption peak the NH_3 in the TPD experiments.

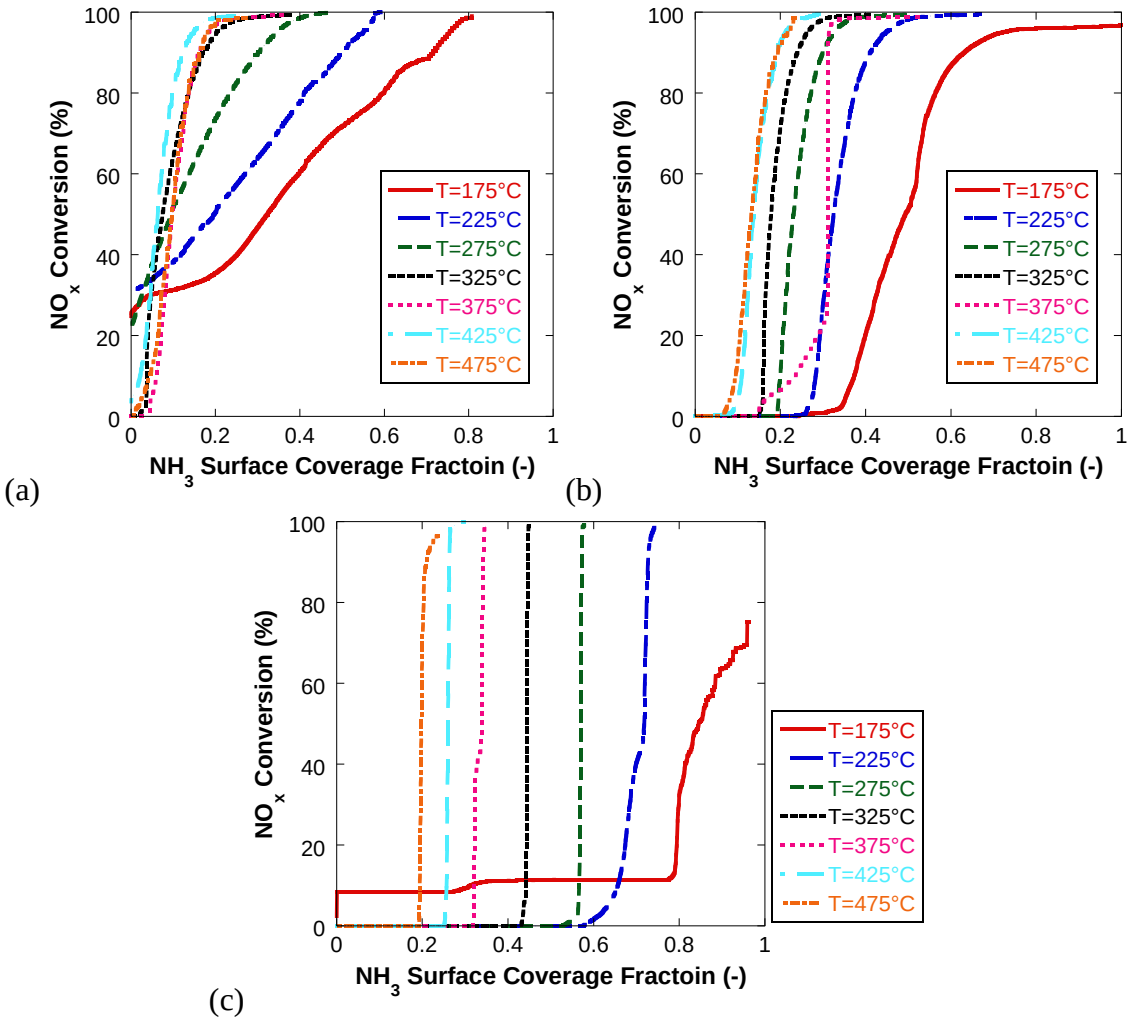

Figure 5.6 – NO_x conversion is highly dependent on the surface coverage fraction of NH_3. Experiments performed with lean pulse (a) $NO:NO_x = 0.0$, (b) $NO:NO_x = 0.5$, (c) $NO:NO_x = 1.0$.

Due to presence of multiple catalytic sites different approaches can be taken to accurately model this process. Sjövall et al. [46] has suggested creating a more detailed kinetic model based on three active sites. Due to the inability to measure catalytic activity as the catalyst is assembled, this process can triple the amount of reactions to modeled and the amount of rate constants to determine.

By examining the results of Figure 5.6 it can be determined that NO_x conversion is proportional to the surface coverage fraction of NH_3 as shown in equation (5.6).

$$\eta_{NO_x} \propto f\left(\theta_{Z(NH_3)}\right) \tag{5.6}$$

A modeling study was performed consistent with one cycle of the long switching experiments shown in Figure 5.4. From this study the NO_x conversion versus the surface coverage fraction of NH_3 is compared for the modeling results and the experimental results as shown in Figure 5.7. It can be seen that the current kinetic model will predict NO_x conversion approximately linearly dependent on the surface coverage fraction of NH_3 while experimental data has mostly proven to show NO_x conversion dependence on the surface coverage fraction of NH_3 is highly non-linear except in the few instances already stated.

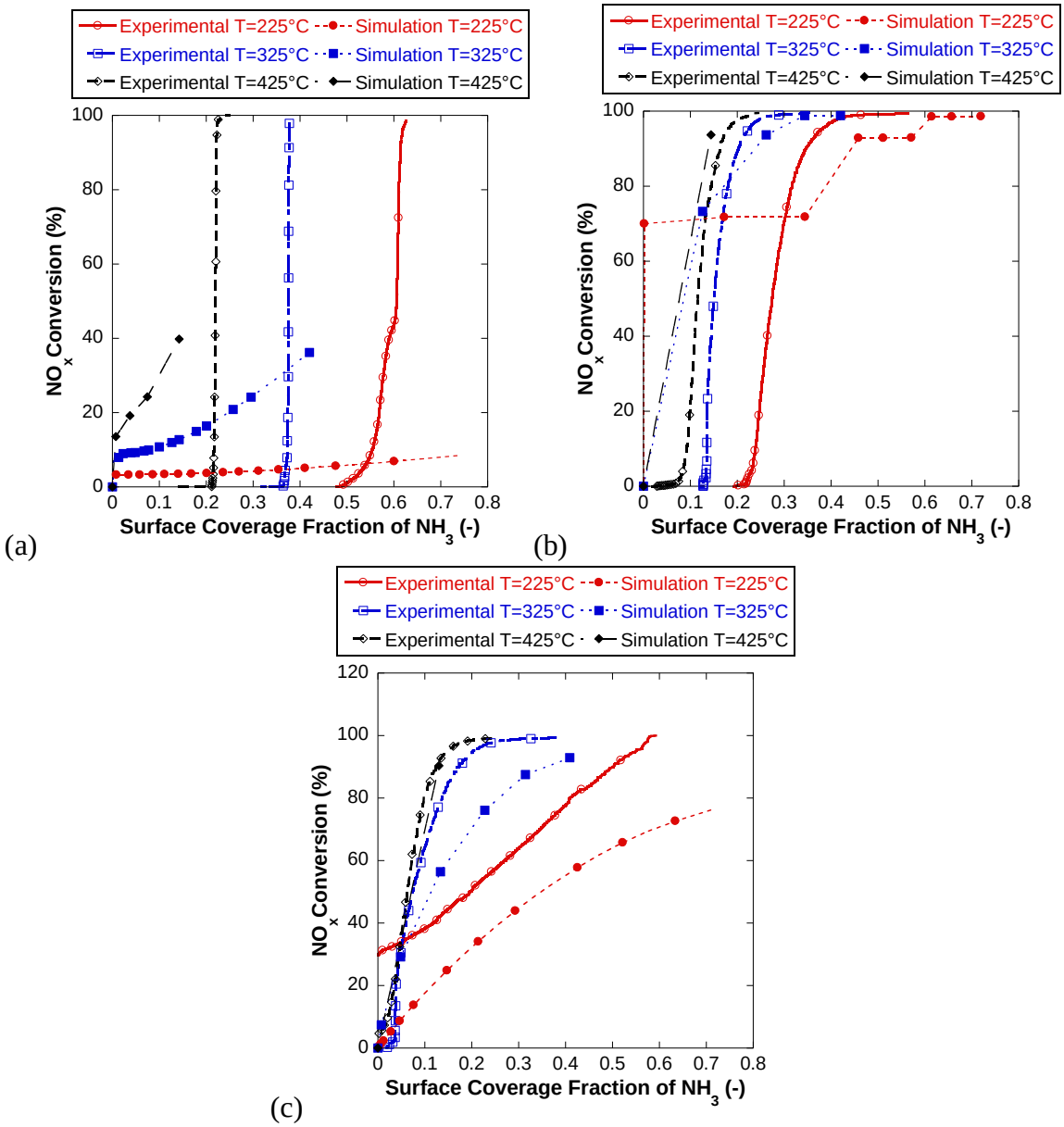

Figure 5.7 – NO_x conversion is based on a linear prediction in the current kinetic mechanism. Modeling predictions are based on a NO:NO_x of (a) 1.0, (b) 0.5, (c) 0.0

5.4 Proposed modifications to the kinetic rate form

Using these findings in Figure 5.6 and Figure 5.7, it can be assumed that the kinetic mechanism shown in Table 5.1 can be improved by changing the dependence of the surface coverage fraction of NH_3 in the rate forms with NH_3 in the reactants. Lietti et al. [95] initially observed NO_x conversion is strongly dependent on the surface coverage

fraction of NH_3 as a reservoir effect where not every site that stores NH_3 is active in NO_x reduction. Lietti has suggested using a kinetic rate form as shown in equation (5.7), where $\theta^*_{Z(NH_3)}$ is the critical NH_3 surface concentration value of storage sites that effect NO_x conversion.

$$R = k \exp^{\left(\frac{-E}{\bar{R} \cdot T}\right)} \left(\prod_{i=\text{reactants}} y_i \right) \theta^*_{Z(NH_3)} \left(1 - \exp^{\left(-\frac{\theta_{Z(NH_3)}}{\theta^*_{Z(NH_3)}} \right)} \right) \tag{5.7}$$

From the experimental data generated in Figure 5.6 it is observed that all sites that store NH_3 are not active in the NO_x removal process. When evaluating the proposed kinetic rate by Lietti in equation (5.7) it can be observed that the critical NH_3 surface concentration can dominate the kinetic rate at extremely low values. Therefore a new approximation can be made which combines work on adsorption isotherms by Kisliuk [151] and work done by Lietti to normalize the reservoir effect to account for the probability of NH_3 being absorbed on an active catalytic site as shown in equation (5.8).

$$R = k \exp^{\left(\frac{-E}{\bar{R} \cdot T}\right)} \left(\prod_{i=\text{reactants}} y_i \right) \left(\frac{1 - \exp^{\left(-\frac{\theta_{Z(NH_3)}}{\theta^*_{Z(NH_3)}} \right)}}{1 - \exp^{\left(-\frac{\theta_{Z(NH_3)=1.0}}{\theta^*_{Z(NH_3)}} \right)}} \right) \tag{5.8}$$

By making the assumption that the kinetic rate is approximately constant except for the surface coverage fraction of NH_3 shown in equation (5.2); the potential NO_x conversion for a constant temperature can be plotted against the surface coverage dependence of NH_3 for the original kinetic rate form (equation (5.1)). This approximation is compared to the approximation by Lietti et al. (equation (5.7)), and the suggested normalized rate form (equation (5.8)). The comparison for the three suggested kinetic rates is shown in Figure 5.8, where the critical NH_3 concentration value is varied to show potential changes to the rate kinetic rate form. It can be seen that the potential

for improvement of the kinetic mechanism can be seen in Figure 5.8 by using the proposed kinetic rate form in equation (5.8) and determining the critical NH_3 concentration through the optimization process.

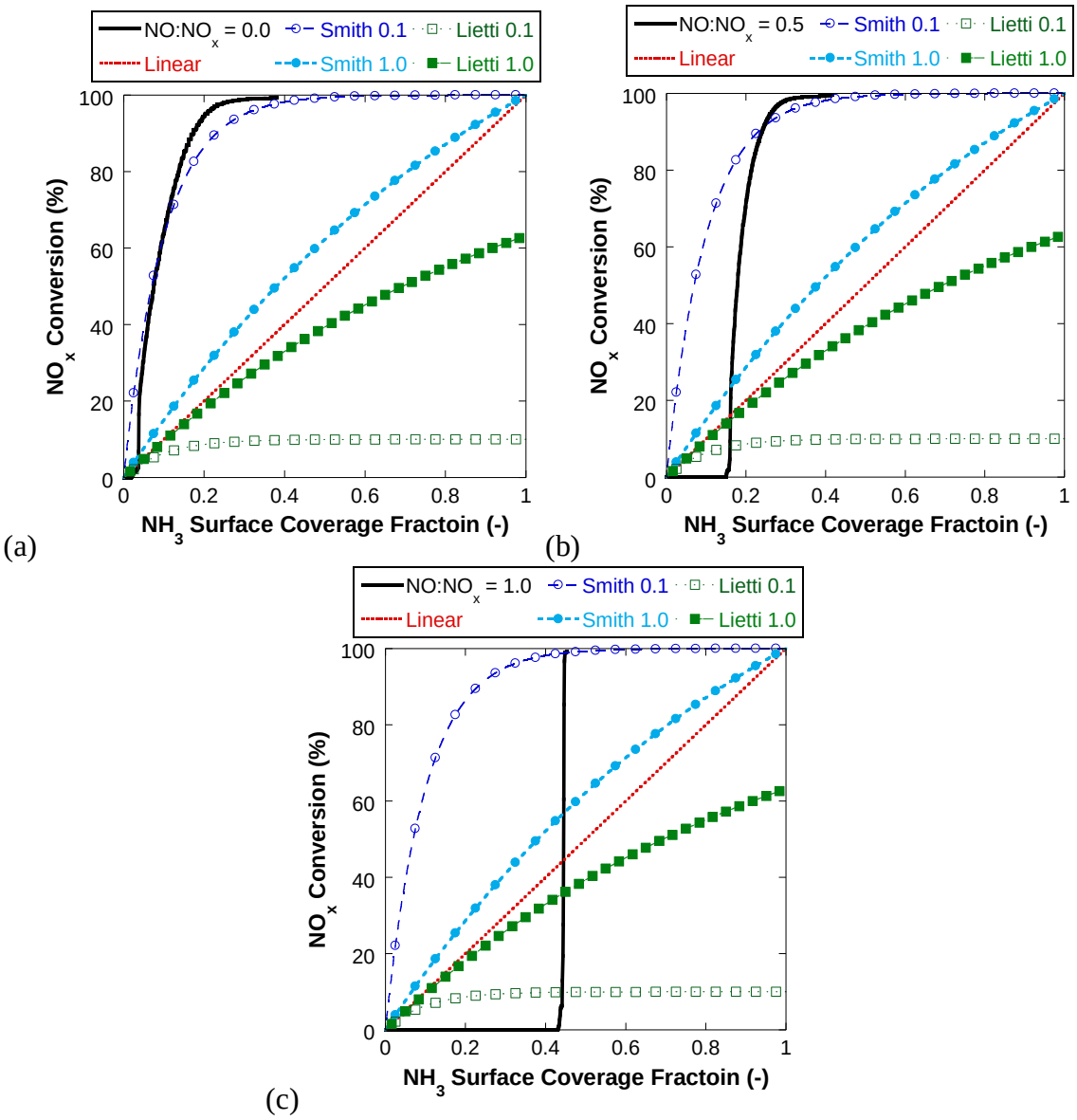

Figure 5.8 − Determination of the dependence on the surface coverage fraction of NH_3 can be determined based on experimental data for (a)$NO:NO_x$ = 0.0, (a)$NO:NO_x$ = 0.5, (c)$NO:NO_x$ = 1.0

5.5 Conclusions

By lengthening the ideal rich lean cycling conditions an experiment was designed to saturate the catalyst with NH_3 and measure the NO_x conversion as all NH_3 is removed from the catalyst. From the long cycling experiments shown in Figure 5.4 the amount of NH_3 stored on the catalyst can be determined as a non-dimensional term called the NH_3 surface coverage. NO_x conversion for each cycle can be plotted against the NH_3 surface coverage fraction, which can then be collapsed to find the trendline signifying the dependence on stored NH_3 for a constant temperature of a given NO to NO_x ratio. The trendlines created were then used to formulate a new approximation to be implemented in the kinetic rates of the NH_3 oxidation reaction (R3) , the Standard SCR reaction (R5), the Fast SCR reaction (R6), the Slow SCR reaction (R7), and the N_2O Production reaction (R8) in the SCR kinetic mechanism shown in Table 5.2. It is suggested not to change the kinetic rate of the Rich Standard SCR reaction (R4) due to the low activity of the reaction. It also suggested to not change the kinetic rate for the N_2O Reduction with NH_3 reaction (R9) however, the kinetic rate can be changed once initial modeling results are analyzed.

Table 5.2 − Summary of chemical reaction and kinetic rates for lean SCR model with new dependence of the surface coverage fraction of NH_3.

	Chemical Reaction	**Kinetics Rate Form**
(R1)	$NO+\frac{1}{2}O_2 \leftrightarrow NO_2$	$R_1 = k_1 \exp^{\left(\frac{-E_1}{\bar{R}T}\right)}\left(y_{NO}\sqrt{y_{O_2}} - \frac{y_{NO_2}}{K_{eq}}\right)$
(R2)	$Z + NH_3 \leftrightarrow Z(NH_3)$	$R_2 = k_{2f} y_{NH_3}\theta_Z - k_{2r} \exp^{\left(\frac{-E_{2r}}{\bar{R}T} - \lambda_{2r}\theta_{Z(NH_3)}\right)}\theta_{Z(NH_3)}$
(R3)	$4Z(NH_3)+3O_2 \rightarrow 4Z+2N_2+6H_2O$	$R_3 = k_3 \exp^{\left(\frac{-E_3}{\bar{R}T}\right)}\left(y_{O_2}\right)^{\gamma_3}\left(\frac{1-\exp^{\left(-\frac{\theta_{Z(NH_3)}}{\theta^*_{Z(NH_3),3}}\right)}}{1-\exp^{\left(-\frac{\theta_{Z(NH_3)=1.0}}{\theta^*_{Z(NH_3),3}}\right)}}\right)$
(R4)	$4Z(NH_3)+6NO \rightarrow 4Z+5N_2+6H_2O$	$R_4 = k_4 \exp^{\left(\frac{-E_4}{\bar{R}T}\right)} y_{NO}\theta_{Z(NH_3)}$
(R5)	$4Z(NH_3)+4NO+O_2 \rightarrow 4Z+4N_2+6H_2O$	$R_5 = k_5 \exp^{\left(\frac{-E_5}{\bar{R}T}\right)} y_{NO}y_{O_2}\left(\frac{1-\exp^{\left(-\frac{\theta_{Z(NH_3)}}{\theta^*_{Z(NH_3),5}}\right)}}{1-\exp^{\left(-\frac{\theta_{Z(NH_3)=1.0}}{\theta^*_{Z(NH_3),5}}\right)}}\right)$
(R6)	$2Z(NH_3)+NO+NO_2 \rightarrow 2Z+2N_2+3H_2O$	$R_6 = k_6 \exp^{\left(\frac{-E_6}{\bar{R}T}\right)} y_{NO}y_{NO_2}\left(\frac{1-\exp^{\left(-\frac{\theta_{Z(NH_3)}}{\theta^*_{Z(NH_3),6}}\right)}}{1-\exp^{\left(-\frac{\theta_{Z(NH_3)=1.0}}{\theta^*_{Z(NH_3),6}}\right)}}\right)$
(R7)	$8Z(NH_3)+6NO_2 \rightarrow 8Z+7N_2+12H_2O$	$R_7 = k_7 \exp^{\left(\frac{-E_7}{\bar{R}T}\right)} y_{NO_2}\left(\frac{1-\exp^{\left(-\frac{\theta_{Z(NH_3)}}{\theta^*_{Z(NH_3),7}}\right)}}{1-\exp^{\left(-\frac{\theta_{Z(NH_3)=1.0}}{\theta^*_{Z(NH_3),7}}\right)}}\right)$
(R8)	$2Z(NH_3)+2NO_2 \rightarrow 2Z+N_2+N_2O+3H_2O$	$R_8 = k_8 \exp^{\left(\frac{-E_8}{\bar{R}T}\right)} y_{NO_2}\left(\frac{1-\exp^{\left(-\frac{\theta_{Z(NH_3)}}{\theta^*_{Z(NH_3),8}}\right)}}{1-\exp^{\left(-\frac{\theta_{Z(NH_3)=1.0}}{\theta^*_{Z(NH_3),8}}\right)}}\right)$
(R9)	$2Z(NH_3)+3N_2O \rightarrow 2Z+4N_2+3H_2O$	$R_9 = k_9 \exp^{\left(\frac{-E_9}{\bar{R}T}\right)} y_{N_2O}\theta_{Z(NH_3)}$

CHAPTER 6

EFFECT OF H_2O AND CO_2 ON SCR REACTIONS

Due to the unique operation of the LNT-SCR aftertreatment system present in the EAS, all of the catalysts will be exposed to rich and lean exhaust conditions where the LNT will generate NH_3 to be used by the SCR when the exhaust becomes rich. By examining the lean ($\varphi < 1$) and rich ($\varphi > 1$) complete combustion equations listed in equations (6.1) and (6.2) respectively, estimates for gas compositions can be determined for engine under different equivalence ratios if the hydrogen to carbon ratio of the fuel is known. For ease of performing estimates of H_2O and CO_2 estimates, H_2 and CO were assumed negligible for the calculations.

$$Fuel + Air \rightarrow CO_2 + \left(\frac{H/C}{2}\right) H_2O + \left(1 + \left(\frac{H/C}{4}\right)\right)\left(\frac{1}{\phi} - 1\right) O_2 + \left(\frac{1 + \left(\frac{H/C}{4}\right)}{\phi}\right)\left(\frac{79}{21}\right) N_2 \quad (6.1)$$

$$Fuel + Air \rightarrow CO_2 + \left(\frac{H/C}{2}\right) H_2O + (\phi - 1) CH_{H/C} + \left(\frac{1 + \left(\frac{H/C}{4}\right)}{\phi}\right)\left(\frac{79}{21}\right) N_2 \quad (6.2)$$

For diesel fuel it can be estimated that the hydrogen to carbon ratio is 1.8 [4]. Results using this hydrogen to carbon ratio and varying the equivalence ratio from 0.5 to 3.0 are shown in Figure 6.1. In Figure 6.1 it can be seen that H_2O and CO_2 levels will change from approximately 6% when lean to approximately 15% when rich. Due to the EAS working between normal engine operation of an equivalence ratio of approximately 0.6 and an equivalence ratio of 1.1 when performing a rich regeneration [19, 20], H_2O and CO_2 levels should be varied between 6% and 12%. From Chapter 3 the effect of oxygen concentration on the SCR reactions was characterized. It should also be noted that the SCR catalyst (located downstream of the LNT and cDPF) may be exposed to H_2, CO, and hydrocarbons when the exhaust stream becomes rich; however the effect of these gases will be studied in the next chapter.

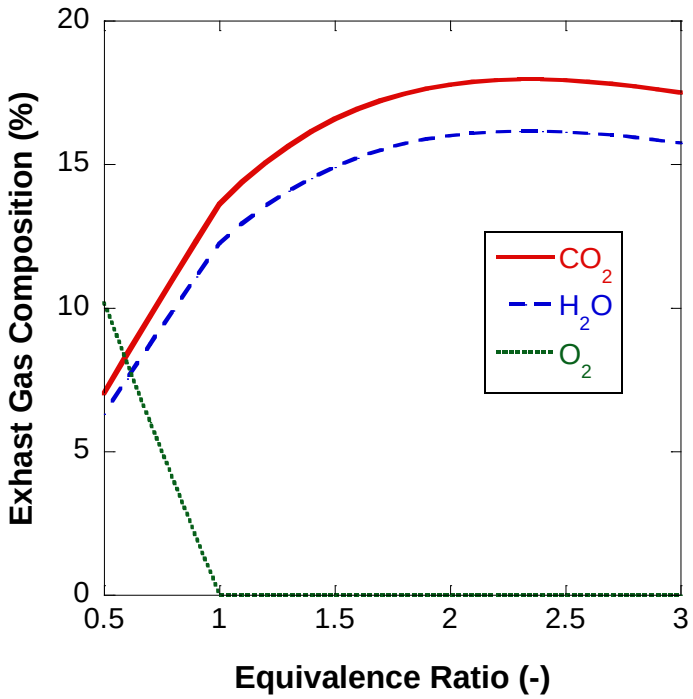

Figure 6.1 − Shows how H_2O and CO_2 concentration increase from 6% to 15% as equivalence ratio increases.

6.1 NO Oxidation

Due to common kinetic rate forms for the oxidation of NO to NO_2 containing a water inhibition term, experiments with varying H_2O and CO_2 values were already studied. In Chapter 3 it was found that water strongly inhibits catalyst activity when comparing experiments with 0% H_2O / CO_2 and a 6% H_2O /CO_2. However, increasing to 10% H_2O / CO_2 did not further affect conversion in the forward or reverse reaction for the oxidation of NO to NO_2. Due to these results the inhibition terms were dropped from the proposed kinetic rate forms because there is no change in conversion in the expected H_2O concentration range of 6 – 10%. The conversion experiments are shown in Figure 6.2.

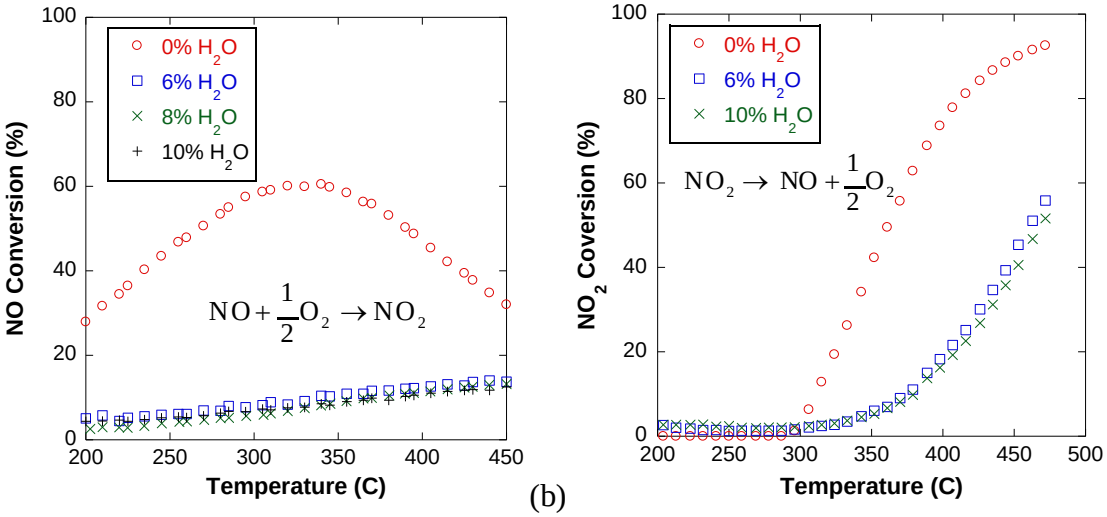

Figure 6.2 – From 0 – 6% water concentration in the feed gas can have large effects on the oxidation of NO to NO_2 and reduction of NO_2 to NO and O_2, while there is little effect on the the forward and reverse reaction when the concentration of H_2O is varied from 6 – 10%, all experiments were performed with 6% O_2, and 1000 ppm NO.

6.2 NH_3 Storage

Due to the drastic change in H_2O and CO_2 concentration it is important to study the effect of each on the NH_3 storage capacity of the catalyst as it is the rate limiting step in NO_x reduction with NH_3. It has been stated that CO_2 has a small effect on storage of

NH_3 [18], but H_2O will have a more significant effect [101]. All TPD experiments to determine NH_3 storage capacity were performed with a gas space velocity of 30,000 hr^{-1}. Error analysis for the TPD experiments is calculated as a RMS combination of the 2% error in NH_3 concentrations from the FTIR and the standard deviation of NH_3 storage capacities from multiple experiments at each temperature and gas compositions. The first series of experiments were performed with only NH_3 in the feed gas, the second series of experiments is performed with NH_3 and CO_2 in the feed gas, and the last series of experiments is performed with NH_3, CO_2, and H_2O in the feed gas with equivalent values of CO_2 and H_2O due to the hydrogen to carbon ratio of diesel fuel being close to a value of 2.0 [4]. For the synthetic gas bench the minimum value of H_2O concentrations is 0 (off) or 4% while the maximum H_2O concentration is 10%.

Figure 6.3 below shows how NH_3 storage capacity is affected by different H_2O and CO_2 concentrations at initial storage temperatures between 175°C–475°C. From this Figure 6.3 it can be determined that CO_2 has little effect on the NH_3 storage capacity of this catalyst except at high temperature when comparing to TPD experiments performed with no H_2O or CO_2 in the feed gas. The experiments performed with no H_2O or CO_2 in the feed gas represent the maximum NH_3 storage capacity for the SCR catalyst. CO_2 high temperature effects on NH_3 storage capacity can be assumed negligible because it has been found that H_2O concentration will have a stronger inhibition effect on NH_3 storage capacity and in combustion exhaust gas H_2O and CO_2 are always present.

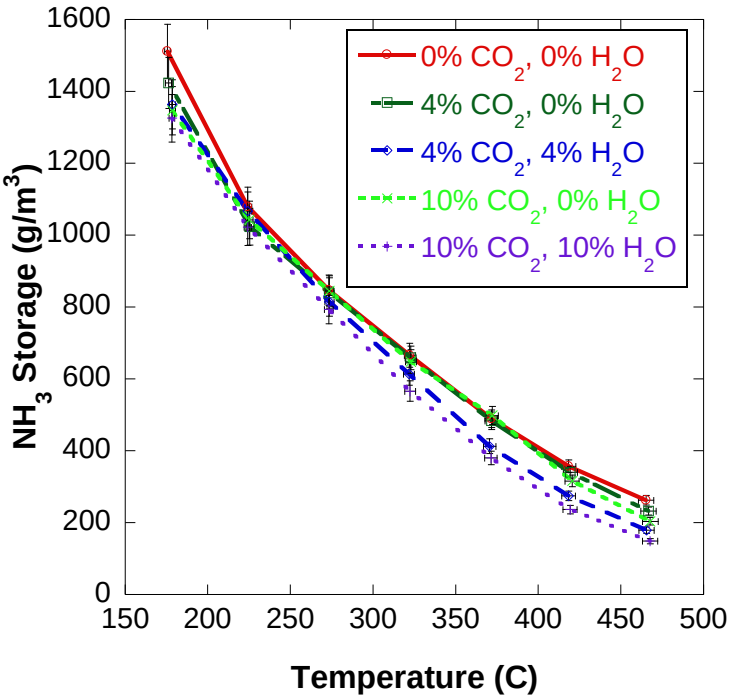

Figure 6.3 − Shows H_2O concentration has a larger effect on NH_3 storage capacity then CO_2 concentration

Figure 6.4 shows the effect of different H_2O and CO_2 gas concentration in the feed gas on NH_3 storage capacity in a series of TPD experiments. The feed gas concentrations of CO_2 and H_2O were held constant for each experiment. A saturation effect is seen as a result from this series of experiments, where NH_3 storage capacity of the catalyst decreases as H_2O concentration increases, however this effect is not linear with H_2O concentration, and shows only small decreases in NH_3 storage capacity as H_2O concentration in the feed gas increases. This is commonly referred to as a saturation effect on a catalyst and commonly occurs when a gas concentration is higher than 2% in the feed gas.

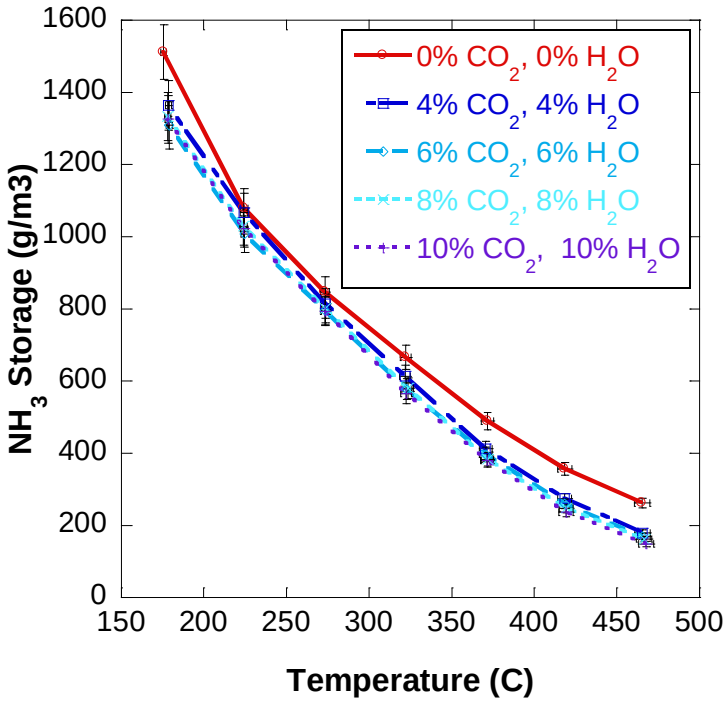

Figure 6.4 − Shows a saturation of the catalyst by H_2O that will not have major effects on NH_3 storage capacity.

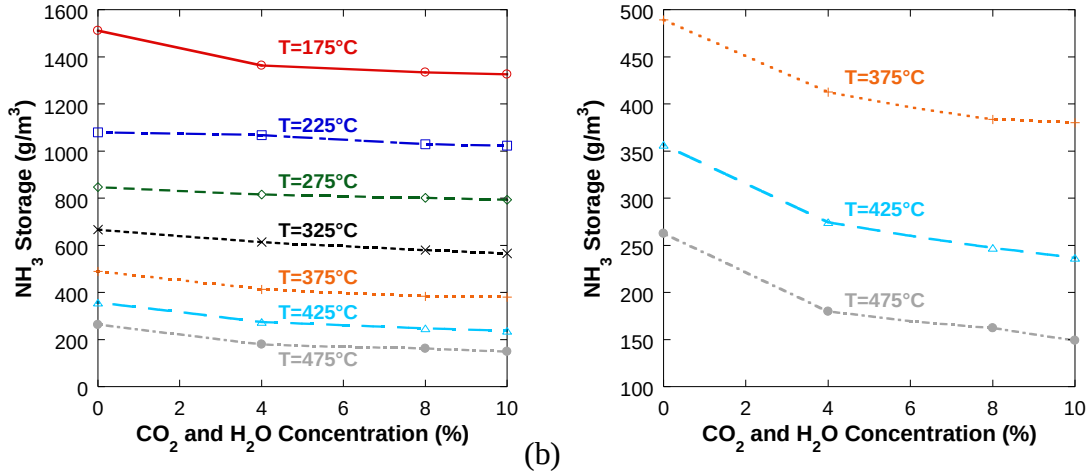

Figure 6.5 – NH_3 storage capacity decreases as temperature increases, and as H_2O concentration increases.

6.2.1 NH_3 Storage Modeling Approach for Varying Water Concentrations

From the results shown in Figure 6.4 it can be seen that NH_3 storage capacity is reduced as the concentration of water increases. It can therefore be proposed that there is

a competition on the active catalytic sites between H_2O and NH_3. It can then be proposed that the NH_3 storage competition with H_2O storage can be defined by the equations in (6.3) and (6.4).

$$Z + NH_3 \underset{\mathbf{R}_{1r}}{\overset{\mathbf{R}_{1f}}{\rightleftharpoons}} Z(NH_3) \tag{6.3}$$

$$Z + H_2O \underset{\mathbf{R}_{2r}}{\overset{\mathbf{R}_{2f}}{\rightleftharpoons}} Z(H_2O) \tag{6.4}$$

To use this method the NH_3 storage reaction (equation (6.3)) will be calibrated to a TPD experiment at an initial storage temperature of 200°C with 0% H_2O and 0% CO_2 in the feed gas. In Chapter 3 it was found that a Tempkin Isotherm kinetic rate yielded higher accuracy then a traditional rate form when mathematically describing the NH_3 storage reaction in equation (6.3). Therefore, the kinetic rate equations shown in (6.5) and (6.6) will be used as the forward and reverse kinetic rates for equation (6.3).

$$\mathbf{R}_{1f} = k_{1f} y_{NH_3} \theta_Z \tag{6.5}$$

$$\mathbf{R}_{1r} = k_{1r} \exp^{\left(-\frac{E_{1r}}{R_u T_m} - \lambda \theta_{Z(NH_3)}\right)} \theta_{Z(NH_3)} \tag{6.6}$$

It was found that when comparing these results to TPD experiments at different initial storage temperatures that the accuracy of the model can increase if an activation energy is added to the forward kinetic rate form as shown in (6.7). While this term is commonly neglected [108], calibration results found that the activation energy to be 5.353 kJ mol^{-1}, which is small, but not negligible.

$$\mathbf{R}_{1f} = k_{1f} \exp^{\left(-\frac{E_{1f}}{R_u T_m}\right)} y_{NH_3} \theta_Z \tag{6.7}$$

The rate forms for the forward and reverse reactions (equations (6.7) and (6.6)) were fit simultaneously for a TPD experiment performed with an inlet feed gas of NH_3 in N_2 without any H_2O or CO_2 present at a catalyst temperature of 200°C (shown in Figure

6.6). The coefficients for equations (6.6)and (6.7) are given in Table 6.1. It should be noted that this is the same approach as used in Chapter 3 to calibrate the NH_3 Storage reaction; however calibration was done to match a TPD experiment with 8% H_2O and 8% CO_2.

Table 6.1 − Parameters developed to model the reaction described by equation (6.3)

Parameter	**Value**	**Units**
Site Density	1.67×10^{-2}	[kmol m^{-2}]
E_{1f}	5.353	[kJ mol^{-1}]
k_{1f}	2.61×10^{0}	[kmol m^{-2} s^{-1} $mole_{NH3}^{-1}$]
E_{1r}	96.340	[kJ mol^{-1}]
k_{1r}	2.99×10^{3}	[kmol m^{-2} s^{-1}]
λ_1	0.256	[-]

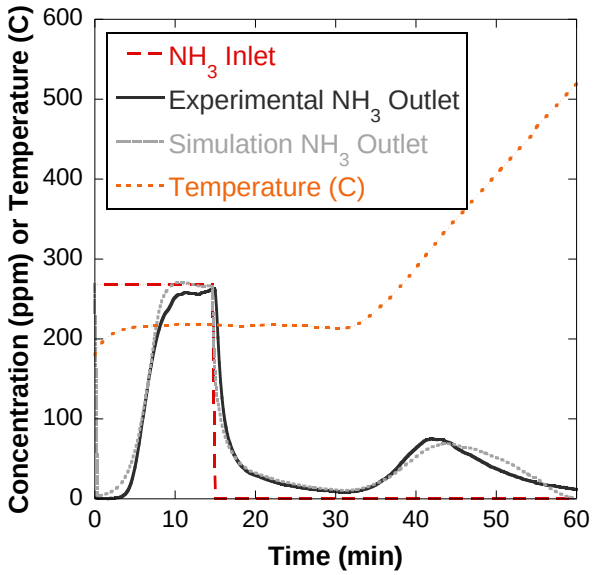

Figure 6.6 − Comparison of experimental and simulation data for a TPD experiment with 0% H_2O and 0% CO_2 in the feed gas.

After the modeling parameters were determined, results from all four TPD experiments with 0% H_2O/CO_2 were compiled with an average error in NH_3 concentration range from 5.52 – 7.36 ppm. Figure 6.7 illustrates that there is good agreement between the model and experimental values. However, the model diverges at the high and low temperatures. This occurs because there is more than one site that can absorb NH_3, as previously found by [91, 104, 109]. As stated before, our global mechanism uses only one active site for the strongly chemisorbed ammonia, and assumes that weakly bonded ammonia is stored on secondary sites that are not modeled. This effect is also prevalent in the NH_3 adsorption behavior during the shoulder at the end of the first stage of the TPD experiment where the NH_3 approaches the inlet concentration values.

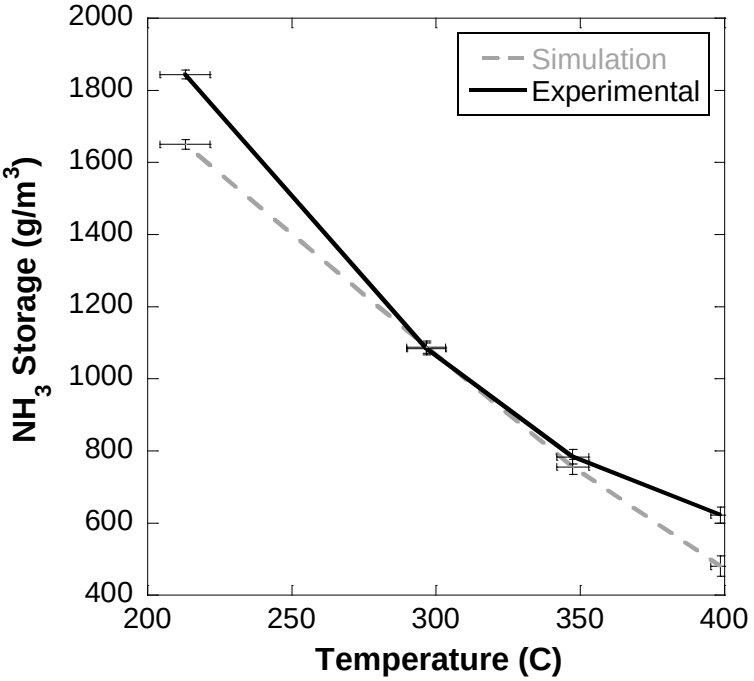

Figure 6.7 − Model shows acceptable agreement with experimental data for total NH_3 storage capacity under varying storage temperatures for experiments with 0% H_2O and 0% CO_2.

Once the NH_3 storage reaction has been calibrated and verified for the TPD experiments with 0% H_2O and 0% CO_2, the H_2O competition reaction shown in equation

(6.4) can be calibrated from TPD experiments at different initial storage temperatures and H_2O and CO_2 levels. The test matrix (Table 6.2) includes four initial storage temperatures (200°C, 300°C, 350°C, and 400°C), and two different H_2O/CO_2 levels (6% and 8%). The experimental data for this test matrix is shown in Figure 6.8

Table 6.2 – Test matrix for a total of 8 experiments to calibrate the H_2O competition on catalyst surface

Initial Storage Temperature	**H_2O / CO_2 Levels**
200°C	6% H_2O / 6% CO_2
300°C	10% H_2O / 10% CO_2
350°C	
400°C	

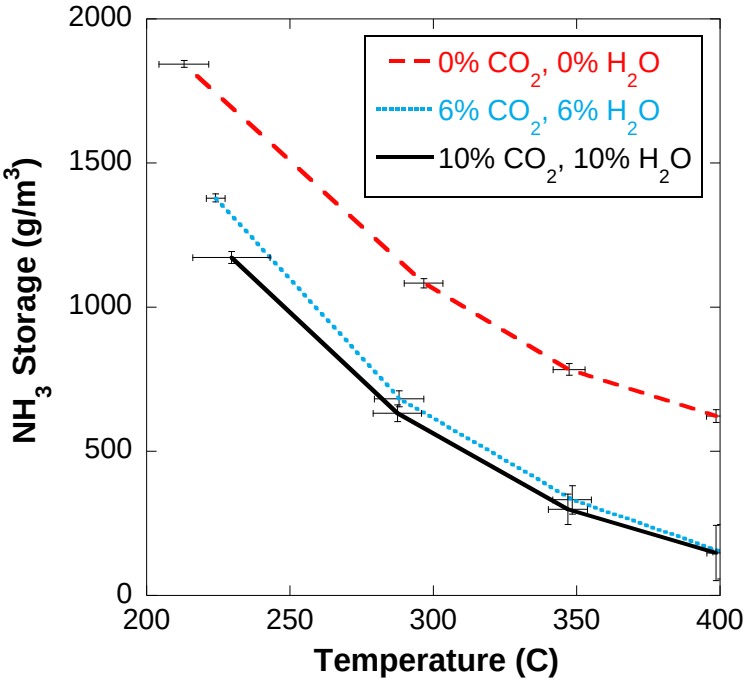

Figure 6.8 − Storage capacity of NH_3 is decreased when CO_2 and H_2O levels are increased at each initial storage temperature.

It is proposed to use standard Arrhenius kinetic rates for the H_2O competition for catalytic sites reaction shown in equation (6.4). Therefore, the corresponding forward and reverse rate forms listed in Equations (6.8) and (6.9) respectively.

$$\mathrm{Z} + \mathrm{H_2O} \underset{\mathbf{R}_{2r}}{\overset{\mathbf{R}_{2f}}{\rightleftharpoons}} \mathrm{Z(H_2O)} \tag{6.4}$$

$$\mathbf{R}_{2f} = k_{2f} \exp\left(-\tfrac{E_{2f}}{R_u T_m}\right) y_{H_2O} \theta_Z \tag{6.8}$$

$$\mathbf{R}_{2r} = k_{2r} \exp\left(-\tfrac{E_{2r}}{R_u T_m}\right) \theta_{Z(H_2O)} \tag{6.9}$$

Table 6.3 provides the parameters for the reaction rate expressions in Equations (6.8) and (6.9). When fitting the H_2O storage reaction (Equation (6.4)), all cases of varying storage temperature and varying H_2O/CO_2 concentration were included to account for how H_2O concentration and temperature influence the amount of stored NH_3 on the catalyst. Once the rate parameters were determined additional simulations were done starting with a H_2O saturated catalyst to tests its effect on NH_3 storage. The results showed negligible differences therefore it can be concluded that H_2O will fill an empty site temporarily, and then release, creating a free site that can store either NH_3 or H_2O depending on feed gas composition.

Table 6.3 − Parameters developed to model the reaction expression derived from equation (6.4).

Parameter	**Value**	**Units**
E_{2f}	47.260	[kJ mol^{-1}]
k_{2f}	2.98×10^{1}	[kmol m^{-2} s^{-1} $mole_{H2O}^{-1}$]
E_{2r}	20.120	[kJ mol^{-1}]
k_{2r}	2.03×10^{-3}	[kmol m^{-2} s^{-1}]

Once calibrated the NH_3 H_2O Competition kinetics (as shown in equations (6.3) and (6.4)) are compared to the original results for the Tempkin Isotherm NH_3 storage kinetics previously calibrated in Chapter 3. Figure 6.9 shows a TPD experiment performed with 250 ppm NH_3 and 6% H_2O/CO_2 in the inlet feed to the catalyst with an initial storage temperature of 300°C to compare both kinetic approaches. In this figure it can be seen that the accuracy of both kinetic approaches is comparable, however by adding a water competition reaction the simulation follows the experimental data as the catalyst becomes saturated with NH_3.

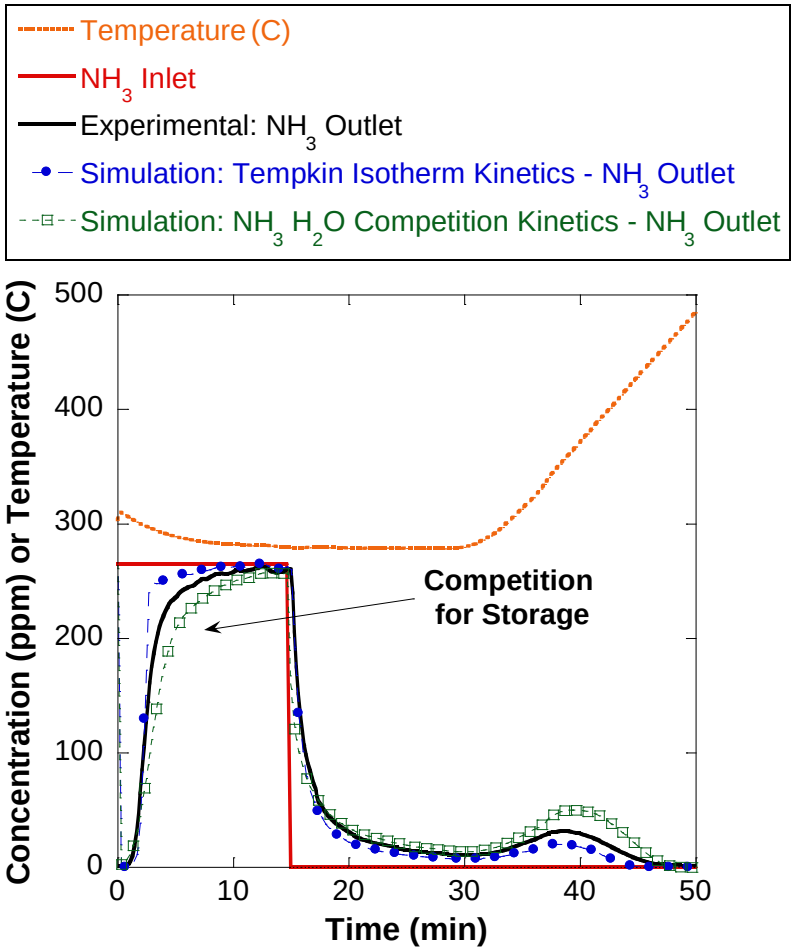

Figure 6.9 – Accuracy is comparable for the two kinetic approaches however the NH_3 H_2O Competition approach follows catalyst saturation data with more accuracy. The experiment was performed with 6% H_2O, 6% CO_2, and 250 ppm NH_3 in the feed gas with an initial storage temperature of 300°C.

Figure 6.10 illustrates how each kinetic approach predicts the NH_3 storage capacity of the catalyst. It can be seen that original Tempkin Isotherm approach will only change the NH_3 storage capacity as the initial storage temperature change, while H_2O levels changes have no effect. The NH_3 H_2O Competition kinetics however allows corrections for temperature and H_2O concentration. It should be noted that when modeling SCR catalysts to be used in only steady-state conditions, H_2O storage effects will remain relatively low. Therefore, modeling complete storage effects with the water reaction is not necessary and the simulation only requires the NH_3 reaction (equation (6.3)) as long as calibration is performed with a representative H_2O/CO_2 level. However, in the case of the LNT-SCR aftertreatment system, the lean/rich switching will cause significant shifts in water concentration. Thus, incorporating H_2O storage in the model is important to account for the amount of stored NH_3 to predict the total NO_x conversion of the LNT-SCR system.

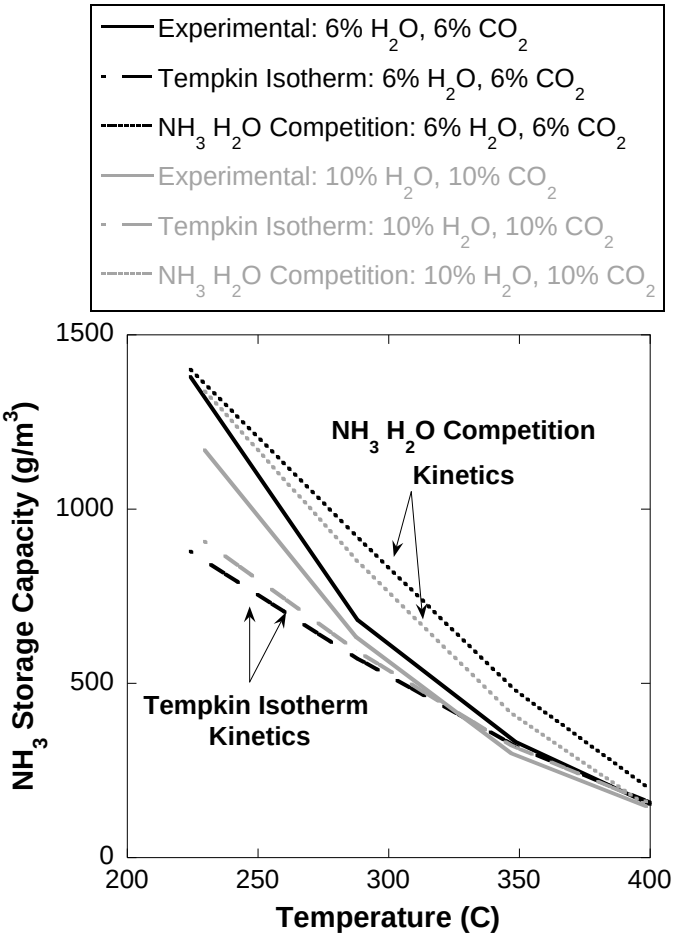

Figure 6.10 – The original Tempkin Isotherm kinetic approach to NH_3 storage capacity only varies with the initial storage temperature, while the NH_3 H_2O Competition kinetic approach allows for changes in NH_3 storage capacity based on temperature and H_2O concentration.

6.3 NH_3 Oxidation

Temperature ramp experiments were performed at different H_2O and CO_2 concentrations for ammonia oxidation experiments. When comparing two experiments with 6% H_2O/CO_2 and 10% H_2O/CO_2 as shown in Figure 6.11, it can be seen that the NH_3 conversion trendlines vs. temperature are similar however these are slight changes in magnitude. From the previous sections it was concluded that H_2O and NH_3 will compete for catalytic sites. Since NH_3 oxidation occurs when NH_3 is on the surface of the catalyst, increases in H_2O concentration will decrease the amount of NH_3 on the catalyst

surface and decrease the conversion with NH_3. It can therefore be concluded that the oxidation of NH_3 is a relatively slow reaction where H_2O competition for catalytic sites affects the NH_3 Conversion. Further corroboration is done by adding the NH_3 H_2O competition reaction shown in (6.4) to the modeling prediction from Chapter 3, where it can be seen that a changes in NH_3 conversion predictions can be accounted for by adding the H_2O storage reaction instead of changing the kinetic reaction rate for the NH_3 oxidation reaction.

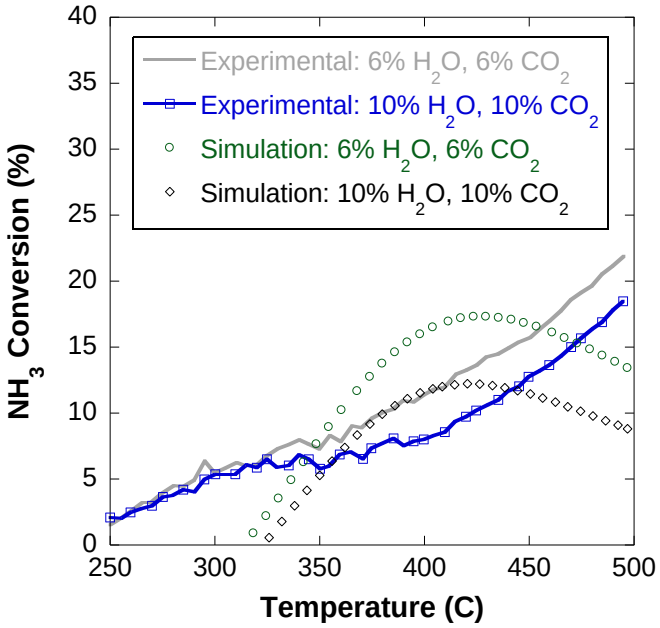

Figure 6.11 − Negligible changes in NH_3 conversion in oxidation experiments when H_2O and CO_2 concentrations are varied from 6% – 10% in the feed gas with 1000 ppm NH_3, and 6% O_2.

6.4 NO_x Reduction with NH_3

Figure 6.12 shows the results of experiments performed while testing varying H_2O and CO_2 levels to in the feed gas. From these results it can be seen that H_2O and CO_2 levels do not have an effect on NO_x conversion with NH_3 for all NO to NO_x ratios. Therefore it can be concluded that NO and NO_2 will react quickly with stored NH_3, therefore H_2O competition for catalytic sites will not affect NO_x conversion.

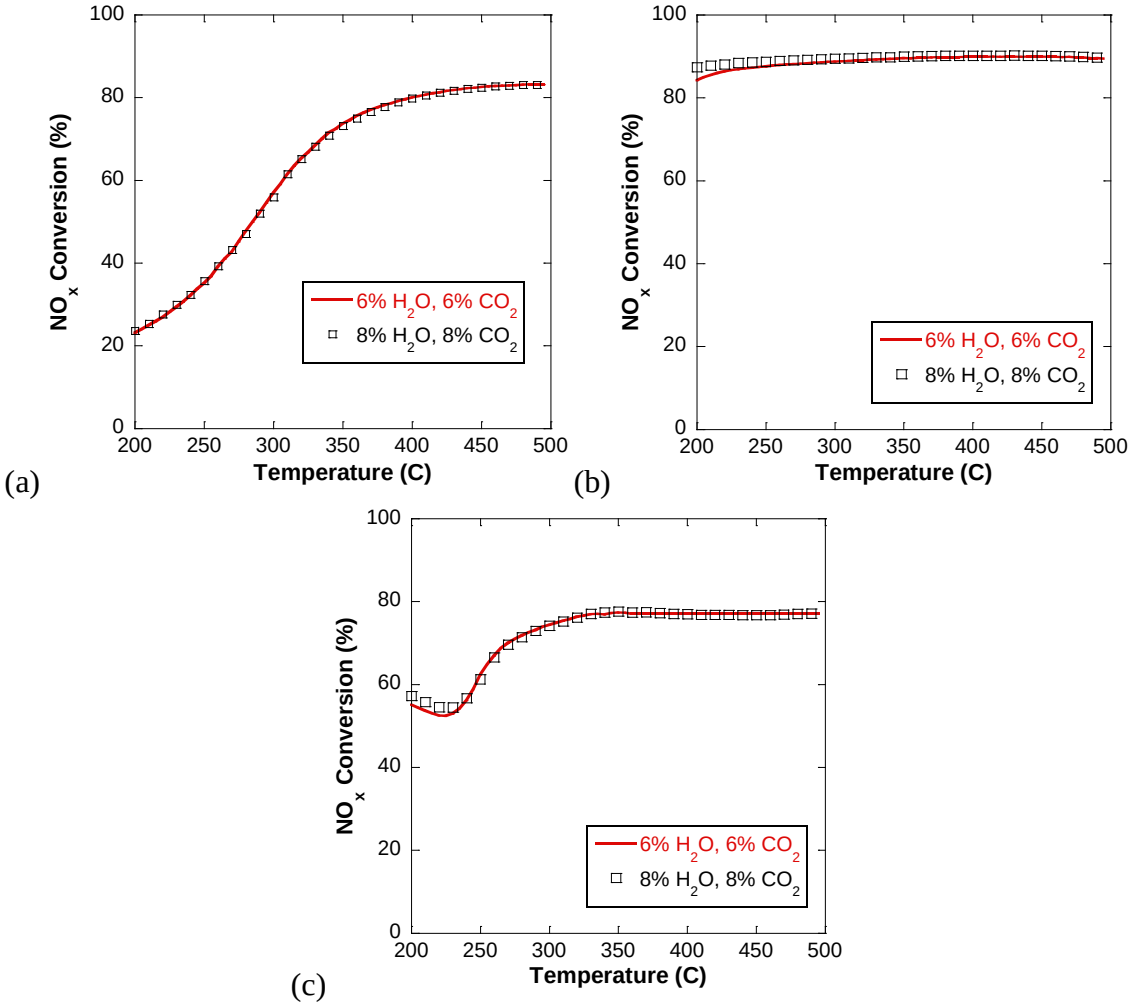

Figure 6.12 − NO_x conversion does not change with as H_2O and CO_2 concentrations increase. Experiments were performed as a temperature ramp with 6% O2, 1000 NH_3, and 1000 NO varying H_2O and CO_2 concentration feed gas (a) NO:NOx = 1.0, (b) NO:NOx = 0.5, (c) NO:NOx = 0.0

6.5 Conclusions

The following conclusion can be made based on experimental and simulations results presented in this chapter.

6.5.1 NO Oxidation Conclusions

It has been determined that the oxidation of NO to NO_2 is affected by H_2O concentration but not in the predicted H_2O concentration range of the EAS. Therefore as shown in Chapter 3, H_2O inhibition term can neglected in the kinetic rate.

6.5.2 NH_3 Storage Conclusions

The experiments described in this study indicate that as exhaust gas becomes rich and H_2O and CO_2 concentrations increase, the storage capacity of NH_3 on an Fe-Zeolite catalyst decreases. This is important for LNT-SCR combination systems where the exhaust stream concentrations can vary from 6% H_2O/CO_2 to 12% H_2O/CO_2. The decrease in storage capacity of NH_3 is larger between 0 – 6% H_2O/CO_2 than between 6 – 10% H_2O/CO_2, which means that if engine conditions were held fairly constant, such as during lean engine operation with only an SCR system, the H_2O competition effect does not need to be included in a global model and only temperature effects need to be considered in the model. In cases where the exhaust stream varies from lean to rich, such as an LNT-SCR system, using an H_2O competition model increases the accuracy of stored NH_3 under the constantly varying exhaust conditions. Since NO_x conversion is a strong function of the surface coverage fraction of NH_3, a method to model the NH_3 H_2O competition for catalytic sites has been proposed to allow NH_3 storage to be affected by temperature and H_2O concentration.

6.5.3 NH_3 Oxidation Conclusions

It has been determined that the oxidation of NH_3 is a relatively slow reaction that occurs on the catalyst. It was observed that varying H_2O concentration will decrease the conversion of NH_3 due to oxidation. It was also shown that this inhibition from H_2O can

be accounted for using the NH_3 H_2O competition approach as shown in the NH_3 Storage section.

6.5.4 NO_x Reduction with NH_3 Conclusions

It was observed that under steady state conditions that NO_x conversion is unaffected by changes in H_2O/CO_2 levels. Therefore there is no inhibition due to H_2O or CO_2 for the NO_x conversion reactions. It can therefore be concluded that each NO_x conversion reaction occurs at a faster rate than the NH_3 oxidation reaction, since increasing H_2O concentration did not decrease the NO_x conversion for each NO to NO_x ratio.

CHAPTER 7

EFFECT OF CO, H_2, AND C_3H_6 ON SCR REACTIONS

SCR catalysts are usually installed on engine systems that operate in only lean exhaust conditions and commonly have a DOC upstream to remove any unburned hydrocarbons, hydrogen, and carbon monoxide from the exhaust stream [3]. Due to the flexibility in the regeneration strategy of the EAS, there is a strong possibility that H_2, CO, and hydrocarbons will become part of the feed gas to the SCR catalyst when optimizing the EAS for maximum NO_x conversion. NO_x conversion with NH_3 is highly sensitive to the NO to NO_x ratio in the feed gas in a SCR. Additionally, Figure 7.1 shows additional reductants of H_2 and CO can slightly increase NO_x conversion while C_3H_6 present will inhibit NO_x conversion. This chapter will study how the additional reductants of H_2, CO, and C_3H_6 will react with NO and NO_2 on the iron based zeolite SCR catalyst in the EAS.

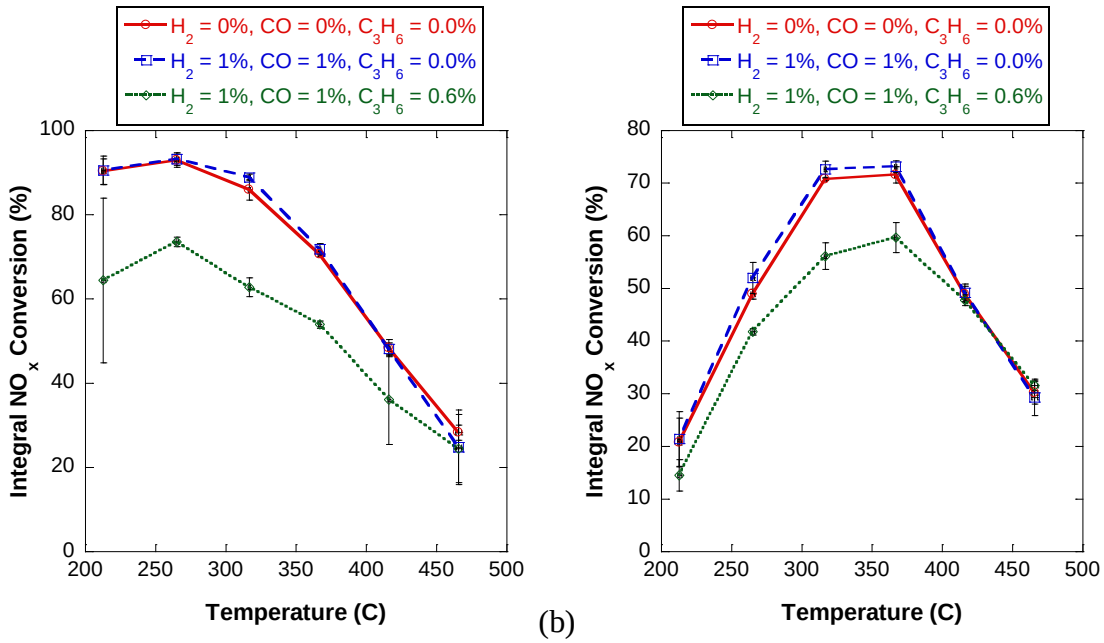

Figure 7.1 − Calculated integral NO_x conversion for (a) $NO:NO_x$=0.5 and (b) $NO:NO_x$=1.0 shows a slight increase in integral NO_x conversion when 1% H_2 and 1% CO are in rich pulse, and a significant hydrocarbon poisoning effect when 1% H_2, 1% CO, and 1% C_3H_6 is in rich pulse. Each experiment is run with a 5 sec rich pulse with 8% H_2O, 8% CO_2, and 1000 ppm NH_3, then a 45 sec lean pulse with 8% H_2O, 8% CO_2, 6% O_2, and 150 ppm NO_x with temperature held constant for 6 cycles.

A literature survey has shown similar inlet concentrations can occur on Three-Way-Catalysts (TWC) and Lean NO_x Traps (LNT). Research has shown that CO and H_2 can be used for conversion of NO and NO_2 to N_2, by using NO and NO_2 to oxidize H_2 to H_2O and CO to CO_2. Due to their strong ability to oxidize H_2, CO, and hydrocarbons to H_2O and CO_2, the conversion of NO_x is commonly seen only with low levels of O_2 present in the exhaust stream [70, 71, 152, 153]. Bohac [154] performed a study of the NO_x regeneration event at the outlet of the reformer catalyst. The results shown in Figure 7.2 indicate that reactions with fuel and the reformer catalyst can yield feed gas concentrations of 4% H_2, 2% CO, and 1% THC at the inlet of the LNT in the EAS. A hydrocarbon speciation analysis of these results yielded a large amount of partially reacted diesel fuel. It has been suggested by Kuo et al. [155] that hydrocarbons in exhaust can approximated as methane (CH_4) and propylene (C_3H_6). Since methane is not very reactive all studies in this chapter will use propylene as a surrogate for hydrocarbons

in all experiments. This is a similar approach taken by Olsson and Anderson [156] on automotive catalysts. It should be noted that the approach listed in the chapter can be used with other hydrocarbons.

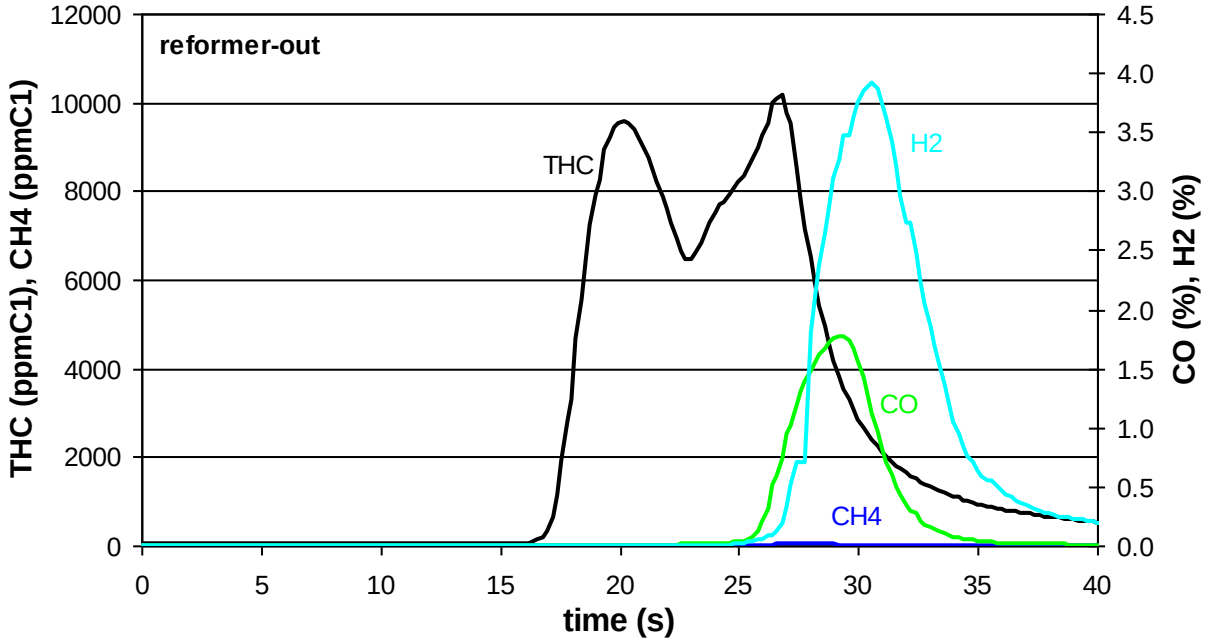

Figure 7.2 – Results from Bohac [154] indicate that large amounts of H_2, CO, and hydrocarbons can be present in the feed gas during a NO_x regeneration event at the inlet of the LNT.

7.1 Water Gas Shift

To study the effect of CO and H_2 on NO chemistry it is important to first look at the potential for a Water Gas Shift (WGS) reaction on the iron based zeolite SCR catalyst. The water gas shift reaction, shown in equation (7.1), is an equilibrium based reversible reaction shows a potential pathway for conversion between CO and H_2O to H_2 and CO_2 [157, 158]. This reaction is the most prominent in the rich phase when oxidation reactions are minimal.

$$CO + H_2O \leftrightarrow CO_2 + H_2 \tag{7.1}$$

Chen et al. found up to 12% conversion from CO and H_2O to H_2 and CO_2 from the WGS shift reaction on an Fe based SCR catalyst [158]. Figure 7.3 shows experiments performed as a temperature ramp with both the forward and reverse constituents in a balance of nitrogen as the only species in the feed gas. From the experimental data shown in Figure 7.3 it can be seen that the WGS reaction on the Fe based zeolite SCR catalyst in the EAS is negligible.

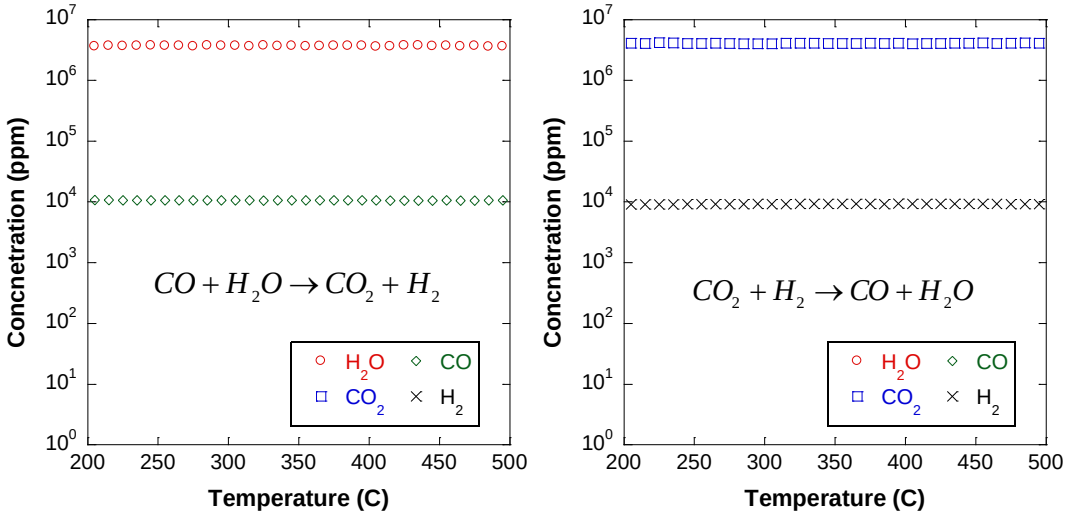

Figure 7.3 – Experimental data shows no water gas shift reaction in either direction across the Fe based SCR catalyst for entire temperature operation range

7.2 H_2, CO, and C_3H_6 Oxidation

After determining there is no effect from WGS it becomes important to understand lean reactions with H_2 and CO on the SCR catalyst. Under lean conditions the oxidation of H_2 and CO is commonly studied in TWC kinetics [152, 153, 157] and DOC kinetics [72].

7.2.1 H_2 Oxidation

Reviewing literature from TWC and DOC kinetics it can be found that the kinetic rates are very high for the oxidation of H_2 to H_2O as seen in the reaction shown in equation (7.2) [71, 72, 157].

$$H_2 + \frac{1}{2}O_2 \rightarrow H_2O \qquad (7.2)$$

From literature results it was found by Oh et al. [159] and Sampara [72] that the oxidation of H_2 to H_2O occurs at temperature below the oxidation of CO which is commonly found to be around 200°C for DOC catalysts. Experimental results for the iron based zeolite SCR catalyst in the EAS testing the oxidation of H_2 to H_2O are shown in Figure 7.4. From these results it can be seen that H_2 oxidation increases as temperature increases, but overall oxidation of H_2 to H_2O is small across the Fe-zeolite SCR catalyst. Therefore it can be concluded that the H_2 oxidation reaction does not need to be included in the kinetic model because the majority of the H_2 is still present in the feed gas.

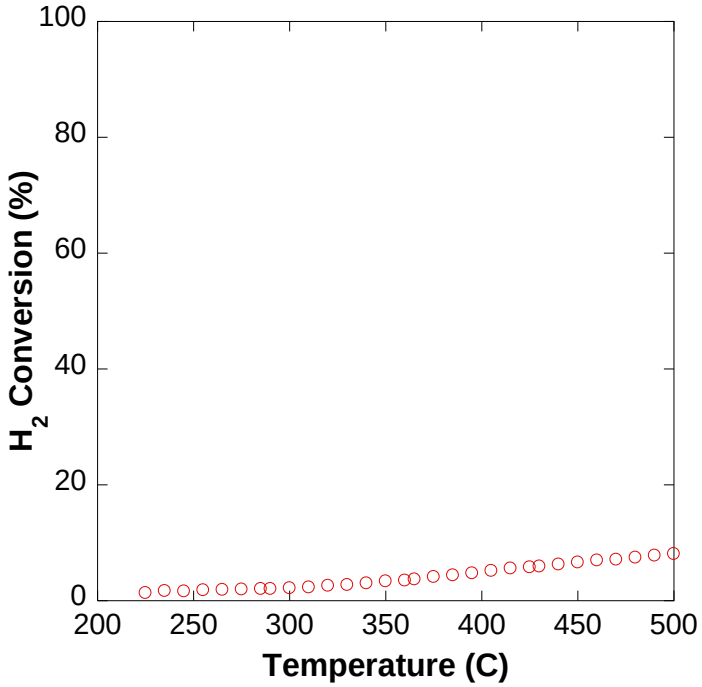

Figure 7.4 – The oxidation of hydrogen to water is negligible on the Fe-based SCR catalyst in the EAS. Results are shown for a temperature ramp experiment with 8% H_2O, 8% CO_2, 6% O_2, and 1% H_2 in the feed gas.

7.2.2 CO Oxidation

Reviewing literature from TWC and DOC kinetics it can be found that the kinetics for the oxidation of CO are high but not as high as H_2 oxidation kinetics,

however there is still a strong preference for CO to oxidize to CO_2 as seen in the reaction shown in equation (7.3) [71, 72, 157, 160].

$$CO + \frac{1}{2}O_2 \rightarrow CO_2 \tag{7.3}$$

From literature it was found that while the oxidation of CO to CO_2 is not quite as high as the oxidation of H_2 to H_2O, complete conversion of CO to CO_2 is expected for DOC catalysts above 200°C [159, 161]. Experimental results for the oxidation of CO to CO_2 for the iron based zeolite SCR catalyst in the EAS are shown in Figure 7.5. From these results it can be seen that there is no change in the oxidation of CO to CO_2 as temperature increases. Additionally the conversion of CO to CO_2 is below 5% for the entire temperature range, therefore it can be concluded that the CO oxidation reaction does not need to be included in the kinetic model.

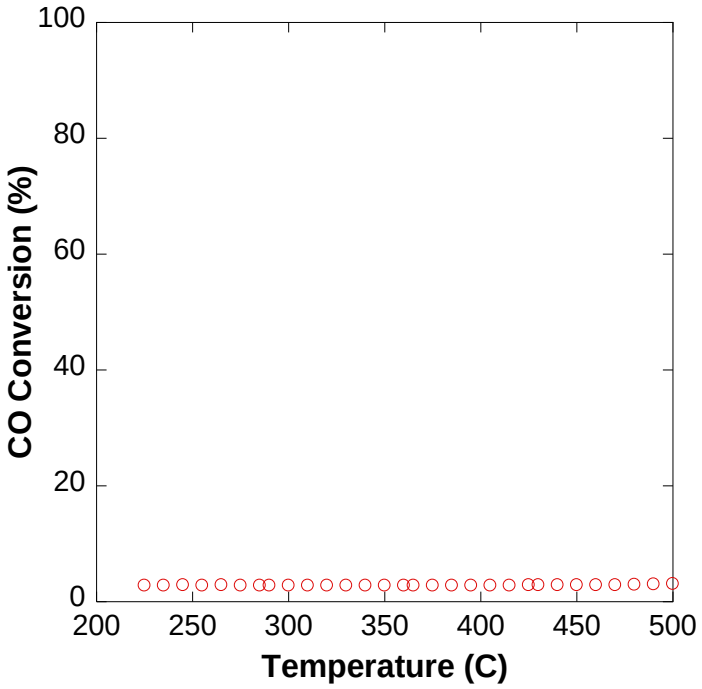

Figure 7.5 − There is a negligible oxidation effect of CO to CO_2 on the Fe-based SCR catalyst in the EAS. Results are shown for a temperature ramp experiment with 8% H_2O, 8% CO_2, 6% O_2, and 1% CO in the feed gas.

7.2.3 C_3H_6 Oxidation

The oxidation of hydrocarbons is commonly included in kinetic mechanisms for LNT, TWC, and DOC global kinetic mechanisms [70, 71, 152, 153, 155-157]. It can be seen in Figure 7.6 that the conversion of C_3H_6 due to oxidation is a strong function of temperature with a maximum conversion of 40% at 500°C.

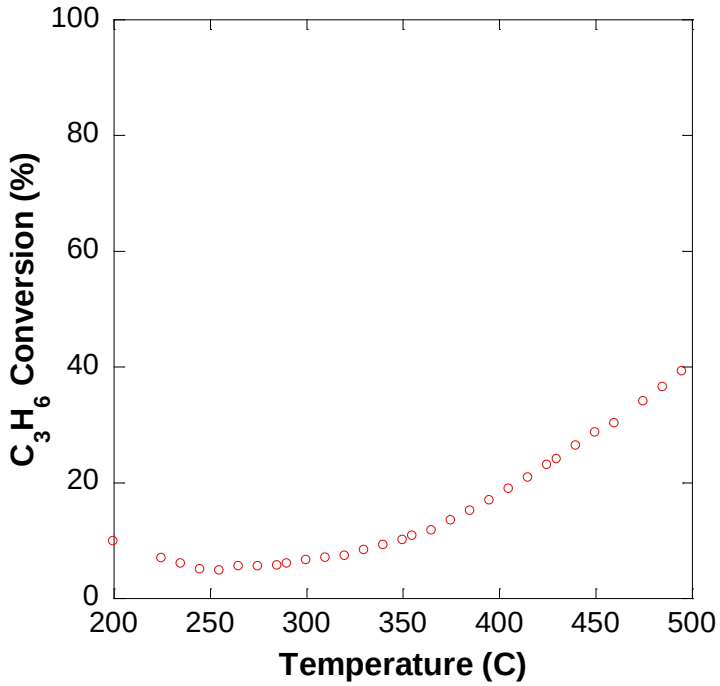

Figure 7.6 – The oxidation of C_3H_6 is a strong function of temperature with a maximum conversion of C_3H_6 around 40%. The experiment was performed as a temperature ramp with a 6% H_2O, 6% CO_2, 6% O_2, and 0.6% C_3H_6 in the feed gas.

Olsson et al. [156] has suggested two reactions that can occur simultaneously for the oxidation of C_3H_6. The first reaction shown in equation (7.4) is defined as the complete conversion of C_3H_6 to CO_2 and H_2O, while the second reaction shown in equation (7.5) shows only partial conversion of C_3H_6 to CO and H_2O. Experimental results in Figure 7.7 show that the dominant pathway for the oxidation of C_3H_6 leads to the formation of large amounts of CO as temperature increases; therefore the reaction shown in equation (7.5) is the dominant pathway in the oxidation of C_3H_6.

$$C_3H_6 + \frac{9}{2}O_2 \rightarrow 3CO_2 + 3H_2O \tag{7.4}$$

$$C_3H_6 + 3O_2 \rightarrow 3CO + 3H_2O \tag{7.5}$$

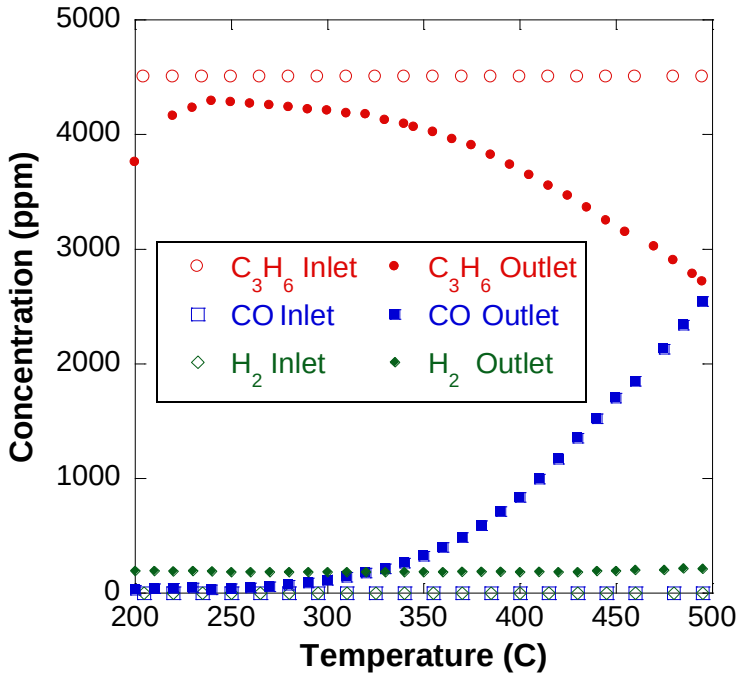

Figure 7.7 – The oxidation of C_3H_6 is a strong function of temperature that yields a large amount of CO as the temperature increases. The experiment was performed as a temperature ramp with a 6% H_2O, 6% CO_2, 6% O_2, and 0.6% C_3H_6 in the feed gas.

7.3 NO_x Reduction with H_2, CO, and C_3H_6

From the experiments shown above in Figure 7.3, Figure 7.4, and Figure 7.5 it has been determined that CO and H_2 reactions with H_2O, CO_2, or O_2 are negligible for a kinetic mechanism. While in Figure 7.6, it can be seen that a significant amount of C_3H_6 will be left to react with NO_x when oxidation is accounted for. Therefore, NO_x reduction possibilities can occur similar to reactions seen TWC and LNT kinetic mechanisms [69, 70, 162, 163]. NO_x is defined as the sum of NO and NO_2 in the exhaust stream. The conversion of NO and the conversion of NO_2 are defined in equations (7.6) and (7.7)

respectively. The conversion of NO_x is the combination of the conversion of NO and the conversion of NO_2 as defined in equation (7.8).

$$\eta_{NO} = \left(\frac{c_{NO\_IN} - c_{NO\_OUT}}{c_{NO\_IN}} \right) \cdot 100 \tag{7.6}$$

$$\eta_{NO_2} = \left(\frac{c_{NO_2\_IN} - c_{NO_2\_OUT}}{c_{NO_2\_IN}} \right) \cdot 100 \tag{7.7}$$

$$\eta_{NO_x} = \left(\frac{\left(c_{NO_2\_IN} + c_{NO\_IN}\right) - \left(c_{NO_2\_OUT} + c_{NO\_OUT}\right)}{\left(c_{NO_2\_IN} + c_{NO\_IN}\right)} \right) \cdot 100 \tag{7.8}$$

Experiments were performed to investigate the NO_x conversion potential for CO, H_2, and C_3H_6. For each reductant two experiments were performed, the first assuming all NO_x in the feed gas was NO, and the second assumes that all NO_x in the feed gas is NO_2. From these experiments (Figure 7.8) it can be seen that NO_x conversion is similar whether the NO_x concentration in the feed gas is all NO or NO_2 except for C_3H_6 where NO_x conversion is significantly higher for an all NO_2 in the feed gas. It should be noted that since the conversion of NO_x is not measured by the generation of N_2, it is possible for NO_2 and C_3H_6 to form organonitrates (CH_3ONO, CH_3ONO_2, CH_3NO_2, etc.) at low temperatures as seen by Kolli et al. [164] on tungstated zirconia-based catalysts.

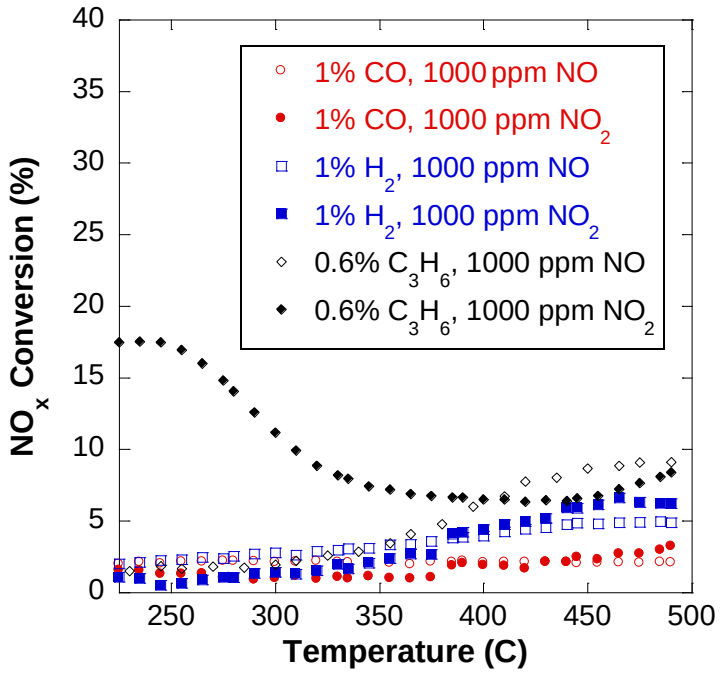

Figure 7.8 – NO_x conversion for each reductant (H_2, CO, and C_3H_6) is similar when the feed gas is NO or NO_2 as the composition of NO_x. The NO_2 reduction experiments were performed with 10% H_2O, 10% CO_2, 0% O2, 1000 ppm NO_2, and varying H_2, CO, and C_3H_6 concentration; while the NO reduction experiments were performed with 8% H_2O, 8% CO_2, 6% O_2, and 1000 ppm NO, and varying H_2, CO, and C_3H_6 concentration.

Conventional engine exhaust NO_x mixtures strongly favor NO with average NO_x mixtures that contain around 95% NO and 5% NO_2 [4]. Because engine exhaust mixtures favor NO most literature sources on TWC and LNT kinetic models contain only NO reduction. From these literature sources it is commonly seen that NO will reduce to N_2 when interacting with the reductants such as CO, H_2, and C_3H_6 in the investigated temperature range. Currently with the wide spread use of low temperature combustion strategies, the ratio of NO_2 is increasing for NO_x composition [165]. However, engine out NO_x composition cannot be approximated because the SCR is located downstream of a LNT and DOC catalyst in the EAS. Estimates for the NO to NO_x ratio at the SCR in the EAS have been determined experimentally from engine results, which yielded NO_x mixtures with a NO to NO_x ratio of 30% to 70%. To investigate the reason for similar

NO_x conversions between the NO only and the NO_2 only experiments a new conversion can be defined for NO_2 conversion to NO $\left(\eta_{NO_2:NO}\right)$ as seen in equation (7.9).

$$\eta_{NO_2:NO} = \left(1 - \frac{c_{NO_2\_IN} - c_{NO\_OUT}}{c_{NO_2\_IN}}\right) \cdot 100 \tag{7.9}$$

By comparing the NO_2 conversion (equation (7.7)) and the NO_2 to NO conversion (equation (7.9)), it can be seen in

Figure 7.9 that the majority of NO_2 is converted to NO when H_2 and CO are added to the feed gas. Therefore it can be assumed when formulating the reaction pathway for NO_2 when using H_2 and CO, that when NO_2 is present it first is converted to NO by the reductants and due to thermal decomposition. The newly formed NO then reacts with CO and H_2 which produces N_2, H_2O, and CO_2 and potentially organonitrates/nitrites. When C_3H_6 is present it can be seen that NO_x conversion is much higher at low temperatures when reacting only with NO_2 then decreases as temperature increases, which is the reverse of the reaction with C_3H_6 and NO where NO_x conversion increases as temperature increases.

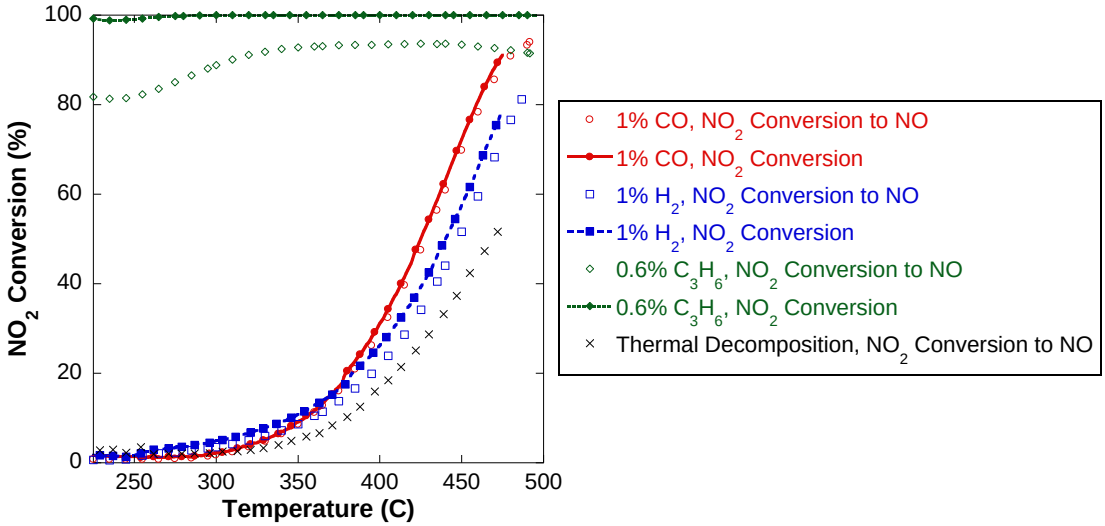

Figure 7.9 − All reductants will increase the conversion of NO_2 to NO compared to thermal decomposition alone. The experiments were performed with 10% H_2O, 10% CO_2, 0% O_2, 1000 ppm NO_2, and varying H_2, CO, and C_3H_6 concentrations.

7.3.1 CO NO_x Reduction

From Figure 7.8 it can be seen that CO will convert less NO_x than H_2 or C_3H_6. This is further corroborated by Figure 7.10 where NO_2 conversion and NO_2 conversion to NO is high but NO_x conversion is less than 5%. Due to conversion of NO_x with CO being less than 5% the NO reduction with CO reaction shown in equation (7.10) can be neglected in the kinetic mechanism.

$$2CO + 2NO \rightarrow 2CO_2 + N_2 \qquad (7.10)$$

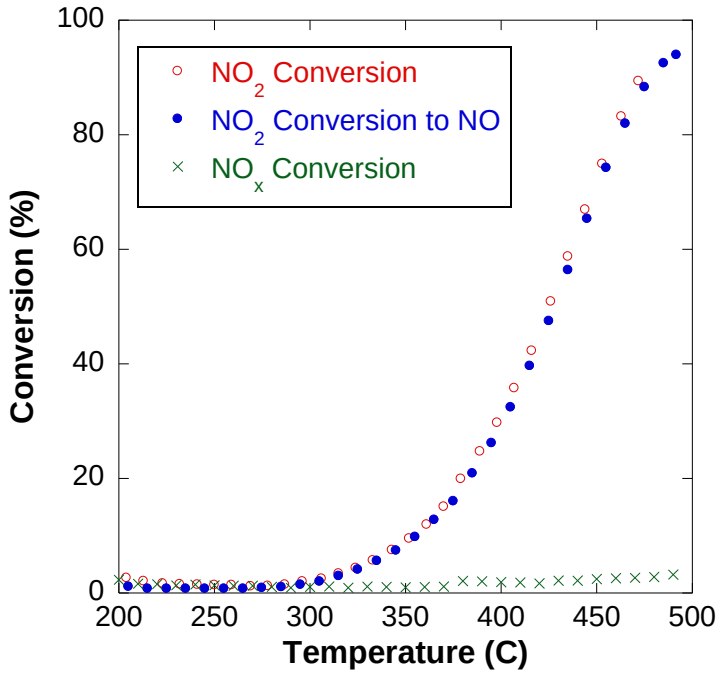

Figure 7.10 – NO_2 conversion with CO is mostly due to NO_2 conversion to NO with less than 5% of the NO being converted to N_2. The experiment was performed with 10% H_2O, 10% CO_2, 0% O_2, 1000 ppm NO_2, and 1% CO.

From Figure 7.11 it can be seen that CO will increase the conversion of NO_2 compared to thermal decomposition alone. It can also be seen that NO_2 conversion increases as CO concentration increases. Figure 7.10 shows that the majority of conversion will be from NO_2 to NO and not NO_x reduction. The CO oxidation with NO_2 reaction shown in equation (7.11) therefore can be used to account for any additional conversion of NO_2 to NO when CO is present.

$$CO + NO_2 \rightarrow CO_2 + NO \tag{7.11}$$

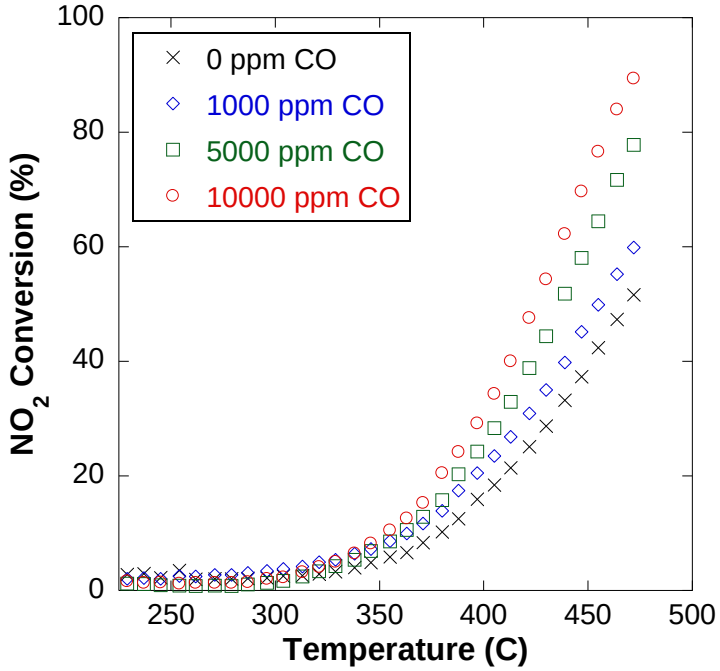

Figure 7.11 − CO increases NO_2 conversion to NO as concentration of CO increases. The experiments were performed with 10% H_2O, 10% CO_2, 0% O_2, 1000 ppm NO_2, and varying CO concentration.

7.3.2 H_2 NO_x Reduction

It can be seen from Figure 7.8 that NO_x conversion with H_2 is higher than with CO. From Figure 7.12 it can be seen that as with CO, NO_2 will converted to NO first before reduction to N_2.

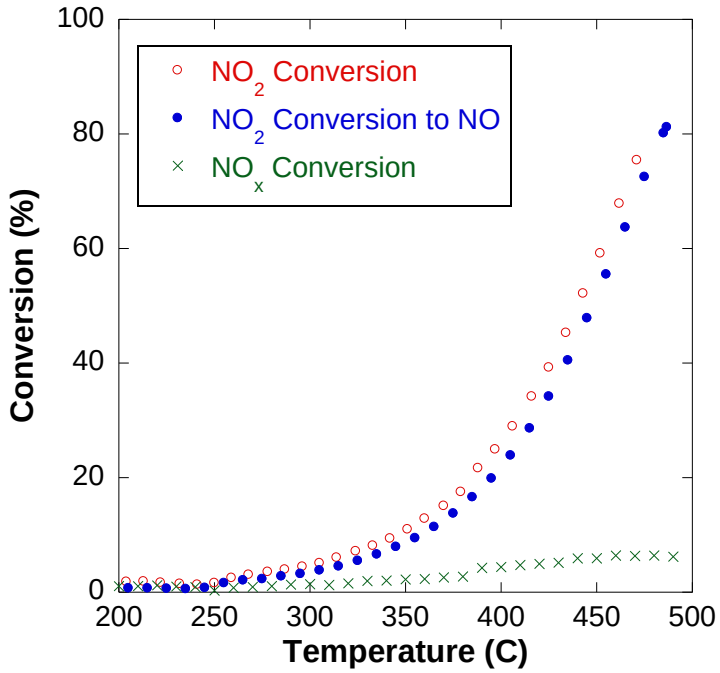

Figure 7.12 – NO_2 conversion with H_2 primarily due to NO_2 conversion to NO with up to 7% of NO_x converted to N_2. The experiments were performed with 10% H_2O, 10% CO_2, 0% O_2, 1000 ppm NO_2, and 1% H_2.

The conversion of NO_2 with H_2 can be further seen in Figure 7.13 where increasing H_2 concentration will increase NO_2 conversion. Due to the increase in conversion of NO_2 to NO with H_2 compared to thermal decomposition the reaction of H_2 being oxidized by NO_2 shown in equation (7.12) can be used to describe this behavior.

$$H_2 + NO_2 \rightarrow H_2O + NO \qquad (7.12)$$

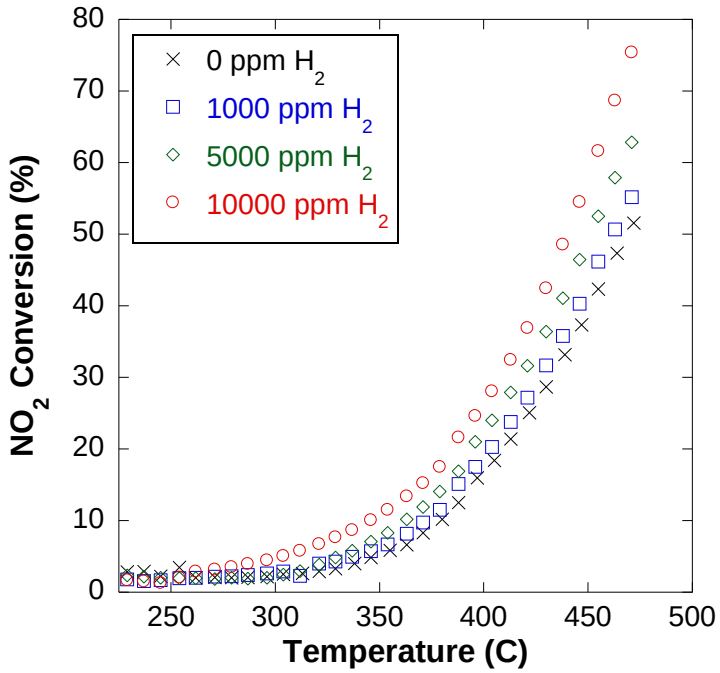

Figure 7.13 − H2 increases NO2 conversion as concentration of H2 increases. The experiments were performed with 10% H2O, 10% CO2, 0% O2, 1000 ppm NO2, and varying H2 concentration.

From LNT kinetic mechanisms [69, 70, 162, 163] H_2 can be used to directly reduce NO stored on the catalysts. Converting this reaction to a gas phase reaction since NO does not store on the iron based SCR catalyst in the EAS, the reaction in equation (7.13) can be formed.

$$2H_2 + 2NO \rightarrow 2H_2O + N_2 \qquad (7.13)$$

An additional experiment was performed with H_2 and NO varying O_2 concentration from 0% to 6%. If the reaction in equation (7.13) is the only reaction occurring NO_x conversion would remain the same. The reaction with 0% O_2 yielded less NO_x conversion, upon further investigation it was found that at temperatures above 300°C, NH_3 can be produced on the catalyst based on the NH_3 Production reaction shown in equation (7.14). The concentration values versus temperature are shown in Figure 7.14, where the experiment was performed with 8% CO_2, 8% H_2O, 0% O_2, 1% H_2, and 1000 ppm NO in the feed gas, with a temperature ramp from 200°C to 500°C. The

production of NH_3 on the catalyst would allow for two pathways for NO conversion on the SCR catalyst. The first pathway titled the "Rich Standard SCR" reaction shown in equation (7.15) yields little conversion in literature surveys, while the second reaction shown in equation (7.16) is titled the "Standard SCR Reaction" where the addition of O_2 creates a preferred pathway to NO_x reduction [45, 47, 48, 129] as also seen in Chapter 3. The conversion of NO for both the Rich Standard SCR reaction and Standard SCR reaction were corroborated for this catalyst in experiments performed in Chapter 3.

$$5H_2 + 2NO \rightarrow 2NH_3 + 2H_2O \tag{7.14}$$

$$4NH_3 + 6NO \rightarrow 5N_2 + 6H_2O \tag{7.15}$$

$$4NH_3 + 4NO + O_2 \rightarrow 4N_2 + 6H_2O \tag{7.16}$$

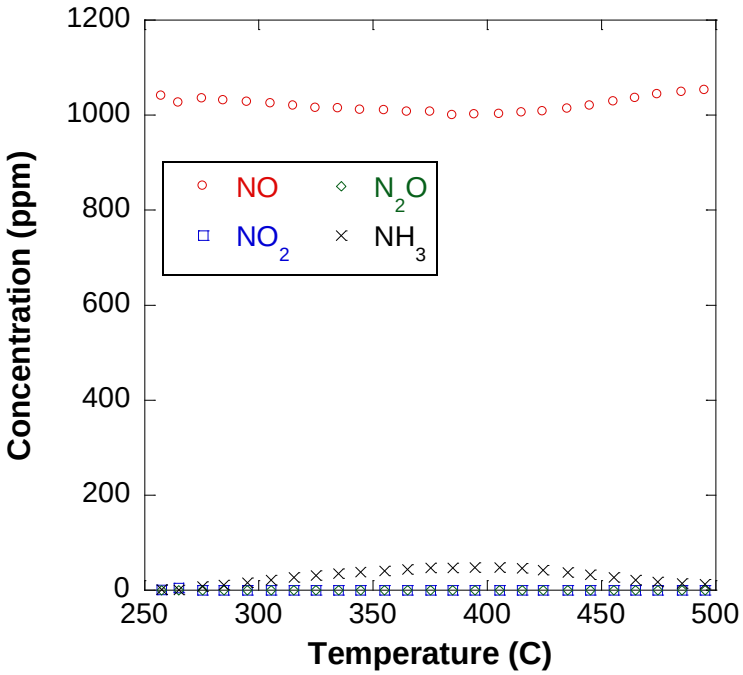

Figure 7.14 − H_2 and NO will combine to form NH_3, which can be used in NO_x conversion. The experiment was performed with 8% H_2O, 8% CO_2, 0% O_2, 1000 ppm NO_2, and 1% H_2.

When examining the H_2 NO experiment with 6% O_2, no NH_3 formation was seen, therefore it can be assumed that any NH_3 formed would then react with NO and O_2 to

convert the NO to N_2. By comparing the NO conversion to NH_3 for the 0% O_2 experiment to the NO_x conversion of 6% O_2 experiment in Figure 7.15, it can be seen that the NH_3 produced accounts for the increase not seen in the NO_x conversion experiments with CO. Therefore it can be assumed that the preferred pathway is H_2 will preferentially react with NO_2 to form NO and H_2O (equation (7.12)). H_2 will then react with NO to form small amounts of NH_3 on the catalyst (equation (7.14)) which will then react with NO and NO_2 according to the NO_x reduction with NH_3 reactions discussed in Chapter 3.

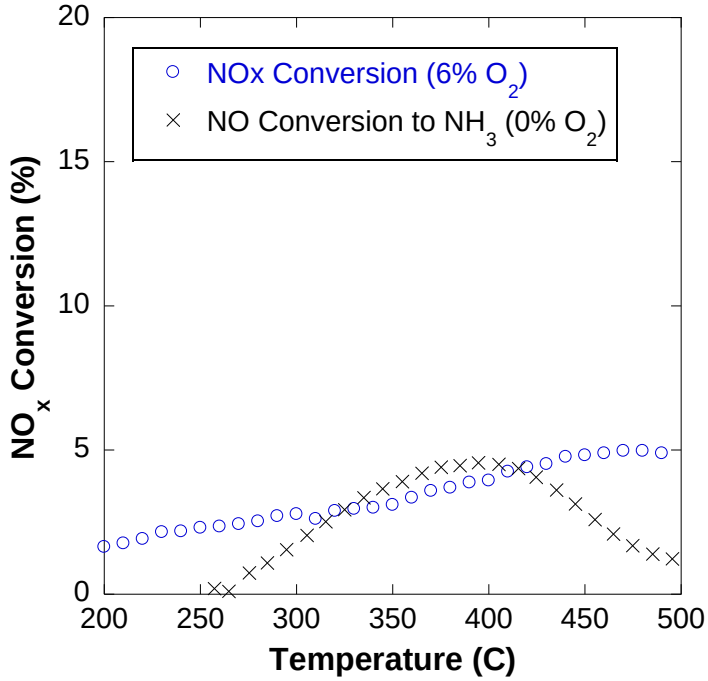

Figure 7.15 − Up to 5% of the NO will combine with H_2 to form NH_3. The experiment was performed with 8% H_2O, 8% CO2, 0% O_2, 1000 ppm NO_2, and 1% H_2.

7.3.3 C_3H_6 NO_x Reduction

As discussed earlier propylene (C_3H_6) is used in the feed gas as surrogate for any fuel that is not converted to H_2 and CO in the fuel reformer based on work by Kuo et al. [155]. It has been observed that C_3H_6 will react with both NO and NO_2. In Figure 7.16 it can be seen that C_3H_6 will remove small amounts of NO. This reaction is a strong

function of C_3H_6 concentration and reaches a maximum conversion of 10% when 0.6% C_3H_6 is in the feed gas. The proposed reaction for C_3H_6 and NO is shown in (7.17).

$$C_3H_6 + 9NO \rightarrow 3CO_2 + 3H_2O + 4.5N_2 \tag{7.17}$$

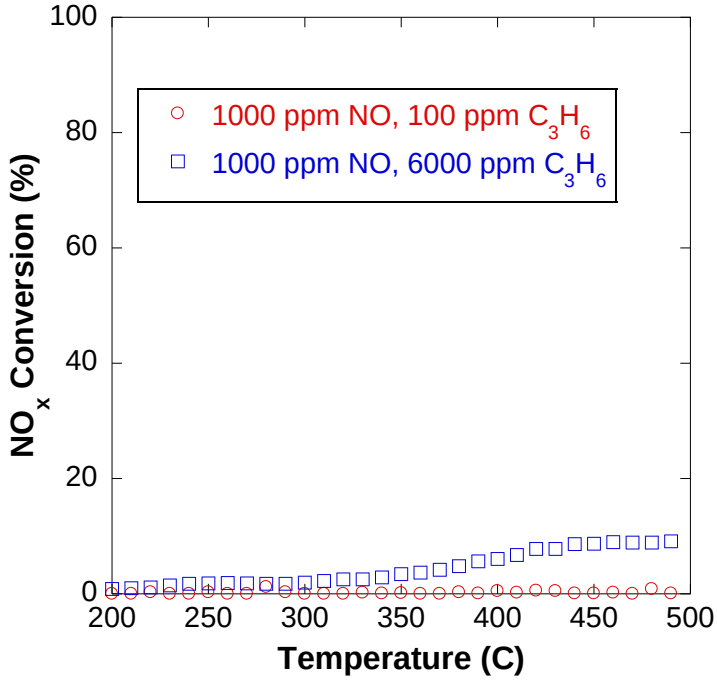

Figure 7.16 – The conversion of NO by C_3H_6 is low and highly dependent on the amount of C_3H_6 in the feed gas. The experiments were performed as a temperature ramp with 8% H_2O, 8% CO_2, 6% O2, 1000 ppm NO, and varying C_3H_6 concentrations.

From Figure 7.17 it can be seen that propylene strongly converts NO_2, and as the concentration of propylene increases NO_2 is completely converted. Figure 7.18 shows that NO_x conversion is the highest at low temperatures and decreases as temperature increases. It can also be seen in Figure 7.18 that NO_x conversion increases as C_3H_6 concentration increases.

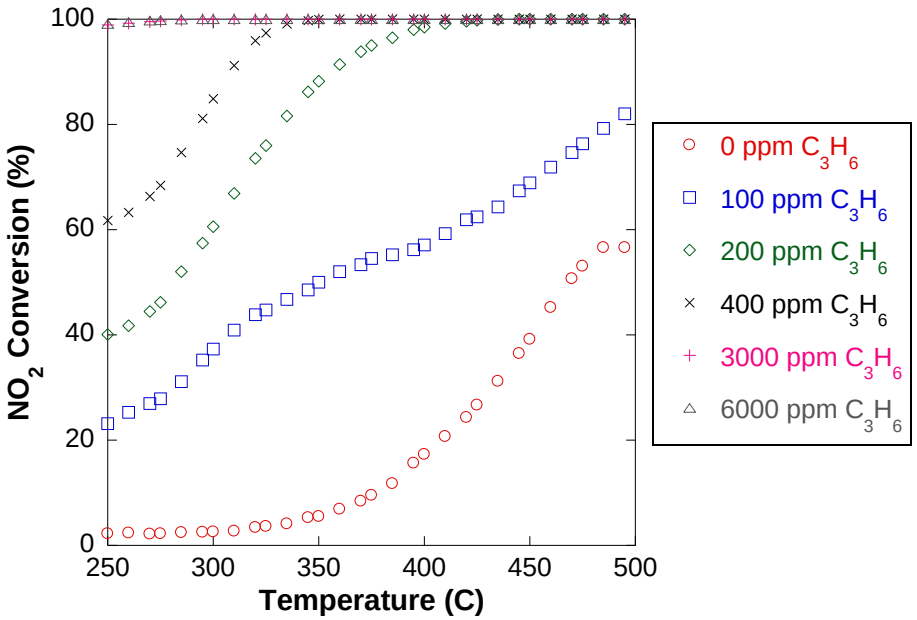

Figure 7.17 – C_3H_6 will be strongly oxidized by NO_2 converting significantly more NO_2 to NO then thermal decomposition alone. The experiments were performed as a temperature ramp with a feed gas composition of 10% H_2O, 10% CO_2, 0% O_2, 1000 ppm NO_2, and varying C_3H_6 concentration.

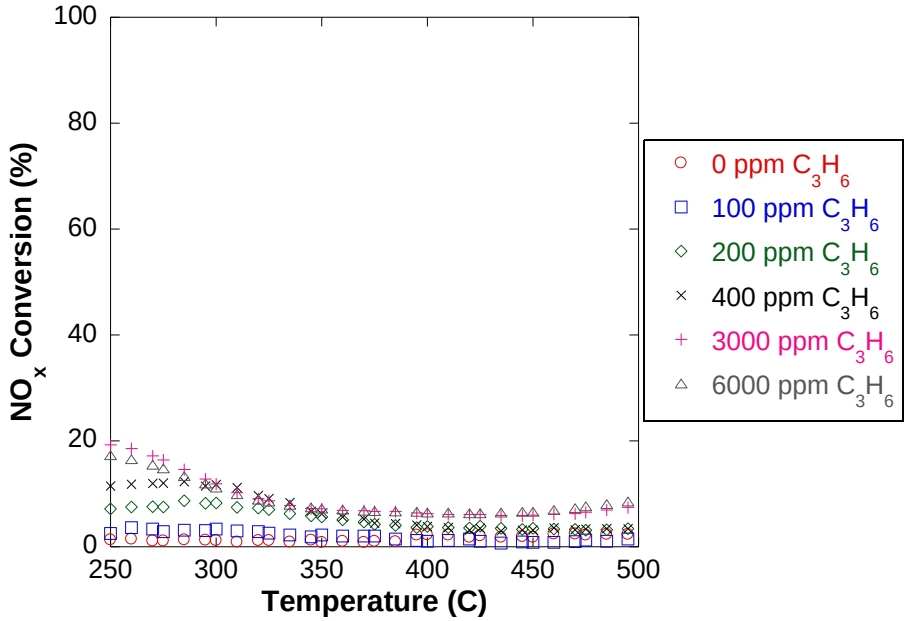

Figure 7.18 – C_3H_6 will convert NO_x at lower temperatures when larger concentrations of C_3H_6 are present. The experiments were performed as a temperature ramp with a feed gas composition of 10% H_2O, 10% CO_2, 0% O_2, 1000 ppm NO_2, and varying C_3H_6 concentration.

From Figure 7.19 it can be seen that high levels of C_3H_6 will completely remove NO_2 across the catalyst. Also in Figure 7.19 it can be seen that the NO_2 conversion to NO accounts for most of the NO_2 conversion leading to the reaction shown in equation (7.18) as the dominant reaction for C_3H_6 and NO_2.

$$C_3H_6 + 9NO_2 \rightarrow 3CO_2 + 3H_2O + 9NO \tag{7.18}$$

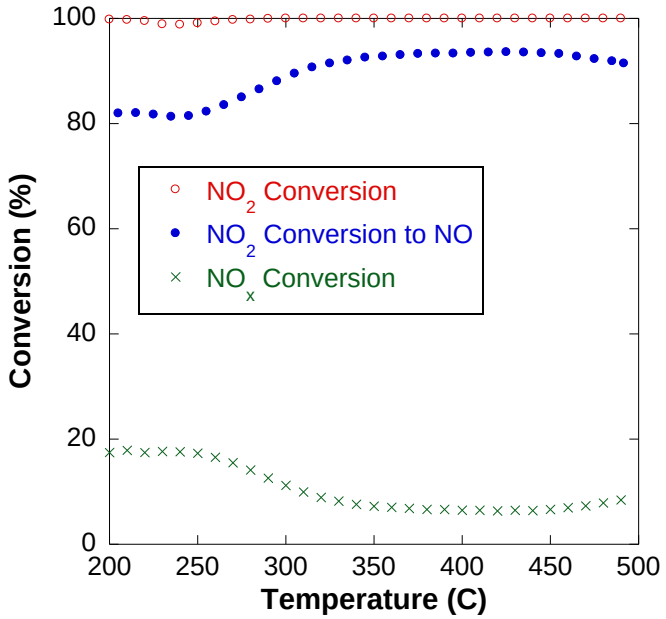

Figure 7.19 – C_3H_6 is the most reactive species with NO_2, where most NO_2 will be converted to NO. The experiments is performed as a temperature ramp with a feed gas composition of 10% H_2O, 10% CO_2, 0% O_2, 1000 ppm NO_2, and 0.6% C_3H_6.

Figure 7.20 shows the concentration values vs. temperature for two experiments performed as temperature ramps with 1000 ppm NO_2 and with varying C_3H_6 concentrations. Due to high levels of H_2O and CO_2 in the feed gas the conversion of C_3H_6 to CO_2 and H_2O could not be measured, however a noticeable rise in CO concentration has been seen as temperature increases for both experiments. This leads to the possible inclusion of the steam reforming reaction shown in equation (7.19).

$$C_3H_6 + 3H_2O \rightarrow 3CO + 6H_2 \tag{7.19}$$

H_2 values were negligible during the experiments shown in Figure 7.20. It was determined previously that H_2 reactions with NO and NO_2 are small. Therefore it can be determined that the reactions with C_3H_6 are not likely to occur due to steam reforming reaction (equation (7.19)) , but are more likely to occur as a reaction where C_3H_6 is oxidized by NO_2 that does not yield complete conversion to CO_2 as shown in equation (7.20).

$$C_3H_6 + 6NO_2 \rightarrow 3CO + 3H_2O + 6NO \qquad (7.20)$$

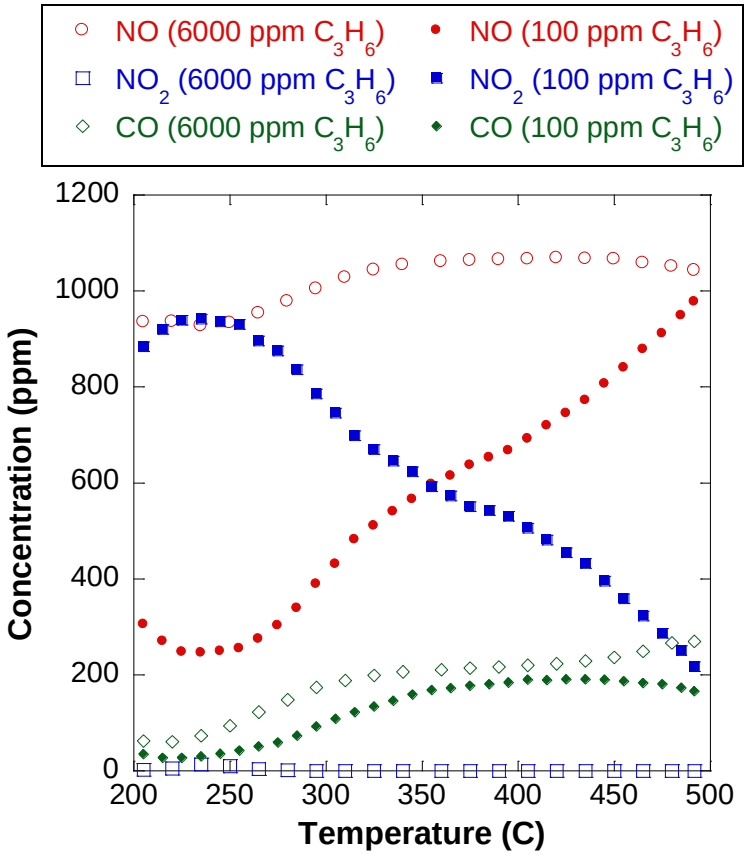

Figure 7.20 – C_3H_6 and NO_2 will react to form CO; however the concentration does not increase as C_3H_6 concentration increases. The experiments were performed as a temperature ramp with 6% H_2O, 6% CO_2, 1000 ppm NO_2, and varying C_3H_6 concentration in the feed gas.

Figure 7.21 compares the NO_x conversions with C_3H_6 for a feed gas with a NO_x composition of all NO (Figure 7.16) and a feed gas with a NO_x composition of all NO_2 (Figure 7.18). At high temperatures C_3H_6 will react with NO_2 to form NO as shown in

equation (7.20), therefore NO_x conversion at high temperatures is similar for both experiments. At low temperatures however NO_x conversion is much higher when the NO_x composition is all NO_2. From Figure 7.20 it can be seen that CO concentration is low in the low temperature range. It can then be theorized that the direct reduction of NO_2 with C_3H_6 reaction shown in equation (7.21) can capture this effect.

$$2C_3H_6 + 18NO_2 \rightarrow 6CO_2 + 6H_2O + 9N_2 \qquad (7.21)$$

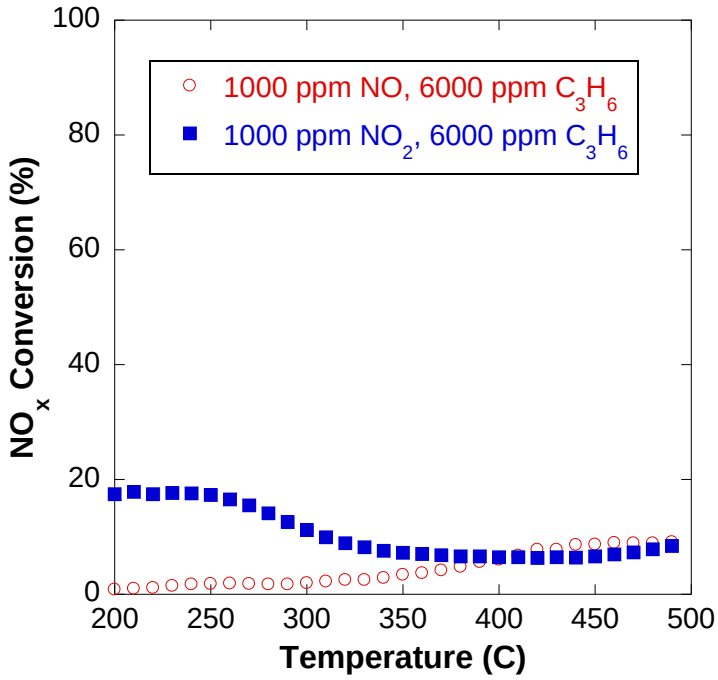

Figure 7.21 – NO_x conversion with C_3H_6 is higher at low temperatures when the NO_x composition is all NO_2 in the feed gas, but as temperature increases NO_x conversion converges for a NO_x composition of all NO in the feed gas with the experiment with a NO_x composition of all NO_2 in the feed gas.

7.4 NH_3 Storage Effects with H_2, CO, and C_3H_6

When performing a regeneration of the LNT it is common for a small portion of the fuel to remain unconverted into H_2 and CO in the fuel reformer. The reductants can in turn slip through the LNT into the feed gas of the SCR. Because this is when NH_3 will be generated by the LNT and then stored on the SCR catalyst it is important to test their

effect on NH_3 storage capacity. As stated earlier the hydrocarbon in the feed gas will be approximated by propylene (C_3H_6).

Since it has been seen in Figure 7.1 that C_3H_6 will store on the catalyst during the rich pulse of a cycling experiment where it will lower the integral NO_x conversion of the entire cycle, it is expected that C_3H_6 will compete with NH_3 for storage on the catalyst surface. Figure 7.22 below shows NH_3 storage capacity is not affected by H_2, CO, or C_3H_6 concentrations in the feed gas. It is because of these results that NH_3 storage capacity can be modeled with a single site global reaction shown in equation (7.22) where NH_3 storage capacity will only be affected by temperature. It can also be concluded that C_3H_6 will need to be modeled to store on a different catalytic site as shown in equation (7.23) which will be discussed in a later section of this chapter.

$$Z + NH_3 \leftrightarrow Z\left(NH_3\right) \tag{7.22}$$

$$Y + C_3H_6 \leftrightarrow Z\left(C_3H_6\right) \tag{7.23}$$

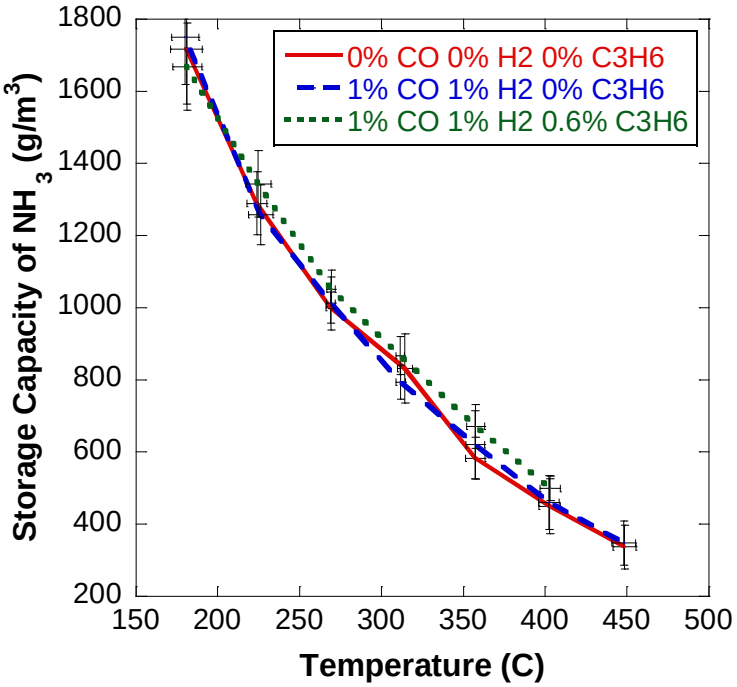

Figure 7.22 − NH_3 storage capacity isn't affected by H_2, CO or C_3H_6 in the feed gas. All experiments were performed with 10% H_2O and 10% CO_2 in the feed gas.

7.5 NH_3 Oxidation Effects with H_2, CO, and C_3H_6

To account for any slip of reductant from the LNT in a LNT-SCR aftertreatment system, further NH_3 oxidation experiments were performed with H_2, CO, and C_3H_6 in the feed gas. From the results shown in Figure 7.23, it can be seen that the addition of H_2 and CO to the feed gas will not affect the conversion of NH_3 due to oxidation. However, it can also be seen that when C_3H_6 is present the conversion of NH_3 due to oxidation will strongly increase. It can be theorized this is due to additional hydroxyl formation from the oxidation of C_3H_6.

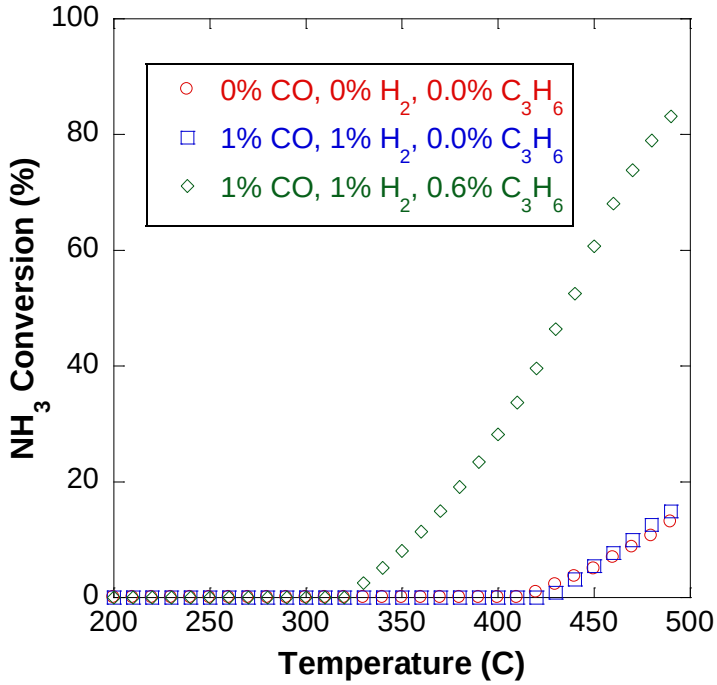

Figure 7.23 – H_2 and CO in the feed gas do not influence the conversion of NH_3 due to oxidation, however the addition of C_3H_6 strongly increases the conversion of NH_3 due to oxidation. All experiments were performed with a feed gas concentration of 8% H_2O, 8% CO_2, 6% O_2, and 1000 ppm NH_3.

Since adding hydroxyl molecules would increase the number of reactions necessary to create a kinetic mechanism for the SCR catalyst, equation (7.24) is proposed as global reaction where NH_3 is oxidized in the presence of C_3H_6. C_3H_6 will still be oxidized as a combination of the reactions shown in equations (7.4) and (7.5).

$$2Z\left(NH_3\right)+C_3H_6+6O_2 \rightarrow N_2+C_3H_6+6H_2O \tag{7.24}$$

$$C_3H_6+\frac{9}{2}O_2 \rightarrow 3CO_2+3H_2O \tag{7.4}$$

$$C_3H_6+3O_2 \rightarrow 3CO+3H_2O \tag{7.5}$$

7.6 NO_x Reduction with NH_3 Effects with H_2, CO, and C_3H_6

The three main NO_x reduction pathways for NO_x reduction with NH_3 are shown in equations (7.25), (7.26), and (7.27). It was observed that reactions with H_2, CO, and C_3H_6 and NO were much smaller than H_2, CO, and C_3H_6 and NO_2 reactions. Therefore, it is proposed the H_2, CO, and C_3H_6 will effect NO_x conversion with NH_3 by affecting the NO to NO_x ratio at the catalyst which has been demonstrated as an important characteristic in NO_x reduction with NH_3 predictions as seen in Figure 3.18.

$$4Z\left(NH_3\right)+4NO+O_2 \rightarrow 4Z+4N_2+6H_2O \tag{7.25}$$

$$2Z\left(NH_3\right)+NO+NO_2 \rightarrow 2Z+2N_2+3H_2O \tag{7.26}$$

$$8Z\left(NH_3\right)+6NO_2 \rightarrow 8Z+7N_2+12H_2O \tag{7.27}$$

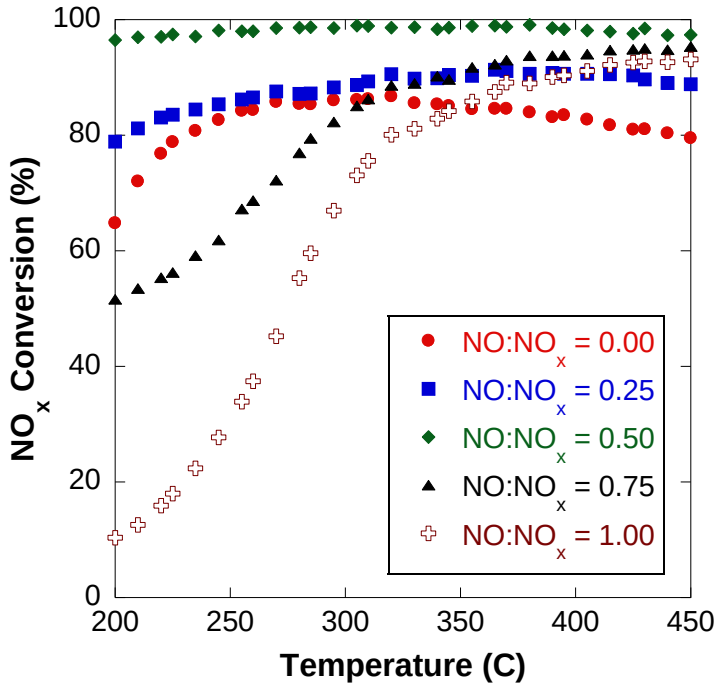

Figure 7.24 – NO_x conversion is highly dependent on the NO:NO_x ratio in the feed gas when comparing experiments performed with a feed gas of 6% H_2O, 6% CO_2, 6% O_2, 400 ppm NH_3, 400 ppm NO_x.

In Figure 7.25 it can be seen that NO_x conversion is inhibited by H_2, CO, and C_3H_6 in the feed gas. It has been proposed that NO_x conversion increases as temperature increases for NO only feed gas compositions with oxygen due to the catalyst's ability to oxidize NO to NO_2. It can therefore be assumed that the inhibition effect of CO, H_2, and C_3H_6 on the Standard SCR reaction (equation (7.25)) is accomplished by using NO_2 formed due to NO oxidation to oxidize H_2, CO, and C_3H_6 instead of increasing NO_x conversion by utilizing the Fast SCR reaction in equation (7.26) when possible.

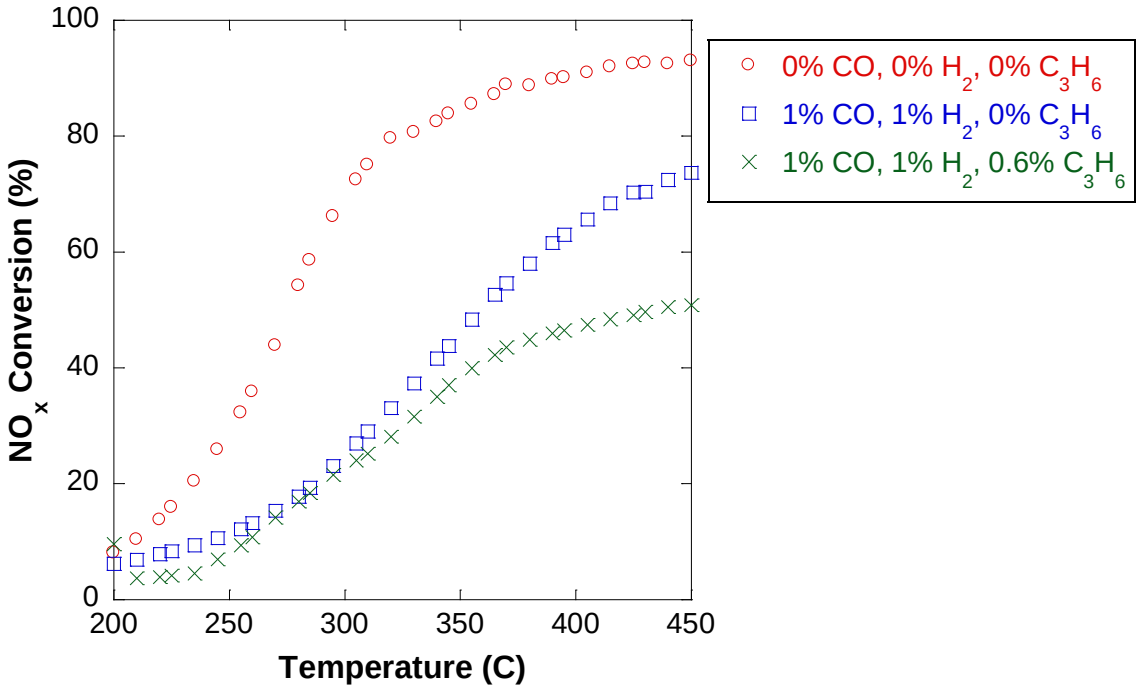

Figure 7.25 – NO_x conversion is strongly affected at high temperatures when H_2, CO, and C_3H_6 are in the feed gas. All experiments are performed with 6% H_2O, 6% CO_2, 6% O_2, 1000 ppm NH_3, and 1000 ppm NO in the feed gas.

Similarly it can be seen in Figure 7.26 that H_2 and CO will not have an effect on the equal molar ratio of NO and NO_2 due to the preference for its reaction with NH_3. It has also been observed that due to the strong reaction with C_3H_6 and NO_2, the NO_2 reduction to NO will drastically decrease the NO_x conversion capabilities when present in steady state reactions.

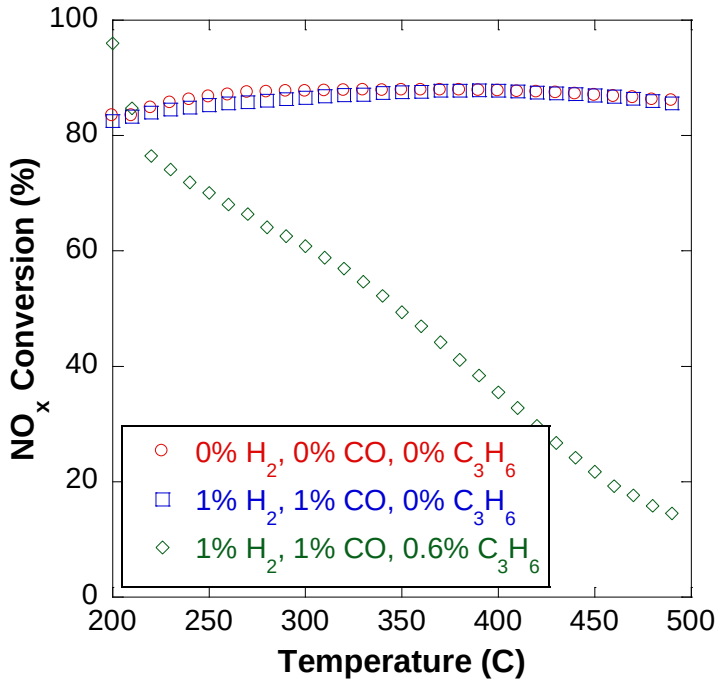

Figure 7.26 – NO_x conversion is strongly affected as temperature increases when H_2, CO, and C_3H_6 are in the feed gas. All experiments are performed with 6% H_2O, 6% CO_2, 0% O_2, 1000 ppm NH_3, 500 ppm NO, and 500 ppm NO_2 in the feed gas.

It can seen be from the experiments in Figure 7.25 and Figure 7.26 that an all NO_2 feed gas flow could achieve some benefits of having H_2, CO, and C_3H_6 in the feed gas due to favorable conversion of NO_2 to NO yielding a more ideal equal molar mixture. In Figure 7.27 it can be seen that H_2 and CO increase NO_x conversion as temperature increases due to their ability to convert more NO_2 to NO increasing the role of the Fast SCR reaction (equation (7.26)) . It can also be seen that the addition of C_3H_6 strongly increases NO_x conversion with NH_3 at low temperatures but strongly inhibits NO_x conversion at higher temperatures due to higher conversion of NO_2 to NO while decreasing amount of NH_3 on the catalyst.

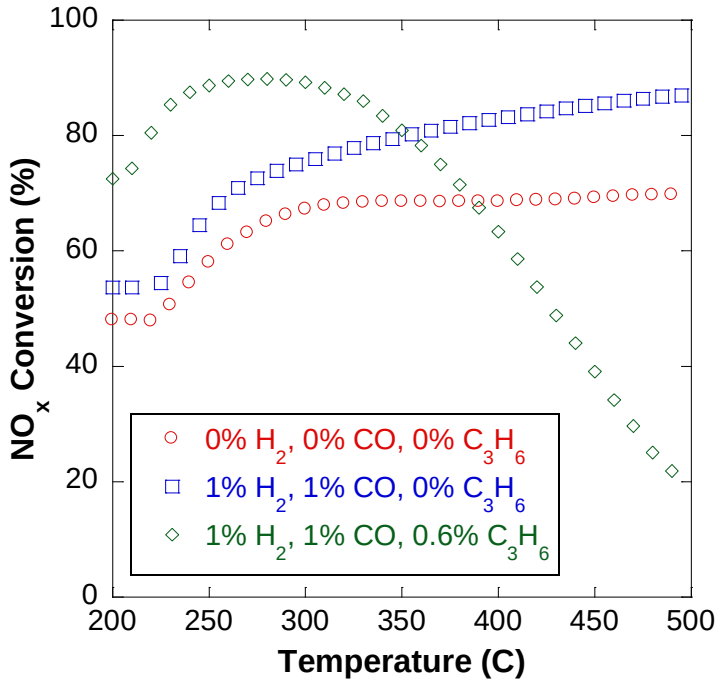

Figure 7.27 − NO_x conversion is affected by H_2, CO, and C_3H_6 by converting NO_2 to NO which can increase NO_x conversion by favoring the Fast SCR reaction when the NO to NO_x ratio favors NO_2. All experiments are performed with 6%H_2O, 6% CO_2, 0% O_2, 1000 ppm NH_3, and 1000 ppm NO_2 in the feed gas.

From Figure 7.25, Figure 7.26, and Figure 7.27 it has been observed that C_3H_6 is the dominant inhibition species for a SCR catalyst by converting NO_2 to NO on the catalyst. It should be noted that similar results are seen when H_2 and CO are in the exhaust stream but to a lesser extent. It has also been determined that H_2, CO, and C_3H_6 can increase NO_x conversion when the NO to NO_x ratio favors NO_2.

Since HC poisoning can have a distinct effect during steady state operation, cycling experiments were performed for the Standard and Fast SCR reactions as shown in Figure 7.28. In Figure 7.28 it can be seen that H_2 and CO in the rich pulse in a cycling experiment have negligible effects on cycling experiments, while C_3H_6 in the rich pulse will strongly inhibit integral NO_x conversion. It can be determined that C_3H_6 will store with NH_3 on the catalyst during a rich pulse and then react with NO_x during the lean pulse as seen in Figure 7.28.

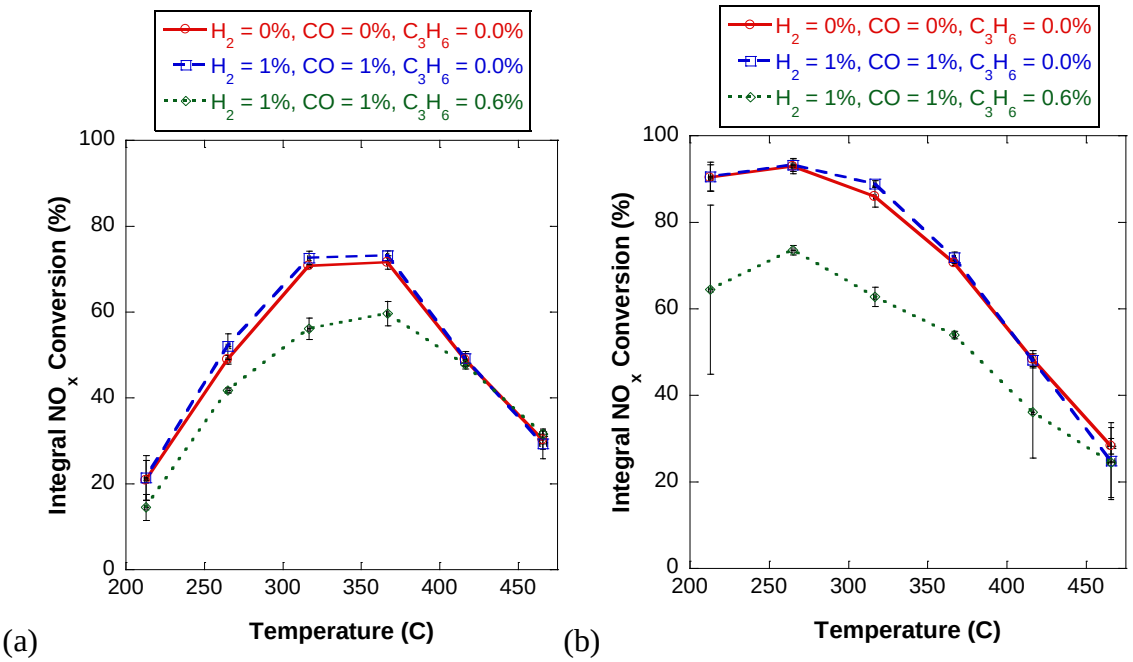

Figure 7.28 − Integral NO_x conversion is changes are negligible when H_2 and CO are in the rich pulse, while C_3H_6 present will decrease the integral NO_x conversion when present in the rich pulse. All experiments are performed with a rich pulse of 8% H_2O, 8% CO_2, 1000 ppm NH_3; and a lean pulse of 8% H_2O, 8% CO_2, 150 ppm NO_x, with (a) $NO:NO_x$ = 1.0 and (b) $NO:NO_x$ = 0.5.

7.7 C_3H_6 Poisoning

When running experiments with high levels of C_3H_6, coking or carbon deposits sticking to the catalyst became obvious as shown in Figure 7.29. Once coking was observed that catalyst was cleaned at 500°C with O_2 and NO_2 for 10 minutes until the original color of the catalyst returned. It was observed through repeated tests that this did not change catalyst activity once cleaned. This effect has been studied by Montreuil and Lambert where a formulation is used to reduce the poisoning effects of hydrocarbons on SCR catalysts [166]. The ability for C_3H_6 to store on the SCR catalyst during the rich pulse of a cycling experiment, where it will reduce the integral NO_x conversion of the catalyst throughout the cycle was shown in Figure 7.28. Due to this poisoning effect and the evidence that C_3H_6 will store on the catalyst this section is dedicated to quantifying the storage capabilities of C_3H_6 on the SCR catalyst.

(a) 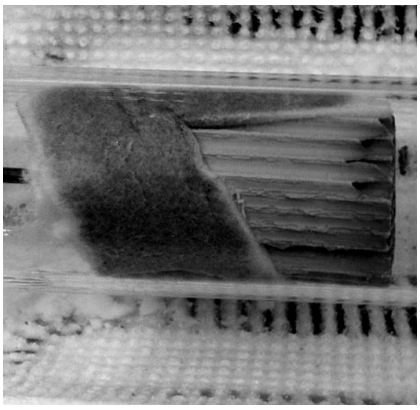 (b) 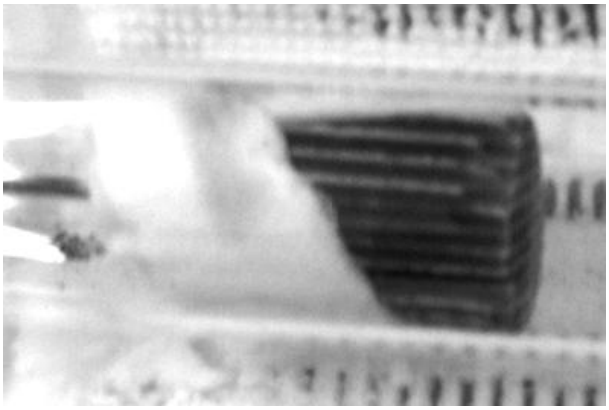

Figure 7.29 – Shows an example of (a) catalyst during normal operation, and (b) a catalyst that has been gone through coking after experiments with high levels of C_3H_6.

7.7.1 Temperature Programmed Desorption with C_3H_6

A Temperature Programmed Desorption (TPD) experiment, similar to the experiments performed for NH_3 storage in Chapter 3, was performed with C_3H_6 to test for the storage capacity of C_3H_6 on the SCR catalyst. From the TPD experiment shown in Figure 7.30 a negligible amount of C_3H_6 is stored on the catalyst. However, as previously as seen in Figure 7.28 the integral NO_x conversion decreased when C_3H_6 was present in the rich pulse of the feed gas into the SCR catalyst.

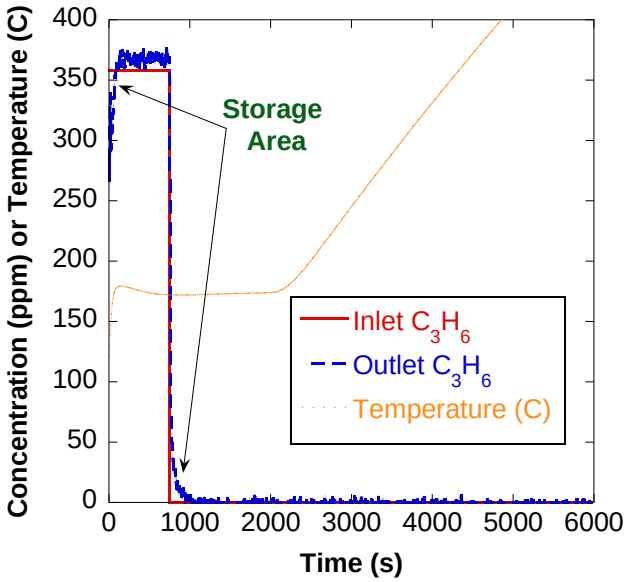

Figure 7.30 − C_3H_6 storage is low when finding storage capacity with a Temperature Programmed Desorption (TPD) experiment. The experiment was performed with a feed gas of 10% H_2O, 10% CO_2, and 350 ppm C_3H_6.

7.7.2 C_3H_6 / NO_2 Lean Rich Switching Experiments

Since storage could not be found using a TPD experiment, a new experiment is designed to calculate the storage capacity of C_3H_6. These experiments operate by holding temperature constant, then flow a feed gas through the catalyst of 1000 ppm NO_2 and 8% H_2O to find the thermal decomposition of NO_2 at the catalyst temperature. Three cycles are then performed with a rich pulse containing 8% H_2O and 0.6% C_3H_6 for 2 minutes followed by an 8 minute pulse of 8% H_2O and 1000 ppm NO_2. The results for each temperature are seen in Figure 7.31.

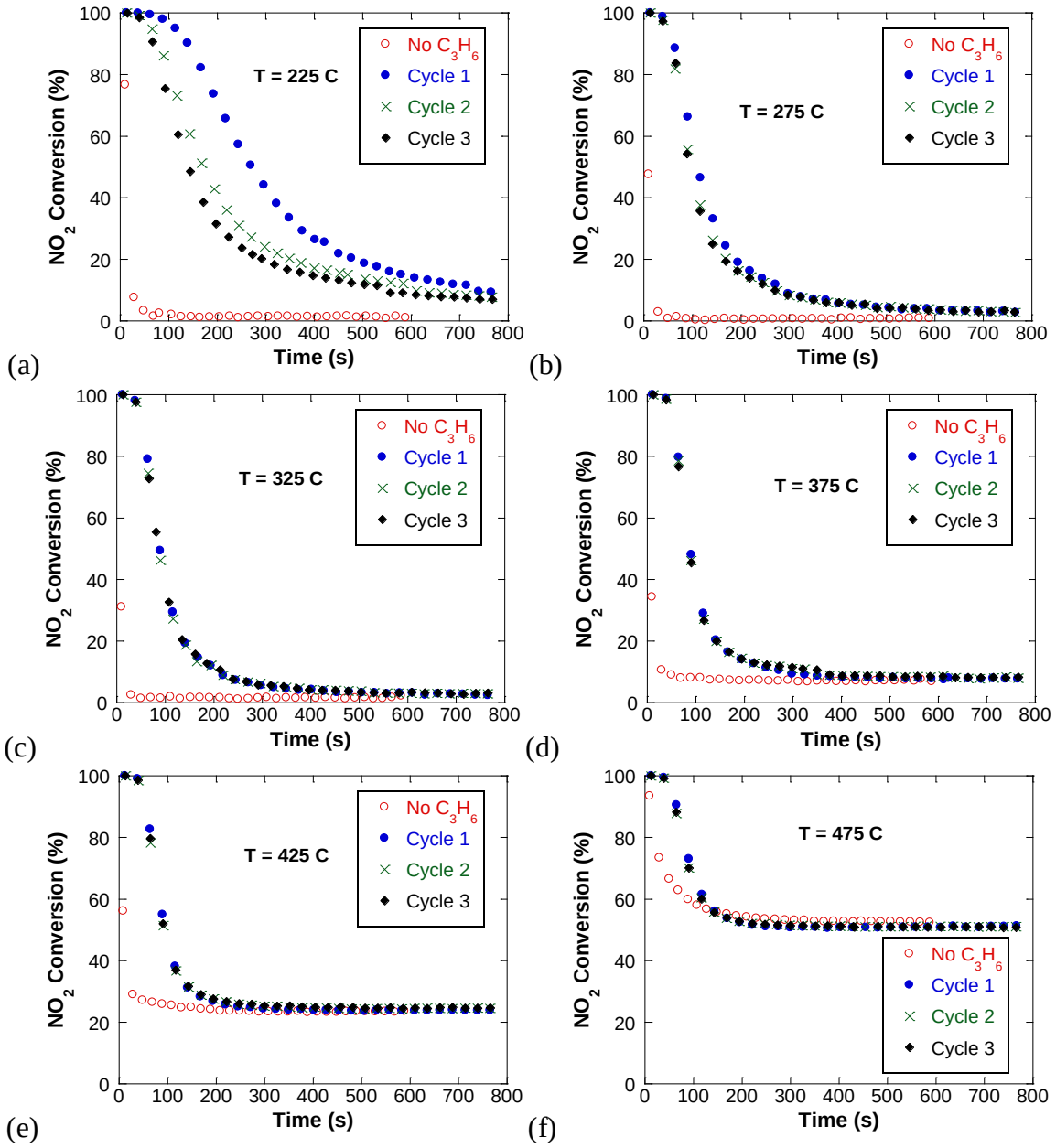

Figure 7.31 − C_3H_6 will store on the catalyst then oxidize with NO_2 to form NO at all temperatures. All experiments are performed while switching from a lean feed gas 6% H_2O, 6% CO_2, and 1000 ppm NO_2 for 780 seconds; and a rich feed gas of 6% H_2O, 6% CO_2, and 0.6% C_3H_6 for 120 seconds at constant temperature of (a) T=225°C, (b) T=275°C, (c) T=325°C, (d) T=375°C, (e) T=425°C, and (f) T=475°C.

When examining the experiment for each temperature in Figure 7.31 it can be seen that C_3H_6 will store on the catalyst and convert more NO_2 than by thermal decomposition alone. The amount of stored of C_3H_6 at each temperature can be found by integrating the NO_x and NO_2 conversion over each cycle of the three cycles, where the

C_3H_6 storage capacity can be related to the average total moles of NO_x converted assuming that NO and NO_2 storage on the catalyst is negligible as shown in Chapter 3.

To calculate the amount of stored C_3H_6 on the catalyst, it must be assumed that total stored mass is small in proportion to the total flow. Once this assumption is made the total molar flow rate ($\dot{N}$) across the catalyst for each time step as shown in equation (7.28) must be calculated first. The molar flow rate of each species ($\dot{N}_i$) can then be calculated by multiplying the total molar flow rate by the mole fraction of species (y_i) as seen in equation (7.29). By integrating (7.29) for a given species over an entire rich lean cycle in the feed gas total moles of species through the entire cycle (N_i) can be calculated as seen in equation (7.30). The integral NO_x conversion for each cycle is calculated using equation (7.31).

$$\dot{N} = \frac{P \cdot \dot{V}}{\bar{R} \cdot T} \tag{7.28}$$

$$\dot{N}_i = y_i \left(\frac{P \cdot \dot{V}}{\bar{R} \cdot T} \right) \tag{7.29}$$

$$N_i = \int_{Cycle} \dot{N}_i dt = \int_{Cycle} y_i \left(\frac{P \cdot \dot{V}}{\bar{R} \cdot T} \right) dt \tag{7.30}$$

$$\eta_{INT\_NO_x\_Conv} = \left[\frac{\left(N_{NO\_IN} + N_{NO_2\_IN} \right) - \left(N_{NO\_OUT} + N_{NO_2\_OUT} \right)}{\left(N_{NO\_IN} + N_{NO_2\_IN} \right)} \right] \cdot 100 \tag{7.31}$$

When performing the switching experiments for C_3H_6 storage, it was found that the average integral NO_x conversion for all three cycles at each temperature is less than 5% as seen in Figure 7.32. Error is calculated as the standard deviation of the integral NO_x conversion for the three cycles.

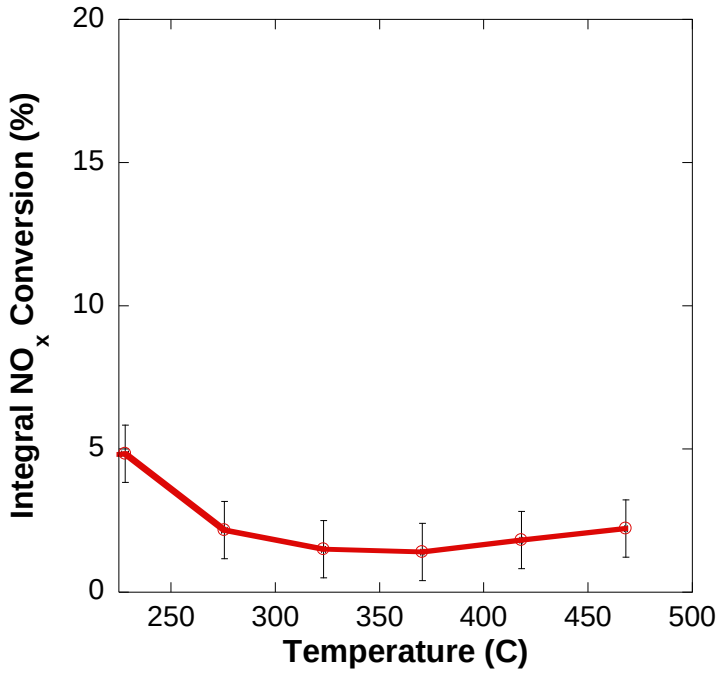

Figure 7.32 − Stored C_3H_6 has negligible conversion of NO on the catalyst.

Since integral NO_x conversion is small the integral NO_2 conversion is calculated using equation (7.32) for the thermal decomposition of NO_2 at the beginning of each temperature, and for the three rich lean cycles where additional NO_2 is converted due to stored C_3H_6. In Figure 7.33 a significant increase can be seen in NO_2 conversion for the rich lean cycling with C_3H_6. Due to the integral NO_x conversion being low, the results shown in Figure 7.33 further verify the results shown earlier that the preferential pathway for C_3H_6 is to react with NO_2 and form NO as shown in the reaction in equation (7.20).

$$\eta_{INT\_NO_x\_Conv} = \left[\frac{N_{NO_2\_IN} - N_{NO_2\_OUT}}{N_{NO_2\_IN}} \right] \cdot 100 \qquad (7.32)$$

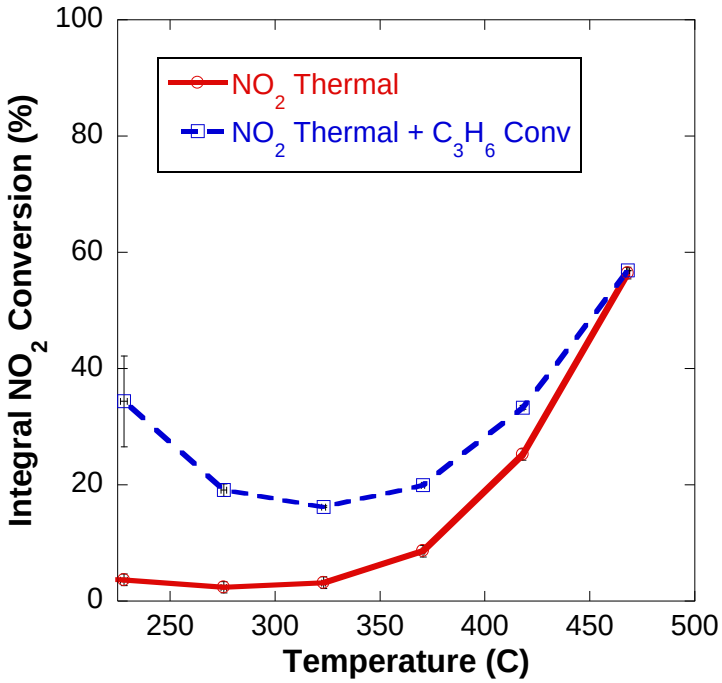

Figure 7.33 − Summarizes the increase over thermal decomposition of NO_2 to NO, when compared to the conversion of NO_2 to NO when C_3H_6 is stored on the catalyst.

To calculate the total storage capacity of C_3H_6 from the switching experiments in Figure 7.31, the integral moles of NO_2 converted by the C_3H_6 can be calculated for the thermal decomposition cycle and the three rich lean cycles using equation (7.33). The integral moles of NO_x converted can be calculated using equation (7.34). By combining equations (7.33) and (7.34) with the stoichiometric coefficients from the C_3H_6 NO_x conversion reactions listed in equations (7.20) and (7.21), equation (7.35) is formed to calculate the amount of stored moles of C_3H_6 on the catalyst which can then be combined with the molecular weight of C_3H_6 and the catalyst volume to calculate the mass of stored C_3H_6 per cubic meter of catalyst as seen in equation (7.36).

$$N_{NO_2\_Converted} = \left(N_{NO_2\_IN} - N_{NO_2\_OUT}\right) \tag{7.33}$$

$$N_{NO_x\_Converted} = \left(N_{NO_2\_IN} + N_{NO\_IN} - N_{NO_2\_OUT} + N_{NO\_OUT}\right) \tag{7.34}$$

$$N_{C_3H_6\_Stored} = 6 \cdot \left(N_{NO_2\_Converted,Cycle} - N_{NO_2\_Converted,Thermal}\right) + 9 \cdot N_{NO_x\_Converted,Cycle} \tag{7.35}$$

$$m_{C_3H_6\_Stored} = \frac{N_{C_3H_6\_Stored} \cdot MW_{C_3H_6}}{V_{Cat}} \tag{7.36}$$

The results for equation (7.36) are shown in Figure 7.34 where it can be seen that the storage capacity of C_3H_6 reduces with temperature. The error in storage capacity is calculated as the standard deviation of the three rich lean cycles from the experiments shown in Figure 7.31. It should be noted that Amin et al. [167] found that NO_x reduction with C_3H_6 on a HC-SCR catalyst is low above 350°C is due to minimal storage of C_3H_6, therefore it is possible that storage of C_3H_6 on the catalyst is in the form of organonitrates, however the effect of strongly reducing NO_2 to NO on the catalyst is still the dominant effect in inhibiting the SCR NO_x reduction process with NH_3.

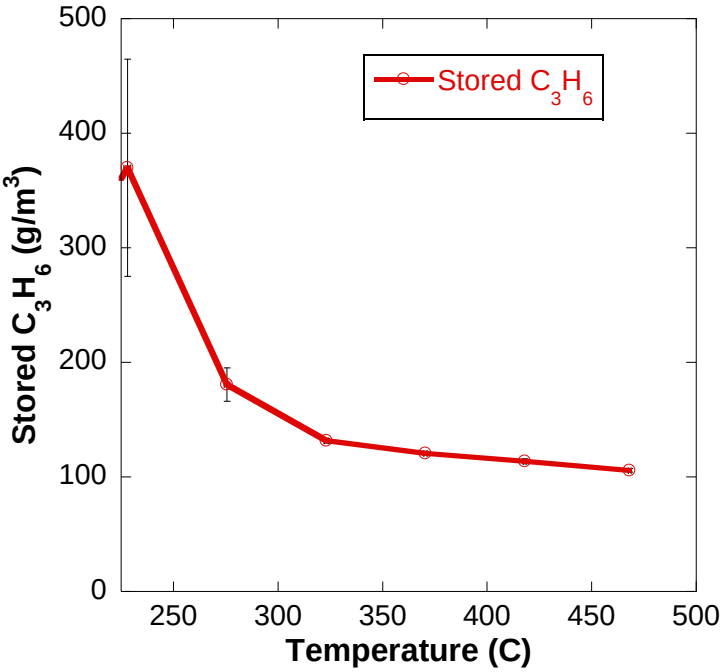

Figure 7.34 − Shows calculated values of C_3H_6 storage on the catalyst, calculated from the experiments shown in Figure 7.31.

7.8 Modeling Approach

Table 7.1 shows the current proposed kinetic mechanism as defined from the previous chapters.

Table 7.1 − Summary of chemical reaction and kinetic rates for lean SCR model with new dependence of the surface coverage fraction of NH_3 and H_2O competition with NH_3 for storage.

	Chemical Reaction	**Kinetics Rate Form**
(R1)	$NO+\frac{1}{2}O_2 \leftrightarrow NO_2$	$R_1 = k_1 \exp^{\left(\frac{-E_1}{\bar{R}T}\right)}\left(y_{NO}\sqrt{y_{O_2}} - \frac{y_{NO_2}}{K_{eq}}\right)$
(R2)	$Z + NH_3 \leftrightarrow Z(NH_3)$	$R_2 = k_{2f} y_{NH_3}\theta_Z - k_{2r}\exp^{\left(\frac{-E_{2r}}{\bar{R}T} - \lambda_{2r}\theta_{Z(NH_3)}\right)}\theta_{Z(NH_3)}$
(R3)	$4Z(NH_3)+3O_2 \rightarrow 4Z+2N_2+6H_2O$	$R_3 = k_3 \exp^{\left(\frac{-E_3}{\bar{R}T}\right)}\left(y_{O_2}\right)^{\gamma_3}\left(\frac{1-\exp^{\left(-\frac{\theta_{Z(NH_3)}}{\theta^*_{Z(NH_3),3}}\right)}}{1-\exp^{\left(-\frac{\theta_{Z(NH_3)}=1.0}{\theta^*_{Z(NH_3),3}}\right)}}\right)$
(R4)	$4Z(NH_3)+6NO \rightarrow 4Z+5N_2+6H_2O$	$R_4 = k_4 \exp^{\left(\frac{-E_4}{\bar{R}T}\right)} y_{NO}\theta_{Z(NH_3)}$
(R5)	$4Z(NH_3)+4NO+O_2 \rightarrow 4Z+4N_2+6H_2O$	$R_5 = k_5 \exp^{\left(\frac{-E_5}{\bar{R}T}\right)} y_{NO}y_{O_2}\left(\frac{1-\exp^{\left(-\frac{\theta_{Z(NH_3)}}{\theta^*_{Z(NH_3),5}}\right)}}{1-\exp^{\left(-\frac{\theta_{Z(NH_3)}=1.0}{\theta^*_{Z(NH_3),5}}\right)}}\right)$
(R6)	$2Z(NH_3)+NO+NO_2 \rightarrow 2Z+2N_2+3H_2O$	$R_6 = k_6 \exp^{\left(\frac{-E_6}{\bar{R}T}\right)} y_{NO}y_{NO_2}\left(\frac{1-\exp^{\left(-\frac{\theta_{Z(NH_3)}}{\theta^*_{Z(NH_3),5}}\right)}}{1-\exp^{\left(-\frac{\theta_{Z(NH_3)}=1.0}{\theta^*_{Z(NH_3),5}}\right)}}\right)$
(R7)	$8Z(NH_3)+6NO_2 \rightarrow 8Z+7N_2+12H_2O$	$R_7 = k_7 \exp^{\left(\frac{-E_7}{\bar{R}T}\right)} y_{NO_2}\left(\frac{1-\exp^{\left(-\frac{\theta_{Z(NH_3)}}{\theta^*_{Z(NH_3),7}}\right)}}{1-\exp^{\left(-\frac{\theta_{Z(NH_3)}=1.0}{\theta^*_{Z(NH_3),7}}\right)}}\right)$
(R8)	$2Z(NH_3)+2NO_2 \rightarrow 2Z+N_2+N_2O+3H_2O$	$R_8 = k_8 \exp^{\left(\frac{-E_8}{\bar{R}T}\right)} y_{NO_2}\left(\frac{1-\exp^{\left(-\frac{\theta_{Z(NH_3)}}{\theta^*_{Z(NH_3),8}}\right)}}{1-\exp^{\left(-\frac{\theta_{Z(NH_3)}=1.0}{\theta^*_{Z(NH_3),8}}\right)}}\right)$
(R9)	$2Z(NH_3)+3N_2O \rightarrow 2Z+4N_2+3H_2O$	$R_9 = k_9 \exp^{\left(\frac{-E_9}{\bar{R}T}\right)} y_{N_2O}\theta_{Z(NH_3)}$
(R10)	$Z+H_2O \leftrightarrow Z(H_2O)$	$R_{10} = k_{10f}\exp^{\left(\frac{-E_{10f}}{\bar{R}T}\right)} y_{H_2O}\theta_Z - k_{10r}\exp^{\left(\frac{-E_{10r}}{\bar{R}T}\right)}\theta_{Z(H_2O)}$

From experimental results in this chapter, the following reactions are proposed in Table 7.2 to account for the more dominant reactions. It should be noted that reactions with CO, H_2, or C_3H_6 and NO are ignored due to the low conversion of for each reaction. The oxidation of CO and H_2 are also ignored for the same reasons.

Table 7.2 − Summary of chemical reaction and kinetic rates for reactions determined from effects on NO, NO_2, O_2, and NH_3 from H_2, CO, and C_3H_6.

	Chemical Reaction	**Kinetics Rate Form**
(R11)	$Y + C_3H_6 \leftrightarrow Y(C_3H_6)$	$R_{11} = k_{11f} \exp^{\left(\frac{-E_{11f}}{\bar{R}T}\right)} y_{C_3H_6} \theta_Y - k_{11r} \exp^{\left(\frac{-E_{11r}}{\bar{R}T}\right)} \theta_{Y(C_3H_6)}$
(R12)	$Y(C_3H_6) + 6NO_2 \rightarrow Y + 3CO + 3H_2O + 9NO$	$R_{12} = k_{12} \exp^{\left(\frac{-E_{12}}{\bar{R}T}\right)} y_{NO_2} \theta_{Y(C_3H_6)}$
(R13)	$Y(C_3H_6) + 9NO_2 \rightarrow Y + 3CO_2 + 3H_2O + 9NO$	$R_{13} = k_{13} \exp^{\left(\frac{-E_{13}}{\bar{R}T}\right)} y_{NO_2} \theta_{Y(C_3H_6)}$
(R14)	$4Z(NH_3) + Y(C_3H_6) + 3O_2 \rightarrow 2Z + Y(C_3H_6) + N_2 + 6H_2O$	$R_{14} = k_{14} \exp^{\left(\frac{-E_{14}}{\bar{R}T}\right)} \left(y_{O_2}\right)^{\gamma_{14}} \theta_{Y(C_3H_6)} \theta_{Z(NH_3)}$
(R15)	$2Y(C_3H_6) + 6O_2 \rightarrow 2Y + 6CO + 6H_2O$	$R_{15} = k_{15} \exp^{\left(\frac{-E_{15}}{\bar{R}T}\right)} \left(y_{O_2}\right)^{\gamma_{15}} \theta_{Y(C_3H_6)}$
(R16)	$2Y(C_3H_6) + 9O_2 \rightarrow 2Y + 6CO_2 + 6H_2O$	$R_{16} = k_{16} \exp^{\left(\frac{-E_{16}}{\bar{R}T}\right)} \left(y_{O_2}\right)^{\gamma_{16}} \theta_{Y(C_3H_6)}$
(R17)	$H_2 + NO_2 \rightarrow H_2O + NO$	$R_{17} = k_{17} \exp^{\left(\frac{-E_{17}}{\bar{R}T}\right)} \left(y_{H_2}\right)\left(y_{NO_2}\right)$
(R18)	$CO + NO_2 \rightarrow CO_2 + NO$	$R_{18} = k_{18} \exp^{\left(\frac{-E_{18}}{\bar{R}T}\right)} \left(y_{CO}\right)\left(y_{NO_2}\right)$

Table 7.3 is a compilation of Table 7.1 and Table 7.2 to highlight the entire proposed kinetic mechanism. It should be noted that the dependence on the surface coverage fraction of NH_3 is defined in equation (7.37).

$$f\left(\theta_{Z(NH_3)}\right) = \left(\frac{1 - \exp^{\left(-\frac{\theta_{Z(NH_3)}}{\theta^*_{Z(NH_3),i}}\right)}}{1 - \exp^{\left(-\frac{\theta_{Z(NH_3)}=1.0}{\theta^*_{Z(NH_3),i}}\right)}} \right) \tag{7.37}$$

Table 7.3 − Summary of chemical reaction and kinetic rates for lean SCR model with new dependence of the surface coverage fraction of NH_3, H_2O competition with NH_3 for storage, and reactions determined from effects on NO, NO_2, O_2, and NH_3 from H_2, CO, and C_3H_6.

	Chemical Reaction	**Kinetics Rate Form**
(R1)	$NO+\frac{1}{2}O_2 \leftrightarrow NO_2$	$R_1 = k_1 \exp^{\left(\frac{-E_1}{\bar{R}T}\right)}\left(y_{NO}\sqrt{y_{O_2}} - \frac{y_{NO_2}}{K_{eq}}\right)$
(R2)	$Z + NH_3 \leftrightarrow Z(NH_3)$	$R_2 = k_{2f} y_{NH_3}\theta_Z - k_{2r} \exp^{\left(\frac{-E_{2r}}{\bar{R}T} - \lambda_{2r}\theta_{Z(NH_3)}\right)}\theta_{Z(NH_3)}$
(R3)	$4Z(NH_3)+3O_2 \rightarrow 4Z+2N_2+6H_2O$	$R_3 = k_3 \exp^{\left(\frac{-E_3}{\bar{R}T}\right)}\left(y_{O_2}\right)^{\gamma_3} f\left(\theta_{Z(NH_3)}\right)$
(R4)	$4Z(NH_3)+6NO \rightarrow 4Z+5N_2+6H_2O$	$R_4 = k_4 \exp^{\left(\frac{-E_4}{\bar{R}T}\right)} y_{NO}\theta_{Z(NH_3)}$
(R5)	$4Z(NH_3)+4NO+O_2 \rightarrow 4Z+4N_2+6H_2O$	$R_5 = k_5 \exp^{\left(\frac{-E_5}{\bar{R}T}\right)} y_{NO}y_{O_2} f\left(\theta_{Z(NH_3)}\right)$
(R6)	$2Z(NH_3)+NO+NO_2 \rightarrow 2Z+2N_2+3H_2O$	$R_6 = k_6 \exp^{\left(\frac{-E_6}{\bar{R}T}\right)} y_{NO}y_{NO_2} f\left(\theta_{Z(NH_3)}\right)$
(R7)	$8Z(NH_3)+6NO_2 \rightarrow 8Z+7N_2+12H_2O$	$R_7 = k_7 \exp^{\left(\frac{-E_7}{\bar{R}T}\right)} y_{NO_2} f\left(\theta_{Z(NH_3)}\right)$
(R8)	$2Z(NH_3)+2NO_2 \rightarrow 2Z+N_2+N_2O+3H_2O$	$R_8 = k_8 \exp^{\left(\frac{-E_8}{\bar{R}T}\right)} y_{NO_2} f\left(\theta_{Z(NH_3)}\right)$
(R9)	$2Z(NH_3)+3N_2O \rightarrow 2Z+4N_2+3H_2O$	$R_9 = k_9 \exp^{\left(\frac{-E_9}{\bar{R}T}\right)} y_{N_2O}\theta_{Z(NH_3)}$
(R10)	$Z + H_2O \leftrightarrow Z(H_2O)$	$R_{10} = k_{10f} \exp^{\left(\frac{-E_{10f}}{\bar{R}T}\right)} y_{H_2O}\theta_Z - k_{10r} \exp^{\left(\frac{-E_{10r}}{\bar{R}T}\right)}\theta_{Z(H_2O)}$
(R11)	$Y + C_3H_6 \leftrightarrow Y(C_3H_6)$	$R_{11} = k_{11f} \exp^{\left(\frac{-E_{11f}}{\bar{R}T}\right)} y_{C_3H_6}\theta_Y - k_{11r} \exp^{\left(\frac{-E_{11r}}{\bar{R}T}\right)}\theta_{Y(C_3H_6)}$
(R12)	$Y(C_3H_6)+6NO_2 \rightarrow Y+3CO+3H_2O+9NO$	$R_{12} = k_{12} \exp^{\left(\frac{-E_{12}}{\bar{R}T}\right)} y_{NO_2}\theta_{Y(C_3H_6)}$
(R13)	$Y(C_3H_6)+9NO_2 \rightarrow Y+3CO_2+3H_2O+9NO$	$R_{13} = k_{13} \exp^{\left(\frac{-E_{13}}{\bar{R}T}\right)} y_{NO_2}\theta_{Y(C_3H_6)}$
(R14)	$4Z(NH_3)+Y(C_3H_6)+3O_2 \rightarrow 2Z+Y(C_3H_6)+N_2+6H_2O$	$R_{14} = k_{14} \exp^{\left(\frac{-E_{14}}{\bar{R}T}\right)}\left(y_{O_2}\right)^{\gamma_{14}}\theta_{Y(C_3H_6)}\theta_{Z(NH_3)}$
(R15)	$2Y(C_3H_6)+6O_2 \rightarrow 2Y+6CO+6H_2O$	$R_{15} = k_{15} \exp^{\left(\frac{-E_{15}}{\bar{R}T}\right)}\left(y_{O_2}\right)^{\gamma_{15}}\theta_{Y(C_3H_6)}$
(R16)	$2Y(C_3H_6)+9O_2 \rightarrow 2Y+6CO_2+6H_2O$	$R_{16} = k_{16} \exp^{\left(\frac{-E_{16}}{\bar{R}T}\right)}\left(y_{O_2}\right)^{\gamma_{16}}\theta_{Y(C_3H_6)}$

(R17)	$H_2 + NO_2 \rightarrow H_2O + NO$	$R_{17} = k_{17} \exp^{\left(\frac{-E_{17}}{\bar{R}T}\right)} \left(y_{H_2}\right)\left(y_{NO_2}\right)$
(R18)	$CO + NO_2 \rightarrow CO_2 + NO$	$R_{18} = k_{18} \exp^{\left(\frac{-E_{18}}{\bar{R}T}\right)} \left(y_{CO}\right)\left(y_{NO_2}\right)$

7.9 Conclusions

It has been found from experimental results that the oxidation of H_2 and CO are negligible for the purpose of kinetic modeling. It is observed that there is no change in CO, H_2, CO_2, and H_2O concentrations due to water gas shift. It was observed that the conversion of NO with H_2 follows a pathway where NH_3 is formed which then reduces NO. It was observed that the conversion of NO with C_3H_6 reaches a maximum of 8%, which is higher than the conversion of NO with CO or H_2. However, due to the low overall conversion values the reactions between NO and C_3H_6, H_2, or CO can be considered negligible for the purpose of kinetic modeling. It was also observed that CO, H_2, and C_3H_6 will increase the conversion of NO_2 to NO over thermal decomposition. It was observed that C_3H_6 is the most reactive with NO_2, followed by H_2, then CO. It was observed that C_3H_6 will store on the catalyst during cycling experiments while H_2 and CO do not. It was observed that C_3H_6 does not compete with NH_3 for catalytic sites, since storage of C_3H_6 could not be determined from a TPD, a method to calculate the storage of C_3H_6 has been proposed. It was observed that C_3H_6 will increase the conversion of NH_3 due to oxidation, which is theorized as due to the increase in hydroxyl radicals created by the oxidation of C_3H_6. It was found that CO, H_2, and C_3H_6 effect NO_x conversions with NH_3 by changing the NO to NO_x ratio at the catalyst by utilizing their strong reactions with NO_2. This has proven beneficial when the NO_x composition is all NO_2, but CO, H_2, and C_3H_6 will inhibit NO_x conversion when NO_x composition favors NO. It was observed that only C_3H_6 will inhibit NO_x conversion in an equal molar NO_x composition due to the reactivity of the Fast SCR reaction. Lastly, proposed changes to the kinetic mechanism are made and shown to capture all of the effects from this chapter.

CHAPTER 8

CONCLUSIONS

When performing steady-state experiments it was determined that modifications to the literature SCR kinetic mechanisms are needed to account for oxygen dependence from saturation. A modification to the kinetic reaction rates involving oxygen has been proposed to account for the effect of oxygen saturation along with an experimental method to determine the oxygen saturation dependence for each oxygen dependant reaction. The oxygen saturation dependence on the standard SCR reaction (NO reduction with NH_3 in the presence of O_2) has been determined have a strong dependence on oxygen and temperature; therefore the proposed oxygen saturation kinetic rate form did not increase the accuracy of the model.

Additional steady-state experiments have yielded modifications to the NO_2 reduction with NH_3 reaction pathways. It has been determined that the current two reactions (Slow SCR reaction and N_2O Production reaction) are important along with a prominent third reaction of N_2O reduction with NH_3 needs to be added to the kinetic mechanism.

From validation data it was determined that the proposed steady-state lean SCR kinetic mechanisms from literature did not accurately predict catalyst behavior under rich lean cycling conditions. It has been determined that the kinetic rate forms from literature are inadequate due to their linear dependence on the surface coverage fraction of NH_3

which will not capture the non-linear relationship between NO_x conversion and the amount of stored NH_3 on the catalyst. A modification to the kinetic rate forms for the prominent reactions involving stored NH_3 has been proposed to account for the reservoir effect of stored NH_3 on the SCR catalyst.

Due to the switch from lean to rich exhaust from the regeneration of the LNT, the effects of varying H_2O and CO_2 concentrations have been studied for the proposed lean SCR reactions. It was found that H_2O strongly affects the storage capacity of NH_3 on the SCR catalyst. The oxidation of NH_3 was also determined to be effected by H_2O concentration; however it has been concluded that this is due to the reduction in the amount of stored NH_3 on the catalyst. It was found that H_2O concentration does not affect the other proposed reactions due to their high reaction rates. From these results an additional reaction has been proposed to capture the effect of H_2O on NH_3 storage.

The affects of H_2, CO, and C_3H_6 were studied to understand their roles in rich exhaust conditions. Experimental results have allowed the water gas shift reaction, the oxidations of H_2 and CO, and reactions between NO and H_2, CO, or C_3H_6 to be disregarded. It was also determined that H_2, CO, and C_3H_6 have no effect on NH_3 storage capacity of the catalyst. However, it was observed that H_2, CO, and C_3H_6 have strong reactions with NO_2 yielding NO. It has been proposed to include a reaction for each reductant with NO_2 in the kinetic mechanism. It was determined that H_2, CO, and C_3H_6 reactions with NO_2 can inhibit NO_x conversion on the SCR catalyst by affecting the NO to NO_x ratio at the catalyst. Since NO_x reduction with NH_3 favors an equal molar ratio of NO and NO_2, it was observed in a feed gas with an all NO_2 NO_x composition that H_2, CO, and C_3H_6 will increase NO_x conversion due their reactions with NO_2 to form NO. It is proposed that all of the effects of CO, H_2, and C_3H_6 on NO_x reduction with NH_3 can be accounted for by adding NO_2 reactions with CO, H_2, and C_3H_6. It was also observed that the oxidation of C_3H_6 will strongly increase the oxidation of NH_3. Since reaction intermediates could not be determined, a global reaction is proposed to account for the

increase in NH_3 oxidation in the presence of C_3H_6. From cycling experiments it was found that CO and H_2 storage on the catalyst is negligible while C_3H_6 has been found to store on the catalyst. Since C_3H_6 could not be determined with a TPD experiment a non-traditional method to determine the storage of C_3H_6 has been used. From these results it was found that C_3H_6 stores on the catalyst but not on the same catalytic sites as NH_3, therefore a new catalytic storage site is used to account for all reaction involving C_3H_6.

The above conclusions are made based on experimental and simulation results shown in this document. The pertinent chemical reactions and suggested kinetic rates from this document are shown in Table 8.1. It should be noted that the reactions shown in (R1) – (R8) are commonly used in kinetic mechanisms for NH_3 SCR catalysts for steady-state operation, while reaction (R9) – (R18) are added to account for observed experimental effects. Additionally the kinetic rate forms for reaction dependant on stored NH_3 as shown in (R3), (R5), (R6), (R7), and (R8) have been changed to account for the determined non-linear effects of stored NH_3 on NO_x conversion

Table 8.1 − Summary of chemical reaction and kinetic rates for lean SCR model with new dependence of the surface coverage fraction of NH_3, H_2O competition with NH_3 for storage, and reactions determined from effects on NO, NO_2, O_2, and NH_3 from H_2, CO, and C_3H_6.

	Chemical Reaction	**Kinetics Rate Form**
(R1)	$NO+\frac{1}{2}O_2 \leftrightarrow NO_2$	$R_1 = k_1 \exp^{\left(\frac{-E_1}{\bar{R}T}\right)}\left(y_{NO}\sqrt{y_{O_2}} - \frac{y_{NO_2}}{K_{eq}}\right)$
(R2)	$Z + NH_3 \leftrightarrow Z(NH_3)$	$R_2 = k_{2f} y_{NH_3}\theta_Z - k_{2r}\exp^{\left(\frac{-E_{2r}}{\bar{R}T} - \lambda_{2r}\theta_{Z(NH_3)}\right)}\theta_{Z(NH_3)}$
(R3)	$4Z(NH_3)+3O_2 \rightarrow 4Z+2N_2+6H_2O$	$R_3 = k_3 \exp^{\left(\frac{-E_3}{\bar{R}T}\right)}\left(y_{O_2}\right)^{\gamma_3} f\left(\theta_{Z(NH_3)}\right)$
(R4)	$4Z(NH_3)+6NO \rightarrow 4Z+5N_2+6H_2O$	$R_4 = k_4 \exp^{\left(\frac{-E_4}{\bar{R}T}\right)} y_{NO}\theta_{Z(NH_3)}$
(R5)	$4Z(NH_3)+4NO+O_2 \rightarrow 4Z+4N_2+6H_2O$	$R_5 = k_5 \exp^{\left(\frac{-E_5}{\bar{R}T}\right)} y_{NO}y_{O_2} f\left(\theta_{Z(NH_3)}\right)$
(R6)	$2Z(NH_3)+NO+NO_2 \rightarrow 2Z+2N_2+3H_2O$	$R_6 = k_6 \exp^{\left(\frac{-E_6}{\bar{R}T}\right)} y_{NO}y_{NO_2} f\left(\theta_{Z(NH_3)}\right)$

(R7)	$8Z\left(NH_3\right)+6NO_2 \rightarrow 8Z+7N_2+12H_2O$	$R_7 = k_7 \exp^{\left(\frac{-E_7}{\bar{R}T}\right)} y_{NO_2} f\left(\theta_{Z(NH_3)}\right)$
(R8)	$2Z\left(NH_3\right)+2NO_2 \rightarrow 2Z+N_2+N_2O+3H_2O$	$R_8 = k_8 \exp^{\left(\frac{-E_8}{\bar{R}T}\right)} y_{NO_2} f\left(\theta_{Z(NH_3)}\right)$
(R9)	$2Z\left(NH_3\right)+3N_2O \rightarrow 2Z+4N_2+3H_2O$	$R_9 = k_9 \exp^{\left(\frac{-E_9}{\bar{R}T}\right)} y_{N_2O} \theta_{Z(NH_3)}$
(R10)	$Z+H_2O \leftrightarrow Z\left(H_2O\right)$	$R_{10} = k_{10f} \exp^{\left(\frac{-E_{10f}}{\bar{R}T}\right)} y_{H_2O} \theta_Z - k_{10r} \exp^{\left(\frac{-E_{10r}}{\bar{R}T}\right)} \theta_{Z(H_2O)}$
(R11)	$Y+C_3H_6 \leftrightarrow Y\left(C_3H_6\right)$	$R_{11} = k_{11f} \exp^{\left(\frac{-E_{11f}}{\bar{R}T}\right)} y_{C_3H_6} \theta_Y - k_{11r} \exp^{\left(\frac{-E_{11r}}{\bar{R}T}\right)} \theta_{Y(C_3H_6)}$
(R12)	$Y\left(C_3H_6\right)+6NO_2 \rightarrow Y+3CO+3H_2O+9NO$	$R_{12} = k_{12} \exp^{\left(\frac{-E_{12}}{\bar{R}T}\right)} y_{NO_2} \theta_{Y(C_3H_6)}$
(R13)	$Y\left(C_3H_6\right)+9NO_2 \rightarrow Y+3CO_2+3H_2O+9NO$	$R_{13} = k_{13} \exp^{\left(\frac{-E_{13}}{\bar{R}T}\right)} y_{NO_2} \theta_{Y(C_3H_6)}$
(R14)	$4Z\left(NH_3\right)+Y\left(C_3H_6\right)+3O_2 \rightarrow 2Z+Y\left(C_3H_6\right)+N_2+6H_2O$	$R_{14} = k_{14} \exp^{\left(\frac{-E_{14}}{\bar{R}T}\right)} \left(y_{O_2}\right)^{\gamma_{14}} \theta_{Y(C_3H_6)} \theta_{Z(NH_3)}$
(R15)	$2Y\left(C_3H_6\right)+6O_2 \rightarrow 2Y+6CO+6H_2O$	$R_{15} = k_{15} \exp^{\left(\frac{-E_{15}}{\bar{R}T}\right)} \left(y_{O_2}\right)^{\gamma_{15}} \theta_{Y(C_3H_6)}$
(R16)	$2Y\left(C_3H_6\right)+9O_2 \rightarrow 2Y+6CO_2+6H_2O$	$R_{16} = k_{16} \exp^{\left(\frac{-E_{16}}{\bar{R}T}\right)} \left(y_{O_2}\right)^{\gamma_{16}} \theta_{Y(C_3H_6)}$
(R17)	$H_2+NO_2 \rightarrow H_2O+NO$	$R_{17} = k_{17} \exp^{\left(\frac{-E_{17}}{\bar{R}T}\right)} \left(y_{H_2}\right)\left(y_{NO_2}\right)$
(R18)	$CO+NO_2 \rightarrow CO_2+NO$	$R_{18} = k_{18} \exp^{\left(\frac{-E_{18}}{\bar{R}T}\right)} \left(y_{CO}\right)\left(y_{NO_2}\right)$

Where: $f\left(\theta_{Z(NH_3)}\right) = \left(\frac{1-\exp^{\left(-\frac{\theta_{Z(NH_3)}}{\theta^*_{Z(NH_3),i}}\right)}}{1-\exp^{\left(-\frac{\theta_{Z(NH_3)}=1.0}{\theta^*_{Z(NH_3),i}}\right)}} \right)$

8.1 NO Oxidation Summary

It has been determined that the oxidation of NO to NO_2 is a reversible reaction with NO_2 experiencing thermal decomposition due to equilibrium at temperatures above 300°C. It was also determined that the oxidation of NO to NO_2 is dependent on O_2

concentration by a half order effect. Additionally, it was determined that O_2 concentration has negligible effects on NO_2 thermal decomposition to NO and O_2. It was observed that a feed gas that includes H_2O and CO_2 will inhibit the oxidation of NO to NO_2 as well as the thermal decomposition of NO_2 to NO and O_2. However, this effect is negligible in the expected concentration range of the EAS. It was confirmed that NO_2 adsorption is small with any adsorbed NO_2 thermally decomposing to NO making NO_2 adsorption negligible for kinetic modeling of the NO oxidation reaction. Since it was found that H_2O, NO, NO_2 and O_2 do not inhibit the oxidation of NO to NO_2 in the forward or reverse directions the kinetic rate shown for (R1) was determined to be sufficient.

8.2 Oxidation of H_2, CO, and C_3H_6, and WGS

It has been found from experimental results that the oxidation of H_2 and CO are negligible for the purpose of kinetic modeling. It was determined that up to 40% of C_3H_6 can be converted due to oxidation. It was observed during these experiments that the oxidation of C_3H_6 occurs through two pathways. The first is the formation of complete combustion products CO_2 and H_2O (R16), while the second leads to the formation of CO and H_2O (R15). It was determined that since at low concentrations large amounts of CO are still formed therefore the CO pathway (R15) is the more dominant pathway. It was also observed that there is no change in CO, H_2, CO_2, and H_2O concentrations due to water gas shift.

8.3 Effect of H_2, CO and C_3H_6 on NO and NO_2

It was observed that the conversion of NO with H_2 follows a pathway where NH_3 is formed which then reduces NO. However, it was observed that the conversion of NO with C_3H_6 reaches a maximum of 8%, which is higher than the conversion of NO with CO or H_2. Due to the low overall conversion values the reactions between NO and C_3H_6,

H_2, or CO can be considered negligible for the purpose of kinetic modeling. It was also observed that CO, H_2, and C_3H_6 will increase the conversion of NO_2 to NO over thermal decomposition. It was observed that C_3H_6 is the most reactive with NO_2, followed by H_2, then CO which are added to kinetic mechanism as shown in (R12), (R13), (R17), and (R18). It was also observed that C_3H_6 will store on the catalyst during cycling experiments while H_2 and CO do not. An experimental method to determine the storage capacity of C_3H_6 has been determined.

8.4 NH_3 Storage Summary

It has been determined that a single site global approximation can be used to model the storage of NH_3 (R2) due to the presence of a single desorption peak in TPD experiments with NH_3. It was also determined that using a kinetic rate based on a Tempkin isotherm increased accuracy for the ammonia storage reaction. It was determined experimentally that as exhaust gas becomes rich and H_2O and CO_2 concentrations increase, the storage capacity of NH_3 on the SCR catalyst decreases. This is important for LNT-SCR combination systems where the exhaust stream concentrations can vary from 6% H_2O/CO_2 to 12% H_2O/CO_2. The decrease in storage capacity of NH_3 is larger between 0 – 6% H_2O/CO_2 than between 6 – 10% H_2O/CO_2, which means that if engine conditions were held fairly constant, such as during lean engine operation with only an SCR system, the H_2O competition (R10) effect does not need to be included in a global model and only temperature effects need to be considered in the model. In cases where the exhaust stream varies from lean to rich, such as an LNT-SCR system, using an H_2O competition (R10) model increases the accuracy of stored NH_3 under the constantly varying exhaust conditions. It was also determined that H_2, CO, and C_3H_6 do not affect the NH_3 storage capacity of the catalyst. Therefore, it can be concluded that C_3H_6 will store on a different catalytic site then NH_3 (R11).

8.5 NH_3 Oxidation Summary

It was determined experimentally that only negligible amounts of NO and N_2O formed when oxidizing NH_3 on the SCR catalyst. It is therefore only important to model the stoichiometric reaction for ammonia oxidation to complete combustion products as shown in (R3). Experimentally it can be seen that increasing O_2 concentration will increase ammonia conversion during ammonia oxidation, although it is not a linear effect between 0.5% and 6% O_2. It was found that to account for ammonia oxidation in a kinetic model where O_2 concentration can drastically vary, such as in the EAS, that a saturation kinetic reaction rate need to be used to increase the accuracy of the model as shown in (R3). It was observed that varying H_2O concentration will decrease the conversion of NH_3 due to oxidation. It was observed that this inhibition from H_2O can be accounted for using the NH_3 H_2O competition reaction (R10). It was observed that C_3H_6 will increase the conversion of NH_3 due to oxidation, which is theorized as due to the increase in hydroxyl radicals created by the oxidation of C_3H_6, which is accounted for as a global reaction shown in (R14). It was also observed that H_2 and CO had negligible effects on the oxidation of NH_3.

8.6 NO_x Reduction with NH_3 Summary

It can be concluded that the NO to NO_x ratio is an important determining characteristic of the feed gas when predicting NO_x conversion with NH_3 with max conversion of NO_x occurring when the feed gas contains equal amounts of NO and NO_2. It can also be determined that NO_x reduction with NH_3 occurs due to five simultaneous global reactions shown in (R4), (R5), (R6), (R7), and (R8). Due the ability for NO_x conversion with NH_3 during cycling experiments; where NH_3 is present in the rich pulse while NO_x is present in the lean pulse, the simultaneous NO_x conversion with NH_3

reactions are written as reactions that take place with NH_3 stored on the surface of the catalyst as shown in (R4) – (R8).

Experimental results with varying oxygen concentration have shown that only NO reduction with NH_3 is dependent on oxygen concentration. It has been determined that the reduction of NO with NH_3 when oxygen is not present is small but can be accounted for using standard kinetic rate expressions as seen in (R4). It can be seen that when oxygen is present NO conversion with NH_3 is strongly dependent on temperature. A method to determine the oxygen dependence for this reaction was used which yielded results that show that the oxygen dependence is also a function of temperature. It is proposed that this is due to the effect of simultaneous nature of the NO Oxidation (R1), NH_3 Oxidation (R3), Fast SCR (R6), and Slow SCR reactions (R7) on the catalyst.

The Fast SCR reaction as shown in (R6) can be modeled as a global reaction with a standard Arrhenius kinetic rate for the 200°C – 450°C temperature range. The Slow SCR reaction as shown in (R7) was determined to be to have the largest hysteresis effect at low temperatures; primarily due to the formation of ammonium nitrate at low temperatures on the catalyst surface. The global Slow SCR reaction with a standard Arrhenius rate simulation was shown to be statistically significant and is therefore considered adequate when predicting NH_3 and NO_x conversion for the entire temperature range tested.

It has been determined that significant amounts of N_2O are produced simultaneously during the reduction of NO_x with NH_3 when the NO to NO_x ratio favors NO_2. It has been determined that up to 80% of NO_2 can be converted to N_2O when reacting with NH_3 (R8). It was determined that NH_3 can be used to in the reduction of N_2O, but the reaction does not start until the catalyst temperature is above 350°C (R9). It was determined that NO_2 formation to N_2O is not the critical pathway the Fast SCR reaction (R6) because NO does not increase the conversion of N_2O with NH_3 below 350°C. It was determined that the Slow SCR reaction (R7) is important by combining

the NO_2 conversion to NO, N_2O conversion with NH_3, and the NO_2 conversion due to thermal decomposition, a to formulate a NO_x conversion estimate.

It was determined from validation experiments that the NO_x conversion is highly dependent on the amount of NH_3 stored on the catalyst. This is confirmed by an experiment where the ideal rich lean cycling conditions are lengthened to saturate the catalyst with NH_3 and measure the NO_x conversion as all NH_3 is removed from the catalyst. From the long cycling experiments the amount of NH_3 stored on the catalyst can be determined as a non-dimensional term called the NH_3 surface coverage fraction. Instantaneous NO_x conversion for each cycle can be plotted against the NH_3 surface coverage fraction, which can then be collapsed to find the trendline signifying the dependence on stored NH_3 for a constant temperature of a given NO to NO_x ratio. The trendlines created were then used to formulate a new approximation to be implemented in the kinetic rates of the NH_3 oxidation reaction (R3) , the Standard SCR reaction (R5), the Fast SCR reaction (R6), the Slow SCR reaction (R7), and the N_2O Production reaction (R8) in the SCR kinetic mechanism shown in Table 8.1. It is suggested not to change the kinetic rate of the Rich Standard SCR reaction (R4) due to the low activity of the reaction. It also suggested to use the standard Arrhenius kinetic rate for the N_2O Reduction with NH_3 reaction (R9) until initial modeling results are analyzed.

It was observed that under steady state conditions that NO_x conversion is unaffected by changes in H_2O and CO_2 levels. Therefore there is no inhibition due to H_2O or CO_2 for the NO_x conversion reactions. It can therefore be concluded that each NO_x conversion reaction occurs much quicker than the NH_3 oxidation reaction, since increasing H_2O concentration did not decrease the NO_x conversion for all NO to NO_x ratios.

It was found that CO, H_2, and C_3H_6 effect NO_x conversions with NH_3 by changing the NO to NO_x ratio at the catalyst by utilizing their strong reactions with NO_2 (R12), (R13), (R17), (R18). This is corroborated when experimental results have shown

increases NO_x reduction when the NO_x composition is all NO_2, by converting the NO_2 to equal amounts of NO and NO_2 at the catalyst where NH_3 is present. This is further shown when CO, H_2, and C_3H_6 will inhibit NO_x conversion when an equal molar NO_x composition is present and an all NO NO_x composition is present by inhibiting the Fast SCR reaction (R6) from taking place.

REFERENCES

1. Peters, L.D. (2004) *U.S. passenger car market should open up to more Turbodiesel cars* Yale Daily News
2. Majewski, W.A. *SCR Systems for Mobile Engines*. DieselNet Technology Guide 2005 [cited 2005 2/9/2006].
3. Majewski, W.A. *Selective Catalytic Reduction*. Diesel Catalysts 2005 [cited 2005.
4. Heywood, J., *Internal Combustion Engine Fundamentals*. 1988, New York: McGraw-Hill Inc.
5. Ball, D., Nunan, N., Blosser, B., Wilson, J., Mitchell, G., Davis, S., and Zammit, M., *FlexMetal Catalyst Technologies.* SAE Paper 2005-01-1111, 2005.
6. Omoto, H., Kobayashi, T., Ishikawa, K., and Yamada, T., *Catalyst Design for Meeting Stringent LEV-2 NOx Regulation.* SAE Paper 2002-01-0348, 2002.
7. Pulkrabek, W., *Engineering Fundamentals of the Internal Combustion Engine*. 1997, New Jersey: Prentice-Hall Inc.
8. Stone, R., *Introduction to Internal Combustin Engines*. Third ed. 1999, Warrendale: Society of Automotive Engineers Inc.
9. Ayala, A., Gebel, M.E., Okamoto, R.A., Reiger, P.L., Kado, N.Y., Cotter, C., and Verma, N., *Oxidation Catalysts Effect on CNG Transit Bus Emissions.* SAE Paper 2003-01-1900, 2003.
10. Maklno, M., Kondo, T., Kunz, A., Ohara, E., Schuetze, F., Hoffmann, M., Groeger, M., Jean, E., Ottaviani, E., Guertler, W., Paule, M., Keppeler,B., and D. Scharr, *Evaluation of Advanced Diesel Oxidation Catalyst Concepts: Part 2.* SAE Paper 2006-01-0032, 2006.
11. Fayard, J.-C. and Sequelong, T., *A New DPF System for Duty Cycle Vehicles.* SAE Paper 2004-01-1937, 2004.
12. Fayard, J.-C., Sequelong, T., and Joubert, E., *A New Active DPF System for "Stop & Go" Duty Cycle Vehicles: Durability and Improvements.* SAE Paper 2005-01-1754, 2005, 2005.
13. Tatur, M., Tomazic, D., Thornton, M., Orban, J., and Slone, E., *Tier 2 Useful Life (120,000 miles) Exhaust Emission Results for a NOx Adsorber and Diesel Particle Filter Equipped LIght-Duty Diesel Vehicle.* SAE Paper 2006-01-0424, 2006.
14. Colliou, T., Lavy, J., Martin, B., Chandes, K., Pichon, G., and Pierron, L., *Coupling of a NOx trap and a cDPF for emissions reduction of a 6-cylinder HD engine.* SAE Paper 2004-01-1945, 2004. **1**.
15. Schmieg, S. and Lee, J., *Evaluation of Supplier Catalysts Formulations for the Selective Catalytic Reduction of NOx with Ammonia.* SAE Paper 2005-01-3881, 2005.

16. Wolf, P., *AdBlue as a Reducing Agen for the Decrease of NOx Emissions from Diesel Engines of Commercial Vehicles*. 2003, DGMK: Hamburg.
17. Fang, H.L. and DaCosta, H.F.M., *Urea thermolysis and NOx reduction with and without SCR catalysts.* Applied Catalysis: B Environmental, 2003. **46**(1): p. 17-34.
18. Gabrielsson, P.L.T., *Urea-SCR in automotive applications.* Topics in Catalysis, 2004. **28**(1): p. 177-184.
19. Chimner, C., *Transient On-Road Emission Reduction of an LNT + SCR Aftertreatment System.* SAE Paper 2008-01-2641, 2008. **1**.
20. Dykes, E., *NOx Performance of an LNT+SCR System Designed to Meet EPA 2010 Emissions: REsults of Engine Dynamometer Emission Tests.* SAE Paper 2008-01-2642, 2008. **1**.
21. Cohn, J., Steele, D., and Anderson, H., *Method of Selectively Removing Oxides of Nitrogen from Oxygen-Containing Gases*. 1961: United States.
22. Lyon, R.K. and Hardy, J.E., *Discovery and Deveolopment of the Thermal DeNOx Process.* Ind. Eng. Chem. Fundam., 1986. **25**(1): p. 19-24.
23. Bowman, C.T., *Mechanisms and Modeling of Gas-Phase Aftertreatment Methods for NO Removal from Combustion Products*, in *Physical and Chemical Aspects of Combustion*, F.L. Dryer and R.F. Sawyer, Editors. 1997, Gordon and Breach Science Publishers: United Kingdom. p. 29-68.
24. Brouwer, J., Heap, M.P., Pershing, D.W., and Smith, P.J. *A Model for Prediction of Selective Non-Catalytic Reduction of Nitrogen Oxides by Ammonia, Urea, and Cyanuric Acid with Mixing Limitations in the Presence of CO*. **Volume**,
25. Glarborg, P., Kristensen, P.G., Jensen, S.H., and Dam-Johansen, K., *A Flow Reactor Study of HNCO Oxidation Chemistry*. Combustion and Flame, 1994. **98**: p. 241-258.
26. Lyon, R.K., *Method for the Reduction of the Concentration of NO in Combustion Effluents Using Ammonia*. 1973, Exxon Research and Engineering Company: United States.
27. Miller, J.A., Branch, M.C., and Kee, R.J., *A Chemical Kinetic Model for the Selective Reduction of Nitric Oxide by Ammonia.* Combustion and Flame, 1981. **43**: p. 81-98.
28. Østberg, M. and Dam-Johansen, K., *Empirical Modeling of the Selective Non-Catalytic Reduction of NO: Comparison with Large-Scale Experiments and Detailed Kinetic Modeling.* Chemical Engineering Science, 1994. **49**(12): p. 1897-1904.
29. Byrne, J.W., Chen, M., and Speronello, B.K., *Selective Catalytic Reduction of NOx using Zeolitic Catalysts for High Temperature Applications.* Catalysis Today, 1992. **13**: p. 33-42.
30. Busca, G., Lietti, L., Ramis, G., and Berti, F., *Chemical and mechanistic aspects of the selective catalytic reduction of NOx by ammonia over oxide catalysts.* Applied Catalysis: B Environmental, 1998. **18**: p. 1-36.
31. Koebel, M., Elsener, M., and Kleemann, M., *Urea-SCR: a promising technique to reduce NOx emissions from automotive diesel engines.* Catalysis Today, 2000. **59**(1): p. 335-345.

32. Andersen, H., *Method of Purifying Gases Containing Oxygen and Oxides of Nitrogen*, U.S.P. Office, Editor. 1962.
33. Andersen, H., Cohn, J., and Glogau, R.C., *Selective Removal of Nitrogen Oxides from Gas Streams*, U.S.P. Office, Editor. 1962.
34. Andersen, H., Green, W.J., and Steele, D.R., *Catalytic Treatment of Nitric Acid Plant Tail Gas.* Industrial and Engineering Chemistry, 1961. **53**(3): p. 199-204.
35. Andersen, H. and Keith, C.D., *Method of Purifying Gases Containing Oxygen and Oxides of Nitrogen*, U.S.P. Office, Editor. 1961.
36. Griffing, M.E., Lamb, F.W., and Stephens, R.E., *Method of Controlling Exhaust Emission*, U.S.P. Office, Editor. 1969.
37. Keith, C.D. and Kenah, P.M., *Process for Catalytically Purifying Gases Containing Oxides of Nitrogen*, U.S.P. Office, Editor. 1967.
38. Markvart, M. and Pour, V., *The influence of oxygen on the catalytic reduction of nitric oxide by ammonia.* Journal of Catalysis, 1967. **7**(3): p. 279-281.
39. Nonnenmacher, H. and Kartte, K., *Selective Removal of Oxides of Nitrogen From Gas Mixtures Containing Oxygen*, U.S.P. Office, Editor. 1966.
40. Otto, K., Shelef, M., and Kummer, J.T., *Studies of Surface Reactions of Nitric Oxide by Nitrogen-15 Isotope Labeling. I. The Reaction between Nitric Oxide and Ammonia over Supported Platinum at 200-250°*. The Journal of Physical Chemistry, 1970. **74**(13): p. 2690.
41. Delahay, G. and Coq, B., *Pollution Abatement using Zeolites: State of the Art and Further Needs*, in *Zeolites for Cleaner Technologies*, M. Guisnet and J.-P. Gilson, Editors. 199?, Imperial College Press.
42. Centi, G. and Perathoner, S., *Nature of active species in copper-based catalysts and their chemistry of transformation of nitrogen oxides.* Applied Catalysis A: General, 1995. **132**: p. 179-259.
43. Rahkamaa-Tolonen, K., Maunula, T., Lomma, M., Huuhtanen, M., and Keiski, R.L., *The effect of NO2 on the activity of fresh and aged zeolite catalysts in the NH3-SCR reaction.* Catalysis Today, 2005. **100**: p. 217-222.
44. Nova, I., Ciardelli, C., Tronconi, E., Chatterjee, D., and Brandl-Konrad, B., *NH3-NO/NO2 Chemistry over V-based catalysts and its role in the mechanism of the Fast SCR reaction.* Catalysis Today, 2006. **114**: p. 3-12.
45. Olsson, L., Sjövall, H., and Blint, R.J., *A kinetic model for ammonia selective catalytic reduction over Cu-ZSM-5.* Applied Catalysis B: Environmental, 2007. **81**: p. 203-217.
46. Sjovall, H., Blint, R., and Olsson, L., *Detailed Kinetic Modeling of NH3 and H2O Adsorption, and NH3 Oxidation over Cu-ZSM-5.* Journal of Physical Chemistry C, 2009. **113**: p. 1393-1405.
47. Kim, J., Cavataio, G., Patterson, J., Laing, P., and Lambert, C., *Laboratory Studies and Mathematical Modeling of Urea SCR Catalyst Performance.* SAE Paper 2007-01-1573, 2007. **1**.
48. Wurzenberger, J.C. and Wanker, R., *Multi-Scale SCR Modeling, 1D Kinetic Analysis and 3D System Simulation.* SAE Paper 2008-01-1540, 2005. **01**.
49. Nova, I., Lietti, L., Tronconi, E., and Frozatti, P., *Transient response method applied to the kinetic analysis of DeNOx-SCR reation.* Chemical Engineering Science, 2001. **56**: p. 1229-1237.

50. Koci, P., Marek, M., Kubicek, M., Maunula, T., and Harkonen, M., *Modelling of catalytic monolith converters with low-and high-temperature NOx storage compounds and differentiated washcoat.* Chemical Engineering Journal, 2004. **97**: p. 131-139.
51. Marangozis, J., *Comparison and Analysis of Intrinsic Kinetics and Effectivenss Factors for the Catalytic Reduction of NO with Ammonia in the Pressence of Oxygen.* Ind. Eng. Chem. Res., 1992. **31**: p. 987-994.
52. Kandylas, I.P., Koltaskis, G.C., and Stamatelos, A.M., *Mathematical modelling of precious metals catalytic converters for diesel NOx reduction.* Proc. Instn. Mech. Engrs., 1999. **213**: p. 279-292.
53. Chen, M. and Williams, S., *Modelling and Optimization of SCR-Exhaust Aftertreatment Systems.* SAE Paper 2005-01-0969, 2005.
54. Chi, J. and DaCosta, H., *Modeling and Control of Urea-SCR Aftertreatment System.* SAE Paper 2005-01-0966, 2005.
55. Ciardelli, C., Nova, I., Tronconi, E., Konrad, B., Chatter, D., Ecke, K., and Weibel, M., *SCR-DeNOx for diesel engine exhaust aftertreatment: unsteady-state kinetic study and monlity reactor modeling.* Chemical Engineering Science, 2004. **59**: p. 5301-5309.
56. Vradman, L., Herskowitz, M., Capek, L., Wichterlová, B., Brosius, R., and Martens, J.A., *Kinetic Experiments and MOdeling of a Complex DeNOx System: Decane Selective Catalytic Reduction of NOx in the Gas Phase and over an Fe-MFI Type Zeolite Catalyst.* Ind. Eng. Chem. Res., 2005. **44**: p. 4523-4533.
57. Epling, B., Hou, P., Luo, J., Wijayakoon, P., Li, W., and Schmeig, S. *Spatially Resolving the Different SCR Reactions*. in *Cross-Cut Lean Exhaust Emissions Reduction Simulations Workshop 2010*. 2010. Deaborn Michigan.
58. Hayes, R.E. and Kolackowski, S., *Introduction to Catalytic Combustion*. 1997, Amsterdam: Gordon and Breach Science Publishers.
59. Froment, G.F. and Bischoff, K.B., *Chemical Reactor Analysis and Design*. 1990, New York: John Wiley & Sons.
60. Perry, R. and Green, D., *Perry's Chemical Engineer's Handbook*. 6th ed. 1984, New York: McGraw Hill.
61. Barin, I., *Thermochemical Data of Pure Substances*. 3rd ed. 1985, New York, London, Sydney: John Wiley & Sons.
62. (Ed.), V.D.I., *VDI-Warmeatlas*. 1991, Dusseldorf: VDI Verlag.
63. Reid, R.C., Puausnitz, J., and Poling, B.E., *The properties of gases and liquids*. 1988, New York: McGraw Hill.
64. Fuller, E.N., Schettler, P.D., and Giddings, J.C., *A new method for the prediction of gas phase diffusion coefficients.* Ind. Eng. Chem. , 1966. **58**: p. 19-27.
65. Laidler, K.J., *Chemical Kinetics*. Third ed. 1997, New York: Benjamin Cummins.
66. Klinkert, S., Hoard, J., Sathasivam, S., Assanis, D., and Bohac, S., *Design of a Flow Reactor for Testing Multi-Brick Catalyst Systems Using Rapid Exhaust Gas Composition Switches.* ASME Paper ICEF2009-14016, 2009.
67. Northrop, W., *Particulate and Gas Phase Hyrdrocarbon Emissions From Partially Premixed Low Temperature Compression Ignition Combustion of Biodiesel*, in *Mechanical Engineering*. 2010, University of Michigan: Ann Arbor. p. 231.

68. Hagena, J., *The Impact of Fuel Injection Parameters on the Combustion , Emissions, and Performance of a Medium - Duty Diesel Engine*, in *Mechanical Engineering*. 2004, Univesity of Michigan: Ann Arbor. p. 111.
69. He, Y., *Development and Application of a Lean NOx Trap Model.* SAE Paper 2006-01-0686, 2006.
70. Depcik, C., Assanis, D., and Bevan, K., *A one-dimensional lean NOx trap model with a global kinetic mechanism that includes NH3 and N2O.* Int, J. Engine Res., 2007. **9**: p. 57-77.
71. Kwon, H., Baik, J., Kwon, Y., Nam, I., and Oh, S., *Detailed reaction kinetics over comercial three-way catalysts.* Chemical Engineering Science, 2007. **62**: p. 5042-5047.
72. Sampara, C., *Global Reaction Kinetics for Oxidation and Storage in Diesel Oxidation Catalysts*, in *Mechanical Engineering*. 2008, University of Michigan: Ann Arbor. p. 168.
73. Kiovsky, J.R., Koradia, P.B., and Lim, C.T., *Evaluation of a New Zeolitic Catalyst for NO_x Reduction with NH_3.* Ind. Eng. Chem. Prod. Res. Dev., 1980. **19**: p. 218-225.
74. Iwamoto, M., Yahiro, H., Mine, Y., and Kagawa, S., *Excessively Copper Ion-exchanged ZSM-5 Zeolites as Highly Active Catalysts for Direct Decomposition of Nitrogen Monoxide.* Chemistry Letters, 1989: p. 213-216.
75. Hamada, H., Kintaichi, Y., Sasaki, M., and Ito, T., *Selective reduction of nitrogen monoxide with propane over alumina and HZSM-5 zeolite.* Applied Catalysis, 1991. **70**: p. L15-L20.
76. Hamada, H., Kintaichi, Y., Sasaki, M., Ito, T., and Tabata, M., *Transition metal-promoted silica and alumina catalysts for the selective reduction of nitrogen monoxide with propane.* Applied Catalysis, 1991. **75**: p. L1-L8.
77. Valyon, J. and Hall, W.K., *Studies of the Surface Species Formed from NO on Copper Zeolites.* J. Phys. Chem., 1993. **97**: p. 1204-1212.
78. Petunchi, J.O. and Hall, W.K., *On the role of nitrogen dioxide in the mechanism of the selective reduction of NO_x over Cu-ZSM-5 zeolite.* Applied Catalysis B: Environmental, 1993. **2**: p. L17-L26.
79. Sjovall, H., Olsson, L., Fridell, E., and Blint, R.J., *Selective catalytic reduction of NOx with NH3 over Cu-ZSM-5 - The effect of changing the gas composition.* Applied Catalysis: B Environmental, 2006. **64**: p. 180-188.
80. Kijlstra, W., Daamen, J., van de Graaf, J., van der Linden, B., Poels, E., and Bliek, A., *Inhibitng and deactivating effects of water on selective catalytic reduction of nitric oxide with ammonia over MnOx/Al2O3.* Applied Catalysis B: Environmental, 1996. **7**: p. 337-357.
81. Hadjiivanov, K., Klissurski, D., Ramis, G., and Busca, G., *Fourier transform IR study of NO_x adsorption on a CuZSM-5 $DeNO_x$ catalyst.* Applied Catalysis B: Environmental, 1996. **7**: p. 251-267.
82. Petunchi, J.O., Sill, G., and Hall, W.K., *Studies of the selective reduction of nitric oxide by hydrocarbons.* Applied Catalysis B: Environmental, 1993. **2**: p. 303-321.
83. Yokoyama, C. and Misono, M., *Catalytic Reduction of Nitrogen Oxides by Propene in the Presence of Oxygen over Cerium Ion-Exchanged Zeolites.* Journal of Catalysis, 1994. **150**: p. 9-17.

84. Grünert, W., Hayes, N.W., Joyner, R.W., Shpiro, E.S., Siddiqui, M.R.H., and Baeva, G.N., *Structure, Chemistry, and Activity of Cu-ZSM-5 Catalysts for the Selective Reduction of NO_x in the Presence of Oxygen.* J. Phys. Chem., 1994. **98**: p. 10832-10846.
85. Stevenson, S.A. and Vartuli, J.C., *The Selective Catalytic Reduction of NO_2 by NH_3 over HZSM-5.* Journal of Catalysis, 2002. **208**: p. 100-105.
86. Stevenson, S.A., Vartuli, J.C., and Sharma, S.B., *The Effects of Steaming and Sodium Exchange on the Selective Catalytic Reduction of NO and NO_2 by NH_3 over HZSM-5.* Journal of Catalysis, 2002. **208**: p. 106-113.
87. Wallin, M., Karlsson, C.-J., Skoglundh, M., and Palmqvist, A., *Selective catalytic reduction of NO_x with NH_3 over zeolite H-ZSM-5: influence of transient ammonia supply.* Journal of Catalysis, 2003. **218**: p. 354-364.
88. Stevenson, S.A., Vartuli, J.C., and Brooks, C.F., *Kinetics of the Selective Catalytic Reduction of NO over HZSM-5.* Journal of Catalysis, 2000. **190**: p. 228-239.
89. Eng, J. and Bartholomew, C.H., *Kinetic and Mechanistic Study of NO_x Reduction by NH_3 over H-Form Zeolites. I. Kinetic and Mechanistic Insights into NO Reduction over H-ZSM-5.* Journal of Catalysis, 1997. **171**: p. 14-26.
90. Delahay, G., Valade, D., Guzmán-Vargas, A., and Coq, B., *Selective catalytic reduction of nitric oxide with ammonia on Fe-ZSM-5 catalysts prepared by different methods.* Applied Catalysis B: Environmental, 2005. **55**: p. 149-155.
91. Krishna, K. and Makkee, M., *Preparation of Fe-ZSM-5 with enhanced activity and stability for SCR of NO_x.* Catalysis Today, 2006. **114**: p. 23-30.
92. Rahkamaa-Tolonen, K., Manunula, T., Lomma, M., Huuhtanen, M., and Keiski, R.L., *The effect of NO_2 on the activity of fresh and aged zeolite catalysts in the NH_3-SCR reaction.* Catalysis Today, 2005. **100**: p. 217-222.
93. Long, R.Q. and Yang, R.T., *Selective Catalytic Reduction of NO with Ammonia over Fe^{3+}-Exchanged Mordenite (Fe-MOR): Catalytic Performance, Characterization, and Mechanistic Study.* Journal of Catalysis, 2002. **207**: p. 274-285.
94. Auroux, A., Picciau, C., and Gervasini, A., *The adsorption and catalytic properties of Cu-ETS and Cu-ZSM molecular sieves in NO_x removal by reduction,* in *Porous Materials in Environmentally Friendly Processes*, I. Kiricsi, et al., Editors. 1999, Elsevier Science B. V. p. 555-562.
95. Lietti, L., Nova, I., Tronconi, E., and Forzatti, P., *Transient kinetic study of SCR-DeNOx reaction.* Catalysis Today, 1998. **45**: p. 85-92.
96. Perdana, I., Creaser, D., Öhrman, O., and Hedlund, J., *NO_x adsorption over a wide temperature range on Na-ZSM-5 films.* Journal of Catalysis, 2005. **234**: p. 219-229.
97. Marangozis, J., *Comparison and Analysis of Intrinsic Kinetics and Effectiveness Factors for the Catalytic Reduction of NO with Ammonia in the Presence of Oxygen.* Ind. Eng. Chem. Res., 1992. **31**: p. 987-994.
98. Brosius, R., Habermacher, D., Martens, J.A., Vradman, L., Herskowitz, M., Čapek, L., Sobalík, Z., Dědeček, J., Wichterlová, B., Tokarová, V., et al., *NO oxidation kinetics on iron zeolites: influence of framework type and iron speciation.* Topics in Catalysis, 2004. **30/31**: p. 333-339.

99. Gordon, S. and McBride, B., *Computer Program for Calculation of Complex Chemical Equilibrium Compositions, Rocket Performance, Incident and Reflected Shocks and Chapman-Jouguet Detonations.* NASA, 1971. **SP-273**.
100. Stull, D. and Prophet, H., *JANAF thermochemical table.s*. 2nd ed. 1971, Washington D. C.: U.S. National Bureau of Standards.
101. Nova, I., Lietti, L., Tronconi, E., and Forzatti, P., *Transient response method applied to kinetic analysis of the DeNOx-SCR reaction.* Chemical Engineering Science, 2001. **56**: p. 1229-1237.
102. Tsutsumi, K., Kajiwara, H., and Takahashi, H., *Characteristic Studies on Dealumination of Faujasite-type Zeolite.* Bulletin of the Chemical Society of Japan, 1974. **47**(4): p. 801-805.
103. Tsutsumi, K., Qui Koh, H., Hagiwara, S., and Takahashi, H., *Direct Measurement of Interaction Energy between Solids and Gases. I. Heat of Adsorption of Ammonia on Zeolite.* Bulletin of the Chemical Society of Japan, 1975. **48**(12): p. 3576-3580.
104. Anderson, J.R., Foger, K., Mole, T., Rajadhyaksha, R.A., and Sanders, J.V., *Reactions on ZSM-5-Type Zeolite Catalysts.* Journal of Catalysis, 1979. **58**: p. 114-130.
105. Auroux, A., Bolis, V., Wierzchowski, P., Gravelle, P.C., and Vedrine, J.C., *Study of the Acidity of ZSM-5 Zeolite by Microcalorimetry and Infrared Spectroscopy.* Journal Chemical Society of Faraday?, 1979. **75**: p. 2544-2555.
106. Auroux, A., Wierzchowski, P., and Gravelle, P.C., *Microcalorimetric Evidence of the Non-Uniform Distribution of Acid Sites in a ZSM-Type Zeolite.* Thermochimica Acta, 1979. **32**: p. 165-170.
107. Kanazirev, V. and Borisova, N., *Temperature programmed desorption studies on the penetration of ammonia into the sodalite cages of A, X and Y type zeolites.* Zeolites, 1982. **2**: p. 23-28.
108. Post, J.G. and van Hooff, J.H.C., *Acidity and activity of H-ZSM-5 measured with NH_3-t.p.d. and n-hexane cracking.* Zeolites, 1984. **4**: p. 9-14.
109. Tøpsoe, N.-Y., Pedersen, K., and Derouane, E.G., *Infrared and Temperature-Programmed Desorption Study of the Acidic Properties of ZSM-5-Type Zeolites.* Journal of Catalysis, 1981. **70**: p. 41-52.
110. Védrine, J.C., Auroux, A., Bolis, V., Dejaifve, P., Naccache, C., Wierzchowski, P., Derouane, E., Nagy, J., Gilson, J., van Hooff, J., van den Berg, J., and J. Wolthuizen, *Infrared, Microcalorimetric, and Electron Spin Resonance Investigations of the Acidic Properties of the H-ZSM-5 Zeolite.* Journal of Catalysis, 1979. **59**: p. 248-262.
111. Xu, L., McCabe, R.W., and Hammerle, R.H., *NO_x self-inhibition in selective catalytic reduction with urea (ammonia) over a Cu-zeolite catalyst in diesel exhaust.* Applied Catalysis B: Environmental, 2002. **39**: p. 51-63.
112. Louis-Rose, I., Methivier, C., and Pradier, C., *Oxidation of NH3 on polycrystalline copper and Cu(1 1 0): a combined FT-IRAS and kinetics investigation.* Catalysis Today, 2003. **85**: p. 267-278.

113. Chatterjee, D., Burkhardt, T., Weibel, M., Tronconi, E., Nova, I., and Ciardelli, C., *Numerical Simulation of $NO/NO_2/NH_3$ Reactions on SCR-Catalytic Converters: Model Development and Applications.* SAE Paper 2006-01-0468, 2006.
114. Hidalgo, C.V., Itoh, H., Hattori, T., Niwa, M., and Murakami, Y., *Measurement of the Acidity of Various Zeolites by Temperature-Programmed Desorption of Ammonia.* Journal of Catalysis, 1984. **85**: p. 362-369.
115. Iwamoto, M., Tajima, M., and Kagawa, S., *The Effect of Zeolite Composition and Structure on the Acidity of Proton-exchanged Zeolites.* J. Chem. Soc., Chem. Commun., 1986: p. 598-600.
116. Schmieg, S.J. and Lee, J.-H., *Evaluation of Supplier Catalyst Formulations for the Selective Catlaytic Reduction of NO_x With Ammonia.* SAE Paper 2005-01-3881, 2005.
117. Centi, G., Nigro, C., Perathoner, S., and Stella, G., *Role of the Support and of Adsorbed Species on the Behavior of Cu-based Catalysts for NO Conversion.* Catalysis Today, 1993. **17**: p. 159-166.
118. Heck, R.M., *Catalytic abatement of nitrogen oxides - stationary applications.* Catalysis Today, 1999. **53**: p. 519-523.
119. Amiridis, M.D., Puglisi, F., Dumesic, J.A., Millman, W.S., and Topsøe, N.-Y., *Kinetic and Infrared Spectroscopic Studies of Fe-Y Zeolites for the Selective Catalytic Reduction of Nitric Oxide by Ammonia.* Journal of Catalysis, 1993. **142**: p. 572-584.
120. Qi, G. and Yang, R.T., *Ultra-active Fe/ZSM-5 catalyst for selective catalytic reduction of nitric oxide with ammonia.* Applied Catalysis B: Environmental, 2005. **60**: p. 13-22.
121. Depcik, C., *Modeling Reacting Gases and Aftertreatment Devices for Internal Combustion Engines*, in *Mechanical Engineering*. 2003, The University of Michigan: Ann Arbor, Michigan.
122. Kato, A., Matsuda, S., Kamo, T., Nakajima, F., Kuroda, H., and Narlta, T., *Reaction between NOx and NH3 on Iron Oxide-Titanium Oxide Catalyst.* Journal of Physical Chemistry, 1981. **85**(26): p. 4099-4102.
123. Li, Y. and Armor, J.N., *Selective NH_3 oxidation to N_2 in a wet stream.* Applied Catalysis B: Environmental, 1997. **13**: p. 131-139.
124. Komatsu, T., Nunokawa, M., Moon, I.S., Takahara, T., Namba, S., and Yashima, T., *Kinetic Studies of Reduction of Nitric Oxide with Ammonia on Cu^{2+}-Exchanged Zeolites.* Journal of Catalysis, 1994. **148**: p. 427-437.
125. Busca, G., Lietti, L., Ramis, G., and Berti, F., *Chemical and mechanistic aspects of the selective catalytic reduction of NO_x by ammonia over oxide catalysts: A review.* Applied Catalysis B: Environmental, 1998. **18**: p. 1-36.
126. Kieger, S., Delahay, G., Coq, B., and Neveu, B., *Selective Catalytic Reduction of Nitric Oxide by Ammonia over Cu-FAU Catalysts in Oxygen-Rich Atmosphere.* Journal of Catalysis, 1999. **183**: p. 267-280.
127. Gekas, I., Gabrielsson, P., Johansen, K., Bjørn, I., Kjær, J.H., Reczek, W., and Cartellieri, W., *Performance of a Urea SCR system combined with a PM and fuel optimized heavy-duty diesel engine able to achieve the Euro V emission limits.* SAE Paper 2002-01-2885, 2002.

128. Narayanaswamy, K. and He, Y., *Modeling of Copper-Zeolite and Iron-Zeolite Selective Catalytic Reduction (SCR) Catalysts at Steady State and Transient Conditions.* SAE Paper 2008-01-0615, 2008. **1**.
129. Lyon, R., *The NH3-NO-O2 Reaction.* International Journal of Chemical Kinetics, 1976. **VIII**: p. 315-318.
130. Stevenson, S., Vartuli, J., and Brooks, C., *Kinetics of the Selective Catalytic Reduction of NO over H-ZSM-5.* Journal of Catalysis, 2000. **190**: p. 228-239.
131. Stevenson, S., Vartuli, J., and Sharma, S., *The Effects of Steaming and Sodium Exchange on the Selective Catalytic Reduction of NO and NO2 by NH3 over HZSM-5.* Journal of Catalysis, 2002. **208**(1): p. 106-113.
132. Eng, J. and Bartholomew, C., *Kinetic and Mechanistic Study of NOx Reduction by NH3 over H-Form Zeolites.* Journal of Catalysis, 1997. **171**: p. 14-26.
133. Komatsu, T., Nunokawa, M., Moon, I., Takkahara, T., Namba, S., and Yashima, T., *Kinetic Studies of Reduction of Nitric Oxide with Ammonia on Cu2+-Exchanged Zeolites.* Journal of Catalysis, 1994. **148**(2): p. 427-437.
134. Grossale, A., Nova, I., Tronconi, E., Chatterjee, D., and Weibel, M., *The chemistry of the NO/NO2-NH3 "fast" SCR reaction over Fe-ZSM5 investigated by transient reaction analysis.* Journal of Catalysis, 2008. **256**: p. 312-322.
135. Ciardelli, C., Nova, I., Tronconi, E., Chatterjee, D., Bandl-Konrad, B., Weibel, M., and Krutzsch, B., *Reactivity of NO/NO2-NH3 SCR system for diesel exhaust aftertreatment: Identification of reaction network as a function of temperature and NO2 feed content.* Applied Catalysis B: Environmental, 2007. **70**: p. 80-90.
136. Devarakonda, M., Tonkyn, R., Tran, D., Lee, J., and Herling, D. *Modeling Competitive Adsorption in Urea-SCR Catalysts for Enhanced Low Temperature NOx Control*. in *2010 DOE Crosscut Workshop on Lean Emissions Reduction Simulation*. 2010. Dearborn, MI.
137. Despres, J., Koebel, M., Krocher, O., Elsener, M., and Wokaun, A., *Adsorption and desorption of NO and NO2 on Cu-ZSM-5.* Microporous and Mesoporous Materials, 2003. **58**: p. 175-183.
138. Komatsu, T., Uddin, M., and Yashima, T. *Zeolites: a refined tool for designing catalytic sites*. in *International Zeolite Symposium*. 1995. Amsterdam: Elsevier.
139. Jobson, E., Smedler, G., Malmberg, P., Bernier, H., Hjortsberg, O., Gottberg, I., and Rosén, Å., *Nitrous Oxide Formation Over Three-Way Catalyst.* SAE Paper 940926, 1994.
140. Koike, N. and Odaka, M., *Methane and Nitrous Oxide (N_2O) Emission Characteristics from Automobiles.* SAE Paper 960061, 1996.
141. Koike, N., Odaka, M., and Suzuki, H., *Reduction of N_2O from Automobiles Equipped with Three-Way Catalyst - Analysis of N_2O Increase Due to Catalyst Deactivation.* SAE Paper 1999-01-1081, 1999.
142. Odaka, M., Koike, N., and Suzuki, H., *Deterioration Effect of Three-way Catalyst on Nitrous Oxide Emission.* SAE Paper 980676, 1998.
143. Ramanathan, V., Cicerone, R.J., Singh, H.H., and Kiel, J.T., *Trace Gas Trends and Their Potential Role in Climate Change.* Journal of Geophysical Research - Atmospheres, 1985. **90**: p. 5547-5566.
144. Bowman, K.P., *Global Trends in Total Ozone.* Science, 1988. **239**(4835): p. 48-50.

145. Callis, L.B. and Natarajan, M., *Ozone and Nitrogen-Dioxide Changes in the Stratosphere During 1979-84.* Nature, 1986. **323**(6091): p. 772-777.
146. Weiss, R.F., *The Temporal and Spatial-Distribution of Tropospheric Nitrous-Oxide.* Journal of Geophysical Research - Atmospheres, 1981. **86**: p. 7185-7195.
147. Brandin, J.G.M., Andersson, L.A.H., and Odenbrand, C.U.I., *Catalytic Reduction of Nitrogen Oxides on Mordenite Some Aspect on the Mechanism.* Catalysis Today, 1989. **4**: p. 187-203.
148. Valyon, J. and Hall, W.K., *Studies of the Desorption of Oxygen from Cu-Zeolites during NO Decomposition.* Journal of Catalysis, 1993. **143**: p. 520-532.
149. Busca, G., Larrubia, M.A., Arrighi, L., and Ramis, G., *Catalytic abatement of NO_x: Chemical and mechanistic aspects.* Catalysis Today, 2005. **107-108**: p. 139-148.
150. Mauvezin, M., Delahay, G., Kiblich, F., Coq, B., and Kieger, S., *Catalytic reduction of N2O by NH3 in the pressence of oxygen using Fe-exchanged zeolites.* Catalysis Letters, 1999. **62**: p. 41-44.
151. Kisliuk, P., *The Sticking Probabilities of Gases Chemisorbed on the Surfaces of Solids.* Journal of Phisics and Chemistry Solids, 1957. **3**: p. 95-101.
152. Koltsakis, G. and Stameatelos, A., *Development and appickation range of mathematical models for 3-way catalysts.* Applied Catalysis B: Environmental, 1997. **12**: p. 161-191.
153. Koltsakis, G. and Stameatelos, A., *Modeling dynamic phenomena in 3-way catalytic converters.* Chemical Engineering Science, 1999. **54**: p. 4567-4578.
154. Bohac, S., *Follow-Up Work On: Compositional Analysis of Reformer - Out Exhaust Gas*. 2009, University of Michigan: Ann Arbor.
155. Kuo, J., Morgan, C., and Lassen, H., *Mathematical Modeling of CO and HC Catalytic Converter Systems.* SAE Paper 710289, 1971.
156. Olsson, L. and Anderson, B., *Kinetic Modeling in Automotive Catalysis.* Topics in Catalysis, 2004. **28**(1-4): p. 89-98.
157. Millet, C. and Benramdhane, S., *A 3WCC Global Kinetic Model: A Calibration Method Using Laboratory Scale and Engine Test Bench Experiments.* SAE Paper 2008-01-0453, 2008. **1**.
158. Chen, W., Hsieg, T., and Jiang, T., *An experimental study on carbon monixed conversion and hydrogen generation from water gas shift reaction.* Energy Conversion and Management, 2008. **49**: p. 2801-2808.
159. Oh, S. and Cavendish, J., *Transients of Monolith Catalytic Converters: Response to Step Changes in Feedstream Temperature as Related to Controlling Automobile Emissions.* Industrial and Engineering Chemistry Product Research and Development, 1982. **21**: p. 29.
160. Depcik, C., Loya, S., and Sriniasan, A., *Adaptive Carbon Monoxide Kinetic for Exhaust Aftertreatment Modeling.* ASME Paper IMECE2009-11173, 2009.
161. Sampara, C., *Global Reaction Kinetics for Oxidation and Storage in Diesel Oxidation Catalysts*, in *Mechanical Engineering*. 2008, University of Michigan: Ann Arbor. p. 147.
162. Forzatti, P., Lietti, L., Nova, I., and Tronconi, E., *Diesel NOx aftertreatment catalytic technologies: Analogies in LNT and SCR catalytic chemistry.* Catalysis Today, 2010.

163. Yang, J. and Jung, H., *The effect of temperature on NOx reduction by H2 in the presence of excess oxygen on a Pt/Al2O3 monolithic catalyst.* Chemical Engineering Journal, 2009. **146**: p. 11-15.
164. Kolli, N., Potvin, C., and Thomas, C., *Evidence for the Facile Formation of Nitrogen-Containing Compounds from NOx and Propene Species on Tungstated Zirconia-Based Catalysts: Are these Compounds Active or Spectator Species in the Selective Catalytic Reduction of NOx by C3H6?* Journal of Catalysis, 2008. **259**(2): p. 240-249.
165. Mosiewicz, P., Porshnev, P., Nester, S., Kennedy, L., Fridman, A., Rabovister, J., and Cygan, D., *Study of Low-Temperature Combustion in a Low-NOx Burner.* Combustion Science and Technology, 2000. **160**(1): p. 1-21.
166. Montreuil, C. and Lambert, C., *The Effect of Hydrocarbons on Selective Catalyzed Reduction of NOx over Low and High Temperature Catalyst Formulations.* SAE Paper 2008-01-1030, 2008. **1**.
167. Amin, N. and Chong, C., *SCR of NO with C3H6 in the Pressence of Excess O2 over Cu/Ag/CeO2-ZrO2 Catalyst.* Chemical Engineering Journal, 2005. **113**(1): p. 13-25.